

Swing eVTOL

Final Report

AE3200: Design Synthesis Exercise
Group 1



Delft University of Technology

This page has intentionally been left blank.

Swing eVTOL

Final Report

by

Group 1

Student Name	Initials	Student Number
Alessandro Tesse	AT	5471990
Brădut-Constantin Stanciu	BS	5534682
Ezra Cerpac	EC	5259347
Gregorio Boccaccini	GB	5484650
Koen Pijnacker	KP	5559138
Philip Groenemeijer	PG	5335574
Salman Mughal	SM	5478847
Stefano Kok	SK	4656091
Tim Guezen	TG	5565448
Zoltán Túri	ZT	5213762

Version	Amendment	Date
1.0	Draft	19/06/24
2.0	Final	25/06/24

Tutors: Prof. dr. F. Scarano, Dr. ir. F. F. J. Schrijer
Coaches: Ir. M. Moradi, Ir. T.M.L. De Ponti
Teaching Assistant: Ing. A. F. Khalil
Project Duration: April - June, 2024
Faculty: Faculty of Aerospace Engineering, Delft

Cover: *Swing eVTOL* render

Executive Overview

This report aims to present an innovative design for an Inter-Urban Air Mobility (UAM) vehicle, poised to transform short-to-medium distance transportation. The design focuses on an electric Vertical Take-Off and Landing (eVTOL) vehicle intended for travel within and between urban areas. A key challenge in Urban Mobility is addressing the last-mile issue; creating a vehicle with a minimal ground footprint that requires less landing space. Therefore, it can land at vertiports in very densely populated areas. Additionally, recognising the imminent environmental challenges, the project prioritises minimising the vehicle’s environmental impact.

The Mission Need Statement (MNS) and Project Objective Statement (POS) are as follows:

MNS: “Achieve Sustainable Inter-Urban Air Mobility with a low ground footprint vehicle.”

POS: “Design a low ground footprint, sustainable, urban transwing electric Vertical Take-Off and Landing vehicle within production costs of 2 M€, by ten students in ten weeks time.”

The Concept

The chosen concept has rotating wings, so the aircraft has two configurations. The first configuration is in cruise, where the wings are fully unfolded, and the *Swing eVTOL* flies like a general aviation aircraft. The second configuration is in hover, where it flies as a rotorcraft. The *Swing eVTOL* will take off in hover configuration, transition mid-air to cruise configuration to fly further and transition back to hover configuration to land. The rotating wings allow for very efficient cruise and a low ground footprint for landing.

Market Analysis

To analyse the rapidly expanding Urban Air Mobility (UAM) market, market segmentation is defined, and competitors are analysed. The current market segments are air taxis, airport shuttles, and interurban transport. Due to the low ground footprint and high range, the *Swing eVTOL* can be used in any of these markets and differentiates itself by also providing last-mile transport. Moreover, the Competition Analysis found that the main competitors are the Joby S4 and Archer Midnight, which both lack the low ground footprint and range combination, which provides the solution to the last-mile problem, establishing the *Swing’s* differentiation factor as can be seen in Table 1.

Table 1: Differentiation of *Swing eVTOL* in market segments

eVTOL	Air Taxi	Airport Shuttle	Intercity Flights	Last-mile transport
<i>Swing</i>	X	X	X	X
Joby S4	X	X	X	-
Archer Midnight	X	X	-	-
EHang 216-S	X	-	-	X

Furthermore, London is found to be the ideal geographical location linked to the four possible segments, and it provides the perfect partner in the UK Air Mobility Consortium. The Consortium will provide the perfect environment for UAM implementation, testing, and regulations.

Technical Risk Analysis

The technical risk analysis is a critical part of the project, as it identifies the likelihood and impact of potential risks associated with the *Swing’s* design and development. Key risks include propulsion failure, structural integrity of the aircraft and hinge, and power system reliability. Then, mitigation strategies and contingency

plans are outlined for each identified risk, ensuring the project can navigate technical challenges effectively. Examples of mitigation strategies are extensive testing and timely maintenance, and examples of contingency plans are detailed emergency procedures and protocols and emergency landing procedures. The successful integration was established through the improved risk maps.

Mission Profile

The mission profile for the *Swing eVTOL* is meticulously designed to ensure optimal performance and energy efficiency. The profile is divided into two main parts: the normal operational range and the emergency deviations. To ensure a longer battery life, only 60 % of the battery is used, but for emergencies, this full battery could be used. The mission profile starts with a vertical climb, followed by a transition to cruise configuration and a climb to cruise altitude. After cruise, the *Swing eVTOL* will descend and transition to hover configuration, so it can land vertically. The altitude and power of the aircraft for a typical mission of 250 km can be seen in Figure 1.

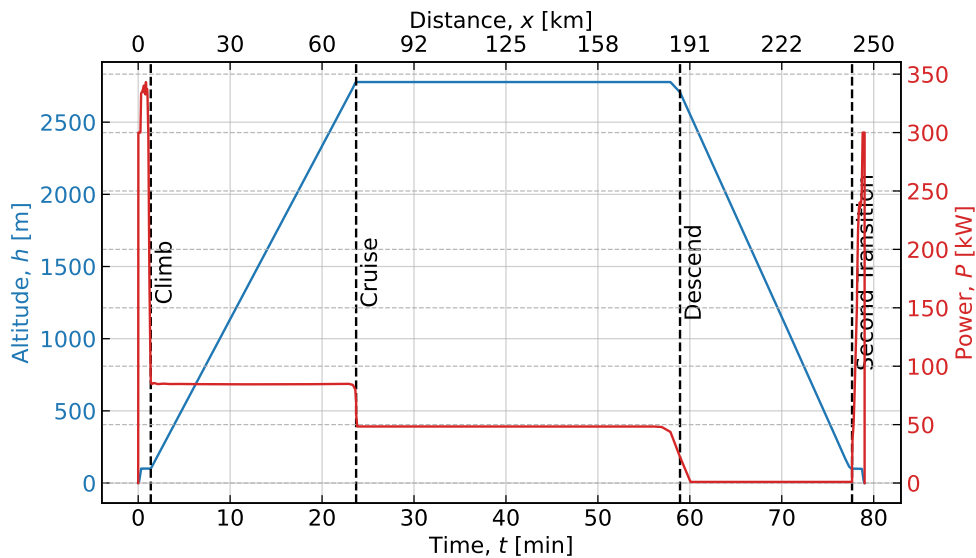
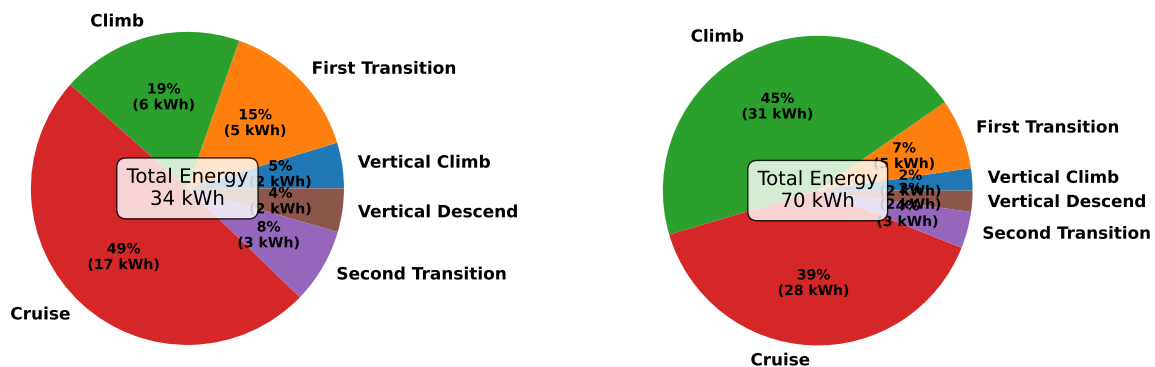


Figure 1: Altitude and engine power over distance and time of the mission profile with maximum range

The mission profile is optimised to minimise the aircraft's total energy consumption. This is achieved through a multiphase optimisation approach, where the different mission phases are modelled and optimised separately. The optimisation process considers various factors, such as the power required, the thrust produced by the engines, and the aerodynamic forces acting on the aircraft. The energy distribution resulting from the optimisation can be seen in Figure 2.



(a) Energy distribution of the nominal mission profile

(b) Energy distribution of the mission profile with maximum range

Figure 2: Energy distribution over the different phases of the mission profiles

Detailed Subsystem Design

Now that the mission profile is known, it is possible to start looking into the detailed design. The detailed design phase can be divided into six main subsystems that shape the *Swing eVTOL*.

Aerodynamics

The first subsystem that was designed is the Aerodynamics subsystem. From class I and class II estimations, a wing area of 14m is found, the wing planform was then optimised for the ground footprint, and the final wing parameters can be found in Table 2. From the airfoil analysis, the Eppler 560 airfoil was considered to be the best fit for the *Swing eVTOL*. After in-depth ergonomic analysis, it was found that the outer fuselage diameter is 1.7 m and that the fuselage should have a tadpole shape with a length of 8 m.

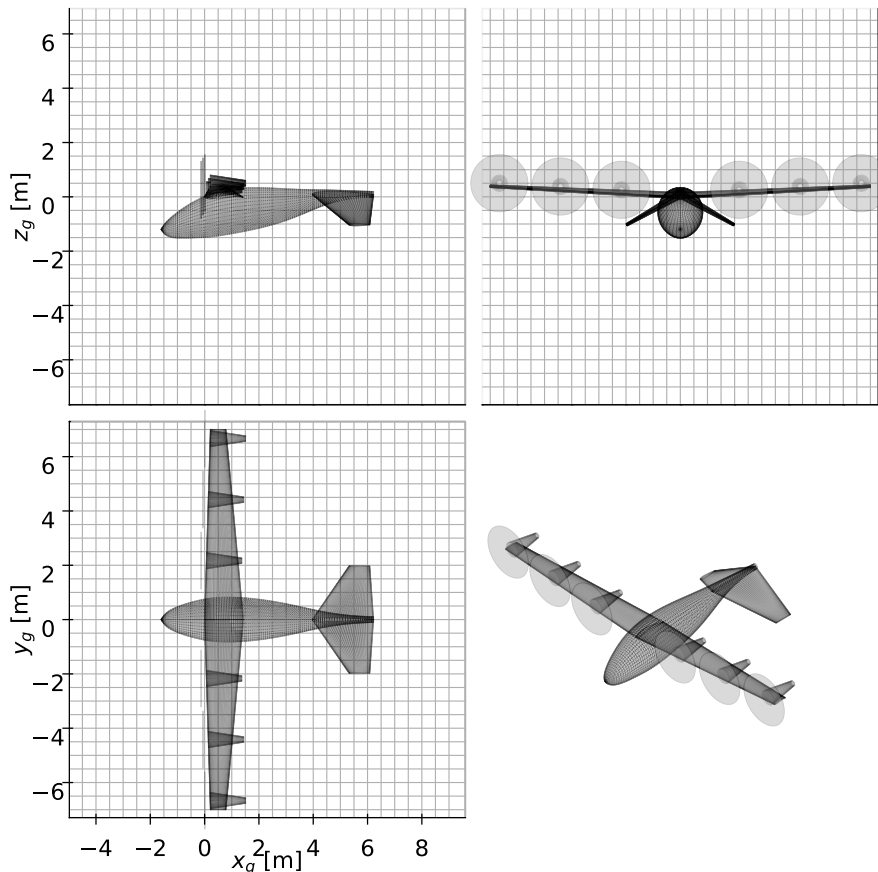


Table 2: Aerodynamic design values

S	14	m^2
b	14	m
A	14	–
c_r	1.42	m
c_t	0.57	m
MAC	1.06	m
y_{MAC}	3.0	m
$\Lambda_{c/4}$	0	deg
Λ_{LE}	2	deg
λ	0.4	–
Γ	1	deg
l_{fuselage}	8	m
d_{fuselage}	1.7	m
C_{D_0}	20.6	10^{-5}

Figure 3: Parametric Model used for Aerodynamic analysis

Class II drag estimations from Raymer [1] were used to find a C_{D_0} of 2.06×10^{-3} . The entire aircraft was then put into the AeroSandbox tool [2] as a parametric model, and more in-depth aerodynamic analysis was done to find stability derivatives. The parametric model can be seen in Figure 3

Power and Propulsion

After the aerodynamics and the weight of the aircraft have been established, with the maximum propeller diameter and number of engines of six (three engines per wing) obtained from considerations on geometry and disk loading, it is possible to determine the power curve of the *Swing eVTOL*. To obtain the power used by the engines as a function of horizontal airspeed, a power model encompassing characteristics of both helicopters and conventional aircraft is used. For the transition, required power and a surplus of power to facilitate acceleration are considered. This makes the transition phase the most power-hungry of the whole mission; Figure 4 is thus inserted in this overview.

Following the maximum total power of 343 kW, along with the noise and thrust requirements, the propellers

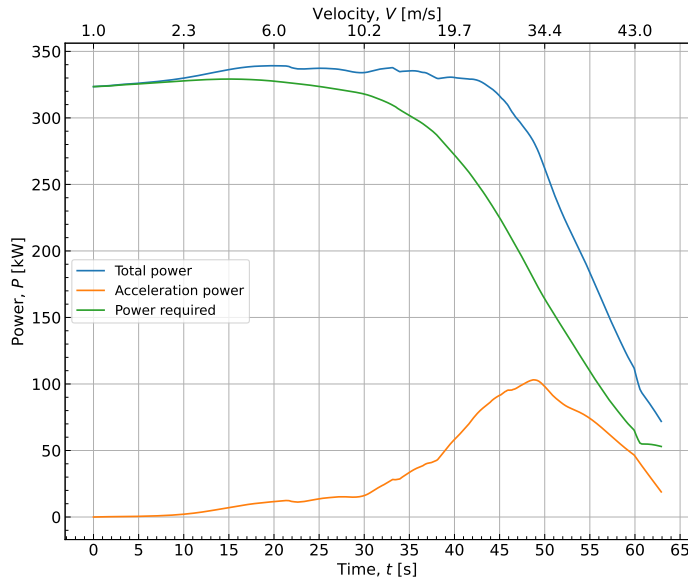


Table 3:
Specifications of
the chosen motor

Motor Name	Emrax 228
P_{\max} [kW]	75
T_{peak} [Nm]	130
RPM_{\max} (@ P_{peak})	6500 (124)
Mass [kg]	13.5
P/W [kW/kg]	5.6
$P_{\text{peak tot}}$ [kW]	450
$D \times L$ [mm]	228×86

Figure 4: Power curve for the transition phase, where the highest power levels are experienced

can be sized and the motor model selected. The specifications of the motor model chosen are tabulated in Table 3, whereas the final design values of the propulsion system are found in Table 4.

Table 4: Final propeller parameters

D_{prop}	Blade airfoil	Average blade chord	B	RPM	β
2.1 m	Clark-Y	14.7 cm	6	500-1300	35°

Structures & Materials

Given its great mechanical properties and weight savings, CFRP was chosen for most of the structure of the *Swing*, except for wing structural components like spars and stiffeners, which are made of aluminium. Glare is used for non-structural components on components most exposed to impacts due to its excellent tolerance to impact and damage.

The structural design focused on the design of the wing structure, as this was found to be the most structurally challenging component of the *Swing* due to the lack of a pressurised fuselage. A maximum load factor of 4.1 and a T/W ratio of 2 were used to compute the loads in cruise and vertical flight, respectively. Wing spars were designed to take the bending moments as well as the torques. The latter is also accounted for by the wing skin sizing, together with the buckling caused by compressive loads. The rib locations are chosen strategically to introduce point forces caused by the engines, hinge, and control surfaces. The final wing structural parameters are shown in Table 5, with their meaning indicated in Figure 5.

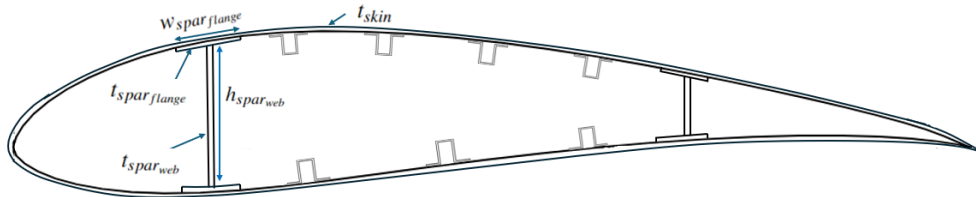


Figure 5: Wing Box structure with optimisation parameters

Table 5: Wing structure parameters. The x locations [m] indicate the distance from the root in meters.

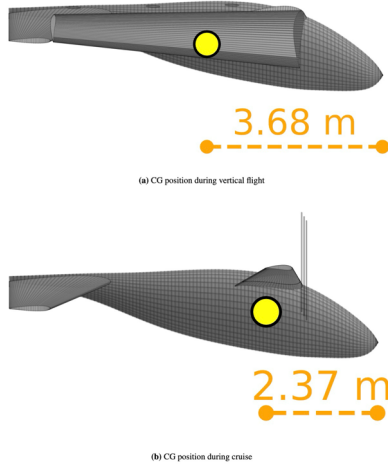
x [m]	$h_{\text{spar}_{\text{web}}}$ [mm]	$t_{\text{spar}_{\text{web}}}$ [mm]	$t_{\text{spar}_{\text{flange}}}$ [mm]	t_{skin} [mm]	$N_{\text{stringers}_{\text{top}}}$ [-]	$N_{\text{stringers}_{\text{bottom}}}$ [-]
0.00	227	1.50	2.8	1.5	4	3
0.85	211	1.50	2.8	1.5	4	3
1.80	192	1.34	2.5	1.0	4	3
2.15	185	1.31	2.5	1.0	4	2
4.50	140	1.11	2.5	1.0	3	2
6.84	94	0.91	2.5	1.0	2	1

After the basic structure of the wing was designed, an STO folding wing type was chosen, inspired by the Grumman F4F-4 Wildcat. The loads on the hinge were then used to size the titanium rod. This resulted in a 7.8 cm radius and a mass of 21.5 kg. An electrical linear actuator was finally chosen to allow for the hinge rotation.

Stability and Control

The report provides an in-depth analysis of the aircraft's stability and control mechanisms, including the design of control surfaces and the empennage. First and foremost, the design was analysed for controllability in the hover phase, making use of the ACAI algorithm [3]. Based on the algorithm, the required centre-of-gravity (CG) range of the design between cruise and hovering has been computed. Thus, a centre of gravity location of $X_{\text{CG}_{\text{cruise}}} = 2.37\text{m}$ during cruise was established, whereas in hover, the CG location was established to have a value of $X_{\text{CG}_{\text{hover}}} = 3.68\text{m}$.

Based on the CG ranges, stability and controllability analysis can be performed during cruise to size the horizontal and vertical stabilisers. Due to the ground footprint requirement, it was determined that a conventional vertical stabiliser is unfeasible. Thus, an inverted V-tail concept was chosen for further design iterations. Scissor plot analysis, as well as weathercock stability and engine inoperative controllability analysis, were performed to size the empennage. The final empennage parameters are provided below:

**Figure 6:** CG position during vertical and cruise flight**Table 6:** Final Tail Design

S_h	4.48	m^2
S_v	2.73	m^2
S_{tail}	7.21	m^2
A_v	1.52	–
A_h	2.50	–
Λ_h	0.40	–
Λ_v	0.40	–
v	31.36	–
b_{tail}	4.59	m
c_r	2.24	m
c_t	0.90	m

Lastly, the ailerons were sized in order to provide roll control. However, due to the increased roll moment caused by the battery placement, the ailerons were assumed to be placed throughout the entire wing. This was still insufficient to provide the required roll control stated in the requirements, only achieving a value of 60° in 6 s, compared to the requirement of 60° in 3.4 s [4].

Autonomous Systems

The conceptual design of the autonomous system was discussed in this report. To perform the route planning for the UAM, a multi-agent simple Probabilistic RoadMaps algorithm was selected [5], [6].

Furthermore, to facilitate unmanned guidance, three main control modes were deducted from the vehicle's mission profile. A position-tracking hexacopter control architecture with proportional derivative controllers was selected for vertical take-off, landing and hovering [7]. A gain-scheduling controller, with attitude altitude and torque impedance controllers, controls the transition [8]. Ultimately, the fixed-wing configuration is steered by a Model Predictive Contouring optimal controller [9], [10].

Finally, a revised sensor selection was performed to ensure that all the required states can be measured directly or indirectly. The obstacle detection and recognition are done by structured light stereo cameras and radar systems [11]. This computer vision performs adequately in low light intensity and bad weather conditions. The full state estimation of the UAM is done by GSNN GPS, IMU, pitot tube and thermal sensors. Furthermore, motor speed encoders, voltmeters, and ammeters are chosen to regulate the inputs of the actuators.

Electric Power System

Knowing the total energy and maximum power required for the mission profile makes it possible to size the power system. Firstly, a general literature study on lithium-ion batteries has been conducted. From this, the discharge behaviour during the mission profile has been retrieved. In particular, it has been made sure that the battery provides the necessary power at each flight phase. This is done by having six battery packs, each containing 768 cells. After knowing these parameters, it was possible to design the battery layout, and the cylindrical cells were chosen to build each pack. Next, the battery degradation process was studied, the life cycle of the battery pack was estimated, and the charging power rating was given. Lastly, battery cooling has been discussed, and liquid cooling has been chosen as a way to dissipate the heat during flight. The final parameters for the Electrical subsystem can be found in Table 7

Table 7: Final electrical system Values

P_{\max} [kW]	E_{tot} [kWh]	U_{nom} [V]	N_{pack} [-]	N_{cells} [-]	w_{eps} [kg]
343	120	710	6	768	400

Resource Allocation and Financial Analysis

The report outlines the resource allocation plan, detailing the interfaces between different subsystems and the overall project timeline. A comprehensive financial analysis is provided, including a detailed cost breakdown and an assessment of operational costs. The analysis is conducted taking into account the production of 200 eVTOLs in the span of five years, reaching the break-even point after 66 vehicles. The production costs of the *Swing* eVTOL are €1.42 million per unit, while the direct operational costs are €0.53 million per year, leading to €181 per flight hour. This breakdown does not, however, include the profit margins of the operator, thus making the cost to the final customer higher. Lastly, financial analysis has shown a return on investment of 10%, making the *Swing* eVTOL captivating for potential investors.

Production Plan

The production plan covers the entire manufacturing process, from the early stages of part design to the final assembly. Firstly, some considerations have been made about vertical and horizontal integration methods of the production process, analysing advantages, disadvantages, and competitors' choices. From this analysis, based on various criteria such as costs or supply chain, it has been possible to decide whether to produce each subsystem in-house or outsource the production. This resulted in most of the components being outsourced while producing in-house novel technologies that are highly specific to the project. Lastly, the production line configuration has been explored, deciding to follow the commercial aeroplane manufacturers' model, dividing the process into several stations for the different subsystems.

Sustainability Approach

A key focus of the project is sustainability. The report emphasises the eVTOL's energy consumption via missions analysis (Table 8) and its potential in revolutionising UAM. Emissions are evaluated, with low emissions predicted thanks to the low cruise speed of 200km/h. A “cradle-to-cradle” approach is adopted to minimise environmental impact, ensuring the repurposing of most of the vehicle components which are not directly recyclable. The impact of the *Swing* on urban environments is then evaluated, with a forecasted drastic alleviation of traffic congestion and significant improvements in urban noise and air pollution. Finally, economic potential is also predicted with the introduction of this vehicle. This is thanks to the creation of new job opportunities, enhanced connectivity between cities, and a boost in tourism.

Table 8: Sample missions energy consumption. Vertical flights include take-off and landing hovering phases.

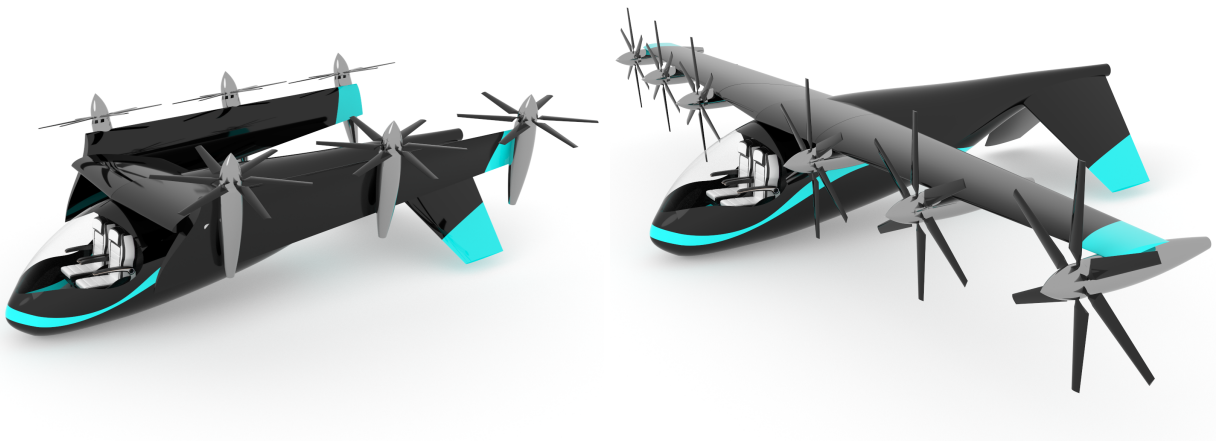
	$D_{\text{ground}}[\text{km}]$	$D_{\text{air}} [\text{km}]$	Avg EV [kWh]	Joby s4 [kWh]	Swing [kWh]
LCY-LHR	62	35	12	90	33
AMS-BRU	203	158	38	128	53

Final Design Overview

The final design can be found in Figures 7a and 7b. The final parameters of the *Swing* eVTOL can be found in Table 9.

Table 9: Final design parameters of the *Swing* eVTOL.

MTOW	1640	kg	Wing span	14.0	m
OEM	1240	kg	Wing area	14.0	m ²
Range	250	km	MAC	1.06	m
Payload	400	kg	Fuselage length	8.0	m
Battery mass	400	kg	No. Engines	6	–
Cruise speed	200	km/h	Battery energy	125	kWh
Stall speed	105	km/h	No. Passengers	4	–
Total Power	344	kW	Production Cost	1.42	M€



(a) Final design of *Swing* eVTOL in hover configuration

(b) Final design of *Swing* eVTOL in cruise configuration

Figure 7: Final design of *Swing* eVTOL

Contents

Executive Overview	i
1 Introduction	1
2 Market Analysis	2
2.1 UAM Market	2
2.2 Market Segmentation	3
2.3 Vertiports	3
2.4 UK Air Mobility Consortium	5
2.5 Competition Analysis	7
3 Functional Analysis	9
3.1 Functional Flow Diagram	9
3.2 Functional Breakdown Structure	9
4 Technical Risk Analysis	10
4.1 Technical Risks	10
4.2 Mitigation Strategies and Contingency Plans	11
5 Design Configuration	13
5.1 Trade-Off	13
5.2 Final Configuration	14
6 Mission Profile	15
6.1 Mission Overview	15
6.2 Mission Optimisation	15
6.3 Flight Performance	20
7 Aerodynamic Design	24
7.1 Wing Configuration	24
7.2 Wing Planform	24
7.3 Airfoil Selection	24
7.4 Fuselage Design	27
8 Aerodynamic Analysis	30
8.1 Drag	30
8.2 Aerodynamics of Full Parametric Model	32
8.3 Verification and Validation	33
9 Power	35
9.1 Power Required Model	35
9.2 Mission Power Curve	36
10 Propulsion	37
10.1 Engines Configuration	38
10.2 Propeller Design	40
10.3 Motor Selection	46
10.4 Verification and Validation (V&V)	47
11 Stability and Controllability	50
11.1 Preliminary Aileron Sizing	50
11.2 Controllability in Hover Mode	52
11.3 CG-Location Determination	54
11.4 Preliminary Estimation of Tail Size	56
11.5 Tail Configuration and Planform	57
11.6 Horizontal Tail Sizing	58
11.7 Vertical Tail Sizing	61
11.8 Dynamic Stability during Cruise	64
11.9 Results and Discussion	65
11.10 Verification & Validation	66
11.11 Further Iterations and Recommendation	68

12 Autonomous System	69
12.1 Autonomous Software Functions	69
12.2 Autonomous Software Architecture	69
12.3 Measurement System	75
13 Electric Power System	76
13.1 Preliminary Calculation	76
13.2 Battery Cells	77
13.3 Battery Design	80
13.4 Design Summary and Recommendations	83
14 Structures and Materials	84
14.1 Materials selection	84
14.2 V - n Diagram	86
14.3 Wing Structural Design	86
14.4 Aeroelastic Analysis	91
14.5 Hinge & Folding Mechanism Design	91
14.6 Undercarriage Design	94
14.7 Verification & Validation	95
15 Resource Allocation and Budget Breakdown	96
16 Interfaces	98
16.1 N2 Chart	98
16.2 Hardware Diagram	98
16.3 Data Handling Diagram	100
17 Operations and Logistics	101
17.1 Vertiports	101
17.2 RAMS Analysis	104
18 Sustainability Approach	108
18.1 Energy Consumption	108
18.2 Impact of the <i>Swing</i> on Urban Environments	109
18.3 Emission Performance Evaluation	109
18.4 Reusability of Vehicle Parts: the “Cradle to Cradle” Approach	110
18.5 Economic Sustainability of the <i>Swing</i> Project	112
19 Financial Analysis	113
19.1 Cost Breakdown Structure	113
19.2 Operational Costs	115
19.3 Return on Investment	116
20 Production Plan	117
20.1 Vertical or Horizontal Integration	117
20.2 Production Method by Subsystem	117
20.3 Assembly Line	118
21 Future Development Of Project	119
21.1 Design and Development Logic	119
21.2 Gantt Chart	119
22 Requirements Compliance	121
23 Conclusion and Recommendations	124
References	126
Appendix	136

1. Introduction

Commercial aviation has become integral to people's lives over the past decade, primarily facilitating long-distance travel between airports and connecting cities worldwide. However, after landing at the airport, usually another form of transportation (taxi, car or public transport) is needed to travel to the final destination. This raises the question: what if the so-called "last mile" can also be travelled by air?

This is where the concept of Inter-Urban Air Mobility (Inter-UAM) emerges. Inter-UAM envisions flying within large metropolitan areas or between smaller cities, offering a more extended range than Urban Air Mobility (UAM), greater than 100 km compared to approximately 30 km, and the capability to take off and land vertically at urban vertiports.

This report aims to identify a promising Inter-UAM design, the *Swing*, focused on minimising the aircraft's ground and environmental footprint. The small ground footprint will enable the vehicle to take off from smaller vertiports, helipads or even driveways, allowing it to penetrate urban areas and land where other UAM vehicles cannot. Additionally, the vehicle will be fully electric, contributing to a greener future. The following Mission Need Statement (MNS) and Project Objective Statement (POS) define the project aims:

MNS: *Achieve Sustainable Inter-Urban Air Mobility with a low ground footprint vehicle.*

POS: *Design a low ground footprint, sustainable, urban transwing electric Vertical Take-Off and Landing vehicle within production costs of 2 M€, by 10 students in 10 weeks.*

The present report can be split into three main parts: the first one focuses on analysing and refining the mission and on the preliminary design. This is done through a market analysis in Chapter 2 to assess the market, customer, and competition. This is followed by an in-depth functional analysis for each mission phase and a risk analysis in Chapters 3 and 4. The mission profile is defined and optimised in Chapter 6 from the functions and market analysis. The final chapter of the first part, Chapter 5, presents the trade-off of different concepts and preliminary sizing, which introduces the concept that will be designed in detail.

The second part of this report focuses on the detailed conceptual design and analysis of the different subsystems of the *Swing* aircraft. In Chapters 7 and 8, the aerodynamic surfaces will be sized and designed, and the aerodynamic properties of the entire eVTOL will be analysed. In Chapter 9, the power curve for the vehicle is constructed, from which the propulsion can be sized in Chapter 10. After this, the stability and control of the aircraft is analysed to design the empennage and control surfaces accordingly, in Chapter 11. Since the aircraft is an autonomous and electric VTOL, the autonomous control system and electric power system are also of great importance and are designed and analysed in Chapters 12 and 13 respectively. Finally, Chapter 14 will analyse the aircraft's structure and the hinge mechanism, where the materials will also be chosen.

The last part of this report will explain the resource allocation and interfaces of the design in Chapters 15 and 16. In Chapter 17, the operations and logistics of the aircraft will be described, followed by the sustainability approach in Chapter 18. Afterwards, a financial analysis is conducted in Chapter 19. In Chapter 20, the concept for the production of the aircraft will be sketched, followed by the future development of the project in Chapter 21. As a conclusion to the report, in Chapter 22 the final design will be checked for compliance with the original requirements, and an extensive compliance matrix is constructed accordingly.

2. Market Analysis

Analysing and understanding the Urban Air Mobility (UAM) market in Section 2.1 lays the foundation for the market entrance of the *Swing eVTOL*. After which, the deeper dive into the market segmentation in Section 2.2, in use cases and geographical locations, can point out the most interesting part of the market. The infrastructure, regulations and even attractive partnerships come with the market segmentation, which is discussed in Sections 2.3 and 2.4. Furthermore, the competition analysis in Section 2.5 provides more market context, paving the way for the differentiation factor of the *Swing eVTOL*.

2.1. UAM Market

The UAM market covers the new ways of transport in the third dimension, using the latest technologies in the eVTOL industry, which is hence of interest to this project. Although relatively new, it can be considered a very promising market. An in-depth market analysis performed by Roland Berger consultancy deems the UAM market to have great potential; by 2050, it could become a 90 billion USD market with 160 000 commercial UAM vehicles in use [12]. While currently at the beginning of its market maturity, it is valued at not even one billion USD, thus suitable for the market penetration of this transwing eVTOL design [13]. The total UAM market consists of at least the following applications: air taxis, airport shuttles, interurban transport, last-mile transport, air metro, private transport, military services, air emergency services, mapping, surveillance, and many more. Hence, various applications are suitable for the *Swing eVTOL*; however, those are discussed later in market segmentation (Section 2.2). Another recent market analysis on UAM that focused more on the air taxi applications, thus point-to-point passenger services, found that air taxis would replace non-discretionary travel of more than 45 min [14]. Therefore, concluding a daily demand of 82 000 passengers in the US only right now, hence around 4000 flight hours for a four-seater eVTOL like the *Swing eVTOL*. The market study also states that in the most conservative estimation, the air taxi market would already account for 2.5 billion USD. Therefore, this design is expected to be most successful in the air taxi segment, as the UAM market is highly dependent on its demand [15], confirmed by the previously discussed paper.

Stakeholders

Considering the UAM market, a distinction can be made between the four main stakeholder entities: lawmakers, users, suppliers, and other involved parties. More detailed stakeholders can be retrieved from these four, together with their interest and influence on this project. After an elaborate stakeholder analysis, which entailed identification and interest/influence estimation, the following stakeholder map is established in Figure 2.1. In particular, the investors, UAM operator prospects, Delft University of Technology, partnerships, maintenance contractors, vertiport operators, passengers, manufacturers, and air and ground regulatory agencies should be managed closely, as these significantly influence this project. Clear communication with these key stakeholders is important in conducting a successful project.

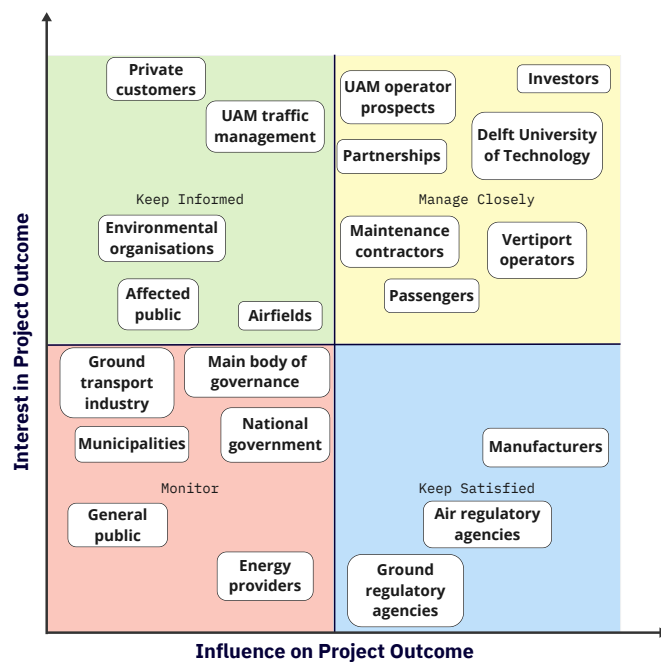


Figure 2.1: Stakeholder analysis

2.2. Market Segmentation

To successfully analyse the suitable market for this design, proper market segmentation needs to be conducted to fully grasp the design's possibilities. From the earlier stated applications, the main focus areas are on three leading use cases: air taxi, airport shuttle, and interurban transport [16]. Moreover, this is further solidified by the discussed 2.5 billion USD air taxi market that is currently possible [14]. A fourth and very specific use case is last-mile transport, which provides transportation to the exact final destination, where the design of the *Swing eVTOL* comes to fruition. Due to the novel transformative wing design, it can account for all these four cases, as it has a great range while still having a low ground footprint. However, this application's (competitive) advantage will be further discussed in Section 2.5.3. It should be noted that the *Swing eVTOL* can be compatible in other use cases as well, but for the first stages, these are the focus areas, hence the chosen market segment.

Before choosing a geographical market segment that fits the use cases, it is helpful to describe each in greater detail for clarification. Urban taxis, with a range of 15 to 50 km [12], account for fast travel times as well as high coverage in urban environments. Hence, needing a broad network of take-off and landing facilities, also known as vertiports and a closely managed UAM traffic control. Airport shuttles, also with a range of 15 to 50 km, establish a much faster airport-to-city, and vice versa, as well as an airport-to-airport network. This would greatly improve transfer times, transportation efficiency, and the experience that comes with airport travel. Interurban transport, with a range of 50 to 250 km, provides a high-speed option for further travel without needing lots of infrastructure while having a relatively predictable demand [16]. The fact that the *Swing eVTOL* can cover both inter- and urban transport due to its greater range for low ground footprint eVTOLs differentiates it from the current market. Lastly, the last-mile transport, or transport, can be in combination with any of the three use cases, hence delivering the option other current eVTOLs cannot satisfy.

Geographical

To thoroughly analyse and choose the market segment, a linked geographic location will benefit the team greatly in terms of the eventual regulations, partnerships, infrastructure, and competition. This also further defines the project's requirements, constraints, and risks. The metropolitan areas in continental Europe have been thoroughly analysed due to innovation, sustainably, and financially driven societies in combination with densely populated areas desperate for a solution. The most interesting candidates concluded Paris (urban transport), The Randstad (interurban transport), and London (inter- and urban transport). Eventually, London was the most attractive geographical market for the *Swing eVTOL* because of its densely populated city centre and surrounding cities that conclude the so-called "London borough". Therefore, making up for a combination of a vast urban environment that also accounts for interurban transport with its surrounding cities, tackling two of the use cases. With the newly found range of 250 km in Chapter 13, intercity flights from London to Manchester would even be possible. The airport shuttle case is also favourable for London, as the metropolitan area has six airports: Heathrow, Gatwick, Stansted, Luton, City, and Southend, with Heathrow being the largest airport in Europe. London is known to be rather traffic-dense, so the third dimension of transport provides the perfect solution. To exemplify, a trip from Heathrow to the city centre of London (32 km) would take 60 to 90 minutes by car and 55 minutes by train. However, with eVTOL vehicles, it would take merely 13 minutes [17], hence 47 to 77 minutes and 42 minutes faster than the current options, respectively. Furthermore, as the *Swing eVTOL* has a low ground footprint, the last-mile transportation is suitable in the tightly packed city of London. More importantly, a consortium has even been established, which focuses on being the front runner of UAM on a greater scale, and will be further discussed in Section 2.4.

2.3. Vertiports

As the infrastructure accommodating UAM is at the forefront of its technology and regulations, a deeper dive into vertiports is of great interest to the design. EASA's main regulatory framework states that a "vertiport means an area of land, water, or structure used or intended to be used for the landing and take-off of VTOL-capable aircraft" (EASA SC-VTOL-01) [18]. Therefore, vertiports is a collection term for

the different configurations of take-off and landing sites that facilitate UAM. They are fundamental to successfully introducing UAM, making for a more efficient means of travel. Considering these vertiports would have to be placed as strategically as possible for their designed transport, they must also include additional infrastructure, such as fast charging stations, maintenance stations, and commercial services. The implementation of vertiports is soon to be realised since the Olympic Games in Paris participates in the first test vertiport, accommodated by Skyports. The apparent benefit of UAM is the time efficiency that comes with it, as a trip to the Olympic stadium will be reduced from 50 to 15 minutes [19].

2.3.1. Typical configurations

These vertiports come in various configurations, personalised to their use case obviously, but also to the preferred size and position. More so with the *Swing eVTOL*, due to its low ground footprint of four parking spaces and wheel configuration, which make taxiing possible. Therefore, vertiports can be defined into three main types; verstops, vertibases, and vertihubs, exemplified in Figure 2.2. The vertistop configuration consist of one Final-Approach and Take-Off area (FATO), thus the most compact type of vertiport, acting only as a stop for the delivery of the payload, hence being applicable in most population-dense areas. Chapter 17 will elaborate further upon the eventual emergency charging systems available in such a minimal configuration. The middle-sized vertiport would be the vertibase; which can either be placed on buildings and ground, and make up more than one FATO, some aprons, one terminal, and some extra services. Lastly, the vertihub concludes the largest configuration, consisting of multiple FATOs, many aprons, multiple terminals, air traffic control, maintenance stations, charging stations, and commercial services. Vertihubs would mainly be positioned at the edges of urban environment, taking up much space, or connected to airports. Due to the novel transwing design, the *Swing* would apply to all applications.



Figure 2.2: Vertiport configurations [19]

2.3.2. Regulations

Due to the already overly full airspace and the environmental impact that UAM will have, clear regulations regarding the vertiports are paramount. The main body regulating UAM in Europe is the European Union Aviation Safety Agency (EASA), while for the US and UK, it is formulated by the Federal Aviation Administration and UK UAM Consortium, respectively. However, because of the novelty of UAM and eVTOLs, the regulations are currently being made and adjusted. An exploratory study by the Dutch government, "Rijksoverheid", is a valuable source that combines all different regulations and analyses in one report [19]. So, combinations of the earlier stated bodies are considered for the regulations. Following the current EASA regulations, eVTOLs are classed in the "certified category", which adheres to the same laws as civil aviation. Although extensive legislation for eVTOL is still lacking, for the moment, it does not allow for automated flight. However, this is expected to change soon due to the implementation of automated flights in places like China and the United Arab Emirates. The latter aims to make Dubai the first city with a fully functioning network of vertiports.

A UAM study by McKinsey concluded that the biggest challenges for UAM, as well as for societal acceptance, consist of noise production, safety, and infrastructure [20]. They all mainly relate to the vertiport infrastructure; however, the noise regulations are somewhat vague at the moment. A report on eVTOLs is

the only one stating that for most urban environments, the maximum allowable noise at 25 feet (almost 8 m) is 88 dBA (A-weighted decibels) for a short period, while 80 dBA for a longer duration [21]. This is in line with the NASA aeroacoustic analysis of the relatively silent eVTOL; Joby S4, which in VTOL configuration produces 65 dBA at 330 feet, thus translates to 88 dBA at 25 feet [22]. Therefore, the *Swing eVTOL* aims to perform similarly to the Joby S4 to stay within the noise regulations.

Moreover, the area responsible for the VTOL operations is still up for debate, as there are many different approaches to the matter that influence safety greatly. The American FAA and Australian CASA still mostly compare vertiport regulations to heliports regarding landing area, noise, downwash, etc. However, EASA has developed the innovative Obstruction-Free Volume (OFV), which revolutionises the new VTOL dimensions used at vertiports (Figure 2.5) [18]. Taking the maximum eVTOL dimensions in their respective diameter, provides for a schematic Final-Approach and Take-Off area (FATO), realising safe operations and logistics. With aspects such as the new steep VTOL segments and the possibility of omnidirectional flight paths. The previously adhered regulations concluded the FATO, also known as the Take-off and Landing Area, as seen in Figure 2.3. Which is the current vertihub configuration as proposed by one of the main eVTOL manufacturers: Lilium. It clearly shows the needed infrastructure to realise a well-established vertihub; however, could even use multiple FATOs to account for the high traffic volume. Although the previously mentioned regulations are of great help, the central focus should be the UK regulations due to the chosen market segment. Hence, the next section will explore those regulations in greater detail.



Figure 2.3: Lilium vertiport configuration [19], [23]

2.4. UK Air Mobility Consortium

As the geographical market segment for this project is projected to be London, the UK Air Mobility Consortium is considered to be of paramount importance. More so, as the consortium accurately described their UAM Concept of Operations (CONOPS) for the London Environment [24], as well as being the main regulatory body of the UK's UAM. The Consortium consists of the UK's leading air traffic control provider; NATS, main airports; Heathrow and London City Airport, eVTOL manufacturers; Eve (Embraer), Vertical Aerospace and Volocopter, UAM developers; Atech (Embraer) and Harris Corporation, the leading vertiport provider; Skyports, and many more industry-leading partners. Hence, adhering to the Consortium's regulations and partnering up is of great interest to this project. The earlier mentioned CONOPS does not only focus on the introduction of UAM, but the whole phase of development of UAM, eVTOLS, and additional challenges are considered. The Consortium strives to be ahead of the technology, thus competition, hence using a wide array of partners. Therefore, the first step when, and even before, entering the market should be joining the UK UAM Consortium, as this project will significantly benefit from it.

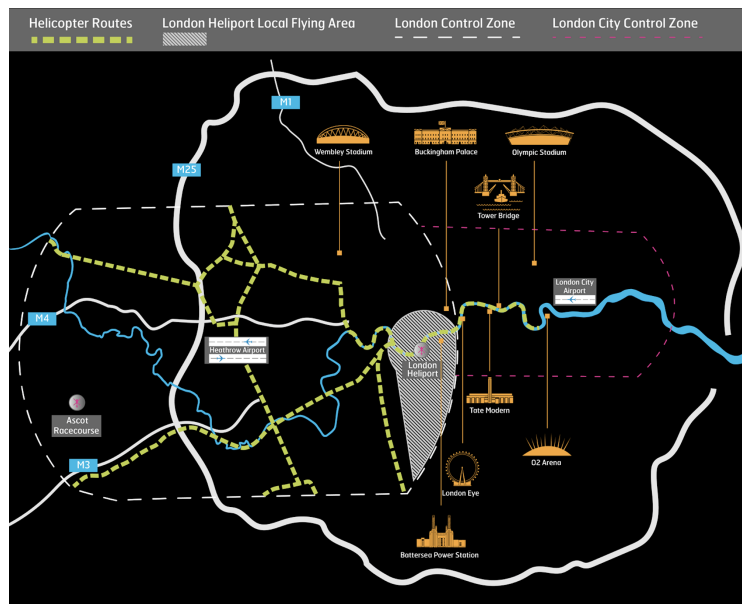


Figure 2.4: London helicopter routes (NATS) [24]

Besides the possibilities that the Consortium brings, it also provides the principal regulations regarding UAM, which is the main framework to adhere to. Therefore, joining the Consortium would relieve the team of much work on certifying and adhering to the current laws. The CONOPS already provides a pre-UAM defined landscape by performing tests with Skyports on a few London-based heliports, but also planning the first flights over the River Thames and highways, which will reduce the noise and privacy concerns of the public. As the network of heliports is already established in the metropolitan area of London, which can be seen from Figure 2.4, it will account for a fluent transition at the beginning of UAM integration. Furthermore, the Consortium also has provided a UAM network possible around the River Thames in London’s tightly packed city centre, mainly consisting of vertistops. Both in the current and future flight paths, due to noise and privacy concerns, mainly the River Thames and highways are considered, as seen from the figure.

Therefore, the extensive CONOPS provided by the Consortium can be seen as the framework for the *Swing eVTOL* and shows the importance of joining it. Also, the active vertiport testbeds by Skyports, which have acquired two active heliports in London, are also available. An interesting addition to the CONOPS would, however, be the integration of the OFV into London vertiports (Figure 2.6), as this is one of the newest additions to UAM regulations, which is there to stay. The adjacent operations and logistics are discussed in Chapter 17 for additional vertiport information.

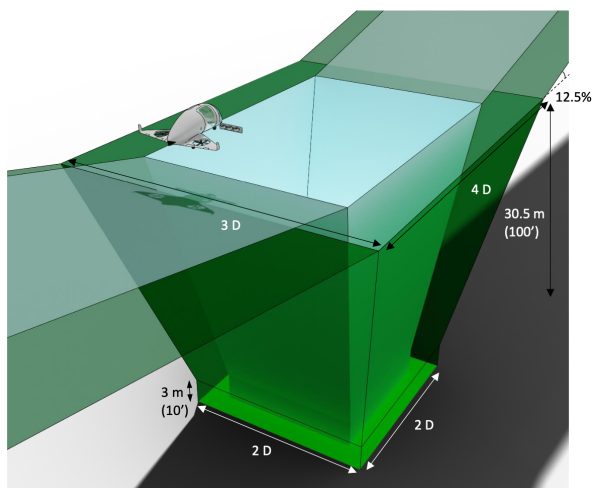


Figure 2.5: EASA's type 1 OFV [18]

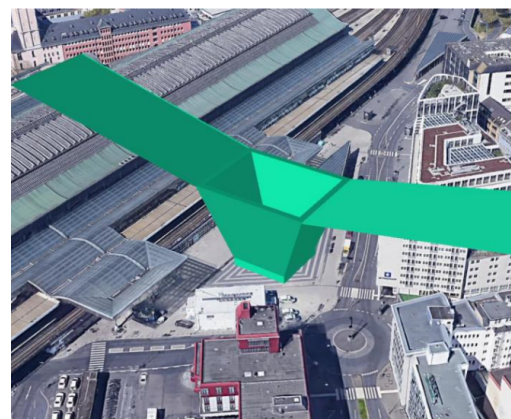


Figure 2.6: OFV train station integration [18]

2.5. Competition Analysis

As the exact market segmentation, infrastructure, and possible partnership have been established, it is helpful to analyse the competition to retrieve the main competitors. Conducting the competition analysis also provides more explicit competitive advantages and eventual disadvantages, further identifying the market position of the *Swing*. As stated earlier, the UAM is still in their infancy, making it easier for companies to penetrate the market. Although many configurations exist among the eVTOL UAM prospects, the ones in Table 2.1 can all facilitate the air taxi industry. However, as can be deduced from the table, the specifications, performances and prices differ significantly; hence, they should be compared to their close competition. The same goes for the *Swing eVTOL*; its main competitors should be identifiable from the table.

Table 2.1: Competition specifications [19], [25]

Configuration	Manufacturer	Project	Propulsion	Ground Footprint [m ²]	MTOW [kg]	Payload [pax]	Range [km]	Price [mil\$]
Multicopter	Volocopter	Velocity	18 rotors	128	900	1 + pilot	65	0.38
Multicopter	eHang	EH216-S	16 rotors	32	250	2	35	0.3
Lift + Cruise	Wisk	Cora	12 rotors + 1 pusher	70	-	2	100	-
Lift + Cruise	Beta Technologies	Alia	4 rotors + 1 pusher rotor	120	3175	4 + pilot	500	4
Lift + Cruise	Volocopter	VoloRegion	6 rotors + 2 ducted fans	-	-	4	100	-
Lift + Cruise	Autoflight	Prosperity I	13 rotors	168	1500	4	250	0.15
Vectored Thrust	Embraer X	EVE	8 rotors + 2 pusher rotors	124	997	4 + pilot	100	2
Vectored Thrust	Airbus	CityAirbus NextGen	8 rotors	182	1600	3 + pilot	80	-
Vectored Thrust	Lilium	Lilium Jet	36 ducted fans	118	3175	6 + pilot	250	4
Tiltrotor	Sabrewing	Rhaegal RG-1	4 ducted tiltrotors	248	4016	2454 kg	185	-
Tiltrotor	Joby Aviation	S4	6 tiltrotors	76	2404	4 + pilot	161	1.3
Tiltrotor	Vertical Aerospace	VX4	4 tilt + 4 stowable rotors	195	-	4 + pilot	161	4
Tiltrotor	Archer Aviation	Midnight	12 rotors (6 tiltrotors)	88	3175	4 + pilot	80	5
Transwing	DSE Group 1	Swing eVTOL	6 rotors	32	1643	4	250	2.2

When looking at Table 2.1, the most apparent distinction between vehicles is their configuration, thus the way of realising UAM. The multicopters, through their drone-like flight, are very stable and flexible in their low ground footprint; however, they lack the range for interurban travel. So-called “Lift+Cruise” configurations conclude separate lift rotors with cruise, or better-known pusher, rotors. The range gets remarkably better due to their wing designs; however, they do not have a low ground footprint suitable for population-dense areas. The same goes for the vectored thrust and tiltrotors configurations, although very innovative, it does not account for the needed low ground footprint. Hence, the transwing configuration perfectly tackles the problem of the competition, delivering the best of both worlds. Moreover, the prices of the last two configurations are considerably higher, while those of the multicopter are the lowest on average.



Figure 2.7: Joby S4 [25]



Figure 2.8: Archer Midnight [25]

2.5.1. Main Competitors

The Joby S4 (Figure 2.7) particularly stand out due to its relatively small wingspan in combination with a great range of 161 km. Also, as previously discussed, it is considered one of the quietest eVTOLs on the market, with a noise production of 65 dBA at 330 feet (100 m) in VTOL configuration, and only 45 dBA at

1640 feet (500 m) in cruise configuration [22], [26]. It is a competitor to be closely monitored, as it is the most promising in-production prospect. Although the *Swing eVTOL* still outperforms the Joby S4 on the ground footprint aspect, which may turn out to be the most constraining. Furthermore, the Archer Midnight (Figure 2.8) has already started production of 2300 units a year and secured a 1-billion-dollar order from United Airlines. It even got approval from the FAA for commercial flight and thus is realistically the main competitor on the market. However, the eVTOL comes with a relatively high price tag of 5 million USD with a limited range of 32 to 80 km and a comparatively high wingspan. Therefore, the *Swing* outperforms the range, ground footprint, and price, making it a more favourable prospect.

2.5.2. Mission SWOT Analysis

As a last measure, a mission Strengths Weaknesses Opportunities and Threats (SWOT) analysis provides the competitive edge of the *Swing eVTOL*. It is essential to note the positives; however, identifying the weaknesses and threats of the mission is of even greater interest. The final mission SWOT analysis is established in Figure 2.9.

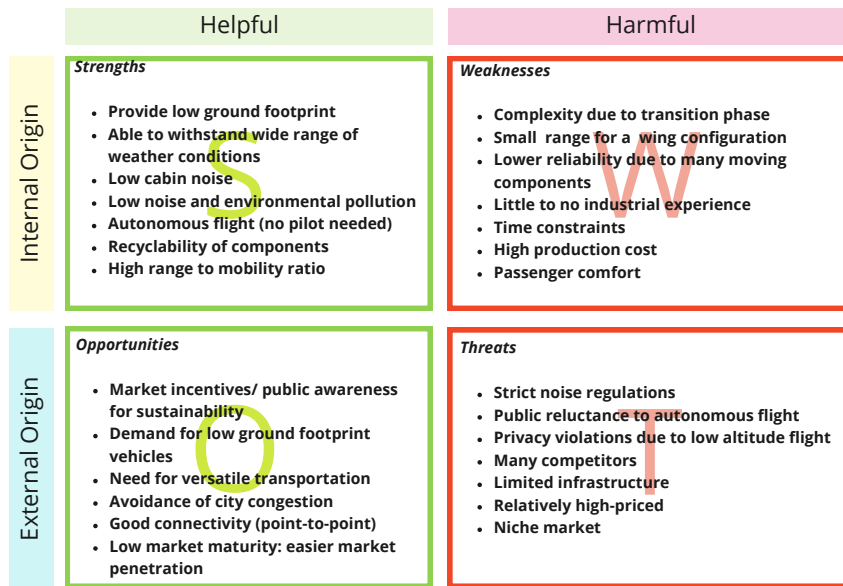


Figure 2.9: SWOT Analysis

2.5.3. Differentiation Factor

Concluding the market analysis, the differentiation factors of the *Swing eVTOL* ought to be discussed. The London metropolitan area is the perfect introductory market segmentation, facilitating all use cases and infrastructure, and a strong UAM partner in the UK Air Mobility Consortium. Moreover, the competition analysis showed the unique selling point of having a greater range while still accounting for a low ground footprint of four parking spots. This can even realise the heavily sought after last-mile transportation while still accommodating intercity flights. Table 2.2 perfectly shows the unique place of the *Swing eVTOL* in the UAM market, being able to capitalise on all the market segments. Moreover, the further competitive edge on energy consumption and cost will be discussed in Section 18.1. In the long term, certifications with ground regulatory bodies, instead of only air traffic, could be of great potential. The four parking spots truly bring a totally new dynamic within the UAM market.

Table 2.2: Differentiation of *Swing eVTOL* in market segments

eVTOL	Air Taxi	Airport Shuttle	Intercity Flights	Last-mile transport
<i>Swing</i>	X	X	X	X
Joby S4	X	X	X	-
Archer Midnight	X	X	-	-
EHang 216-S	X	-	-	X

3. Functional Analysis

This chapter outlines the analysis of the functions that have to be performed by the design. The analysis is based on the previously discussed market analysis in Chapter 2 and on the determined mission profile as showcased in Chapter 6.

3.1. Functional Flow Diagram

The project's functional flow is presented through a Functional Flow Diagram (FFD). The system requirements can be analysed based on the functional analysis to ensure mission performance within the desired characteristics. The FFD is presented in the Appendix and split into six phases, each describing the steps required for the product to reach design fulfilment. Different layers have been colour-coded to enhance the understanding of the flow diagram. The top layer (Layer 1) is blue, the first detail layer (Layer 2) is light-yellow, and the second detail layer (Layer 3) is purple. Additionally, to clarify the flow, special operators like "AND" and "OR" are used throughout the diagram to indicate whether one or both options should be considered further.

Another aspect that ought to be discussed is the expansion of the most critical layers, which will help further understand the design's functions. For each expansion, the corresponding layer element is illustrated. Additionally, due to space constraints, for some layers, such as the "Distribution" phase layer, the complete expanded layer could not be accommodated on the same A3 page. Therefore, layer expansions marked with B and C were moved to the following page.

The selection of functions of the vehicle that are presented in the functional flow was conducted based on the relevance of the functions throughout the vehicle's lifetime. Hence, the following phases are considered: designing, producing, testing, distributing, operating and recycling the product at the end of its life. Afterwards, each function is further detailed to provide a deeper understanding of the actions that need to be performed for the design to succeed. To further clarify, a legend is provided to showcase the generic layout. However, it is essential to note that the functions apply to any vehicle built in the production series. Therefore, the "Production" and "Testing" phases of the mission functions should be conceptualised based on the procedures used for any mass-produced vehicle. In contrast, the production and certification of the prototype is considered a sub-level of the design phase, meaning that the design certification itself is included within the design phase.

3.2. Functional Breakdown Structure

The following tool employed to achieve the mission profile is the Functional Breakdown Structure (FBS). It is a hierarchical representation of the functions to be conducted and, thus, a decomposition of the previously identified functions in the Functional Flow Diagram (FFD). Its purpose is to provide a detailed overview of the functions that must be performed. The same colour scheme as the FFD is used to aid in understanding the diagram. A new layer of detail, coloured cyan, is added to enhance comprehension of the functions. This extra layer is displayed as a list to provide a more precise overview of the functions to the diagram. Unlike the FFD, the FBS does not present functions in chronological order. Instead, they are grouped based on overarching logic using an "AND"-tree structure. The Appendix shows the flow breakdown structure of the *Swing eVTOL*, along with a legend to illustrate the generic layout of each of the four layers.

4. Technical Risk Analysis

This chapter performs a proper technical risk analysis to assess the *Swing eVTOL* extensively. Firstly, in Section 4.1, the risk likelihood and impact metrics are defined, as well as the risks themselves. Subsequently, the mitigation strategies and contingency plans are established in Section 4.2 to improve the risk maps (Figure 4.1).

4.1. Technical Risks

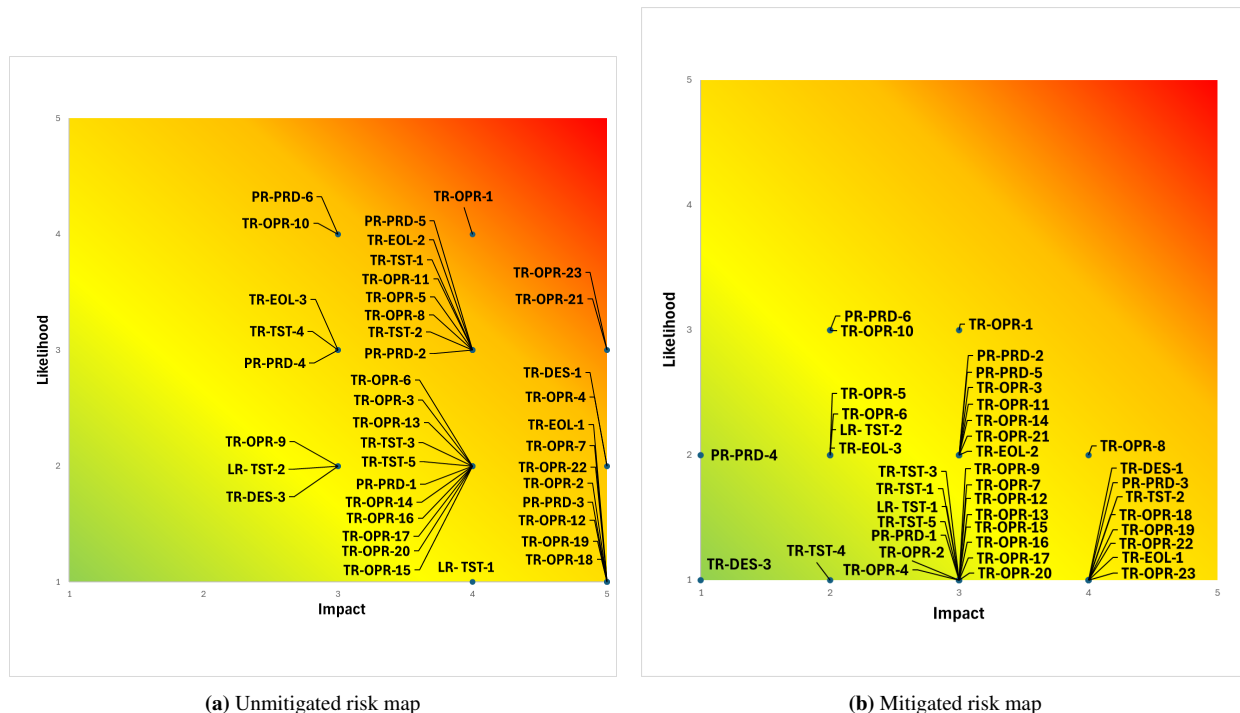
To identify and quantify risks correctly, in Tables 4.1 and 4.2, the following risk metrics for likelihood and impact are used. Through the use of these metrics, a well-defined risk analysis can be performed, multiplying each risk’s likelihood and impact, then dividing it by five to retrieve the risk factor. Table 4.3 establishes all the technical risk, each consisting of a risk ID, the main risk period, and a description of both risk and its impact. The risk ID contains the category, period, and chronological numbering in its ID, which will be mainly used for the identification in the risk maps. The risk factors, retrieved from Table 4.3, are plotted in the unmitigated risk map in Figure 4.1a, which will later be compared after the implementation of mitigation strategies and contingency plans.

Table 4.1: Likelihood metrics

Likelihood	Description	Probability
5	Very High	$P \geq 0.7$
4	High	$0.5 \leq P < 0.7$
3	Moderate	$0.3 \leq P < 0.5$
2	Low	$0.05 \leq P < 0.3$
1	Very Low	$P < 0.05$

Table 4.2: Impact metrics

Impact	Description
5	Catastrophic
4	Critical
3	Marginal
2	Acceptable
1	Negligible



(a) Unmitigated risk map

(b) Mitigated risk map

Figure 4.1: Technical risk maps

Table 4.3: Technical risks

Risk ID	Period	Risk Description	Impact Description	Unmitigated Risk		
				Likelihood	Impact	Risk
TR-DES-1	Design	Deficient thrust generation	Unable to take-off	2	5	2.0
TR-DES-2	Design	Unavailable Additive Manufacturing facilities	No 3D-model, so no visualisation of the design	2	3	1.2
PR-PRD-1	Production	Components too complex to manufacture	Part cannot be manufactured, thus an unfeasible design	2	4	1.6
PR-PRD-2	Production	Subcontractor does not meet deadlines	Delay of construction of the vehicle, testing and operations	3	4	2.4
PR-PRD-3	Production	Subcontractor's part not meeting requirements	Failure of components results into a delay of production	1	5	1.0
PR-PRD-4	Production	Part manufacturing costs go over-budget	Less budget for other segments or a budget shortfall	3	3	1.8
PR-PRD-5	Production	The required material is unavailable	Delay of production	3	4	2.4
PR-PRD-6	Production	Increase in material costs	Less budget for other segments or a budget shortfall	4	3	2.4
LR- TST-1	Testing	<i>Swing</i> is damaged during transportation	Extra time and budget needed to repair the <i>Swing</i>	1	4	0.8
LR- TST-2	Testing	Unavailable testing facility	Delay in testing or lack of physical test data	2	3	1.2
TR-TST-1	Testing	Hinge mechanism fails under wing loading	Crash of prototype, and repair/redesign needed	3	4	2.4
TR-TST-2	Testing	Unrealistic simulation data	Under-performance or crash of the <i>Swing</i>	3	4	2.4
TR-TST-3	Testing	Vehicle violates the noise regulations	Aero-acoustics have to be redesigned	2	4	1.6
TR-TST-4	Testing	No validation of the models	Uncertain if the design is valid and flyable	3	3	1.8
TR-TST-5	Testing	Inaccurate stability analysis	Unstable during flight stages	2	4	1.6
TR-OPR-1	Operations	Excessive maintenance	Unable to use vehicles, which increases delay and costs	4	4	3.2
TR-OPR-2	Operations	Power grid failure	Unable to charge the vehicles	1	5	1.0
TR-OPR-3	Operations	Damaged vertiport	Unable to take off or land properly	2	4	1.6
TR-OPR-4	Operations	Payload mass loaded is more than maximum	Unable to take off or causing emergency	2	5	2.0
TR-OPR-5	Operations	Sensors provide faulty or no data	Faulty navigation or output by systems	3	4	2.4
TR-OPR-6	Operations	Interference of communications	Navigation interference	2	4	1.6
TR-OPR-7	Operations	Power system fails	Loss of thrust, navigation and control	1	5	1.0
TR-OPR-8	Operations	Power drainage higher than expected in-flight	Unable to fly full range and diversion to other vertiport	3	4	2.4
TR-OPR-9	Operations	Navigation system fails	Unable to determine location and heading of the vehicle	2	3	1.2
TR-OPR-10	Operations	Damages infrastructure during take-off / landing	Increase in maintenance, repair costs and time	4	3	2.4
TR-OPR-11	Operations	Contact with animal	Possible fatal crash, involving casualties	3	4	2.4
TR-OPR-12	Operations	Contact with human	Possible fatal crash, involving casualties	1	5	1.0
TR-OPR-13	Operations	Folding mechanism malfunction during take-off	Unable to transition to cruise	2	4	1.6
TR-OPR-14	Operations	Folding mechanism malfunction during landing	Unable to land vertically	2	4	1.6
TR-OPR-15	Operations	One engine failure in VTOL configuration	No yaw control, causing undesired spinning	2	4	1.6
TR-OPR-16	Operations	Aileron failure	Limited roll control, oscillations may not be damped	2	4	1.6
TR-OPR-17	Operations	Ruddervator failure	Limited pitch and yaw control	2	4	1.6
TR-OPR-18	Operations	Battery pack failure	Total energy drop, not able to land vertically	1	5	1.0
TR-OPR-19	Operations	Autonomous system failure	Vehicle is not controlled	1	5	1.0
TR-OPR-20	Operations	Landing gear failure	Unable to land properly, causing an emergency landing	2	4	1.6
TR-OPR-21	Operations	Cybersecurity breach	Harmful intentions could result in a catastrophe	3	5	3.0
TR-OPR-22	Operations	In-flight fire	Immediate emergency landing	1	5	1.0
TR-OPR-23	Operations	Unforeseen flight conditions	Aircraft damaged and uncontrollable; emergency landing	3	5	3.0
TR-EOL-1	End of life	Vehicle suffers total breakdown	Unable to be fulfil its required lifetime	1	5	1.0
TR-EOL-2	End of life	Unable to be recycled after its life	Cannot meet the set sustainability goals	3	4	2.4
TR-EOL-3	End of life	Recycled components fail within 10 years	Cannot meet the set sustainability goals	3	3	1.8

4.2. Mitigation Strategies and Contingency Plans

To account for the established risks, mitigation strategies and contingency plans are in place to decrease the likelihood and impact, respectively. These are all listed in Table 4.4, and conclude the new risk factors in Table 4.5. Also, a responsible team member related to the area of risk is appointed to monitor and manage the risk carefully. With the newly acquired risk values, a mitigated risk map can be plotted in Figure 4.1b. The new risk map clearly illustrates a shift in risk likelihood and impact to better risk levels; hence, the mitigation strategies and contingency plans are successful. In the map, it can be also seen that TR-OPR-1 and TR-OPR8 are still situated in the orange level, a moderate risk level, and thus should be monitored closely throughout the project. The other risks have, however, decreased to a low to medium risk level (green and yellow), which makes the project less susceptible to risks.

Table 4.4: Mitigation strategies and contingency plans for risk management

Risk ID	Mitigation Strategy	Contingency Plan
TR-DES-1	Conduct thrust performance analysis	Alternative drop-in propulsion systems
TR-DES-3	Reserve a place at the AM facility ahead of time	Make use of personal 3D-printer
PR-PRD-1	Elaborate use of CAD and AM to visualise model	Use different materials and design options in CAD
PR-PRD-2	Constant monitoring and communication for deadlines	Change contractors or impose costs
PR-PRD-3	Use of test samples and prototypes before production	Change contractors or impose costs
PR-PRD-4	Establish cost agreements in contracts	Include extra budget for unforeseen costs
PR-PRD-5	Track material availability and buy in bulk	Establish material replacements beforehand
PR-PRD-6	Buy material in bulk, when the prices are within budget	Include extra budget for unforeseen costs
LR- TST-1	Elaborate inspection and testing before transportation	Multiple spare parts available
LR- TST-2	Clear communication with the testing facility	Multiple possible testing facilities
TR-TST-1	Use safety factors in loading analysis	Have spare hinge mechanism and wings available
TR-TST-2	Test subsystems thoroughly beforehand	Conduct limited testing and retrieve information
TR-TST-3	Extensive aeroacoustics analysis before testing	Retrieve aeroacoustics data and redesign
TR-TST-4	Use of validated models from similar research	Perform subsystem testing for validation
TR-TST-5	Use of Computational Fluid Dynamics (CFD)	Analyse and redesign control surfaces
TR-OPR-1	Design low-maintenance parts	Look for extra or better trained maintenance staff
TR-OPR-2	Careful power grid structure design	Have diesel generators available as backup
TR-OPR-3	Use of safety regulations near vertiports	Have an emergency alternative vertiport available
TR-OPR-4	Conduct mass estimation before take-off	Decrease payload by unloading passengers/cargo
TR-OPR-5	Conduct frequent inspection and maintenance	Emergency landing procedure to nearest vertiport
TR-OPR-6	Implement redundant communication systems	Emergency landing procedure to nearest vertiport
TR-OPR-7	Conduct regular inspections of power systems	Use backup power system or emergency landing
TR-OPR-8	Active battery monitoring on power consumption	Emergency landing procedure to nearest vertiport
TR-OPR-9	Redundant navigation systems	Emergency landing procedure to nearest vertiport
TR-OPR-10	Use of safety regulations and surroundings analysis	Determine emergency procedures and protocols
TR-OPR-11	Use of animal detection system	Determine emergency procedures and protocols
TR-OPR-12	Strict flight safety protocols	Determine emergency procedures and protocols
TR-OPR-13	Conduct extensive testing and maintenance	Emergency landing procedure to nearest vertiport
TR-OPR-14	Conduct extensive testing and maintenance	Emergency landing procedure to nearest airport
TR-OPR-15	Test engines before each flight and regularly inspection	Programmed emergency landing to nearest vertiport
TR-OPR-16	Conduct extensive testing and maintenance	Use of thrust differential to induce roll and land quickly
TR-OPR-17	Conduct extensive testing and maintenance	Use of thrust differential to induce yaw and land quickly
TR-OPR-18	Use active cooling and a battery management system	Isolate faulty battery pack and land quickly
TR-OPR-19	Implement hard and software redundancy	Implement Fail-Safe Mode to transition the vehicle safely
TR-OPR-20	Perform regular system checks	Programmed emergency landing to nearest vertiport
TR-OPR-21	Encryption of data and communication	Pre-programmed emergency landing or manual override
TR-OPR-22	Use of fire-resistant materials and coatings	Immediate descent and use of fire extinguishing system
TR-OPR-23	Use of weather forecasting and radar system	Immediate descent or navigate out of heavy weather
TR-EOL-1	Frequent maintenance and inspection	Investigate its cause
TR-EOL-2	Use of sustainable and recyclable materials	Extensive analysis on recyclable materials
TR-EOL-3	Frequent maintenance and inspection	Investigate its cause

Table 4.5: Mitigated risks

Risk ID	Responsible	Likelihood	Impact	Risk	Risk ID	Responsible	Likelihood	Impact	Risk
TR-DES-1	P&P DC	1	4	0.8	TR-OPR-7	P&P DC	1	3	0.6
TR-DES-3	CADM	1	1	0.2	TR-OPR-8	C&S DC	2	4	1.6
PR-PRD-1	CADM	1	3	0.6	TR-OPR-9	C&S DC	1	3	0.6
PR-PRD-2	CM	2	3	1.2	TR-OPR-10	FP DC	3	2	1.2
PR-PRD-3	CM	1	4	0.8	TR-OPR-11	RM	2	3	1.2
PR-PRD-4	CM	2	1	0.4	TR-OPR-12	RM	1	3	0.6
PR-PRD-5	RM	2	3	1.2	TR-OPR-13	S&M DC	1	3	0.6
PR-PRD-6	CM	3	2	1.2	TR-OPR-14	S&M DC	2	3	1.2
LR- TST-1	SE	1	3	0.6	TR-OPR-15	P&P DC	1	3	0.6
LR- TST-2	CO	2	2	0.8	TR-OPR-16	C&S DC	1	3	0.6
TR-TST-1	S&M DC	1	3	0.6	TR-OPR-17	C&S DC	1	3	0.6
TR-TST-2	QAO	1	4	0.8	TR-OPR-18	P&P DC	1	4	0.8
TR-TST-3	Aero DC	1	3	0.6	TR-OPR-19	C&S DC	1	4	0.8
TR-TST-4	SM	1	2	0.4	TR-OPR-20	FP DC	1	3	0.6
TR-TST-5	Aero DC	1	3	0.6	TR-OPR-21	C&S DC	2	3	1.2
TR-OPR-1	CM	3	3	1.8	TR-OPR-22	FP DC	1	4	0.8
TR-OPR-2	P&P DC	1	3	0.6	TR-OPR-23	FP DC	1	4	0.8
TR-OPR-3	QAO	2	3	1.2	TR-EOL-1	PM	1	4	0.8
TR-OPR-4	S&M DC	1	3	0.6	TR-EOL-2	SO	2	3	1.2
TR-OPR-5	C&S DC	2	2	0.8	TR-EOL-3	SO	2	2	0.8
TR-OPR-6	C&S DC	2	2	0.8					

5. Design Configuration

This chapter elaborates on the *Swing*'s configuration, using an earlier extensively performed trade-off in Section 5.1 and the preliminary design of the final configuration in Section 5.2.

5.1. Trade-Off

Previously, four different concepts were generated, differing in propulsion, wing and fuselage design. These concepts are preliminary sketches in Figure 5.1. A trade-off was conducted to select the best design, in which the concepts were graded based on six different criteria: transition efficiency, structural complexity, energy efficiency, safety and noise emissions. The concepts were scored on these criteria based on preliminary calculations.

The Class I preliminary sizing and Class II sizing were conducted to perform the trade-off. In Class I, the wing and power loading diagrams were constructed by setting constraints on the different mission phases. An initial surface area and power were calculated using the retrieved Class I information and competitor historical data. These values were used as input for the Class II sizing. In the Class II sizing, a method described by Ugwueze, Statheros, Horri et al. [27], which relies on the Cessna II method from Roskam [28], was used to design the initial subsystem mass, power and geometry. Moreover, a preliminary noise model was implemented to estimate the noise since this is a requirement set by the customers: Te-2-STK07-1-2. "The noise level within the cabin shall never exceed 65 [dBA]". After the preliminary sizing, the trade-off was conducted, which was won by C2.1 and can be seen in Table 5.1.

Table 5.1: Final trade-off

Criteria Concepts	CR-01	CR-02	CR-03	CR-04	CR-05	CR-06	Final Score
C1.5 (Winged Rotorcraft)	Full-sized model (4)	Excellent control, low CEF ¹ (3)	Six moving parts, low complexity, low loads (3)	Energy consumption 67.0 kWh (4)	Full redundancy (5)	Engine noise 122.7 dB, obstruction area 9m ² (3)	3.5
C2.1 (Rotating Wing)	Scale model highly tested (3)	Good control, excellent CEF (5)	Two moving parts, low complexity, high loads (3)	Energy consumption 73.2 kWh (3)	Fatal hinge failure (3)	Engine noise 125.2 dB, obstruction area 0.5m ² (4)	3.8
C2.6 (Folding Wing)	Full-sized model (4)	High control, low CEF (3)	Six moving parts, high complexity, medium loads (2)	Energy consumption 66.9 kWh (4)	Full redundancy (5)	Engine noise 120.6 dB, obstruction area 7.1m ² (3)	3.4
C2.10 (Variable Skew Quad Plane)	Scale model (2)	High control, low CEF (3)	One moving part, low complexity, medium loads (4)	Energy consumption 78.4 kWh (2)	Fail-safe (4)	Engine noise 134.2 dB, obstruction area 6m ² (2)	2.8

¹conversion effectiveness factor

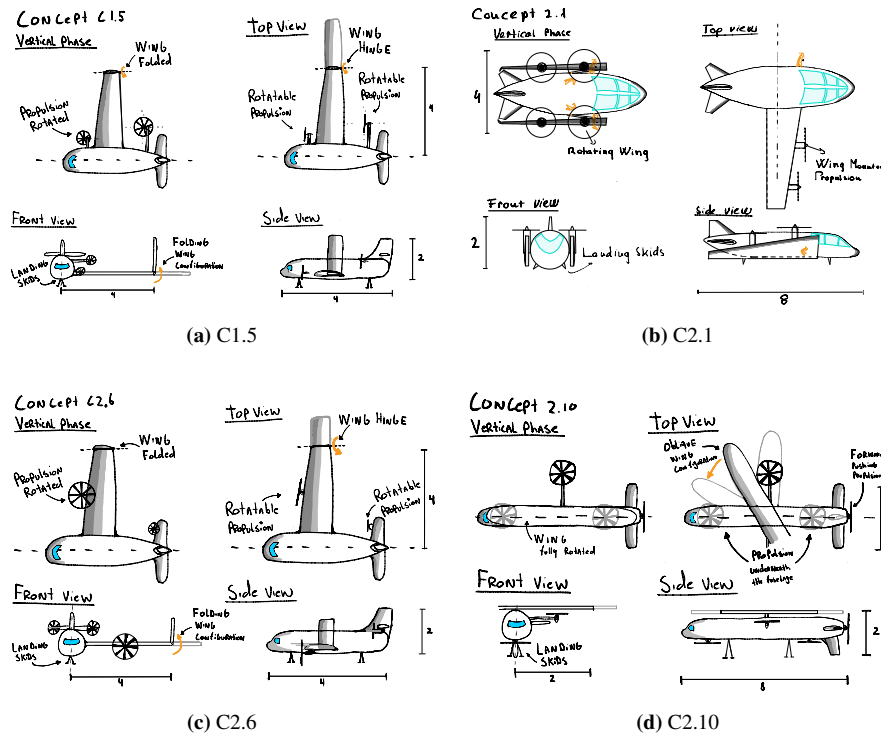


Figure 5.1: Four concepts eVTOL

5.2. Final Configuration

The final configuration, C2.1, utilises rotating wings to take off vertically and transform into a propeller aircraft at a higher altitude, better described in Section 6.1. The propulsion is fixed on the wings, so it rotates with the wing from vertical to horizontal alignment. To do so, a special hinge with only one specific axis of rotation is designed. From the preliminary sizing explained above, initial design parameters were obtained, which can be seen in Table 5.2.

Table 5.2: Preliminary parameters

Parameter	C2.1
Wingspan [m]	14.0
Wing surface [m ²]	25.4
Total mass [kg]	1500
Battery mass [kg]	345

Table 5.3: Updated parameters inputted

Parameter	C2.1
Wingspan [m]	14.0
Wing surface [m ²]	14.0
Total mass [kg]	1650
Battery mass [kg]	400

These values from Table 5.2 have been iterated, and from these adjusted values, some critical design configuration changes have been made. First, it was determined to use six engines instead of four because the system should be redundant and not fail if an engine fails, but also due to noise, efficiency, and downwash creation. Moreover, a high-wing configuration was chosen because of the fuselage clearance during hover. Subsequently, a downward V-tail was chosen because of the vertical height requirement of two meters, and it helped the landing configuration. Finally, the wing surface area is almost halved to 14 m² to relieve the bending moment on the hinge and because of the overestimated lift. All these aspects shall be discussed in more detail throughout this report. The updated values are seen in Table 5.3

6. Mission Profile

The Mission Profile can be seen as the blueprint for the mission, providing the direction for the design. Section 6.1, through the use of a clear visual, establishes the total mission in great detail. Subsequently, Section 6.2 is responsible for optimising different phases, each with different goals, which conclude the flight performance in Section 6.3.

6.1. Mission Overview

The mission profile (Figure 6.1) for the *Swing eVTOL* is divided into two main parts: the normal operational range (part A), and the emergency deviations (part B).

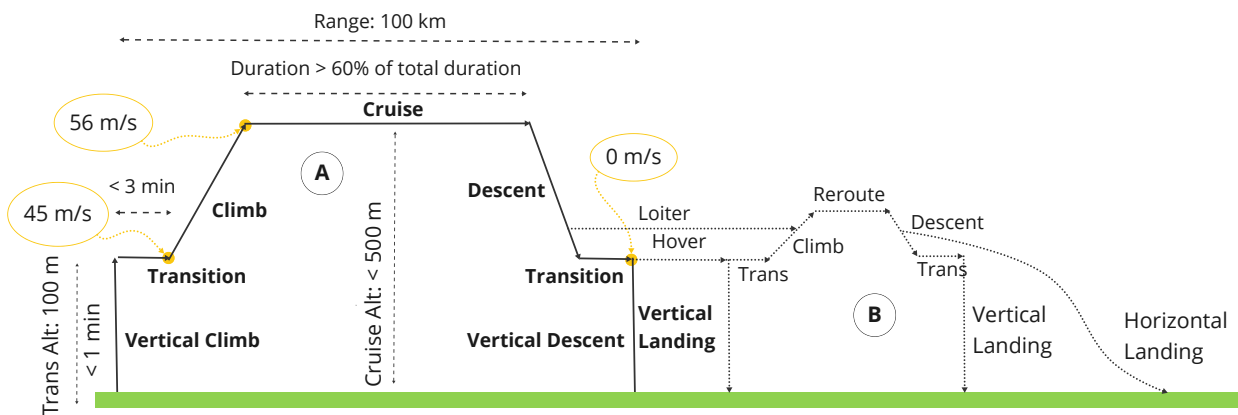


Figure 6.1: Mission profile of the eVTOL aircraft

Considering part A of the profile, the mission starts with a vertical take-off from a vertiport in an urban area. Then it ascends vertically in the take-off configuration until it has reached transition altitude, set at 100 m above ground level; this vertical climb phase has a maximum duration of 1 min. After reaching the desired altitude, the aircraft transitions to the horizontal configuration. During the transition, the vehicle accelerates to a velocity of 45 m/s while maintaining altitude within a time frame of 3 min. Once in the horizontal configuration, the aircraft climbs to the cruise altitude of 500 m. For cruise, the aircraft will fly at a speed of 200 km/h, for which the minimum duration of the cruise phase is set to be 60% of the total mission time, for a nominal flight distance of 100 km. After the cruise, the aircraft descends in horizontal configuration to an altitude of 100 m above ground level and slows down to the transition speed of 45 m/s. While descending, the engine will be throttled back to idle; then the *Swing* transitions back to the vertical configuration whilst decelerating to a hover. The aircraft will then descend vertically to the landing site within 1 min and land.

Part B of Figure 6.1 is illustrated as well since the mission should account for emergency deviations. The *Swing eVTOL* can use its total battery capacity in an emergency. Although the battery discharge constraints are set to account for better battery life, there is still enough margin left for an emergency deviation, paving the way for an emergency diversion to other vertiports.

6.2. Mission Optimisation

For the mission profile described in Section 6.1, the objective is to minimise the total energy consumption of the aircraft. To achieve this, a multiphase optimisation approach is used, as described by Kelly [29]. The different mission phases have been modelled and optimised separately. This enabled utilising different equations of motion, constraints, assumptions, and simplifications for each phase. The following principles apply to all mission phase optimisations:

- The energy consumption per phase is calculated as the sum of the used power multiplied by the time

step.

- The used power is set as a variable constrained by the maximum engine power.
- The power required is calculated using a combination of the equations of motion and the power required curve in Figure 9.1.

The different mission phases are optimised, utilising the optimisation software within the Aerosandbox Python package [2]. This optimisation software utilises the open-source CasADi library [30] for nonlinear optimisation and algorithmic differentiation, and the IPOPT solver [31] for large-scale nonlinear optimisation.

6.2.1. Equations of Motion

The equations of motion for the aircraft are based on Newton's second law of motion. The aircraft is modelled as a point mass, and the forces acting on it are gravity, thrust, lift, and drag. The equations of motion are given by:

$$\mathbf{x}(t) = \int_{t_0}^t \mathbf{v} dt \quad (6.1)$$

$$\mathbf{v}(t) = \int_{t_0}^t \mathbf{a} dt \quad (6.2)$$

$$\mathbf{a}(t) = \frac{1}{m} \sum \mathbf{F}(t) \quad (6.3)$$

$$\mathbf{F}(t) = \mathbf{F}_{\text{gravity}} + \mathbf{F}_{\text{thrust}}(t) + \mathbf{F}_{\text{aero}}(t) \quad (6.4)$$

$$\int_{t_i}^{t_{i+1}} f(t) dt \approx \frac{t_{i+1} - t_i}{6} \left[f(t_i) + 4f\left(\frac{t_i + t_{i+1}}{2}\right) + f(t_{i+1}) \right] \quad (6.5)$$

$$\int_{t_0}^{t_n} f(t) dt \approx \sum_{i=0}^{n-1} \int_{t_i}^{t_{i+1}} f(t) dt \quad (6.6)$$

Where \mathbf{x} is the position vector, \mathbf{v} is the velocity vector, \mathbf{a} is the acceleration vector, m is the mass of the aircraft, \mathbf{F} is the total force vector acting on the aircraft, $\mathbf{F}_{\text{gravity}}$ is the gravitational force vector, $\mathbf{F}_{\text{thrust}}(t)$ is the thrust force vector produced by the engines, and $\mathbf{F}_{\text{aero}}(t)$ is the aerodynamic force vector consisting of lift and drag. The equations of motion are integrated using Simpson's 1/3 rule (Equation (6.5)), which is a numerical integration method based on quadratic interpolation.

6.2.2. Vertical Climb and Descent Phases

The vertical climb and descent phases are modelled and optimised using a single point optimisation approach [29]. It begins with the eVTOL resting on the ground and ends when it reaches the transition altitude of 100 m above ground level. The vertical descent phase begins when the aircraft reaches the transition altitude and ends when it lands on the ground with a maximum vertical speed of 0.5 m/s.

The optimisation problem is formulated as a point mass model with 1D vertical dynamics. The aircraft is assumed to be a point mass, and the forces acting on it are gravity and the thrust the engines produce.

Aerodynamic forces are neglected in this phase, as the aircraft is assumed to be in a vertical climb with low vertical speed and no horizontal motion. To validate this assumption, the worst-case maximum drag force is calculated with the AeroBuildup Aerodynamic engine, as explained in Section 8.2. The maximum drag force is found to be 35 N, which is negligible compared to the thrust and weight of the aircraft in the order of 10 kN.

Moreover, the thrust is modelled as a function of the power available and the aircraft's figure of merit (FM), which measures the rotor system's efficiency. The forces acting on the aircraft are visualised in Figure 6.2

The objective of the optimisation is to minimise the aircraft's total energy consumption during the vertical climb phase. By minimising the total energy instead of the power consumption, the optimiser makes an efficiency-speed trade-off between climbing in less time and climbing efficiently. The total energy is calculated as the integral of the power available throughout the climb, which is a decision variable in the optimisation problem, and it is constrained to be less than the maximum engine power. The optimisation problem also includes constraints on the altitude and vertical speed of the aircraft. The altitude must increase from zero to the transition altitude, and the vertical speed must be non-positive (indicating upward motion). The duration of the climb is also a decision variable, and it is constrained to be less than 60 s. Lastly, the maximum vertical acceleration and deceleration are constrained to be less than 2 m/s^2 to ensure a smooth ride for the passengers. The solution to the optimisation problem provides the optimal thrust level as a function of time and altitude, which minimises the total energy consumption of the aircraft during the vertical climb phase.

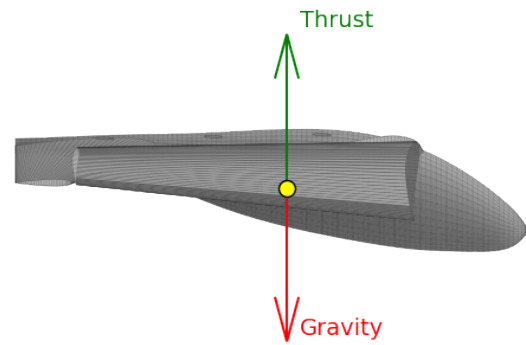
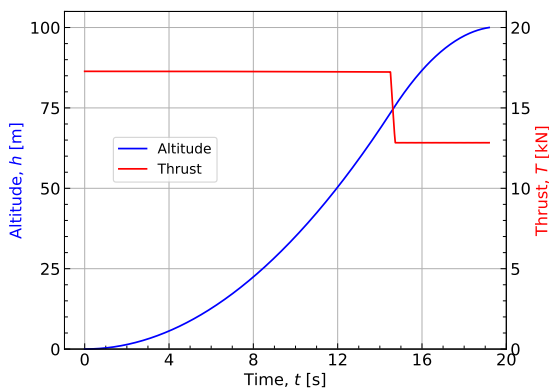
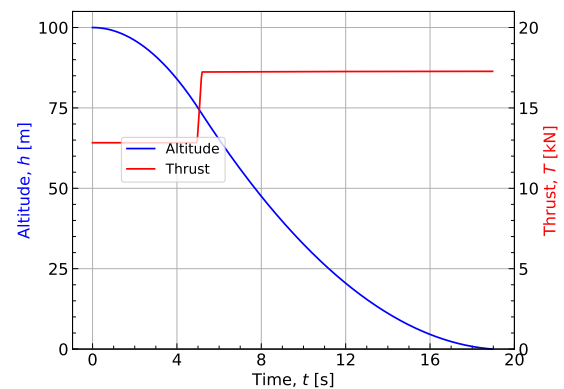


Figure 6.2: Modelled forces acting on the aircraft during the vertical climb and descent phases



(a) Altitude and total thrust over time of the vertical climb phase



(b) Altitude and total thrust over time of the vertical descent phase

Figure 6.3: Altitude and total thrust over time of the vertical climb and descent phases

As can be seen in Figure 6.3, the vertical climb and descent phases are completed within 20 s, well within the maximum duration of 60 s. The total energy consumption of the aircraft during both phases is roughly 1.6 kWh.

6.2.3. Transition Phase

The transition phase is when the aircraft changes from vertical to horizontal flight configuration. This phase is modelled and optimised using a single point optimisation approach [29], similar to the vertical climb

phase. The optimisation problem is formulated as a point mass model with 1D horizontal dynamics. Where the power required is calculated at each point during the transition and over the velocity range. This required power consists of induced, profile, and parasite power, which is explained in more detail in Figure 9.1. Furthermore, the additional thrust needed to accelerate the aircraft is a free variable in the optimisation problem. The power used for acceleration is computed from this additional thrust, taking into account the direction the engines are pointing at the current transition parameter, as can be seen in Figure 6.4.

As can be noted from the figure, the extra thrust is split into a vertical and horizontal component. The extra vertical thrust is then ignored, as the required vertical speed is to be zero to simplify the model. Therefore, the aircraft will gain altitude during the transition phase in a real-world scenario. This would make the following climb phase more efficient, as the aircraft would start at a higher altitude.

The second free variable in the optimisation problem is the transition parameter used to determine the aircraft's configuration between vertical and horizontal flight. The transition parameter is constrained to start at one (vertical flight) and end at zero (horizontal flight). The transition parameter is also constrained to be a smooth decreasing function of time to ensure a smooth transition between the two configurations. It should be noted that the power required curve is a function of the transition parameter, as the aircraft's configuration affects the aerodynamic forces acting on it. Those aerodynamic forces are computed using the AeroBuildup Aerodynamic engine, as explained in Section 8.2.

The horizontal speed is required to increase from zero to the transition speed, and the transition duration is constrained to be less than 180 s. The eventual solution to the optimisation problem provides the optimal power available, power required, thrust level, velocity, and control inputs as functions of time, distance, and velocity, which minimises the maximum power required during the transition phase. The control inputs include the angle of attack and the transition parameter, which determines the aircraft's configuration between vertical and horizontal flight.

As can be seen in Figure 6.5, the transition phase starts with the aircraft in vertical flight configuration, with a horizontal speed of 1 m/s to avoid division by zero in the power required curve. The aircraft then slowly transitions, increasing the forward momentum. As the vehicle transitions, the required thrust increases to maintain the desired altitude (see Figure 6.4). When the aircraft flies with a horizontal velocity of around 10 m/s after 30 s in the transition phase, the required power starts to decrease, as seen in Figure 6.6. From this point, the aircraft starts to accelerate and transition more aggressively, keeping the maximum power peak as low as possible. The remaining ΔV of around 35 m/s, and 70% of the transition, is achieved in the second half of the transition phase. The transition phase ends with the aircraft flying with a velocity of 45 m/s in horizontal flight configuration. The transition phase is completed in 63 s, which is well within the maximum duration of 180 s.

The second transition phase, however, has not been modelled, as it is assumed to be less power-intensive than the first. The aircraft will not require additional thrust to decelerate to the hover velocity of 0 m/s. Thus, for the total mission, the power is assumed to increase linearly from cruise power to hover power.

6.2.4. Climb, Cruise, and Descent Phases

The climb, cruise, and descent phases are modelled and optimised using a single-phase full-dynamics optimisation approach [29]. The optimisation problem is formulated as a point mass model with 2D

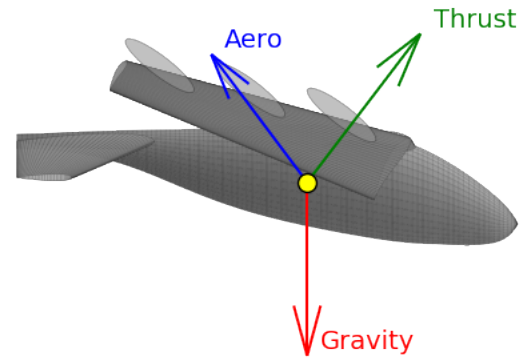


Figure 6.4: Modelled forces acting on the aircraft during the transition phase

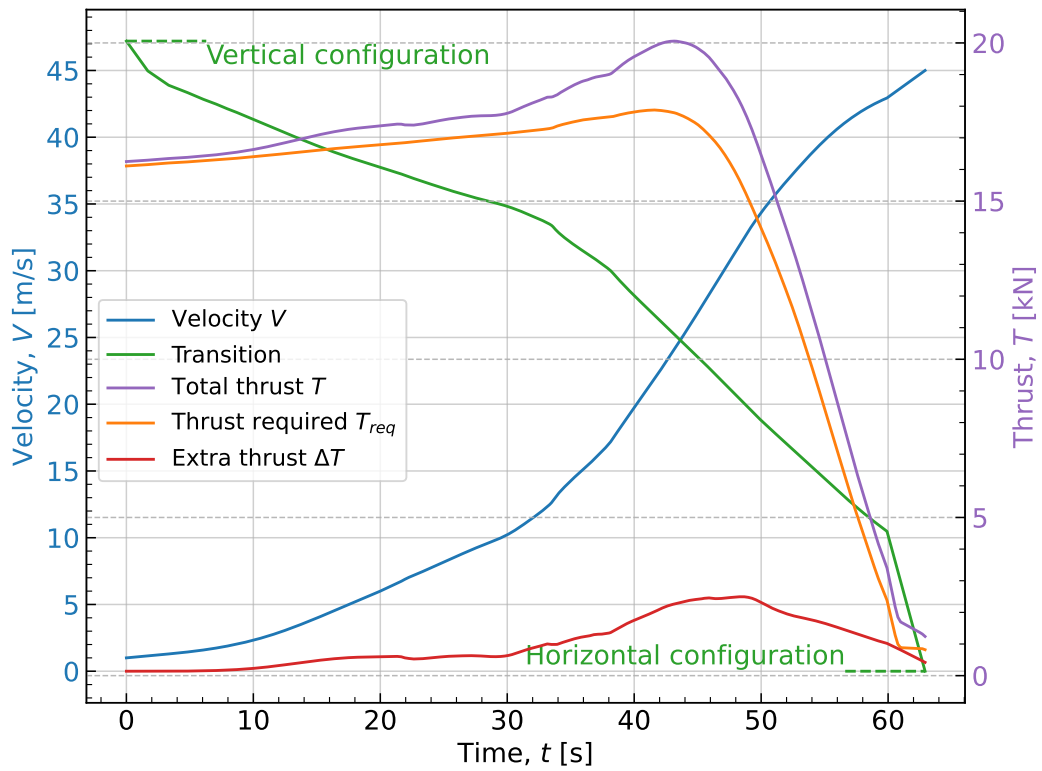


Figure 6.5: Extra horizontal thrust, transition parameter, and velocity over time during the transition phase

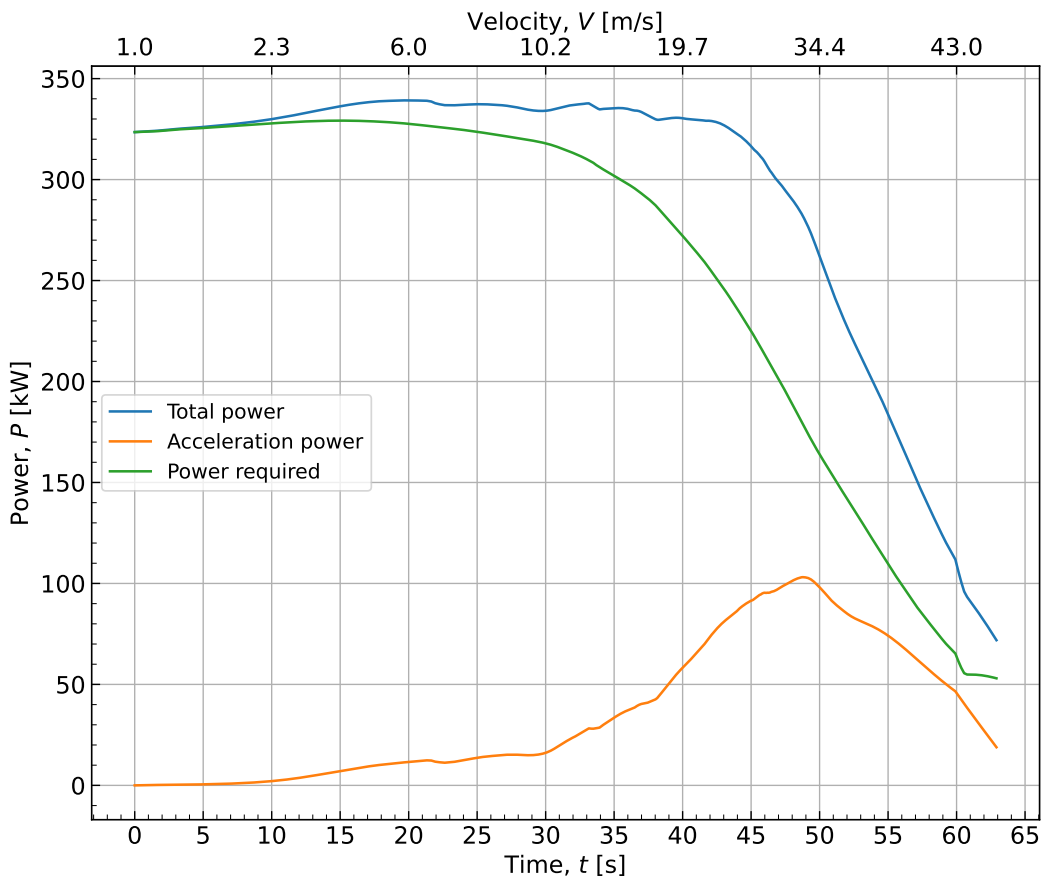


Figure 6.6: Power required and acceleration power over velocity and time during the transition phase. A detailed explanation of the power required curve is given in Section 9.2

dynamics, where the aircraft is assumed to be a point mass, and the forces acting on it are gravity, the thrust produced by the engines, and the aerodynamic forces. The thrust is the free variable in the optimisation problem. Moreover, the general 2D equations of motion are used to calculate the aircraft's velocity, acceleration, and position at each point during the climb, cruise, and descent phases. The forces acting on the aircraft are visualised in Figure 6.7

The objective of the optimisation is to minimise the total energy consumption of the aircraft during these phases. The total energy is calculated as the integral of the power available over the duration of each phase, which is calculated as a function of the thrust produced by the engines and the aircraft's velocity, based on the power curve in Figure 9.1.

The optimisation problem includes constraints on the aircraft's altitude, vertical speed, and horizontal speed. The altitude is required to increase from the transition altitude to the cruise altitude during the climb phase, remain constant at the cruise altitude during the cruise phase, and decrease from the cruise altitude to the transition altitude during the descent phase. The vertical speed is required to be positive (indicating upward motion) during the climb phase, zero (indicating no vertical motion) during the cruise phase, and negative (indicating downward motion) during the descent phase. The horizontal speed is required to increase from the transition speed to the cruise speed during the climb phase, remain constant at the cruise speed during the cruise phase, and decrease from the cruise speed to the transition speed during the descent phase. The duration of each phase is also a free variable, and it is constrained to be less than the maximum duration of the phase. The solution to the optimisation problem provides the optimal power available, thrust level, and alpha as functions of time, which minimise the total energy consumption of the aircraft during the climb, cruise, and descent phases.

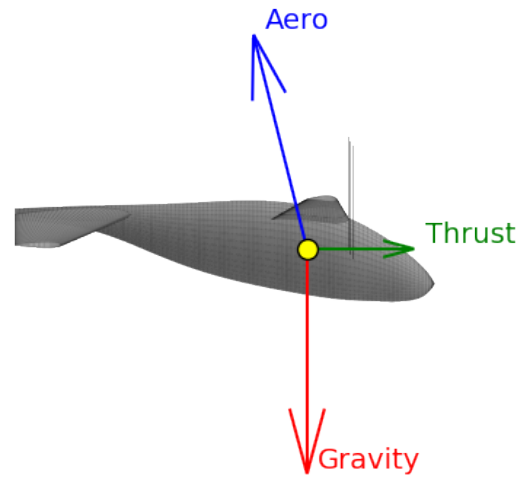


Figure 6.7: Modelled forces acting on the aircraft during the climb, cruise, and descent phases

As can be seen in Figure 6.8, the climb phase starts with the aircraft at the transition altitude of 100 m above ground level. The aircraft then climbs to the cruise altitude of 500 m above ground level, with an average vertical speed of 1.5 m/s and an average power of 80 kW. The fluctuation in the vertical speed is likely due to anomalies from the optimisation, but it is not expected to influence the results significantly. The cruise phase starts with the aircraft at the cruise altitude of 500 m above ground level, and the aircraft flies at a constant horizontal speed of 200 km/h, with an average power level of 50 kW. The descent phase starts with the aircraft at the cruise altitude of 500 m above ground level, and the aircraft descends to the transition altitude of 100 m above ground level, with an average vertical speed of -2.4 m/s, and average idling power of 0.1 kW. The descent phase ends with the aircraft at the transition altitude of 100 m above ground level.

6.3. Flight Performance

The flight performance of the *Swing eVTOL* is evaluated based on the optimised mission profile described in Section 6.2. The performance metrics include the total energy consumption, the maximum power required, the maximum thrust level, and the flight time for each phase of the mission. The performance metrics are calculated for the nominal mission profile and different mission profiles with variations in the mission parameters, such as increased range. In the future, other mission profiles can be evaluated as well, such as increased cruise velocity or different payload configurations.

6.3.1. Nominal Mission Profile Results

The optimised mission profile for the *Swing* is shown in Figure 6.10a, including altitude and engine power over distance and time. The energy distribution over the different phases of the mission is shown in

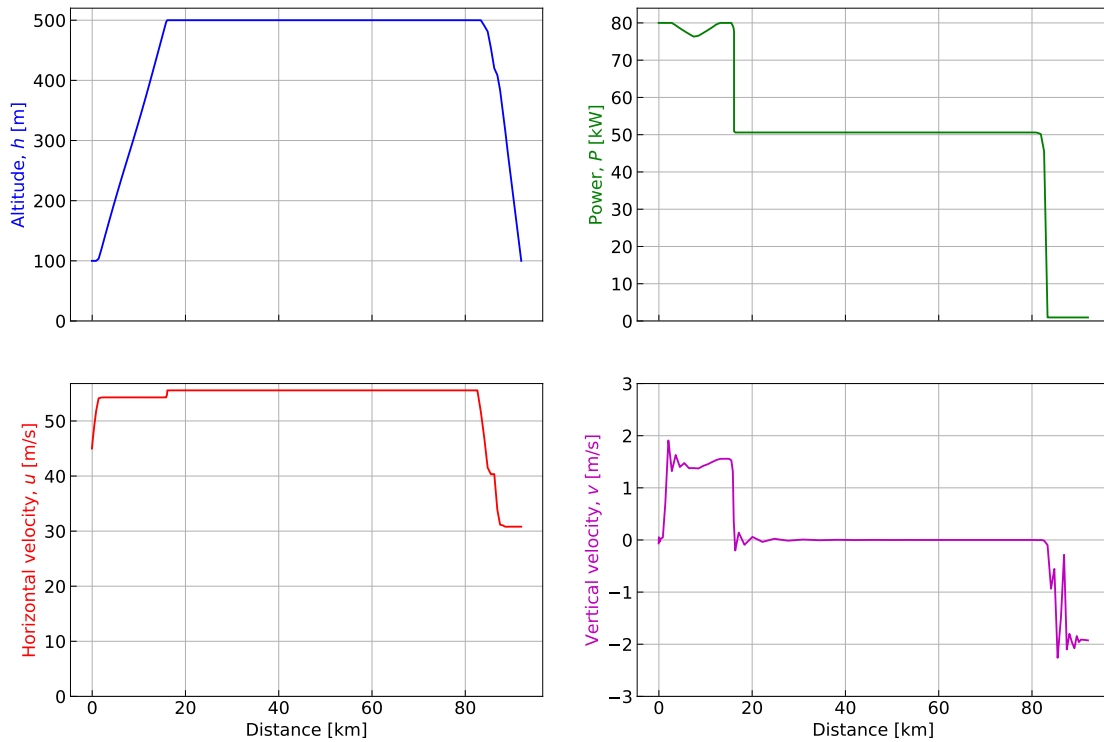


Figure 6.8: Altitude, horizontal speed, vertical speed, and engine power over distance during the climb, cruise, and descent phases

Figure 6.11a. Where the total energy consumption of the aircraft during the nominal mission profile is 34 kWh. The maximum power required by the aircraft during the mission is 343 kW, and the maximum thrust level is 20.2 kN. Furthermore, the total flight time of the nominal mission profile is 32 min. The results show that the aircraft can complete the mission with the given constraints while minimising the total energy consumption and the maximum power required.

6.3.2. Mission Profile with Maximum Range

The mission profile for the maximum range is found by increasing the total distance to 250 km. Extending the cruise period for the maximum amount of time whilst keeping the State of Charge of the battery between 90% and 20%, which is explained in greater detail in Chapter 13 Assuming that only the Climb, Cruise, and Descent phases are affected by the increased range, only the horizontal optimisation of Section 6.2.4 is rerun. The optimisation results are shown in Figure 6.9. As can be seen in the figure, it is more efficient to fly at a higher altitude during the cruise phase, as the power required is lower at higher altitudes.

The new mission profile for the maximum range is shown in Figure 6.10b, and the energy distribution over the different phases of the mission is shown in Figure 6.11b. It can be seen that the climb phase is now the most energy-intensive phase of the mission since the aircraft has to climb to a higher altitude. The energy for the cruise phase went down relative to the total mission energy, as the aircraft spends more time in the climb and descent phases. The total energy consumption of the aircraft during the mission with maximum range is 70 kWh. Subsequently, the total flight time of the mission with maximum range concludes 79 min.

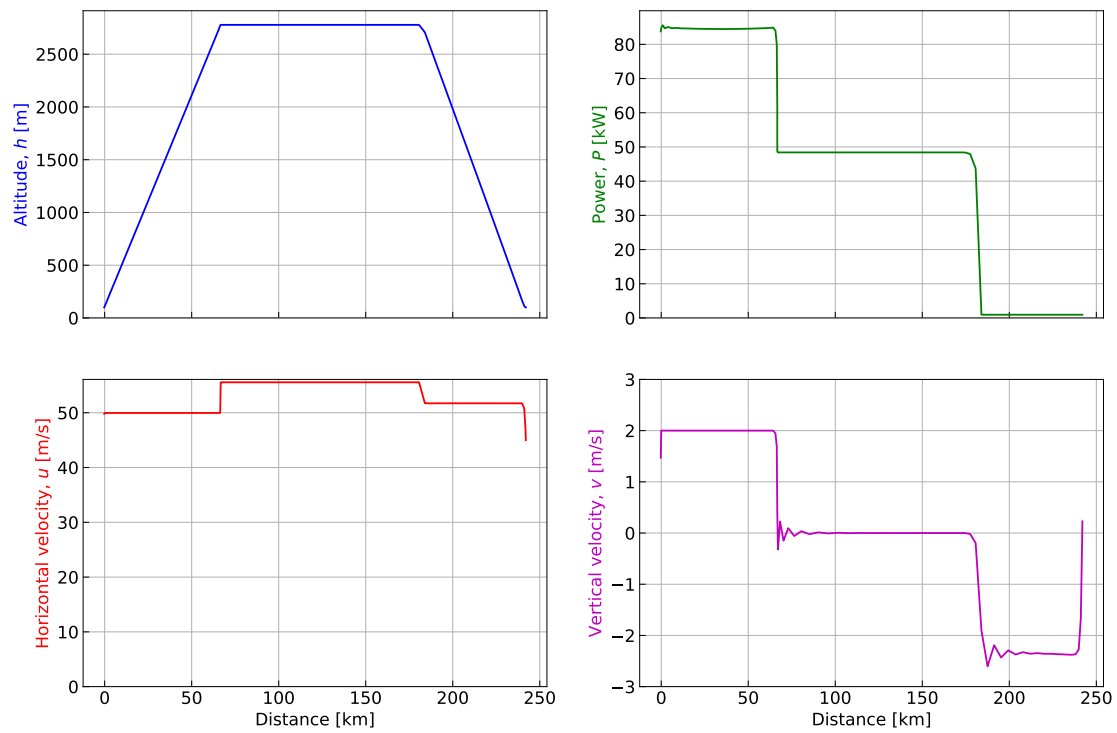
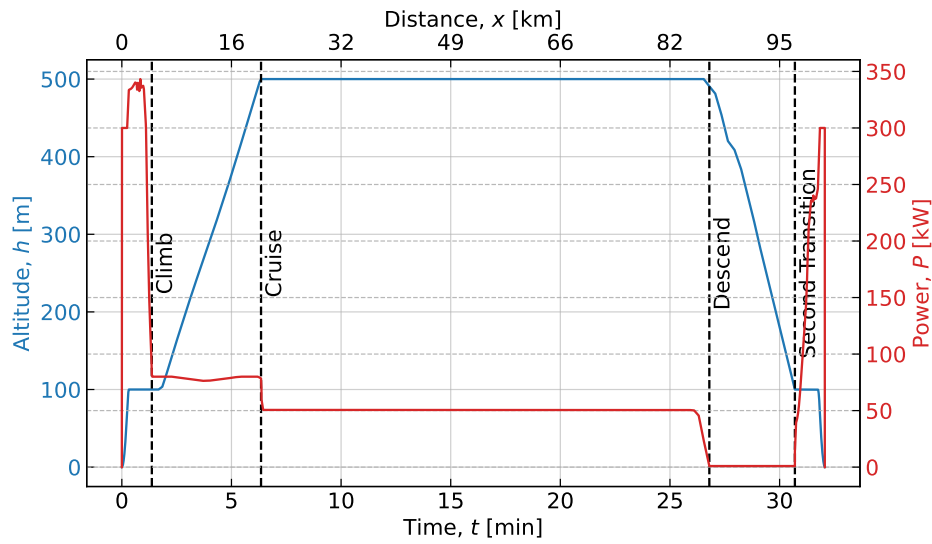
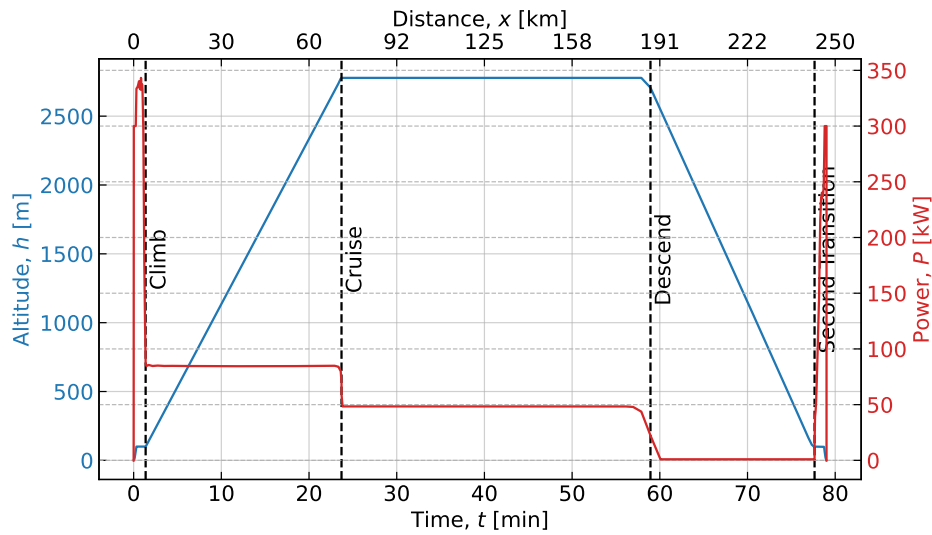


Figure 6.9: Altitude, horizontal speed, vertical speed, and engine power over distance during the climb, cruise, and descent phases for the maximum range mission profile

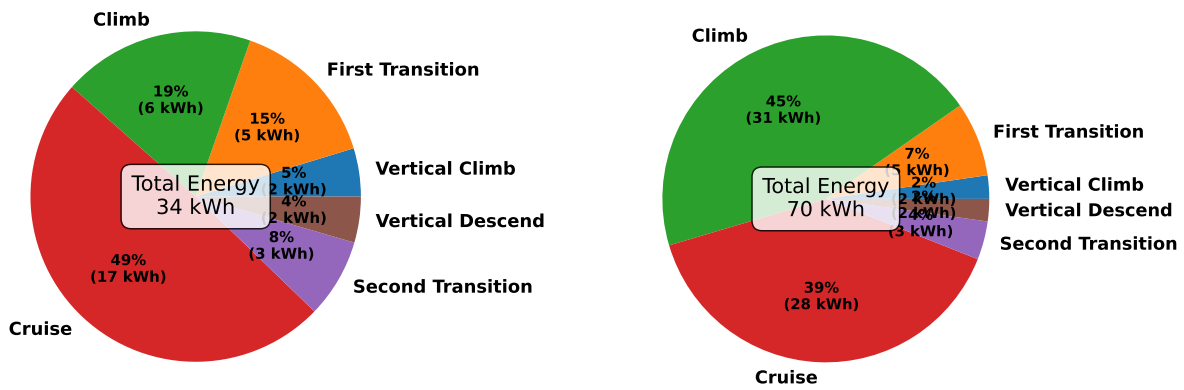


(a) Altitude and engine power over distance and time of the nominal mission profile



(b) Altitude and engine power over distance and time of the mission profile with maximum range

Figure 6.10: Mission profile results for the nominal mission profile and the mission profile with maximum range



(a) Energy distribution of the nominal mission profile

(b) Energy distribution of the mission profile with maximum range

Figure 6.11: Energy distribution over the different phases of the mission profiles

7. Aerodynamic Design

This chapter delves deeper into the design of wing and fuselage subsystems. The empennage will be discussed in Chapter 11, because it is mainly dependent on stability characteristics. Since many dependencies and iterations influence the wing and fuselage design, this chapter will discuss the methods of designing these subsystems, and each section will end with an overview of the final parameters after the iteration of all subsystems.

7.1. Wing Configuration

Three different wing configurations are possible for the vehicle: low-wing, mid-wing or high-wing. Each configuration has its advantages and disadvantages, and therefore, a trade-off needs to be made between the three configurations. The low-wing configuration immediately drops out because the rotors would collide with the fuselage during vertical ascent since the wings are folded, and the ground footprint limits to place the engines more outward. For the mid-wing configuration, this same principle holds. From historical data, a taper ratio of 0.4 [32] was taken and the fact that three engines are mounted on the wing, the propellers would collide with the fuselage. Therefore, the vehicle will have a high-wing configuration. This allows placing the fuselage closer to the ground, making payload loading easier. Moreover, the propellers will have more ground clearance and do not collide with the fuselage [1].

7.2. Wing Planform

During the preliminary sizing, the surface area of the wing was calculated using class I and class II estimations. From this, the wing sizing and shaping can be conducted. Since the vehicle is set to have a cruise speed of 200 km/h, the vehicle will fly with Mach numbers in the subsonic regime. Hence, it can be assumed, from historical data that the quarter chord sweep, $\Lambda_{c/4}$, is zero and that the taper ratio, λ , is equal to 0.4 [32]. From the surface area, S , span, b , and taper ratio, λ , the root and tip chord, c_r and c_t can be calculated in Equations (7.1) and (7.2), respectively. After finding the root chord (c_r), the Mean Aerodynamic Chord (MAC) is calculated using Equation (7.3). The y -location of the MAC (y_{MAC}) can be retrieved using the taper ratio and wing span in Equation (7.4). Moreover, the leading-edge sweep (Λ_{LE}) is calculated using the quarter chord sweep angle, taper ratio and the aspect ratio in Equation (7.5).

$$c_r = \frac{2S}{(1+\lambda)b} \quad (7.1)$$

$$c_t = c_r \lambda \quad (7.2)$$

$$MAC = \frac{2}{3} c_r \left(\frac{1+\lambda+\lambda^2}{1+\lambda} \right) \quad (7.3)$$

$$y_{MAC} = \frac{b}{6} \left(\frac{1+2\lambda}{1+\lambda} \right) \quad (7.4)$$

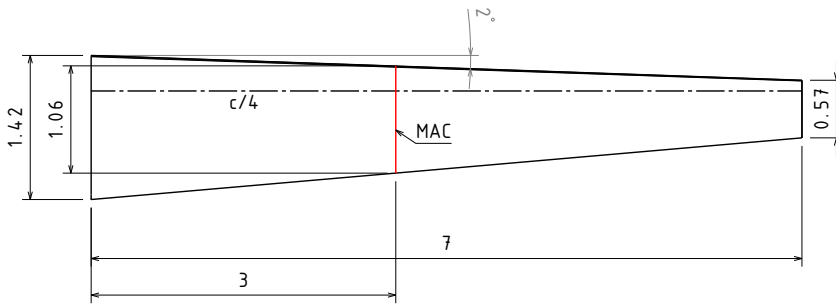
$$\Lambda_{LE} = \tan(\Lambda_{c/4}) + \frac{(1-\lambda)}{A(1+\lambda)} \quad (7.5)$$

The values for the wing platform design, obtained from the equations, can be visualised in Table 7.1. The dihedral angle, Γ , was chosen for a high-wing configuration with unswept wings obtained from historical data from Raymer [1]. The final wing geometry can be visualised in figure 7.1.

7.3. Airfoil Selection

After the wing planform has been fixed, it is crucial to select an airfoil which is fit for the mission requirements. Literature research was performed on airfoils used for similar eVTOL designs as well as reference aircraft, which operate at similar velocities to the *Swing* while carrying a similar payload mass. The airfoil selection was performed keeping in mind the fact that the vehicle shall operate at a low altitude, leading to a high Reynolds number due to increased density:

$$Re = \frac{\rho V l}{\mu} \quad (7.6)$$

**Table 7.1:** Wing platform design values

S	14	m^2
b	14	m
A	14	–
c_r	1.42	m
c_t	0.57	m
MAC	1.06	m
y_{MAC}	3.0	m
$\Lambda_{c/4}$	0	deg
Λ_{LE}	2	deg
λ	0.4	–
Γ	1	deg

Figure 7.1: Top view of half wing with MAC highlighted

In this equation, ρ represents the density at cruise altitude, V the velocity, l describes the characteristic length, which in the case of aircraft wings, can be considered to be the mean aerodynamic chord length (MAC). Finally, μ is the dynamic viscosity of air, which can be estimated from the International Standard Atmosphere (ISA). At a cruise altitude of $h = 500\text{ m}$, $\mu = 1.77 \times 10^{-5}\text{ kg m/s}$.

Using Equation (7.6), a Reynolds number of 4.0×10^6 is calculated, which is used in the airfoil analysis. Based on this particular Reynolds number, a selection of airfoils was performed that shall then be analysed in further detail and traded off. Hence, the following six different airfoils were considered in the airfoil trade-off [33]–[35]:

- NASA Langley LS(1) 0417
- NACA 4416
- NACA 4412
- Eppler 423
- Eppler 560
- Eppler 562

After the airfoil selection, the trade-off criteria should be established for the final design choice. While the airfoils can only be analysed based on their technical parameters, it is important to consider the mission requirements when selecting the airfoil. Therefore, a list of criteria was compiled, with each criterion being allotted importance on a scale from one to three. Afterwards, each criterion was translated into technical parameters based on the relative importance of each parameter in each of the criteria. The values for each parameter were then summed up and converted into percentages, enabling setting-up a technical trade-off for the airfoil selection. The criteria considered, as well as the final importance determined for each technical parameter, shall be presented in Table 7.2.

It is important to note that, as can be seen in the trade-off, when determining the importance of the parameter, the value of the importance of the criteria was multiplied by the relevance of the criteria before summing up to obtain the final score. Thus, the aforementioned percentages shall be used to score each of the proposed airfoil configurations. Additionally, the relevance of each of the technical parameters for the airfoil trade-off shall be briefly explained below:

- C_{l_0} : The higher the lift coefficient at zero angle of attack, the higher the efficiency for cruise.
- $C_{d_{\text{min}}}$: The lower the minimum drag of the airfoil, the more efficient cruise will be.

Table 7.2: Airfoil criteria

Importance	Criteria	C_{l_0}	$C_{d_{min}}$	$C_l/C_{d_{max}}$	C_{m_0}	t/c	α_{stall}
2	Structural Weight					3	
3	Power required		3	2		1	
1	Stability				3		1
2	High lift	3		2		1	
2	Safety				1	2	2
	Design Parameter Importance	6	9	10	5	15	5
	Percentage	12	18	20	10	30	10

- $C_l/C_{d_{max}}$: The higher the value, the better, the more range and higher efficiency for the cruise.
- C_{m_0} : The more negative the C_{m_0} value, the better the controllability for the aircraft will be
- t/c : A high t/c ratio reduces the structural weight, increases the lift and increases available space for battery storage if required.
- α_{stall} : The stall characteristics depend on the stall angle of the airfoil. During transition, stall is not desired. However, the angled thrust will counteract this; therefore, the weight is low.

In order to compare the technical performance of the aforementioned selected airfoils, specialised software such as XFOIL should be used. This software requires an airfoil shape, of which the data can be obtained from an airfoil database provided by the TU Delft that then can be used as input for the XFOIL and XFLR5 software [36]. The airfoils were analysed for each of the criteria stated above using XFOIL and XFLR-5, set at a Reynolds number of 4.0×10^6 and a Mach number of 0.16, which is obtained from the cruise speed requirement. The results can be seen in Table 7.3.

Table 7.3: Airfoil parameter values at $Re = 4.0 \times 10^6$ and $M = 0.16$

	C_{l_0}	$C_{d_{min}}$	$C_l/C_{d_{max}}$	C_m	t/c	α_{stall}
LS(1)-0417	0.55	4.7	120	-0.12	17	18
NACA4412	0.47	8.8	120	-0.10	12	14
NACA4416	0.51	6.1	168	-0.10	16	17
E560	0.72	6.1	162	-0.17	16	16
E562	0.61	5.7	160	-0.15	15	17
E423	1.16	6.4	220	-0.25	12.5	14

Based on the aforementioned airfoil technical parameters, the airfoils were then scored for each criterion on a range from one to five. Subsequently, the scores were added up based on the weight of each parameter, leading to the final airfoil choice Table 7.4.

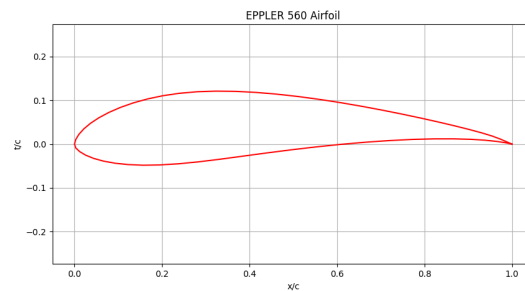
From Table 7.4, it can be seen that the E560 wins the trade-off. However, the airfoil final scores are in a close range compared to each other, therefore a sensitivity analysis was conducted. Firstly, each parameter was removed separately, and the final score was analysed. The E560 won five out of six times, meaning the weights are robust. The winner in each of the cases, as well as the final score, is presented in Table 7.5. Secondly, the weights were adjusted by $\pm 5\%$ In all cases; the E560 won the trade-off. The airfoil shape is presented in Figure 7.2.

Table 7.4: Airfoil trade-off

Weight	Parameter	LS(1)-0417	NACA 4412	NACA 4416	E560	E562	E423
12	C_{l_0}	2	1	2	4	3	5
18	$C_{d_{min}}$	5	1	3	3	4	2
20	$C_l/C_{d_{max}}$	1	1	4	4	4	5
10	C_m	2	2	2	4	3	5
30	t/c	5	1	4	4	3	1
10	α_{stall}	5	2	4	4	4	2
Final Score		3.5	1.2	3.4	3.8	3.5	3.0

Table 7.5: Airfoil sensitivity analysis

Parameter Removed	Winning Airfoil
C_{l_0}	E560
$C_{d_{min}}$	E560
$C_l/C_{d_{max}}$	LS(1)-0417
C_m	E560
t/c	E560
α_{stall}	E560

**Figure 7.2:** Plot of the Eppler 560 airfoil

7.4. Fuselage Design

An aircraft's fuselage has many functions, which all need to be fulfilled by the design. For this eVTOL concept, the following functions were considered the most important:

- Fit the passengers in a comfortable and spacious manner.
- Offer load-path for lifting surfaces and landing gear.
- Accommodate the layout of electrical and control systems.
- Contain easily accessible compartments for luggage.
- Provide easy and quick boarding and disembarking of the aircraft.

The first function is chosen to be important since the design is supposed to be a luxurious mode of transportation and thus should provide enough space and comfort. Furthermore, the fuselage design should aim to keep the fuselage drag at a minimum while still ensuring all the above functions are satisfied.

The first step in designing the fuselage is to look at how the payload will fit inside and, thus, how it will satisfy the first function. To do this, the following mannequin seen in Figure 7.3 is used. It shows the

dimensions of the 99th percentile male, meaning that 99% of the male population will have equal or smaller dimensions.

To keep the cross-sectional area of the fuselage to a minimum, a seating position with the lower legs at 45 degrees was chosen. To further decrease the cross-sectional area and still take passenger comfort into account, the seats are tilted backwards. According to [37], the backrest inclination is comfortable between an angle of 65 and 85, while the seat inclination is comfortable between 5 and 15 degrees; this is confirmed by research by [38]. To also be comfortable if the aircraft is climbing or descending, a seat inclination of 10 degrees and a backrest inclination of 75 degrees are chosen. This results in the seated position seen in Figure 7.3.

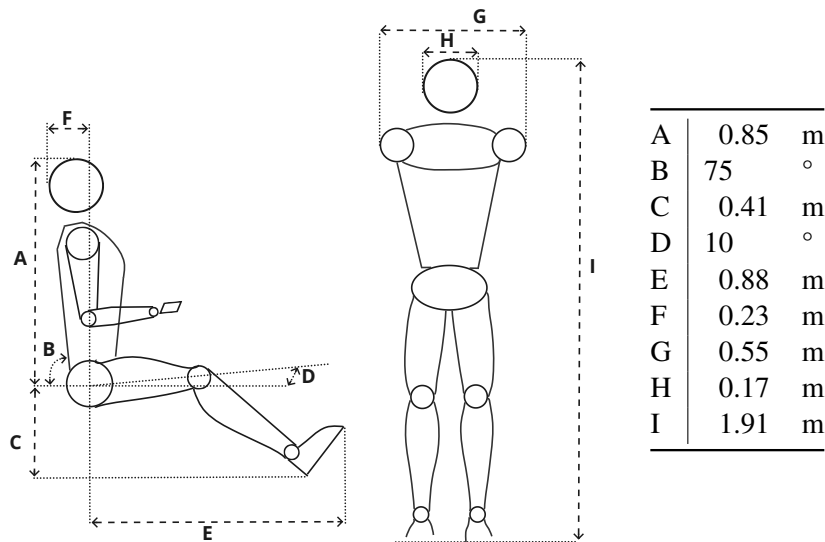


Figure 7.3: 99th percentile male in standing and seating configuration, adapted from Gudmundsson [39].

From this seated position, a cross-section of the fuselage can be drawn, which can be seen in Figure 7.4. This cross-section gives an inner diameter and width data from literature [32]; it can be concluded that for a non-pressurised composite aeroplane, 5 cm thickness of the fuselage is sufficient, and therefore, the outer diameter of the fuselage is found to be 170 cm.

After the cross-section, it is important to look at the longitudinal shape of the fuselage. Since the aircraft does not need to have a large internal volume, a tadpole fuselage shape was chosen. The forward part of the fuselage is shaped to sustain a laminar boundary layer and a wetted area of more than 25%. This is less than a conventional fuselage [39]. The standard tadpole design, found in almost all sailplanes nowadays, was adapted to fit the *Swing eVTOL*. The main difference is the decrease in the l/d (length over diameter) ratio since the length of the *Swing* is limited by the ground footprint, and the diameter of the fuselage is bigger since it has two seats abreast.

Due to the wings being next to the aeroplane when in hover configuration, entering the back two seats with a normal door is not a possibility. The solution to this problem is that the front two seats are on rails such that they can be moved forward. The rear seats can be boarded via a door at the side of the fuselage in front of the wing. The final design of the fuselage gives passengers the same amount of comfort as a business class seat in a general aviation aircraft while being smaller in diameter than a *Cessna Citation Ultra*. The final fuselage design is displayed in Figure 7.5.

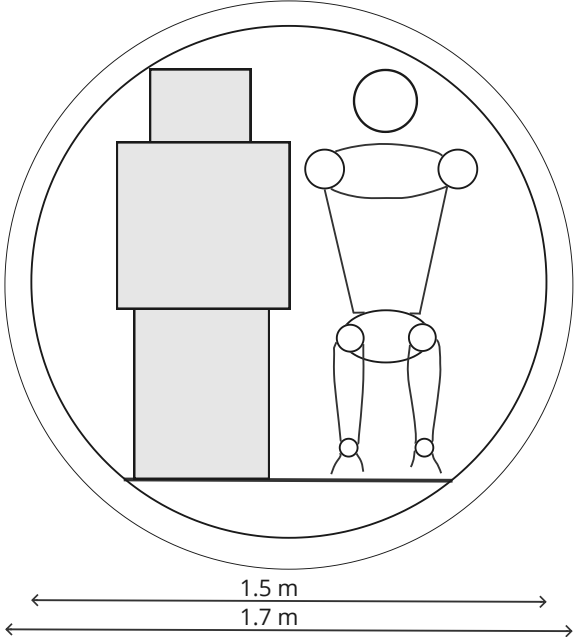


Figure 7.4: Drawing of the fuselage cross-section with passengers loaded

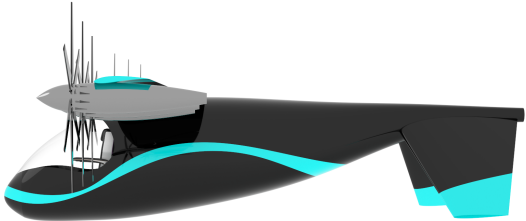


Table 7.6: Fuselage design values

l_{fus}	8.0 m
d_{inner}	1.6 m
d_{outer}	1.7 m

Figure 7.5: Side view of the fuselage

8. Aerodynamic Analysis

In this chapter, the aerodynamic properties of the entire aircraft in cruise will be assessed. First, in Section 8.1, the drag will be analysed, after which the aerodynamics of the full parametric model will be studied in Section 8.2, and both will be verified and validated in Section 8.3

8.1. Drag

Drag consists of lift-induced drag and parasite drag, with the latter mainly depending on the shape and interaction of various UAV components. Unless explicitly stated otherwise, all formulas and statements in this section are from the Raymer book [1]. The drag polar is defined by the following equation:

$$C_D = C_{D0} + \frac{C_L^2}{\pi AR e} \quad (8.1)$$

Here, C_D is the total drag coefficient, C_{D0} is the zero-lift drag coefficient, C_L is the lift coefficient, AR is the aspect ratio of the main wing, and e is the Oswald efficiency factor. The parasite, or zero-lift, drag can be further broken down using the component build-up method from Raymer [1]:

$$C_{D0} = \frac{\sum C_{f_c} FF_C Q_C S_{wet,c}}{S_{ref}} + C_{D_{misc}} + C_{D_{L\&P}} \quad (8.2)$$

Where the subscript c denotes the component and the other parameters are defined as follows:

- C_f : Flat-plate skin-friction drag coefficient.
- FF: Form factor related to pressure drag from viscous separation.
- Q : Interference factor
- S_{wet} : Wetted surface area, exposed to air
- S_{ref} : Reference surface area, the wing's projected area.
- $C_{D_{misc}}$: Miscellaneous drag from special features
- $C_{D_{L\&P}}$: Drag from leaks and protuberances

The different components will be assessed for each parameter, and after that, they will be summed up. This allows for determining the miscellaneous drag and drag from leaks and protuberances, which will be added to obtain the zero-lift drag coefficient. The four subsystems that will be considered are the wing, fuselage, empennage and the nacelles. Due to the iterative nature of the drag, the design of the empennage will be further discussed in Chapter 11, and the nacelles will be further discussed in Chapter 10. Furthermore, it is important to state that all variables given in the tables in this section are the variables after the entire aeroplane has been integrated and converged.

Flat-Plate Skin-Friction Coefficient

The flat-plate skin-friction coefficient differs for laminar and turbulent flow, calculated using the following equations for laminar and turbulent cases, respectively:

$$R = \frac{\rho V l}{\mu} \quad (8.3) \quad C_{f_{laminar}} = \frac{1.328}{R} \quad (8.4)$$

$$C_{f_{turbulent}} = \frac{0.455}{(\log_{10} R)^{2.58} (1 + 0.144 M^2)^{0.65}} \quad (8.5)$$

Here, M is the Mach number, ρ is air density, V is free stream velocity, l is characteristic length, and μ is kinematic viscosity. The overall skin friction coefficient is the weighted average of laminar and turbulent cases, requiring an estimation of the laminar flow portion. Since the fuselage has a tadpole shape and is composite, around 25% of the fuselage has laminar flow, and the wing and tail surfaces can achieve about 40% laminar flow. With all this information, the flat-plate skin-friction coefficient for each of the four subsystems can be calculated, and the values used and final values can be found in Table 8.1.

Table 8.1: Skin friction coefficient values

Group	Reynolds Number[10^6]	Laminar[%]	$C_{f_{lam}}$ [-]	$C_{f_{tur}}$ [-]	C_f [-]
Wing	4.00	40	0.00067	0.0035	0.0023
Fuselage	28.5	25	0.00024	0.0025	0.0020
Empennage	4.50	40	0.00061	0.0034	0.0023
Nacelles	4.75	0	0.00060	0.0034	0.0034

Form Factor

The form factor for wings and empennage is calculated using the following equation.

$$FF = \left[1 + \frac{0.6}{(x/c)_m} \left(\frac{t}{c} \right) + 100 \right] \left(\frac{t}{c} \right)^4 \left[1.34M^{0.18} (\cos \Lambda_m)^{0.28} \right] \quad (8.6)$$

Where (t/c) is the maximum thickness-to-chord ratio and $(x/c)_m$ is the position where this maximum ratio is found along the chord. M is the Mach number, and Λ_m the sweep of the maximum thickness line. The form factor considering the fuselage and nacelle would conclude the following equations, leading to the resultant values in Table 8.2.

$$FF_{fuselage} = \left(1 + \frac{60}{f^3} + \frac{f}{400} \right) \quad (8.7) \quad FF_{nacelle} = 1 + (0.35/f) \quad (8.8)$$

where:

$$f = \frac{l}{d} \quad (8.9)$$

Table 8.2: Form factor values

Group	Form Factor[-]
Wing	1.45
Fuselage	1.58
Empennage	1.45
Nacelles	1.07

Interference Factor

The interference factor describes component interference, which adds drag and is estimated as follows:

- $Q_{wing} = 1.0$ for a high-wing configuration.
- $Q_{fuselage} = 1.0$, as it also has negligible interference.
- $Q_{tail} = 1.03$, for a smooth V-tail,
- $Q_{nacelle} = 1.3$, since the nacelle is less than one diameter from the wing.

Wetted Surface Area

Finally, the wetted surface area for each component is defined as the Table 8.3.

Table 8.3: Wetted surface area values

Group	$S_{\text{wet}}[\text{m}^2]$
Wing	24.9
Fuselage	24.6
Empennage	9.9
Nacelles	1.9

Miscellaneous, Leak, and Protuberances Drag

These types of drag consider the whole aircraft and are therefore not calculated with the component buildup method but rather defined as a percentage of the sum of the component buildup method. The only component that has not yet been considered for miscellaneous drag is the landing gear. The landing gear will be discussed more in-depth in Chapter 14, but for now, based on literature and the design, it is assumed that the landing gear will add 3% to the C_{D_0} of the component build-up method. Leaks and protuberance drag are more difficult to predict. With enough care, the protuberance drag can also be reduced to nearly zero, but at a considerable expense. Since the *Swing* is made mainly of composites and therefore does not have rivets or skin panels, it has little protuberance drag, but because of the hinge mechanism, the protuberance drag increases again. The hinge mechanism will also cause more leakage drag. For general aviation aircraft, the leakage and protuberance drag can be estimated to be between 2–5% and for fighters this is between 5–10%. To account for the hinge in the design and taking into account the fact that the *Swing* is made from composites, the drag due to leakage and protuberance is assumed to be 12% of the C_{D_0} of the component build-up. Therefore, the total increase due to miscellaneous and L&P drag is 15%

Total Parasite Drag

Table 8.4: Parasite drag values

Component	C_f	FF	Q	S_{wet}	$C_{D_0, c}$	$C_{D_{\text{Misc, L\&P}}}$
Wing	0.0023	1.45	1.0	24.9	0.0024	
Fuselage	0.0020	1.58	1.0	24.6	0.0061	
Empennage	0.0023	1.45	1.03	9.9	0.0054	
Nacelles	0.0034	1.07	1.3	1.9	0.0039	
Sum					0.0179	0.0026
C_{D_0}						0.0206

8.1.1. Lift Induced Drag

The lift-induced drag is only dependent on the wing shape, which has been defined in Chapter 7. The lift-induced drag is defined by:

$$C_{D_{\text{ind}}} = \frac{C_L^2}{\pi \text{AR} e} \quad (8.10)$$

Where AR is the aspect ratio, which is 14, C_L is the lift coefficient, and e is the Oswald efficiency factor, defined by Equation (8.11):

$$e = 1.78 (1 - 0.045 \text{AR}^{0.68}) - 0.64 \quad (8.11)$$

which gives an efficiency factor of 0.658. With these values, the drag as a function of lift, also known as the drag polar, can be computed, which can be seen in Figure 8.2:

8.2. Aerodynamics of Full Parametric Model

To improve the understanding of the aerodynamics of the aircraft, a full parametric model of the *Swing* was constructed and analysed using the AeroSandbox tool [2]. The parametric model was constructed using the dimensions and properties of the *Swing* as defined in the previous chapters. It is displayed in Figure 8.1.

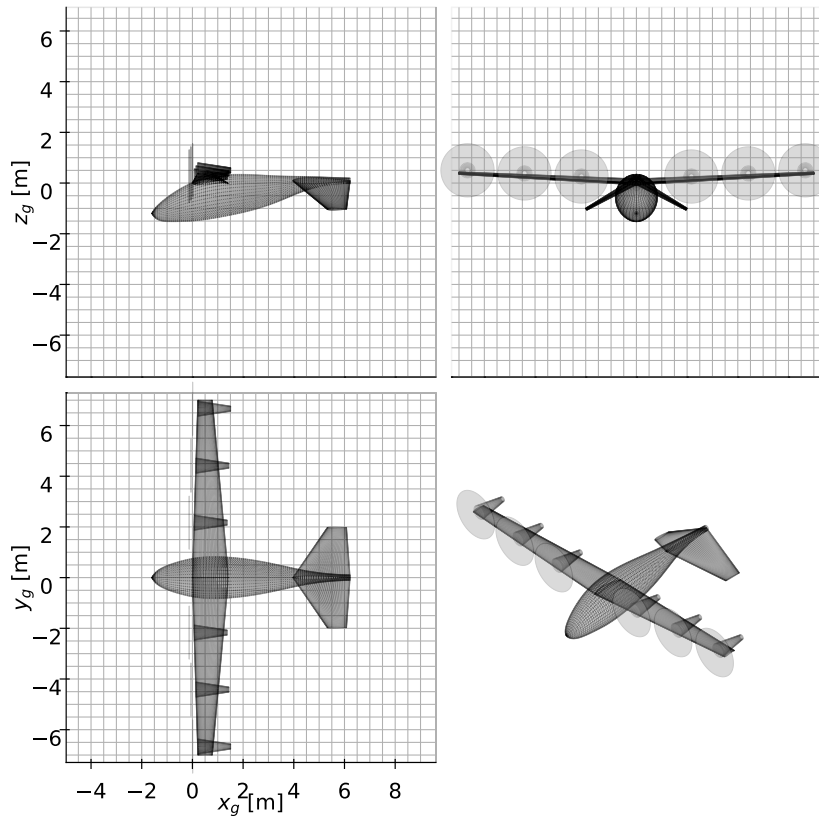


Figure 8.1: Three-view of the parametric model of the *Swing eVTOL*

For the aerodynamic analysis, the AeroBuildup Aerodynamics Engine in AeroSandbox was used. It is designed for conceptual design and preliminary design of aircraft, and is based on the USAF DATCOM methodology [40]. It computes aerodynamic forces, moments, and stability derivatives, modelling viscous and compressible effects on wings and fuselages across any orientation and arbitrary angular rates. Using the engine proved to be invaluable in the design process, as it allowed for a more detailed analysis of the aerodynamic properties across a wider range of conditions than the class II estimation.

In addition to the engine's base functionality, AeroBuildup has been extended to include the ability to model the aerodynamic properties of rotating wings. Also, a method was added to compute the stability derivatives with respect to elevator and aileron deflections. This was done by changing the parametric model to include control surfaces and then computing the aerodynamic forces for different deflections of the control surfaces. The stability derivatives were then computed by fitting the aerodynamic forces to a linear model. The results of the stability derivatives are shown in Table 8.5.

8.3. Verification and Validation

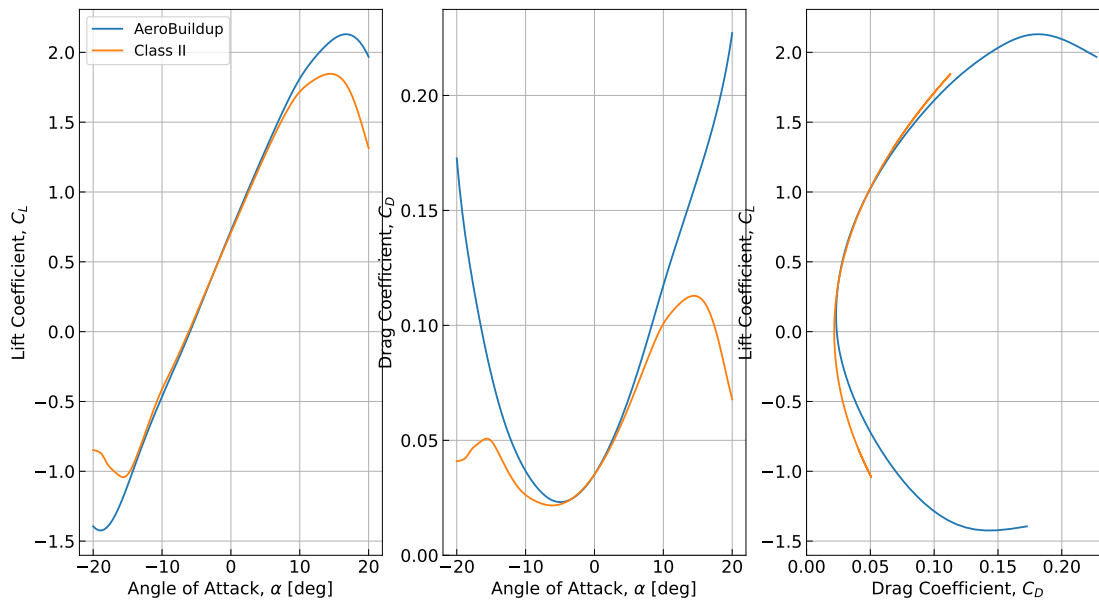
To verify the drag polar, the zero-lift drag components have been hand-calculated for a single iteration of the aircraft. Initially, some values did not match when rounded to three significant digits. For instance, the tail was not within three decimals of the result from the model, which turned out to be due to a wrong assumption about the tail area. Furthermore, the AeroSandbox tool was used to analyse the aerodynamic properties of the *Swing* as explained in Section 8.2. A comparison was made between the AeroSandbox and the class II estimation. As can be seen in Figure 8.2, they are similar for an α range between -5 and 10 degrees, after which it starts to divert. The main difference in drag polar is for high negative lift, but it is not crucial since the aircraft will not fly in a negative lift.

Also, the custom methods in the aerodynamic engine from Section 8.2 are validated by comparing the results with data from the Cessna 172 aircraft. The stability coefficients had the same sign and order of magnitude as

Table 8.5: Stability coefficients of the *Swing* for $\alpha = 0$, $\beta = 0$, $\delta_e = 0$, $\delta_a = 0$, and $V = 200$ km/h

Forces		Moments	
$C_{X\alpha}$	0.591	$C_{l\beta}$	-7.94
$C_{X\delta_e}$	-0.0341	$C_{l_{\beta\dot{\alpha}}}$	0.0287
C_{X_u}	-0.0711	$C_{l_{\delta_a}}$	-0.752
$C_{Y\beta}$	-0.441	C_{l_p}	-0.537
$C_{Y\dot{\beta}}$	0.0639	C_{l_r}	0.114
$C_{Y\delta_a}$	-0.190	$C_{m\alpha}$	-1.60
C_{Y_p}	-0.0660	$C_{m\dot{\alpha}}$	0.700
C_{Y_r}	0.254	$C_{m\delta_e}$	-5.12
C_{Z_0}	-0.639	C_{m_q}	-36.6
$C_{Z\alpha}$	-6.89	$C_{n\beta}$	0.0127
$C_{Z\dot{\alpha}}$	-0.0502	$C_{n\dot{\beta}}$	-0.0166
$C_{Z\delta_e}$	-1.32	$C_{n\delta_a}$	-4.26
C_{Z_q}	-2.63	C_{n_p}	-0.0915
C_{Z_u}	-1.46	C_{n_r}	-0.0659

the Cessna 172, which is a good indication that the custom methods are working correctly. Some deviations are found, but these are expected due to the differences in the aircraft's design, for instance, the large tail of the *Swing* compared to the Cessna 172.

**Figure 8.2:** Comparison of the lift and drag polars between the class II estimation and the AeroSandbox model

9. Power

An effective mission analysis is crucial to estimating the power required to operate the *Swing* over the whole mission profile; hence, this chapter heavily builds upon the findings of Chapter 6.

9.1. Power Required Model

The model presented in Equation (9.1) is used to estimate the power required by the *Swing* to operate nominally [41], as established in Chapter 6. Where P_{req} is the total required power, P_p the profile power, P_i the induced power and lastly, P_{par} is the parasite power. Such power components are explained in detail in the following paragraphs.

$$P_{\text{req}} = P_p + P_i + P_{\text{par}} \quad (9.1)$$

Profile Power

It incorporates the power required to overcome the profile drag of the rotor blades and wings (lifting surfaces), inherently due to their aerodynamic shape and skin friction, as they move through the air [41]. It is calculated as shown in Equation (9.2). With σ being the solidity of a single rotor, ρ the density of air, Ω the rotor rotational velocity in rad/s, V the horizontal velocity in m/s, and R the rotor radius in m. Lastly, multiplication by N_{eng} is needed to compute the total profile power of the vehicle. \bar{C}_{Dp} is the coefficient of rotor profile drag determined by empirical, rotor-specific relations [42]. Normally contributing thinly to the total required power during flight, the profile power increases with increasing vehicle horizontal speed.

$$P_p = N_{\text{eng}} \cdot \frac{\sigma \bar{C}_{Dp}}{8} \rho (\Omega R)^3 \pi R^2 (1 + 4.65 \mu^2), \quad \text{with } \mu = \frac{V}{\Omega R} \quad (9.2)$$

Induced Power

It represents the power required to overcome induced drag in an aircraft, particularly significant in vertical flight (in which very high rotor-induced velocities are generated). Induced drag is the aerodynamic resistance generated as a byproduct of lift creation [41]. Equation (9.3) is the formulation of induced power used in the present model. Where k is a factor ranging from 1.1 to 1.2, T is the total thrust required by the vehicle at a specific moment, and v_i the velocity induced by each rotor, which can be computed as $v_i = \bar{v}_i \cdot \sqrt{\frac{W}{2N_{\text{eng}}\rho\pi R^2}}$. The parameter \bar{v}_i can be found numerically by computing the roots of Equation (9.4), valid for low horizontal speeds [41]. Induced drag is, therefore, inversely proportional to the square of the airspeed. Moreover, as high thrust settings are experienced during the first stages of transition (low horizontal velocity), even higher induced power levels are expected at lower speeds, decreasing significantly at higher speeds.

$$P_i = kT v_i \quad (9.3)$$

$$\bar{v}_i^4 + \bar{V}^2 \bar{v}_i^2 - 1 = 0, \quad \text{with } \bar{V} = \frac{\text{horizontal speed}}{\sqrt{\frac{W}{2\rho\pi R^2}}} \quad (9.4)$$

Parasite Power

Lastly, it is the power required to overcome aerodynamic resistance generated by the aircraft's non-lifting surfaces and components moving through the air is required. It can be accurately computed per each horizontal velocity thanks to the aerodynamic model from Section 8.2, following from Equation (9.5). With $A_{\text{par}, i}$ being the parasite drag areas of each non-lifting element of the vehicle. From Equation (9.5), it can be derived that P_{par} will swiftly increase with the cube of the horizontal velocity.

$$P_{\text{par}} = \Sigma A_{\text{par}, i} \frac{1}{2} \rho V^3 \quad (9.5)$$

9.2. Mission Power Curve

Table 9.1 summarises the parameters determined in the previous chapters, which are inputted into the power model described in Section 9.1. The result is a plot of power required over horizontal speed, as shown in Figure 9.1.

Table 9.1: Parameters used for the power model

R [m]	Ω [rad/s]	W [N]	RPM [-]	σ [-]	k [-]	$A_{\text{par, tot}}$ [m ²]	T [N]
1.05	163 ¹	16200	1560	0.28	1.1	Simulated	Simulated

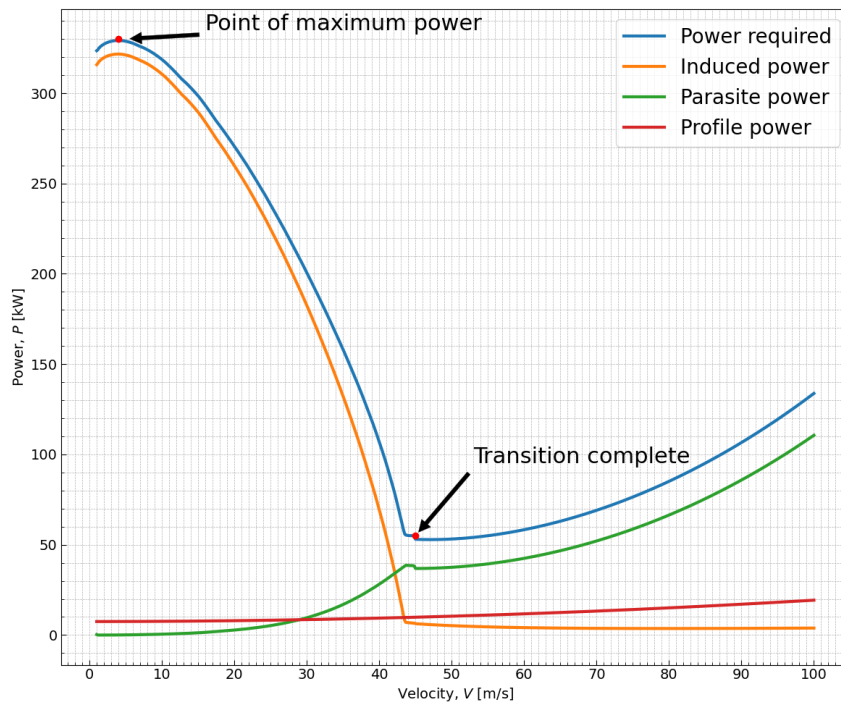


Figure 9.1: Power required over velocity profile.

Several observations can be made from Figure 9.1. First and foremost, as an inherent form of validation, it can be seen how the individual power contributions follow the trends predicted in Section 9.1. The point at which transition is complete and that at which the peak of power required is estimated to occur is indicated, respectively, at 45 m/s and about 3 m/s. Interestingly, the power peak of 330 kW is reached at a velocity of 3 m/s (at $\sim 30\%$ of transition from vertical to horizontal flight, and not during hover, when $V=0$ m/s), likely as a consequence of the extra thrust required to be delivered by the engines to compensate for a loss in lift caused by the inclination of the thrust line. The thrust required to keep vertical equilibrium during the transition, causing very high values of induced power, mainly depending on the transition stage (or transition value); extensive discussion on this can be found in Section 6.2.3. Hereafter, the power required swiftly decreases to match standard horizontal flight conditions at 45 m/s. Being the cruise speed of about 56 m/s (200 km/h), the required power is expected to stay well within 60 kW at all times during cruise, making the aircraft very efficient in horizontal flight [43].

¹For a conservative power estimate, Ω is taken equal to the rotational rate associated with 1300RPM, the highest RPM setting the *Swing* is designed for

10. Propulsion

In this chapter, the procedure to size the propulsion subsystem of the *Swing* will be presented, discussed, motivated and performed. The design procedure of the propulsion subsystem is summarised and shown in the flowchart of Figure 10.1. Insights on the correlation between key requirements and design variables are instead found in Figure 10.2. After a brief introduction to the concept of disc loading, following directly from the structure proposed in Figure 10.1, Section 10.1 will determine the ideal number of engines and their placement along the wing. To follow is the design of the propellers in Section 10.2 and the choice of suitable OTS engines in Section 10.3. The chapter is concluded by Section 10.4 in which the numerical models used are verified and validated.

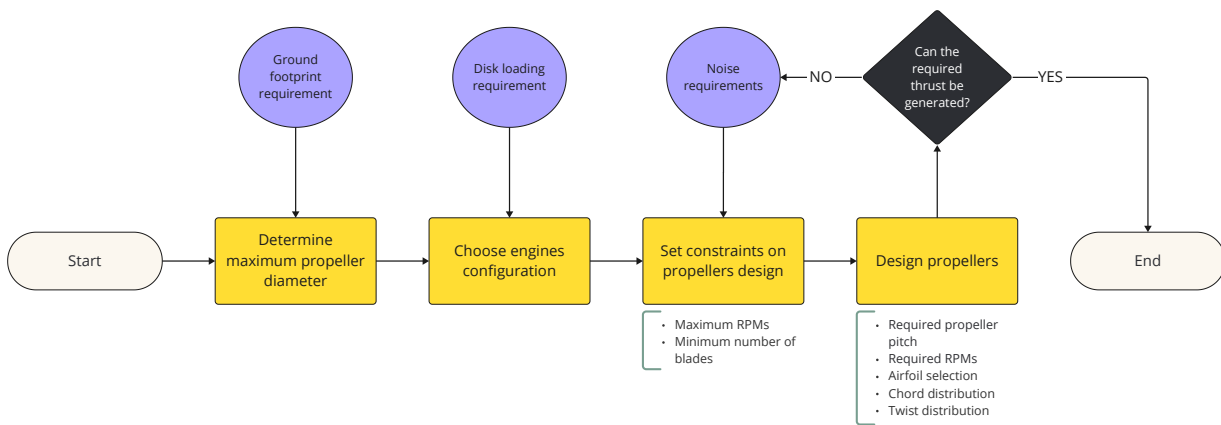


Figure 10.1: Flowchart of the propulsion sizing procedure.

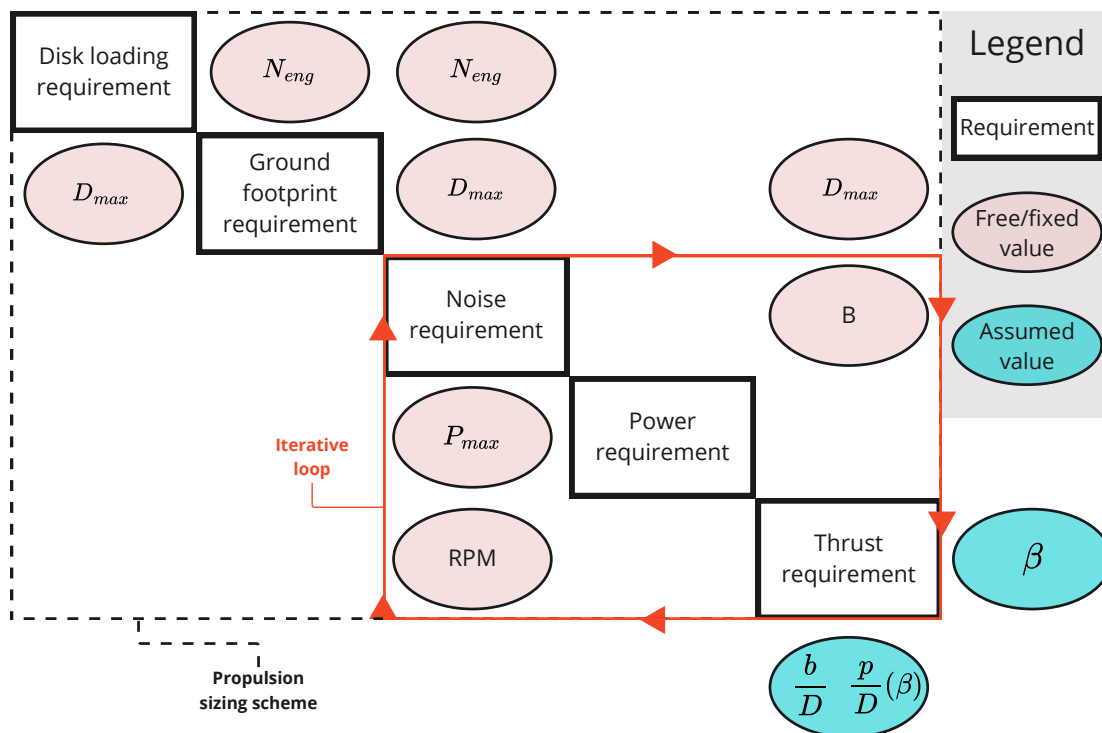


Figure 10.2: N2 chart for propulsion sizing.

Disc Loading

Being of crucial importance, the concept of disc loading is here preemptively introduced, and will be used extensively in the sections to follow. The disc loading is a parameter that influences the performance in many ways, accounting for the average change of pressure over the rotor disc; it can thus be seen as an indication of how heavily each rotor is loaded. Its maximum (limiting) value can be computed as indicated in Equation (10.1):

$$DL = \frac{T_{\max}}{S_{\text{disc}} \cdot g \cdot N_{\text{eng}}} \quad (10.1)$$

DL being the disc loading in kg/m^2 , T_{\max} the maximum thrust experienced over the mission span, S_{disc} the area of one rotor, g the gravitational acceleration, and N_{eng} the number of engines contributing to producing the total thrust. Here T_{\max} is taken to be $2 \cdot W_{\text{MTOW}}$, in agreement with the maximum thrust requirement (CO-3-STK03-3). Since the general requirement for multicopters, which accounts for the *Swing* in VTOL configuration, is that the rotors should create twice the thrust required to hover [44], the design thrust-to-weight ratio ought to be 2 (requirement CO-3-STK03-3).

10.1. Engines Configuration

Before delving deeper into propulsion sizing, the ideal number of engines, N_{eng} , must first be determined (engines configuration) as it forms the baseline for any type of propulsion calculations and assessments. The choice was ultimately based on considerations regarding disc loading and safety, as discussed below, leading to the trade-off of Table 10.2.

10.1.1. Disc Loading Analysis and Discussion

Only configurations comprising of four, six, eight, and ten total rotors are considered, as less than four engines would unacceptably hinder vehicle controllability [3] while having more than ten would not allow meeting the requirement on disc loading ($DL < 400 \text{kg}/\text{m}^2$, requirement CO-3-STK03-2) at all times, as shown in Table 10.1.

Table 10.1: Maximum disc loading per configuration. Here, $T_{\max} = 2 \cdot W_{\text{MTOW}}$

N_{eng}	D_{\max}	DL_{\max}
4	3.70	99
6	2.22	183
8	1.59	268
10	1.23	354
12	0.93	442
14	0.79	529
16	0.70	616

The maximum obtainable propeller diameter, D_{\max} , is determined per configuration from geometrical considerations, based on the maximum ground footprint constraint ($4 \times 8 \text{m}^2$), the wing span of the design (14 m) and the width of the fuselage (1.7 m). These constraints allow to determine the maximum diameter of the propeller as a function of the number of propellers present on the vehicle. There also needs to be a clearance between the propeller blades, this clearance is taken as 1.2 m in total [45]. This is done to prevent a bias towards lower propeller counts. The area and diameter can thus be calculated with Equations (10.2) and (10.3).

$$A = \frac{\pi D^2}{4} \cdot N_{\text{eng}} \quad (10.2)$$

$$D = \frac{B - F - d_{\text{clearance}_{\text{tot}}}}{N_{\text{eng}}} \quad (10.3)$$

Where B is the wingspan in m, F is the fuselage width in m, $d_{\text{clearance}_{\text{tot}}}$ is the total clearance distance in m and N_{eng} is the number of propellers per configuration. The maximum, theoretical, diameter in Table 10.1 does not include factors such as the width of the nacelle; therefore, the final propeller diameter will be lower.

The so-called computed diameter, though, still gives a valid and consistent indication of how efficiently space is used by the propulsion system within the geometrical constraints. Disc loading plays a preponderant role in assessing hovering efficiency, noise, downwash effects and gust resistance of a vehicle. Its effect on each of such aspects is briefly discussed in the paragraphs to follow.

Hovering Efficiency

As it can be seen in Equation (10.4), the hover efficiency is inversely proportional to the square root of the disc loading, where the hover efficiency is defined by $\frac{w_0}{P}$ [46]. P being the total shaft power and w_0 representing the weight of the eVTOL. Other variables include the figure of merit (FM), density (ρ), thrust (T), and the rotor disc area (S_{disc}).

$$\frac{w_0}{P} = \frac{w_0 \sqrt{2\rho S_{\text{disc}}}}{(T)^{3/2}} \cdot \text{FM} \quad (10.4)$$

Hence, a high disc area, thus low disc loading, allows for higher hover efficiency. Therefore, a lower disc loading is distinctly favourable due to minimising the power required for vertical take-off and landing.

Downwash Effects and Noise

Furthermore, the lower lift efficiency at higher disc loading configurations, due to the smaller movements of downward air, results in high downwash speeds. Hence, the noise creation and other apparent effects need to be taken into account, once again favouring a lower disc loading. Thoroughly discussed [16], lower downwash speeds are preferred for UAM as it leads to safer and more urban-environmentally sustainable vehicles. This is because high downwash speeds can even cause damage or injuries by soil projection on vertistops or account for a substantial increase in noise production due to the aerodynamic interactions with the take-off and landing environment.

Gust Resistance

Although the previous two arguments make a good case for a low disc loading configuration, there are a few benefits to having a higher disc loading. In particular, the sensitivity to gusts, which is higher for low disc loading configurations. Therefore, higher disc loadings are preferable for gust resistance, as gust load factors are inversely proportional to disc loading [47]. Moreover, smaller rotor configurations, thus higher disc loadings, tend to permit a lower motor torque [48].

10.1.2. Safety and Controllability Analysis and Discussion

To evaluate the safety of the propulsion configuration, One Engine Inoperative (OEI) events are analysed, as they critically influence the safety of the *Swing*, for cruise and VTOL configurations separately.

In a VTOL configuration, an OEI condition would still allow the *Swing* to fly, however, losing the yaw control [49], which would be unacceptably unpleasant and unsafe for the passengers. Hence, a minimum of six engines is considered necessary for maintaining a stable and controlled flight even in an OEI situation. Also assessing the safety of the *Swing* in its cruise configuration, in the event of failure of two opposing engines, a minimum of six engines is needed to keep flying [50].

Most eVTOLs have their propeller count between six and twelve, as can be deduced from Table 2.1. This is mostly in the interest of noise and low system complexity, as having more propellers is likely to decrease the need for variable pitch propellers [51]. A fixed pitch with variable RPM system stands out as a more viable and efficient option, significantly reducing the complexity of the vehicle. Moreover, a variable RPM vehicle is less sensitive to motor-rotor coupling and transient dynamics of the variable pitch option [52].

10.1.3. Engines Configuration Trade-Off

Conclusions can now be drawn from the information gathered in Section 10.1.1. In order to perform an informed choice with respect to the engines configuration, such conclusions are concisely assembled in Table 10.2, in which a trade-off is performed

Table 10.2: Engines configuration trade-off summary table.

Number of Engines	Disc Loading	Hovering Efficiency	Noise	Gust Resistance	Score
6	3	3	3	1	2.5
8	2	2	2	2	2.0
10	1	1	1	3	1.5

As is clear from Table 10.2, the configuration consisting of six engines is considered the most appropriate for the *Swing*. Each criterion is assigned an equal weight of 25% (column widths are therefore not to scale), and each configuration is ranked from 1 to 3 according to the disk loading values of Table 10.1.

10.2. Propeller Design

Now that a configuration is chosen such that the requirements on disc loading and ground footprint are met, it is time to size the propellers, following the structure proposed in Figure 10.1. The diameter, D , and number of engines are fixed, as determined in Section 10.1. Instead, the blade number per rotor B , design RPM, blade pitch at 0.75R, β , twist distribution as a function of β , $\frac{p}{D}(\beta)$, and chord distribution $\frac{b}{D}$, are yet to be determined to fully fix the propeller geometry.

As shown in Figure 10.1, first the maximum allowable RPM and optimal blade count are set from noise requirements in Section 10.2.1; after this, a suitable combination of β and RPM is chosen in Section 10.2.2 so that the thrust requirement is met; iterations are performed if needed, as indicated in Figures 10.1 and 10.2. Accurately determining the optimal blade airfoil, chord and twist distributions is out of the scope of this report, mainly in the interest of time. An airfoil, $\frac{p}{D}(\beta)$ and $\frac{b}{D}$ are therefore assumed as explained in Section 10.2.2.

10.2.1. Propeller Noise Analysis

Noise is a very restraining requirement for UAM applications, as the vertiports will mostly be located in urban environments, where, in return, the noise production will also be highest due to take-off and landing configuration. Moreover, due to the surroundings in an urban environment, noises are likely to be amplified. Surrounding buildings may increase noise levels by 5 dB, as well as surrounding noises that may amplify the noise production to even 40 dB, hence the focus on minimising the frequency of the noise to decrease the dBA [53]. All showing the impact of the noise and its environment. As the maximum allowable noise differs per urban environment, most of the time, the maximum is 88 dBA at 25 feet for a short period and 80 dBA for a prolonged amount of time [21].

In a collaborative effort with NASA, Joby performed an extensive noise analysis on its aircraft [22]. In take-off configuration, the aircraft achieves noise levels of 65 dBA at 330 feet, 88dBA at 7 feet and 45.2dBA at 1640 feet in cruise configuration; more detail on the noise-wise comparison with Joby can be found in Section 10.4.1. The noise model will, therefore, take the 65dBA, 88 dBA and 45.2dBA at 330, 7 and 1640 feet, respectively, as requirements to numerically retrieve the maximum RPM from. Compliance with requirement CO-3-STK07-2 will be instead checked in Section 14.1. To assess the noise generated by the *Swing*, a computational model is created by directly implementing a procedure proposed by NASA (JPL) [54]. The formula used to calculate the far-field noise (defined as noise at a distance further than one diameter of the propeller) for a single propeller is shown in Equation (10.5)

$$SPL_{\text{overall}} = L_1 + 20\log_{10}\left(\frac{4}{B}\right) + 40\log_{10}\left(\frac{15.5}{D}\right) + C_{\text{Mach}} + C_{\theta} - 20\log_{10}(r-1) \quad (10.5)$$

In this equation, the first term L_1 is the reference noise level; it is based on the motor power and it is obtained from Figure B.2 in [54]. The next two terms are corrections for the number of blades, B , and propeller diameter, D (in ft). The next term, C_{Mach} , is a correction for the tip Mach number, obtained from Figure B-3 in [54]. C_{θ} is instead a correction which accounts for the direction in which the noise is being calculated

and it is obtained from Figure B-8 in [54]. For this calculation, it was decided to use a correction of +4 dB, which is the maximum value of the average curve, to obtain the noise at the position in which it is at a maximum. Lastly, the last term, where r is the distance in ft at which the noise is to be calculated, accounts for the noise attenuation due to propagation from source to observer.

As shown in Equation (10.5), a higher number of blades results in less noise. This is because more blades distribute the pressure increment to the flow more equally, which favours selecting a high number of blades for the design of the propellers. Equation (10.5) holds for one propeller, so to calculate the combined noise from all propellers, Equation (10.6) is used, where L represents the noise in dB or dBA. This equation results in the sum of the noise by each propeller when calculated under isolated conditions and assuming incoherent sources, but it does not take into account the aerodynamic and aero-acoustic propeller-propeller and propeller-fuselage interactions. These effects are difficult to model and thus not taken into account in this preliminary analysis; it is in other words assumed that, respecting the minimum clearance determined in Section 10.1.1, would keep such interactions at a minimum, making them negligible.

$$L_{\text{tot}} = 10 \log_{10} \left(\sum_{i=1}^n 10^{(L_{\text{prop},i}/10)} \right) \quad (10.6)$$

It was decided to apply Equation (10.5) and to iterate on the maximum allowable RPM, after having fixed the number of blades per rotor, B , to 6. Having more blades per rotor leads to less aerodynamic noise, but a price is paid in terms of hovering efficiency, as explained in Section 10.1.1. Adopting 6 blades is believed to allow for a satisfying trade-off between aerodynamic efficiency and low propeller noise [55], [56]. With a known diameter of 2.1 m, blade count of 6, and maximum shaft horsepower per engine of 76 Hp (refer to Figure 6.6), Equations (10.5) and (10.6) can be applied with the aim of determining the maximum RPM the propellers can spin at, to satisfy the noise requirements.

Once SPL_{overall} was computed per the three cases (hover at a distance of 330 ft and 7 ft, and cruise at a distance of 1640 ft) used for noise analysis, the result (in dB) was corrected for harmonic number (following Figure B-6 in [54]) and lastly converted to A-Weighted dB (dBA) following the correction indicated in Figure 10.3.

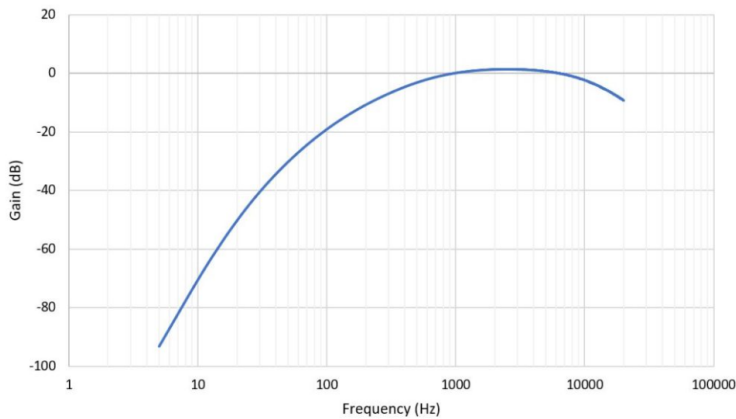


Figure 10.3: A-Weighting curve [57]

The noise levels are plotted per integer multiples of the Blade Passage Frequency (BPF) up to 20 kHz, the upper limit of the audible frequency range, in Figure 10.4. The results are plotted, and the overall SPL in dBA (OASPL) is indicated in Figure 10.4, computed per each case as indicated in Equation (10.7).

$$\text{OASPL} = 10 \log_{10} \left(\int_0^{\infty} \frac{L(f)}{\text{BPF}} \cdot df \right), \quad \text{with } L(f) = 10^{\frac{\text{SPL}(f)}{10}}, \quad \text{and } \text{BPF} = \frac{B \cdot \text{RPM}}{60} \quad (10.7)$$

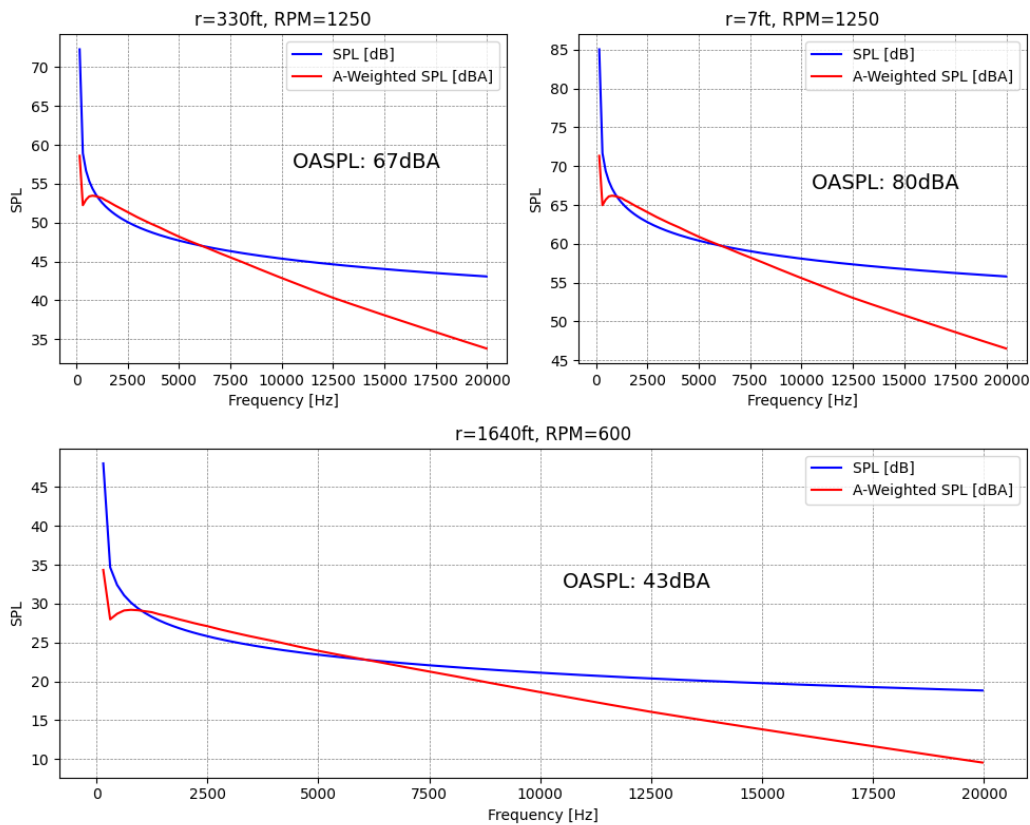


Figure 10.4: SPL spectrums conforming to the noise requirements over audible frequency range, for varying distance and RPM setting.

The noise estimation tool was run for increasing RPM, at steps of 50 RPM, and the results of Figure 10.4 were the first to meet the noise requirements set to a satisfying extent. The following values of cruise and hover RPM are therefore taken as the threshold values for the following steps of the analysis:

Vertical Flight Maximum RPM 1250 | Cruise Flight Maximum RPM 600

It is important to note that such values are ideally only respected during the nominal operation of the vehicle. If, for instance, an event of emergency occurs, such values can be momentarily exceeded.

10.2.2. Propeller Available Thrust Analysis

Now that in Section 10.2.1 the maximum RPM allowing to meet the noise requirements is established, it can be checked if the thrust requirement can be met within such requirements. This is the iterative loop indicated in red in Figure 10.2. Accurately estimating the thrust generated by a propeller given geometric parameters and RPM settings is no easy task, as it involves the numerical implementation of theories such as Blade Element Method (BEM) and momentum theory [41]. In the interest of time, such procedures are not carried out in this report, where the available thrust will, therefore, be assessed by means of empirical methods, building upon available literature on conventional aircraft propeller designs. In wind-tunnel tests conducted by D. Biermann [58] specifically, thrust curves were experimentally determined for single-rotating, six-blade propeller of 3 m in diameter. Such propellers were operated with Reynold's numbers (Re) of approximately 10^6 , comparable to the predicted Re of 5×10^6 the propellers of the *Swing* will experience during operation. The thrust coefficient, defined as in Equation (10.8), is plotted in Figure 10.5 against both the advance ratio J and RPM, per varying β

$$C_T = \frac{T}{\rho n^2 D^4}, \quad J = \frac{V}{nD} \quad (10.8)$$

n is the revolutions per second, and V the propeller axial (freestream) velocity. As previously mentioned the blade airfoil, twist and chord distributions used in [58] are assumed for the *Swing* as well, for simplicity's sake. The blade airfoil is therefore taken to be the Clark-Y, whereas the twist and chord distributions are taken from Figure 1 of [58]. Thanks to the assumptions above, to be reviewed in later design stages, Figure 10.5 can be constructed.

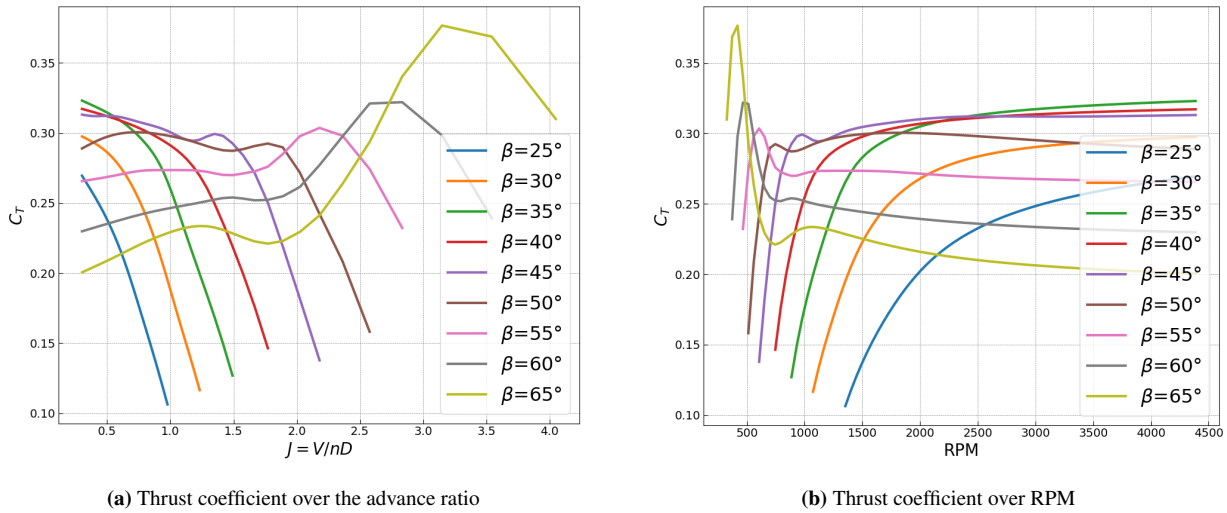


Figure 10.5: Thrust coefficient over advance ratio and RPM for a six-blade, single-rotating propeller

Horizontal (cruise) and vertical flight will be separately assessed in the paragraphs to follow, following from the diagrams of Figure 10.6 and Figure 10.7.

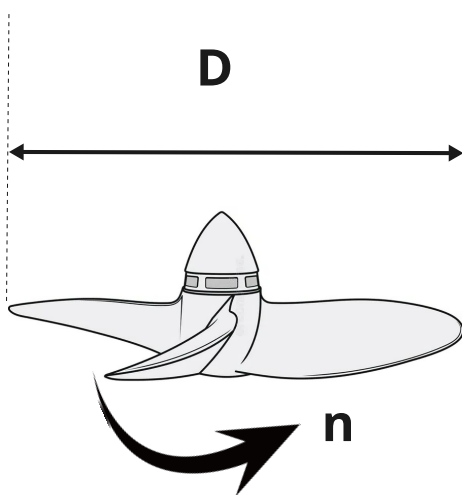


Figure 10.6: Rotor during vertical flight, $V = 0$ km/h

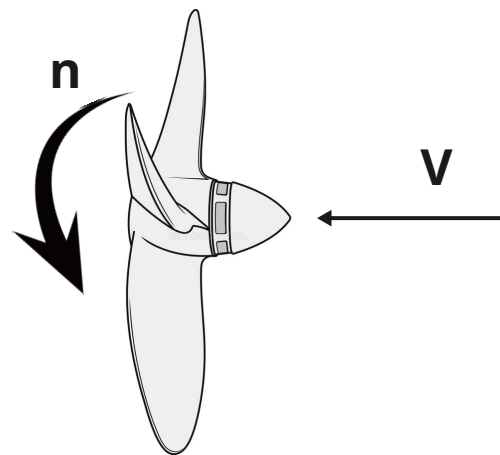


Figure 10.7: Propeller during horizontal flight (cruise, $V = 200$ km/h).

Available Thrust During Cruise Combining Figure 10.5a and Figure 10.5b using $V = 200$ km/h in $J = V/nD$, allows to plot the estimated overall thrust generated per propeller, and under standard atmospheric conditions ($\rho = 1.225$ kg/m³, $Re \sim 10^6$), as a function of its RPM (throttle setting). The result is the graph shown in Figure 10.8. Here, for graphic clarity, fewer values of β are plotted for ease of visualisation; however, the whole continuous interval $[20^\circ, 65^\circ]$ is considered during the analysis.

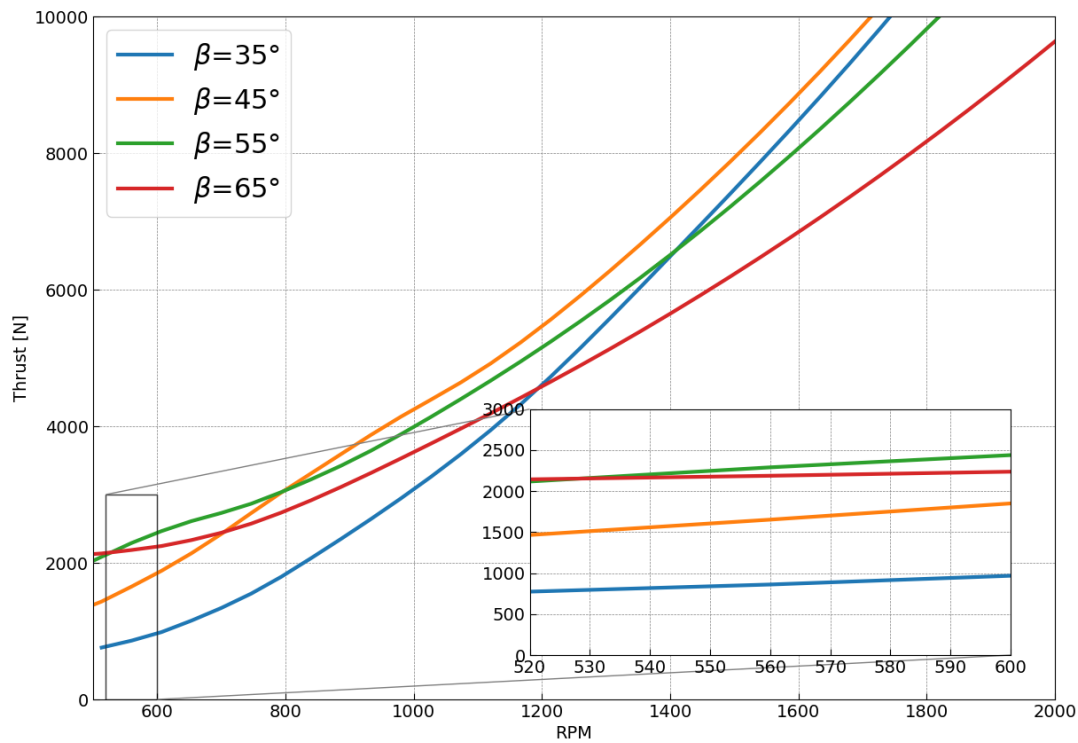


Figure 10.8: Thrust over RPM for a six-blade, single-rotating propeller

Following from Figure 10.8 is obvious that in order to meet the cruise thrust requirement of 2500 N, translating to 417 N per propeller during normal operations, from merely an available thrust point of view, virtually any choice of pitch angle at $0.75R$ of the blade could do the job. It is important to note that, during the cruise, higher pitch angles are beneficial for aerodynamic efficiency as opposed to lower pitch blades [59]. This is reflected in the fact that pitch angles of 45° , 55° and 65° are optimal for generating thrust at lower RPM and higher values of the advance ratio (in general, higher thrust in cruise conditions).

Available Thrust During Vertical Flight and Hovering This flight condition turns out to be the most constraining, given the high thrust requirement of 32 000 N, or 5333 N per engine (CO-3-STK03-3). Overall phases of vertical flight, for simplicity's sake, it is assumed that the axial propeller speed be 0km/h. This entails that $J = 0$, allowing to directly read the values of C_T as a function of β from Figure 10.5a. The above, through the application of Equation (10.8), are used to create the thrust curves in Figure 10.9. As it can be seen from Figure 10.9, in order to generate the required thrust of 5333 N per engine, the $RPM_{\max} = 1250$ set in Section 10.2.1 is not sufficient. Indeed, in order to meet the vertical flight thrust requirement, the rotors have to rotate at 1300RPM with $\beta = 35^\circ$ (as shown in Figure 10.9b), violating the noise requirements. The exact repercussions of this result are discussed in detail in Section 10.2.4.

10.2.3. Propeller Interference Discussion

Due to the novel transition of the propellers, the effect of the propeller slipstream on the wing and other static surfaces should be carefully taken into account, as this will influence the previously defined performance parameters greatly. A Stokkermans et al. paper (2021) on the propeller slipstream influence in eVTOL configurations is of great use [60], as it dives deeper into the effects of transitioning as well, thus very valuable for this design. The study found a strong relation of interaction effects with the geometric lay-out, as interaction effects are reduced with increasing the distance between propellers. Moreover, during take-off and transition, the interaction effects are weak at small angle of attack (AoA), while great for larger AoA.

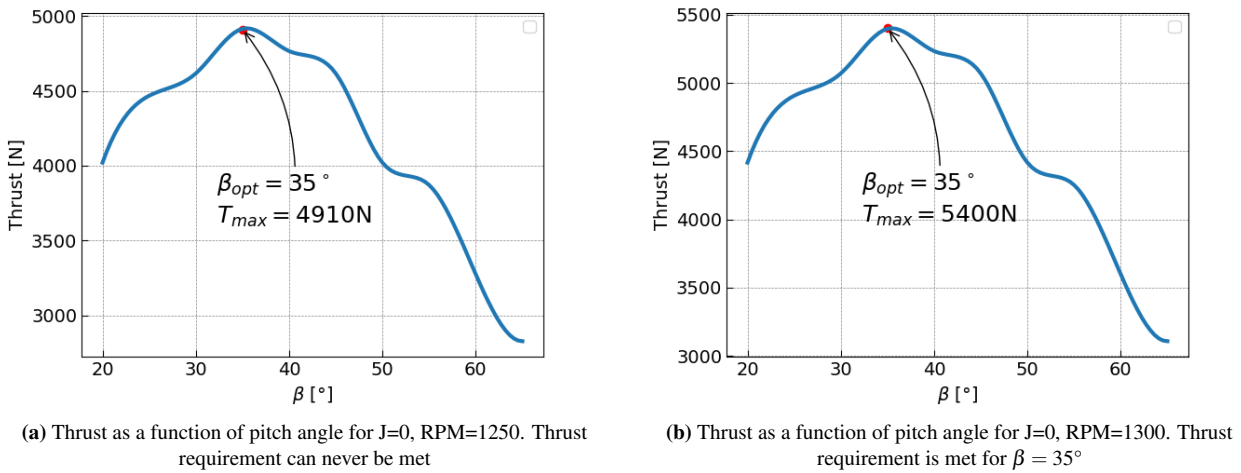


Figure 10.9: Thrust curve over blade pitch angle for different RPM settings of a six-blade, single-rotating propeller

This is a great area of focus, due to the high AoA that is reached in the transition phase. Furthermore, with an increasing AoA comes a greater reduction in C_T and C_P , compared to isolated propeller configurations. Hence, a propeller thrust loss of 30% was even found for the rear propeller, which would result in a total power loss of up to 13% in order to keep constant thrust by increasing the rotational speed of propellers. However, it should be noted that the study only covered a two-propeller interaction, as well as so-called “side-by-side” and “one-after-another” configurations, whereas this design is a combination of the two during the transition.

Lift and drag are other parameters which greatly influence the flight performance as well; it is interesting to look at the changes due to propeller interference. Since eVTOL configurations have propellers for vertical take-off and landing, as well as for cruise, a correct decision should be made regarding the propellers. Whether all are the same, thus useful in both operations or if making use of redundant engines. The last option considers having either feathered or windmilling redundant propellers; however, these are found to be less favourable for flight performance. Since, in cruise, feathered blades can reduce lift by 25% and increase drag up to 70%, while for windmilling the drag can even increase by 90% [61]. Although the windmilling solution could account for 50% of the required cruise power, the redundant engines are no real viable option. It is, however, found that the aerodynamic performance of working propellers on the wing is beneficial. Because of the induced airflow, it seems to increase lift produced by the wing up to 8%, while 3% in high-lift conditions [62]. Therefore, it is hereby confirmed that the chosen configuration is the most beneficial for the aircraft. Although it should be noted that the propellers were placed above the wing, and not in front of the wing, like this project’s design. Moreover, the separation AoA is generally found to be higher, due to the propeller interference with the wing [63].

Because of the above-stated reasons, the propeller interaction effects can be of great help in sustaining the aircraft in the transition phase, as this phase will endure the highest AoA.

10.2.4. Conclusions on Propeller Design

Now that the propellers have been designed in compliance with the related key requirements, conclusions can be drawn. Given the very low thrust requirement of the *Swing* during cruise, excellent noise levels can be reached while still generating more than satisfying levels of thrust, also comfortably allowing for proper handling of OEO situations and emergency manoeuvres. During vertical flight, however, it turns out 1300 RPM are necessary to fulfil the required T/W value. Therefore, Figure 10.4 is generated again in Figure 10.10, with the new RPM value in.

As it can be noted from Figure 10.10, the new maximum RPM setting leads to an increase in SPL of 0.63dBA, meaning a roughly 12% louder aircraft, thus slightly violating the noise requirements. However,

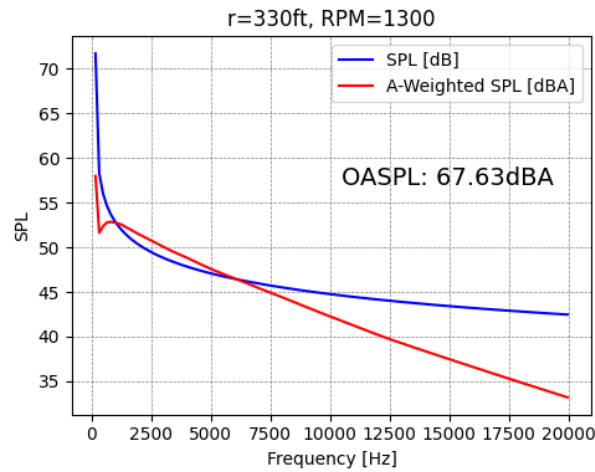


Figure 10.10: SPL spectrum recomputed at a sample distance of 330ft, with the new RPM setting of 1300

it is important to note that such high-thrust (and therefore high-RPMs, ultimately leading to high SPL) flight conditions will rarely be met during normal operations. Lastly, a blade pitch angle at $0.75R$ (β) of 35° is chosen, offering optimal performances during vertical flight and transition, and slightly suboptimal performances during cruise (optimal cruise pitch would be around 55°). Achieving optimal performance during cruise would, therefore, require the implementation of a variable propeller pitch system, the complexity and cost of which was considered to not outweigh its -not so substantial- advantages.

10.3. Motor Selection

Since the propellers have now been properly sized, as well as its performance parameters, the trade-off on the end of the motor selection can be performed. In the interest of cost, time and vehicle reliability, it was decided to opt for using OTS electric motors, specifically designed and optimised for eVTOLs. An extensive literature study was performed to identify state-of-the-art, certified electric engines suitable for UAM applications. Bearing in mind the total power requirement of $343 \text{ kW}/6 = 56 \text{ kW}$ per engine from Section 6.2.3, only the motors capable of delivering at least 56 kW of continuous maximum power¹ (P_{\max}) are presented in Table 10.3.

Table 10.3: Tabulated results of motors literature study

	P_{\max} [kW]	T_{peak} [Nm]	RPM_{\max} (@ P_{peak})	Mass [kg]	P/W [kW/kg]	$P_{\text{peak,tot}}$ [kW]	$D \times L$ [mm]
Emrax 208	56	90	6000 (86)	10.3	5.4	336	208 × 85
Emrax 228	75	130	6500 (124)	13.5	5.6	450	228 × 86
Evo Motor AF340	282	780	5000 (660)	122	2.3	1692	380 × 333
MagniX Magni350	320	-	2300 (350)	128	2.5	1920	675 × 550
Remy HVH250HT	100	440	10 600 (150)	43	2.3	600	242 × 180
Rotex REB 90	30	-	2800 (80)	23	1.3	180	270 × 212
Yasa 750R	70	400	3250 (200)	37	1.9	420	368 × 98

With T_{peak} being the maximum torque that can be exerted by the engine. P_{peak} , as opposed to P_{\max} , is the power that can be delivered by the engine only in short bursts of a couple of seconds. D is the motor diameter, L the motor length. Based on Table 10.3, a quick trade-off is set up and performed in Table 10.4, where each criterion is given an equal weight of 25% (column widths are not to scale). Scores are given on a scale from 1 to 5 according to Table 10.3, rounding Equation (10.9) to the nearest integer.

$$\text{rescaled value} = 1 + \left(\frac{\text{value} - \text{min value}}{\text{max value} - \text{min value}} \right) \times (5 - 1) \quad (10.9)$$

¹Power which can be continuously delivered to the propeller for more than 60 seconds.

Table 10.4: Motor selection trade-off summary table

Motor	Mass	P/W	D	L	Score
Emrax 228	5	5	5	5	5.0
Evo Motor AF340	1	1	1	4	2.3
MagniX Magni350	1	2	1	1	1.3
Remy HVH250HT	4	1	4	5	3.5
Yasa 750R	4	1	4	5	3.5

It is clear that the Emrax 228 wins this trade-off. Given an expected maximum RPM of 1300 and a maximum torque experienced, during transition, of $T_{\max} = 525.2 \cdot \text{PHP}/\text{RPM} = 70\text{Nm}$ (given the shaft horsepower per engine PHP, and rotor RPM), the Emrax 228 is selected as the engine to be mounted on the *Swing*.

10.4. Verification and Validation (V&V)

In this section, the computational models used in Section 10.2.1 and Section 10.2.2 to size the propulsion subsystem will be verified and validated. For verification, the models are to be checked for correctness of implementation and coherence with the underlying theory. During validation, the results provided by the models are checked against known real-life results, allowing the model to be deemed reliable [64].

10.4.1. Noise Model V&V

Verification As previously explained, the noise model derives from the direct implementation of the procedure outlined in [54]. Unit tests were performed on individual code functions to make sure plotting and basic calculations were working in order and according to theory. Moreover, results and plot trends comparable to those found in [54] are obtained in Section 10.2.1, therefore allowing to confidently state the model is verified - as its results are in full accordance with the theoretical framework it is based on.

Validation With respect to model validation, it was chosen to run the tool with parameters taken from the Joby aircraft (listed in Table 10.5), for which an in-depth noise analysis was performed [22], allowing it to compare its results against those outputted by the model of Section 10.2.1. Running the tool with the parameters indicated below for various distances (in ft) at which the noise is to be calculated, leading to the plots of Figure 10.11.

Table 10.5: Joby parameters used for noise model validation

Rotor diameter [ft]	Blade count per rotor [-]	Hovering RPM	Hovering Power [kW]
6	5	800	411

From Figure 10.12 the actual vehicle noise in dBA can be determined, at vertical distances of 50, 100 and 200 ft. Putting together the information from Figures 10.11 and 10.12, Table 10.6 can be constructed, summarising the results of this validation procedure.

Table 10.6: Tabulated results of the noise model validation procedure

Vertical Distance [ft]	Actual Noise [dBA]	Simulated Noise [dBA]
50	85	88
100	75	82
200	62	69

From Table 10.6 it can be observed that the model of Section 10.2.1 consistently overestimates the OASPL generated. This result is considered beneficial, as it suggests that there is room for further improving the

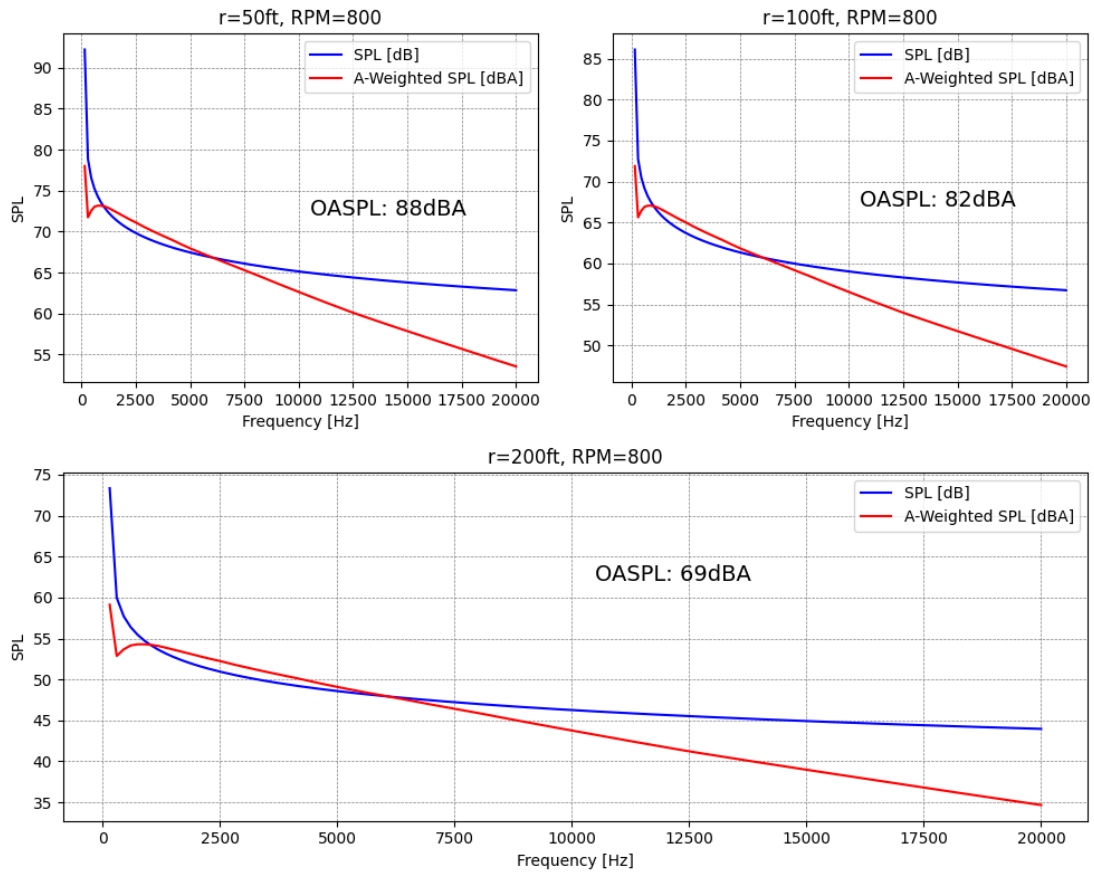


Figure 10.11: Output of the noise model running on Joby parameters

generated OASPL of the *Swing* by aerodynamic optimisations of the vehicle surfaces (both lifting and non-lifting).

10.4.2. Thrust Model V&V

Verification As for the noise model, the thrust model outlined in Section 10.2.2 is considered to be verified by appropriate unit tests and accordance; comparing Figure 10.5a against the corresponding graphs in [58] allows proving the model was implemented correctly.

Validation To instead validate the model, a sensitivity analysis will be performed. As it can be seen from Figure 10.2, rotor diameter (D), blade count (B) and RPM are inputs to the thrust model. From this, Table 10.7 can be constructed.

Variable Change	Expected Output	Model Output	Pass/Fail
$B \downarrow$	$T \downarrow$	$T \downarrow$	Pass
$D \uparrow$	$T \uparrow$	$T \uparrow$	Pass
$D \downarrow$	$T \downarrow$	$T \downarrow$	Pass
$RPM \uparrow$	$T \uparrow$	$T \uparrow$	Pass
$RPM \downarrow$	$T \downarrow$	$T \downarrow$	Pass

Table 10.7: Variable changes and their effects on thrust output

Following the results of Table 10.7, the thrust model is said to be validated.

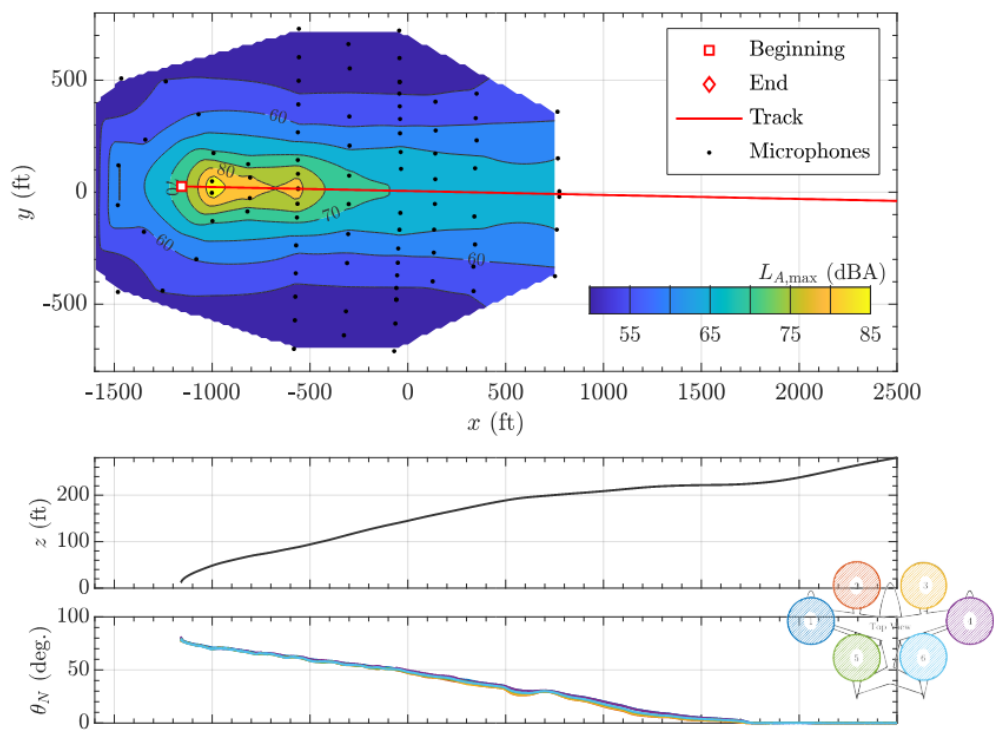


Figure 10.12: Noise analysis empirically performed on Joby

11. Stability and Controllability

In this chapter, the procedure used to ensure the stability and controllability of the *Swing* design is described in detail. In Section 11.1 the ailerons are sized, after which a hover control analysis has been performed in Section 11.2. From this, the CG is estimated in Section 11.3 after which the tail is sized in Section 11.4. The final configuration and the sizing of the horizontal and vertical tail sizing are done in Section 11.5, Section 11.6 and Section 11.7 respectively. After the final sizing, the dynamic stability during cruise is assessed in Section 11.8, discussed in Section 11.9 and verified in Section 11.10.

11.1. Preliminary Aileron Sizing

One of the first steps that can be taken to ensure that the design is controllable is to design the control surfaces in order to meet the rolling requirement. According to CS 23 requirements, a General Aviation Aircraft should meet a 60° in 1.3 second rolling requirement [65]. However, since the aircraft is autonomous, flying quality level 3 can be used. Additionally, from the mission profile of Chapter 6 it becomes apparent that the *Swing* will not have a conventional landing or take-off. Therefore, the flight phase category B can be used [4]. This results in a roll rate requirement of 60° in 3.4 seconds.

It is important to consider that due to an increase in moment of inertia, which is caused by the battery placement as will be discussed in Section 11.3, the roll rate achieved will be smaller. However, in the case of the preliminary sizing of the ailerons, the impact of the moment of inertia is not considered yet. To be able to size the ailerons, the aileron roll rate equation should be considered first. The roll rate is determined based on Equation (11.1)

$$P = -\frac{C_{l_{\delta_a}}}{C_{l_p}} \delta a \left(\frac{2V_{MC}}{b} \right) \quad (11.1)$$

First, the minimum control speed used in the aileron sizing can be easily determined. It can be assumed to maintain as much control as possible that the minimum control speed is equal to the stall speed [66]. Based on this, the minimum control speed can be determined based on the stall speed equation:

$$V_{MC} = \sqrt{\frac{2W}{S\rho C_{N_{max}}}} \quad (11.2)$$

The next parameter that can be determined empirically is the aileron deflection. Equation (11.3) can be used to estimate the aileron deflection.

$$\delta a = \frac{\delta a_{up} + \delta a_{down}}{2} \quad (11.3)$$

Thus, it is important to determine the upward and downward assumed aileron deflection. It can be assumed that a typical aileron has a maximum deflection of 30° . Additionally, an efficiency of 75% of the aileron is assumed [39]. Thus, the aileron deflection value can be assumed to be equal to $\delta_a = 22.5^\circ$. The next aspect that has to be determined is the airfoil used for the aileron sizing. In the case of ailerons, typically used airfoils are symmetrical. Therefore, the ailerons shall be sized taking a NACA0010 aileron airfoil into account. This enables the determination of the aileron control derivative based on the following empirical equation [39].

$$C_{l_{\delta_a}} = \frac{2c_{l_\alpha} \tau}{S_{ref} b} \int_{b_1}^{b_2} c(y) y dy \quad (11.4)$$

The term c_{l_α} can be obtained from the airfoil characteristics, and it is equal to $c_{l_\alpha} = 6.51/rad$. Additionally, the aileron effectiveness parameter τ can be determined empirically, taking into account an aileron chord

ratio of $c_f/c = 0.25$. This leads to an assumed value of $\tau = 0.45$, see Figure 11.1.

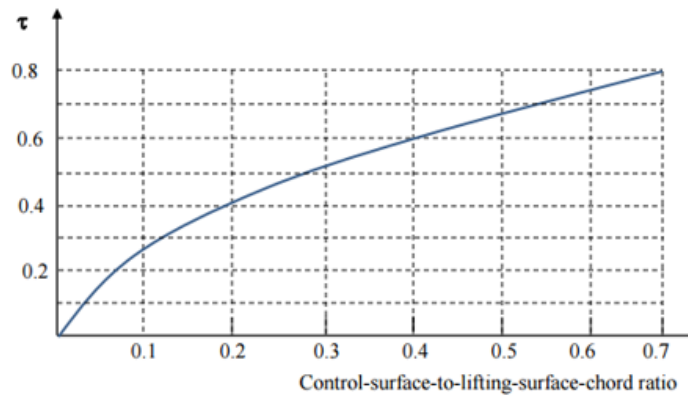


Figure 11.1: Aileron effectiveness as a function of the ratio of the aileron chord to the total airfoil chord [67]

Since the values of S_{ref} and b are known based on the wing planform, the last element that has to be calculated is the integral $\int_{b_1}^{b_2} c(y)ydy$. To compute this integral, the chord as a function of span has to be determined. This can be done based on Equation (11.5):

$$C(y) = C_r - \left(\frac{C_r - C_t}{b/2} \right) y \quad (11.5)$$

It can be determined that $c(y) = 1.42 - 0.122y$. The only variable that has to be iterated is the aileron placement over the wing. The last parameter that has to be determined is the roll damping derivative. This can be done using Equation (11.6).

$$C_{l_p} = -\frac{4(c_{l_\alpha} + c_{d_0})}{S_{\text{ref}}b^2} \int_0^{b/2} y^2 c(y) dy \quad (11.6)$$

The parameters c_{l_α} and c_{d_0} can be determined based on the NACA0010 airfoil used, whereas the integral can be computed based on the aforementioned chord equation. Therefore, the roll damping derivative can be determined based on the position of the aileron on the wing. It is important to note that the variables b_1 and b_2 represent the starting and end positions of the ailerons on the wingspan, and these variables are the variables that shall be sized for in this section. Before starting the iterations, a table with all the required constants for calculating the roll damping and the aileron roll rate, as well as their values, are presented in Table 11.1.

Table 11.1: Constants used in determining roll coefficients

c_{l_α}	τ	S_{ref}	b	C_{d_0}
6.5/rad	0.45	14 m ²	14 m	0.005

Now that all the constants have been determined to compute the roll rate in Equation (11.1), the position of the aileron on the wing has to be iterated to reach the required roll rate. The final aileron position and dimensions, as well as the achieved roll rate, shall be presented in Table 11.2, along with the required derivative parameters.

Table 11.2: Aileron design values

Airfoil	b_1	b_2	δ_a	V_{MC}	$C_{l_{\delta_a}}$	C_{l_p}	P
NACA0010	5.53 m	6.86 m	22.5°	29.1 m/s	0.43	-0.85	47.17 °/s

11.2. Controllability in Hover Mode

The controllability during hover is analysed to increase the safety of the passengers and surroundings. During hover, aerodynamic control surfaces will not be effective. To analyse the vehicle's controllability, the following method of Du, Quan, Yang et al. [3]. The paper uses a linear dynamic model for the controllability with the assumption that rotorcraft, during hovering, ignores the aerodynamic damping and stiffness matrices, which results in Equation (11.7). It utilises linearisation of the Newton Euler equations around hover conditions following from Pounds, Mahony, Hynes et al. [68].

$$\dot{\mathbf{x}} = \mathbf{A}\mathbf{x} + \mathbf{B}(\mathbf{F} - \mathbf{G}), \quad \text{with:} \quad (11.7)$$

$$\mathbf{x} = [h \ \phi \ \theta \ \psi \ v_h \ p \ q \ r]^T \in \mathbb{R}^8$$

$$\mathbf{F} = [T \ L \ M \ N]^T \in \mathbb{R}^4$$

$$\mathbf{G} = [mg \ 0 \ 0 \ 0]^T \in \mathbb{R}^4$$

$$\mathbf{A} = \begin{bmatrix} \mathbf{0}_{4 \times 4} & \mathbf{I}_4 \\ \mathbf{0}_{4 \times 4} & \mathbf{0}_{4 \times 4} \end{bmatrix} \in \mathbb{R}^{8 \times 8}$$

$$\mathbf{B} = \begin{bmatrix} \mathbf{0}_{4 \times 4} \\ \mathbf{J}_f^{-1} \end{bmatrix} \in \mathbb{R}^{8 \times 4}$$

$$\mathbf{J}_f = \text{diag}(-m, J_x, J_y, J_z)$$

The state vector, \mathbf{x} , is dependent on the altitude h , the roll angle ϕ , the pitch angle θ , the yaw angle ψ , vertical speed v_h , pitch rate p , roll rate q and yaw rate r . \mathbf{F} is the force vector, where T is thrust, L is roll torque, M is the pitch torque and N is yaw torque. \mathbf{G} is the gravitational vector, \mathbf{A} is the state transition matrix, \mathbf{B} the control input matrix and \mathbf{J}_f the mass moment of inertia matrix. The input vector \mathbf{u} , is defined as $(\mathbf{F} - \mathbf{G})$.

These input parameters for the ACAI are the locations of the rotors, the maximum thrust per engine, the total mass, the rotor efficiency, the rotational direction of the propellers, clockwise or anticlockwise, the efficiency parameter η_i , ranging from zero to one, and the reactive torque coefficient k_μ . This coefficient is the ratio between the reactive torque and the lift. This value was calculated to be equal to 0.1 complying with the literature [3].

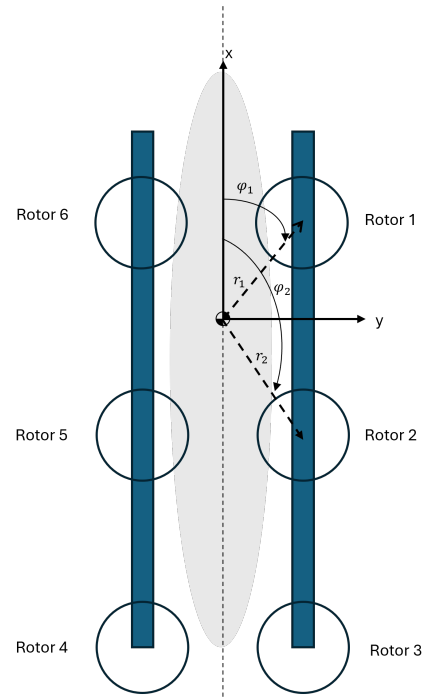
The rotational direction configuration was set at PPNNPN, where P stands for clockwise rotation and N for anticlockwise rotation since this was stated to be most controllable in case of an engine failure [3]. To regard for engine failure, η_i was set to zero for i_{th} engine. The final control effectiveness matrix B_f , which can be seen Equation (11.8).

$$B_f = \begin{bmatrix} \eta_1 & \cdots & \eta_m \\ -\eta_1 r_1 \sin(\phi_1) & \cdots & -\eta_m r_m \sin(\phi_m) \\ \eta_1 r_1 \cos(\phi_1) & \cdots & \eta_m r_m \cos(\phi_m) \\ \eta_1 w_1 k_\mu & \cdots & \eta_m w_m k_\mu \end{bmatrix} \quad (11.8)$$

Where r_1 is the arm of from the CG to the propeller and ϕ_m the angle from the x-axis to the rotor, as can be seen in Figure 11.2. It has to be noted that the CG in Figure 11.2 is preliminary and will be calculated later in section 11.3. Table 11.3 shows the x- and y-locations of the engines measured from the nose of the vehicle.

Table 11.3: Coordinates of the engines measured from the nose of the vehicle

Engines	x-coordinate [m]	y-coordinate [m]
1,6	2.30	± 1.95
2,5	4.65	± 1.95
3,4	7.00	± 1.95

**Figure 11.2:** Rotor configuration *Swing*; Not to scale

The total thrust/torque vector \mathbf{F} is dependent on the control effectiveness matrix and the thrust per engine \mathbf{f} , which is put into a vector and is constraint by Equation (11.9)

$$\mathbf{f} \in F = \prod_{i=1}^m [0, K_i] \quad (11.9)$$

Where K_i is the maximum lift of i th rotor in N. Using the geometry of the system and the mapping from the rotor lift, the system thrust/torque can be calculated as seen in Equation (11.10)

$$\mathbf{F} = \mathbf{B}_f \mathbf{f} \quad (11.10)$$

From Equation (11.9) and Equation (11.10), \mathbf{F} is constrained by:

$$\Omega = \{\mathbf{F} \mid \mathbf{F} = \mathbf{B}_f \mathbf{f}, \mathbf{f} \in F\} \quad (11.11)$$

Following from this, \mathbf{u} is constrained by:

$$U = \{\mathbf{u} \mid \mathbf{u} = \mathbf{F} - \mathbf{G}, \mathbf{F} \in \Omega\} \quad (11.12)$$

It can be seen from Equations (11.9), (11.11) and (11.12), F , Ω , and U are convex and closed subsets. The purpose is to analyze the controllability by altering \mathbf{u} under the constraint of subset U . From this, a measure is defined as can be seen in Equation (11.13).

$$\rho(X, \partial\Omega) \triangleq \begin{cases} \min\{\|X - F\| : X \in \Omega, F \in \partial\Omega\} & \text{if } X \in \Omega, F \in \partial\Omega \\ -\min\{\|X - F\| : X \in \Omega^c, F \in \partial\Omega\} & \text{if } X \in \Omega^c, F \in \partial\Omega \end{cases} \quad (11.13)$$

Where $\partial\Omega$ is the boundary of Ω and where Ω^c is the complementary set of Ω . $\rho(X, \partial\Omega)$ is the radius of the maximum enclosed sphere in the control set Ω , centred at \mathbf{G} . This can be seen as the maximum control/torque produced in all directions and is therefore defined as the ACAI of the system [3]. It is based

on the minimum Euclidean norm of the control force on the boundary of the control set Ω . Moreover, the ACAI is independent on time.

The final ACAI was calculated using a Matlab Toolbox which was developed by Du, Quan, Yang et al. [3]. This toolbox calculated the ACAI, using the control effectiveness matrix, the minimum and maximum thrust setting per engine and the total thrust as input. The vehicle is deemed controllable if the ACAI is greater than zero. The CG (centre-of-gravity) was ranged between the most front and aft engine placement to analyse the controllability over the CG range, which can be seen in Figure 11.3.

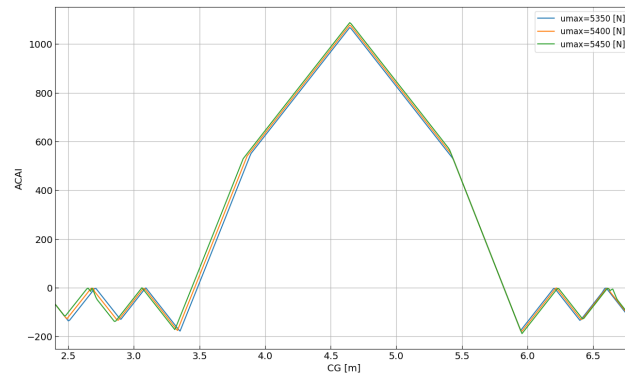


Figure 11.3: ACAI value of the CG range at different thrust settings

As can be seen in Figure 11.3, the vehicle is controllable if the CG is greater than 3.4 m and smaller than 5.8 m measured from the nose. Therefore, the vehicle has to be sized to be within that CG range. In case a safety factor of 1.1 is applied, the CG is stable from 3.67 m.

One of the requirements is that the aircraft has to be operative if one engine fails during flight. This was analysed by setting η_i to zero for the designated engine. This was performed for all engines separately, and in all configurations, the aircraft was deemed controllable. However, the maximum thrust per engine had to be increased, and thus, violated the noise requirement. However, if an engine fails, this is considered an emergency and therefore violating the requirement is allowed.

11.3. CG-Location Determination

The first step in the determination of the stability and controllability of the vehicle during operation is the determination of the location of the centre-of-gravity. This shall be done in two steps. Firstly, the CG-location is determined empirically based on the design of the fuselage and wings. Afterwards, a loading diagram is created to ensure that the CG is within the desired range.

11.3.1. Class I CG Determination

First and foremost, it can be considered that the wing placement is performed based on the fuselage shape as well as the ground footprint requirement. Additionally, since the difference in required CG for cruise as well as for hovering is rather significant. As shall be described during this chapter, it was intended that the wing has a large CG excursion during transition to obtain the required CG shift. Based on these considerations as well as on the shape of the fuselage, the leading edge of the wing was placed 1.6 m from the front of the fuselage.

Another aspect that influences the CG shift is the position of the batteries. To ensure the required CG excursion and to save as much space as possible, the batteries are placed in the nacelles of the engines situated in the wing. The engines situated closest to the tip shall carry most of the battery weight to ensure the required CG shift. However, this decision has a significant drawback with regard to the rolling requirement. This is caused by the increase in moment of inertia which limits the dynamic characteristics of the design.

The reduced rolling performance shall be discussed in more detail in Section 11.8

After establishing these preliminary aspects, it is important to discuss how the centre of gravity is determined for both phases. To compute the CG excursion, Equation (11.14) shall be used, where i represents a particular weight component. Those weight components have to be established.

$$X_{CG} = \frac{\sum M_i \cdot X_i}{\sum M_i} \quad (11.14)$$

Another aspect that has to be taken into account for the determination of the CG, is that in cruise four different CGs must be considered:

- Operating Empty Weight (OEW) CG
- OEW + luggage
- OEW + luggage + back-row passengers
- OEW + full payload

A table with all the CG components, their masses and the locations of the components, as well as the final CG values for the cruise configuration, shall be provided in Table 11.4.

Table 11.4: Cruise CG Range

Component	Position on x-axis [m]	Mass [kg]
Fuselage, fixed equipment	2.40	284
Wing	2.17	349
Empennage	7.20	27
Engine nacelle 1	2.25	61
Engine nacelle 2	2.39	61
Engine nacelle 3	2.54	61
Front seat	1.65	160
Back seat	2.50	160
Luggage	3.00	80
Battery	2.31	400
<i>Fuselage Group</i>	<i>2.50</i>	<i>711</i>
<i>Wing Group</i>	<i>2.28</i>	<i>933</i>
Total	2.37	1644

Now that the cruise configuration centre of gravity is determined, the next step is to determine the CG during the VTOL phase. It is important to ensure that in hovering, the CG is situated in between the values determined with the use of the ACAI tool as described in Section 11.2.

To determine the CG during hover, it is crucial to understand which components have different CGs in hovering compared to the cruising phase. The shift in CG is mostly caused by the change in the position of the wing with respect to the longitudinal position. Thus, the centre of gravity of the wing, the engines as well as the batteries change while the other components remain fixed. Based on these considerations, the following centre of gravity is obtained for hover configuration in Table 11.5.

Table 11.5: Hovering CG Range

Component	Position on x-axis [m]	Mass [kg]
Fuselage, fixed equipment	2.40	284
Wing	2.96	349
Empennage	7.20	27
Engine nacelle 1	2.30	61
Engine nacelle 2	4.65	61
Engine nacelle 3	6.99	61
Front seat	1.65	160
Back seat	2.50	160
Luggage	3.00	80
Battery	5.97	400
<i>Fuselage Group</i>	<i>2.50</i>	<i>711</i>
<i>Wing Group</i>	<i>4.58</i>	<i>933</i>
Total	3.68	1644

Initially, the CG during hover was situated outside the ACAI requirement. However, to tackle this issue, the battery mass was increased leading to a further backward shift of the CG. Therefore, with a battery mass increase to 400 kg, the final CG position during hover is situated within the controllability limits of the hovering phase.

11.3.2. Loading Diagram

The next crucial step is to establish whether the design is stable and controllable during the cruise phase. To achieve this step, it is crucial to size the aircraft tail as well as establish its configuration. This step has to be performed after a more detailed centre-of-gravity analysis is performed. To be able to find out a more detailed CG excursion, a loading diagram analysis should be performed.

In the loading diagram, the loading of the cargo and the passengers is taken into account. Before delving into the CG determination, it is important to note that the vehicle shall be restricted to load back to front due to the fact that the backward seats are only accessible when the front seats are folded. To determine the CG for every new loading case, the following Equation (11.15) shall be employed.

$$X_{CG_{new}} = \frac{W_{old} \cdot X_{CG_{old}} + W_{item} \cdot X_{CG_{item}}}{W_{old} + W_{item}} \quad (11.15)$$

In this equation, the starting weight is considered to be the operating empty weight as determined previously. Based on these assumptions, the following loading diagram is obtained for the SWING design in Figure 11.4.

To determine the tail size, the most aft CG location has to be considered as well as the CG range. From the diagram it can be seen that the values for the most aft and most forward CG are the following: $X_{aftCG} = 2.46$ m and $X_{fwCG} = 2.37$ m. Thus, the CG range is situated between 64 and 72% of the mean aerodynamic chord. The next step that has to be taken to ensure stability and controllability is determining the tail size.

11.4. Preliminary Estimation of Tail Size

To be able to properly determine the size of the tail and enable proper iterations, it is important to first size the tail based on previous aircraft designs. This ensures that the preliminary estimations are feasible and provide valuable insight with regard to the sizing of the tail. This step is crucial; since the size of the tail is very restricted, due to the ground footprint restrictions. Thus, with the preliminary estimations of the tail size, the location and dimensions, as well as the tail configuration, can be determined. Thus, to determine the preliminary size of the tail, it is crucial to assume the tail volume coefficients. These coefficients can be assumed based on literature and previous designs. According to Roskam and Kansas [69], $\bar{V}_h = 0.9$.

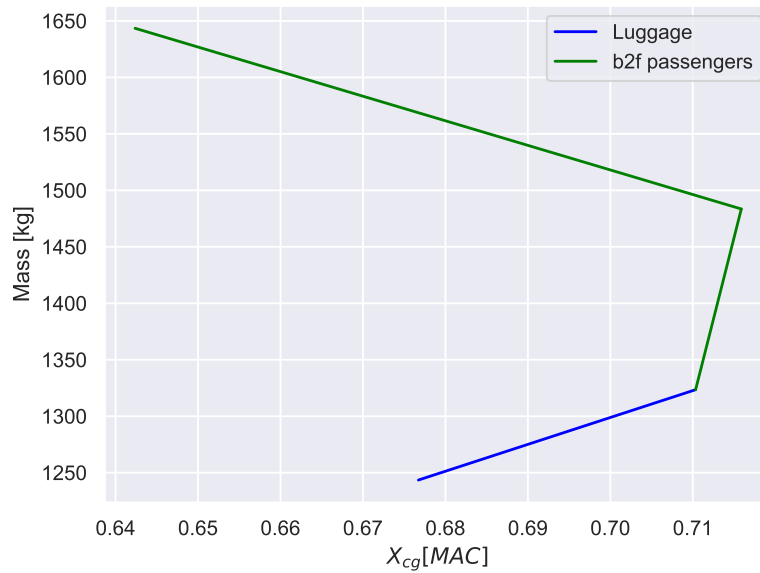


Figure 11.4: SWING loading diagram

Scholz [70] states that $\bar{V}_v = 0.0601$.

After considering the tail volume coefficients, the horizontal tail surface area can be computed using the following equation:

$$\bar{V}_h = \frac{(X_h - X_{\text{aftCG}})S_h}{S\bar{c}} \quad (11.16)$$

where X_h is the spanwise location of the mean aerodynamic chord of the horizontal tail, X_{aftCG} is the spanwise location of the most aft centre of gravity of the aircraft, S_h is the surface area of the horizontal tail, S is the surface area of the wing, and \bar{c} is the mean aerodynamic chord of the wing. The value of S_h is then calculated assuming the value of X_h as determined in the CG location calculations. Additionally, the vertical tail surface area can be determined by use of a similar equation:

$$\bar{V}_v = \frac{(X_v - X_{\text{aftCG}})S_v}{Sb} \quad (11.17)$$

Now that the surface areas are determined and fixed, the tail planform can be properly determined. In order to achieve this goal, the aspect ratios of the tails have to be considered. However, if a typical value of the aspect ratio of the vertical tail of 2 is assumed [71] and a taper ratio of 0.4 is also considered, the span of the vertical tail can be calculated to have a value of 2.6 meters. Taking this value into account, the span would exceed the vertical ground footprint requirement of 2 meters, and as such, a conventional tail configuration would be unfeasible. This requires analysis of different concepts which shall be performed in the next section.

11.5. Tail Configuration and Planform

First and foremost, it is important to note that the design shall make use of a high-wing configuration. This, in turn, implies that there would be a significant wake on the horizontal stabiliser of a conventional tail. Thus, only two different tail configurations would be feasible, the T-tail and the V-tail. However, due to the limited vertical footprint requirement, the T-tail configuration is impossible to design for. Thus, the only feasible design option is an inverted V-tail.

To size the inverted V-tail, several steps have to be determined, based on the fact that the horizontal contribution and vertical contribution of the tail are integrated into one single angled surface. The first step that has to be taken to size the surface is to determine the angle at which the inverted V-tail is situated with

respect to the horizontal plane. This can be done on the basis of Equation (11.18) [71]:

$$v = \arctan \frac{S_v}{S_h} \quad (11.18)$$

with the values of S_v and S_h determined in Section 11.4. While the analytical method suggests that the final area of the design shall be equal to $S_{tail} = \sqrt{S_v^2 + S_h^2}$ due to inefficiencies of the V-tail design, it has to be assumed that $S_{tail} = S_v + S_h$. Now that the total tail surface has been calculated, the new vertical and horizontal components should be redetermined to enable sizing of the wing planform:

$$S_{v_{new}} = S_{tail} \cdot \sin(v), \quad S_{h_{new}} = S_{tail} \cdot \cos(v) \quad (11.19)$$

After having determined the surface areas of each component, it is important to be able to determine the geometrical parameters of the tail itself. Since it is clear that the horizontal footprint is limiting, the chord of the design shall be determined based on the horizontal tail, and then the other properties of the vertical tail shall be determined.

Based on the literature, vertical tails usually have an aspect ratio situated between 1 and 2 [69]. To reduce the chord size of the tail, an aspect ratio of two was assumed for the initial sizing. It is known that $A = b^2/S$, which implies that the vertical ‘wingspan’ of the tail can be determined. Thus, the space occupied by the tail on the vertical plane can be determined by using the following equation:

$$b_v = \sqrt{A_v \cdot S_{v_{new}}} \quad (11.20)$$

To determine the space occupied in the vertical plane, the total span should now be halved. The division by 2 is caused by the fact that the V-tail is composed of two elements, the total span on the horizontal plane represents the sum of the contribution of each of the two components. This leads to a vertical contribution which is double compared to the vertical space taken. Thus, $h_{tail} = b_v/2$. Performing preliminary calculations, it can be seen that the tail height is lower than 2 meters, so it can be ensured that the tail fits within footprint requirements.

After the span is computed, the root chord of the aircraft can be determined from which the horizontal component span and aspect ratio can be determined. The horizontal components as well as the total tail span can be computed using the following formulas:

$$c_r = \frac{2 \cdot S_v}{1 + \lambda \cdot b_v} \quad (11.21) \quad b_h = \frac{2 \cdot S_h}{1 + \lambda \cdot c_r} \quad (11.22)$$

$$A_h = \frac{b_h^2}{S_h} \quad (11.23) \quad b = \sqrt{b_h^2 + b_v^2} \quad (11.24)$$

Thus, taking into account that $c_t = \lambda \cdot c_r$, all the tail parameters are computed and the preliminary tail planform can be finalised.

11.6. Horizontal Tail Sizing

Now that the tail has finally been preliminarily sized, it is crucial that the tail planform is designed to ensure that it provides both enough stability and controllability on the horizontal plane. This step is taken by use of a scissor plot, whose creation method shall be expanded upon in this section.

11.6.1. Stability Requirement

When it comes to the longitudinal stability requirement, the primary stability condition is that the centre of gravity of the aircraft is located ahead of the stick-fixed neutral point of the design. Thus, the first curve that

is used in configuring the scissor plot is the stick-fixed stability curve, given in Equation (11.25).

$$\frac{S_h}{S} = \frac{1}{\frac{C_{L\alpha_h}}{C_{L\alpha_{A-h}}} \left(1 - \frac{d\varepsilon}{d\alpha}\right) \frac{l_h}{\bar{c}} \left(\frac{V_h}{V}\right)^2 \bar{x}_{c.g.}} - \frac{\bar{x}_{ac} - 0.05}{\frac{C_{L\alpha_h}}{C_{L\alpha_{A-h}}} \left(1 - \frac{d\varepsilon}{d\alpha}\right) \frac{l_h}{\bar{c}} \left(\frac{V_h}{V}\right)^2} \quad (11.25)$$

In this equation, the second term represents a safety margin of 5% that is assumed to ensure that the design is not susceptible to stability issues. It is clear that in order to properly size the curve, several parameters such as $C_{L\alpha_h}$ are yet undefined. Thus, first and foremost the values of \bar{x}_{ac} , $C_{L\alpha_h}$, $C_{L\alpha_{A-h}}$, $d\varepsilon/d\alpha$ and V_h/V have to be determined.

The first parameter that can be analysed is the V_h/V ratio. This represents the velocity of the airstream that reaches the horizontal tail with respect to the wing. Due to the position of the wing (high wing), as well as the inverted position of the tail, the interference of the wing on the tail airflow is considered to be minimal. Thus, the tail is assumed to be similar to a fin-mounted stabiliser in the velocity ratio aspect, and thus the ratio is assumed to have a value of $\frac{V_h}{V} = 0.95$ [72].

On the basis of the tail position, the downwash is also estimated to be 0 since the interference is minimal. Thus $\frac{d\varepsilon}{d\alpha} = 0$. The next parameter that needs to be determined is $C_{L\alpha_h}$, the lift rate coefficient of the horizontal tail. This can be calculated using Equation (11.26)[40]

$$C_{L\alpha_h} = \frac{2\pi A_h}{2 + \sqrt{4 + \left(\frac{A_h\beta}{\eta}\right)^2 \left(1 + \frac{\tan^2(\Lambda_{0.5c_h})}{\beta^2}\right)}} \quad (11.26)$$

With $\beta = \sqrt{1 - M^2}$, $M = V/a$ and finally, $a = \sqrt{TR\gamma}$, using ISA conditions to obtain the temperature based on the cruise altitude. Additionally, the lift coefficient of the tailless aircraft has to be considered $C_{L\alpha_{A-h}}$. This parameter can also be determined on the basis of an empirical equation [73]:

$$C_{L\alpha_{A-h}} = C_{L\alpha_w} \left(1 + 2.15 \frac{b_f}{b}\right) \frac{S_{net}}{S} + \frac{\pi b_f^2}{2 S} \quad (11.27)$$

In this equation, the parameters b_f and S_{net} represent the width of the fuselage and the net wing surface area (the section inside the fuselage is removed).

Lastly, the aerodynamic centre of the aircraft can also be computed through the calculation of the influences of the nacelles, the wing and the fuselage. The contribution of the wing and the fuselage shall be determined with the use of Equation (11.28).

$$\left(\frac{x_{ac}}{\bar{c}}\right)_{wf} = \left(\frac{x_{ac}}{\bar{c}}\right)_w - \frac{1.8}{C_{L\alpha_{A-h}}} \frac{b_f h_f l_{fn}}{s\bar{c}} + \frac{0.273}{1 + \lambda} \frac{b_f c_f (b - b_f)}{\bar{c}^2 (b + 2.15 b_f)} \tan(\Lambda_{1/4}) \quad (11.28)$$

The first term of Equation (11.28) is the contribution of the wing, which is found experimentally[73]. The second term is the forward shift of the aerodynamic centre due to the fuselage nose's contribution to lift. Lastly, the third term is the aft shift of the aerodynamic centre due to the loss of lift at the intersection of the fuselage and wing. The contribution of the nacelles is now calculated in Equation (11.29) [73].

$$\Delta_n \frac{x_{ac}}{\bar{c}} = \sum k_n \frac{b_n^2 l_n}{s\bar{c} (C_{L\alpha})_{A-h}} \quad (11.29)$$

Where $k_n \approx -4$ for nacelles mounted in front of the leading edge of the wing. It is important to note that in Equation (11.29) $C_{L\alpha}$ should be in $[\text{rad}^{-1}]$ and l_n is considered positive when the nacelle is located in front of the 1/4 MAC.

Now that all the data is obtained, the stability curve can be plotted.

11.6.2. Controllability Requirement

As it is clear from the stability equation, moving the CG forward enables a more stable aircraft design. However, when taking controllability into account, it is more relevant to move the CG aft, since a forward CG implies an increase in pitching up and a pitching down moment required. Thus, when it comes to the controllability requirement, the tail size with respect to the wing size as a function of CG can be described based on the following equation:

$$\frac{S_h}{S} = \frac{1}{\frac{C_{L_h}}{C_{L_{A-h}}} \frac{l_h}{\bar{c}} \left(\frac{V_h}{V}\right)^2} \bar{x}_{c.g.} + \frac{\frac{C_{m_{ac}}}{C_{L_{A-h}}} - \bar{x}_{ac}}{\frac{C_{L_h}}{C_{L_{A-h}}} \frac{l_h}{\bar{c}} \left(\frac{V_h}{V}\right)^2} \quad (11.30)$$

Based on this equation, several parameters have to be analysed. First and foremost, the lift coefficient of the horizontal tail used on the aircraft C_{L_h} can be derived using analytical relations. This is dependent on the type of tail that is used, whether fixed, adjustable or full moving. To improve the controllability of the design, a full moving tail is chosen; therefore, $C_{L_h} = -0.35 \cdot A_h^{1/3}$.

Another parameter that has to be sized is the pitching moment coefficient at the aerodynamic centre of the aircraft, which can be found by calculating the moment contributions of the fuselage, wing and engine nacelles [73]:

$$C_{m_{ac}} = C_{m_{ac,w}} + \Delta_{fus} C_{m_{ac}} + 2 \cdot \Delta_{nac} C_{m_{ac}} \quad (11.31)$$

It is important to note that the design shall not undergo typical take-off and landing procedures. Therefore, there is no need to make use of flaps to increase the lift coefficient of the aircraft. This implies that the contribution of the flaps to the moment can be ignored. The contribution of the wing and fuselage are found using empirical equations [73]:

$$C_{m_{ac,w}} = C_{m_{0,airfoil}} (A \cos^2(\Lambda) / (A + 2 \cos(\Lambda))) \quad (11.32)$$

$$\Delta_{fus} C_{m_{ac}} = -1.8 \left(1 - \frac{2.5b_f}{l_f}\right) \frac{\pi b_f h_f l_f}{4S\bar{c}} \frac{C_{L_0}}{C_{L_{\alpha,(A-h)}}} \quad (11.33)$$

Thus, to be able to correctly determine the wing contribution to the pitching moment, the airfoil contribution has to be inferred first. This can be done considering the assumed sweep and aspect ratio and taking into account the pitching moment of the chosen Eppler 423 airfoil. Additionally, to determine the total fuselage contribution, the lift at zero angle of attack has to be determined. Lastly, the nacelle pitching moment increment should be analysed as well. This can be calculated using the following equation [74]:

$$\Delta_{nac} C_{m_{ac}} = C_{m_{ac_0}} + C_{L_w} \cdot \left(-\Delta_n \frac{x_{ac}}{\bar{c}}\right) \quad (11.34)$$

Where the nacelle contribution has already been calculated in Equation (11.29). Thus, to determine the nacelle pitching moment, the wing lift has to be determined as well as the zero-lift nacelle pitching moment. The lift of the aircraft wing can be retrieved based on the design of the wing and has a value of $C_L = 0.73$. The zero-lift nacelle pitching moment can be estimated by assuming that the wing has no fillet and considering the fact that the aircraft has a high wing configuration $C_{m_{ac_0}} = 0.004$ [74].

11.6.3. Scissor Plot

Considering the parameters explained in Sections 11.6.1 and 11.6.2, the scissor plot can be obtained in Figure 11.5:

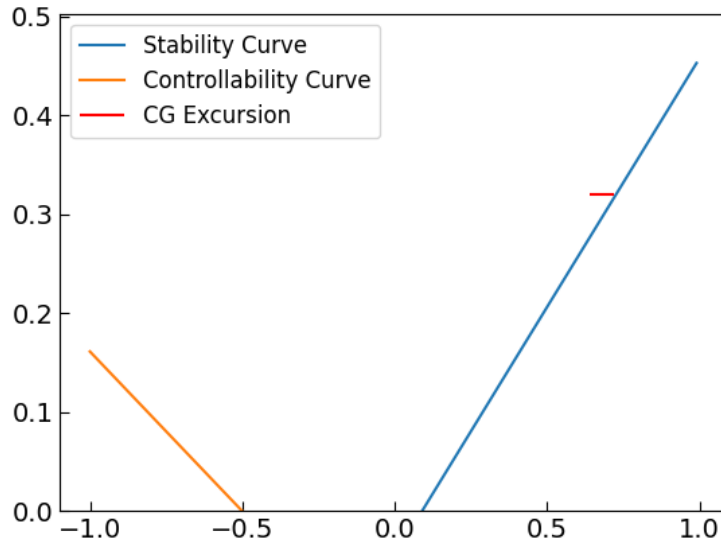


Figure 11.5: Scissor plot

As it can be noticed, the horizontal tail ratio has to have a minimum value of around $\frac{S_h}{S} = 0.32$ to meet the stability requirement. Additionally, it is noticeable that the controllability requirement is not constraining. This is reasonable since the tail is sized for cruise conditions, not landing conditions since landings shall be performed in VTOL configuration. Thus, a final horizontal tail surface ratio of 0.32 shall be taken into account when sizing the final design. Therefore, the final horizontal tail size can be assumed to have a value of 4.48 m².

11.7. Vertical Tail Sizing

The vertical tail will be sized on two criteria, namely, the weathervane stability and the engine inoperative. The most limiting criteria will determine the size of the vertical tail.

11.7.1. Vertical Tail Sizing Stability Requirement

To achieve stability, the stability derivative C_{N_β} (the weathervane stability) needs to be positive. To achieve sufficient static directional stability C_{N_β} should be greater or equal than $0.0571 \frac{1}{rad}$ [69]. C_{N_β} can be calculated using Equation (11.35).

$$C_{N_\beta} = (C_{N_\beta})_f + (C_{N_\beta})_w + (C_{N_\beta})_v \quad (11.35)$$

Where f is the fuselage contribution, v is the contribution of the vertical tail and w is the contribution of the wing. The contribution of the wing is neglected because “The contribution to C_{N_β} of a wing without sweep is very small” [75]. The vertical tail and fuselage contributions can be found using Equations (11.36) and (11.37)

$$(C_{N_\beta})_f = -\frac{2v}{Sb} \quad (11.36)$$

As can be seen in Equation (11.36) [76] the fuselage has a destabilising effect on the directional stability of the aircraft. v is the volume of the equivalent fuselage, S is the wing area and b is the wing span.

$$\left(C_{N\beta}\right)_v = -C_{Y_{v\alpha}} \cdot \left(1 - \frac{d\sigma}{d\beta}\right) \cdot \left(\frac{V_v}{V}\right)^2 \cdot \frac{S_v l_v}{Sb} \quad (11.37)$$

In Equation (11.37) [75] $C_{Y_{v\alpha}}$ is the derivative of the side force of the vertical tail with respect to the angle of the vertical tail. $\frac{d\sigma}{d\beta}$ is the side wash, which because of simplicity is assumed to be 0. $\frac{V_v}{V}$ is the ratio between the free stream velocity and the velocity at the vertical tail, this ratio is assumed to be 1. The side force generated due to the vertical tail ($C_{Y_{v\alpha}}$) is the negative of the lift coefficient of the vertical tail ($C_{L_{v\alpha}}$). l_v is the moment arm of the vertical tail. Rewriting Equations (11.35) and (11.37) results in the required vertical tail surface.

$$\left(\frac{S_v}{S}\right)_{\text{required}} = \frac{C_{n\beta} - \left(C_{n\beta}\right)_f}{C_{L_{v\alpha}}} \cdot \frac{b}{l_v} \quad (11.38)$$

11.7.2. Vertical Tail Sizing Control Requirement

Another important aspect to consider that is crucial in achieving a complete design, is the controllability requirement of the vertical tail. This requirement is determined by the all-engine inoperative requirement, where all engines fail on one side of the aircraft. The aircraft is required to maintain equilibrium with the help of rudder deflection in the case of a multi-engine failure [65].

Thus, the moments generated by the active engines compared to the failed engines have to be computed first, as well as the moment generated by the drag of the inoperative engines. The following formulas are given for calculating each engine's moment contribution with respect to the symmetry plane due to the thrust of the active engine as well as the drag of the inoperative engine:

$$N_E = T_{\max} \cdot y_E \quad (11.39) \quad N_D = 0.75 \cdot N_E \quad (11.40)$$

Equation (11.40) is estimated based on the fact that the design shall make use of fixed-pitch propellers. In these equations, N_E represents the moment caused by the active engine, y_E is the placement of the engine on the span, whereas N_D is the moment generated by the drag of the inoperative engine.

To be able to size the vertical stabiliser, the condition is that all engines on one side of the aircraft fail. Thus, all moment contributions of all engines have to be summed up: $N_{E_{\text{tot}}} = \sum N_{E_i}$ and $N_{D_{\text{tot}}} = \sum N_{D_i}$. To correct the engine thrust asymmetry generated sideslip, it is assumed that only the rudder surface is used as correction of the moment. The moment caused by the rudder can be calculated based on DATCOM [40]:

$$N_V = \frac{1}{2} \rho V_{\text{MC}}^2 \cdot \delta_f \cdot \frac{C_{l,\delta}}{C_{l,\delta_{\text{theory}}}} \cdot C_{l,\delta_{\text{theory}}} \cdot K' \cdot K_{\Lambda} \cdot S_v \cdot l_v \quad (11.41)$$

In this equation, V_{MC} represents the minimum control speed and is equal to the same speed as used to size the ailerons in Section 11.1. Thus, if the design is sized for equilibrium such that $N_{E_{\text{tot}}} + N_{D_{\text{tot}}} = N_V$, the tail size can be determined with the following formula:

$$S_v = \frac{N_{E_{\text{tot}}} + N_{D_{\text{tot}}}}{\frac{1}{2} \rho V_{\text{MC}}^2 \cdot \delta_f \cdot \frac{C_{l,\delta}}{C_{l,\delta_{\text{theory}}}} \cdot C_{l,\delta_{\text{theory}}} \cdot K' \cdot K_{\Lambda} \cdot l_v} \quad (11.42)$$

Thus, to be able to come up with the final tail design, several parameters such as K' and K_{Λ} have to be defined. The definition of these parameters shall be provided in Table 11.6. Afterwards, the value for each of the parameters shall be explained in more detail.

Table 11.6: Values required to determine the vertical tail size for engine inoperative

N_E	N_D	ρ	V_{MC}	$C_{l,\delta_{theory}}$	$\frac{C_{l,\delta}}{C_{l,\delta_{theory}}}$	K'	K_Λ	δ_f	l_v	S_v
146 kNm	109 kNm	1.17 kg/m ³	29.1 m/s	3.6	0.74	0.65	0.92	25°	4.74 m	2.73 m ²

Now, the values computed for N_E and N_D are based solely on the thrust determined in Chapter 10 as well as the locations of the engine. The density is based on the mission profile as described in Chapter 6, whereas the minimum control speed is determined in Section 11.1. Lastly, the moment arm of the tail is determined based on the CG position of the tail.

The parameters that have to be determined empirically are the other parameters. First and foremost, the theoretical flap efficiency has to be determined, as well as the ratio between the flap efficiency and the theoretical one ($C_{l,\delta_{theory}}$ and $\frac{C_{l,\delta}}{C_{l,\delta_{theory}}}$). This can be done assuming that the rudder shall employ a NACA0012 flap as well as a 0.2 flap chord-to-empennage chord ratio. Figures 11.6 to 11.8 shall be used for the determination of these parameters [77].

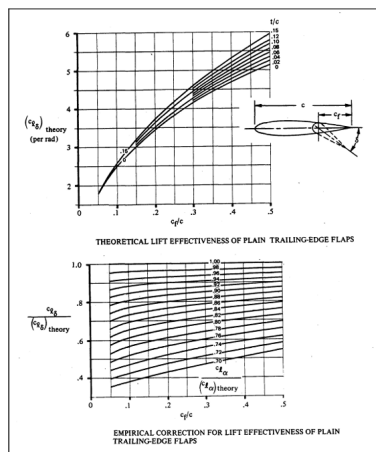


Figure 11.6: Lift effectiveness of plain trailing-edge flaps

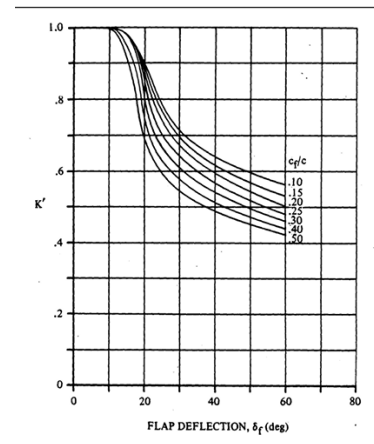


Figure 11.7: Empirical correction for non-linear effects at bigger flap angles

The next parameters that should be determined are K' and K_Λ . K' can be determined considering the 0.2 assumed chord ratio, based on empirical data plots. Additionally, a flap deflection of $\delta_f = 25^\circ$ based on typical rudder deflections is assumed [77]. This yields a K' value of 0.65 as per Figure 11.7:

Lastly, the sweep correction factor K_Λ can also be sized empirically. First of all, the empennage sweep has to be assumed. The empennage sweep must be equal to 0 to ensure that the tail is situated within the ground footprint requirement. Thus, $K_\Lambda = 0.65$ based Figure 11.8 [78]:

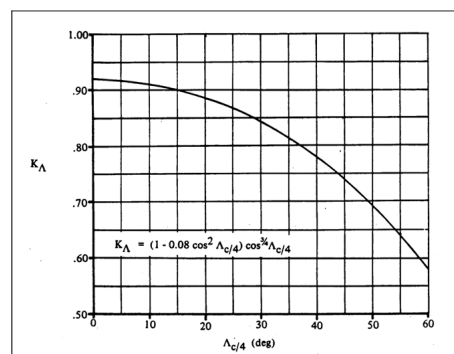


Figure 11.8: Sweep correction factor

With all these empirical factors determined, the final minimum vertical tail size can be computed. This yields a value of 2.73 m^2 .

11.8. Dynamic Stability during Cruise

To analyse the dynamic stability of the *Swing* during cruise, a state space model is created. Both for the longitudinal and lateral cases the model is created.

11.8.1. Longitudinal Stability

The equations of motion for the longitudinal stability can be found in Equation (11.43) [75]. The stability parameters used in the equations of motion are gathered from the AeroSandbox tool [2]. This is explained in more detail in Section 8.2, and the stability coefficients can be found in Table 8.5. The eigenvalues ($\lambda = \xi_c + \eta_c j$) of the 4×4 matrix determine the stability of the *Swing* eVTOL. The real part of all the eigenvalues need to be negative to insure dynamic stability. The eigenvalues can be determined by replacing the D_c by λ and then solving for λ . The eigenvalues can be found in Figure 11.9a, it can be seen that all the real part of each eigenvalue is negative.

$$\begin{bmatrix} C_{X_u} - 2\mu_c D_c & C_{X_\alpha} & C_{Z_0} & C_{X_q} \\ C_{Z_u} & C_{Z_\alpha} + (C_{Z_\alpha} - 2\mu_c) D_c & -C_{X_0} & C_{Z_q} + 2\mu_c \\ 0 & 0 & -D_c & 1 \\ C_{m_u} & C_{m_\alpha} + C_{m_\alpha} D_c & 0 & C_{m_q} - 2\mu_c K_Y^2 D_c \end{bmatrix} \begin{bmatrix} \hat{u} \\ \alpha \\ \theta \\ \frac{q\bar{c}}{V} \end{bmatrix} = \begin{bmatrix} -C_{X_{\delta_e}} \\ -C_{Z_{\delta_e}} \\ 0 \\ -C_{m_{\delta_e}} \end{bmatrix} \delta_e \quad (11.43)$$

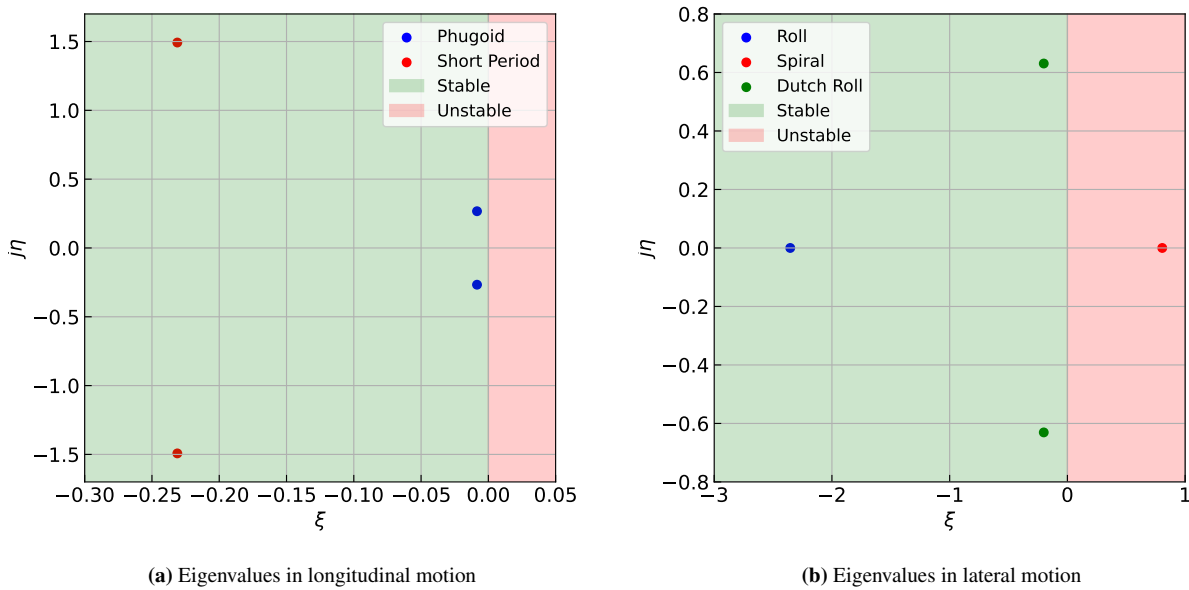


Figure 11.9: Eigenvalues dynamic model

With the eigenvalues, one can calculate the time to half the amplitude, the period, the damping ratio and the natural frequency. Equations (11.44) to (11.46) can be used to calculate these, in Table 11.7 these characteristics can be found. For the longitudinal stability, the two eigenmodes are the *Short Period* and *Phugoid*.

$$T_{\frac{1}{2}} = \frac{\ln \frac{1}{2} \bar{c}}{\xi_c V} \quad (11.44)$$

$$P = \frac{2\pi \bar{c}}{\eta_c V} \quad (11.45)$$

$$\zeta = \frac{-\xi_c}{\sqrt{\xi_c^2 + \eta_c^2}} \quad (11.46)$$

Table 11.7: Characteristic values of eigenmotions

Eigenmotion	Period [s]	Damping Ratio [-]	Amplitude Halving Time [s]
Short Period	4.21	0.153	3.00
Phugoid	23.5	0.0316	82.2
Dutch Roll	9.96	0.303	3.45
Roll Subsidence	-	1	0.294
Spiral	-	-1	-0.861

11.8.2. Lateral Stability

The Lateral stability has been performed similarly to the longitudinal stability. The equations of motion can be found in Equation (11.47) [75]. In Figure 11.9b the eigenvalues of the lateral motion can be found, in contrast to the eigenvalues of the longitudinal motion; not all the eigenvalues are negative. The real part of the eigenvalue that is correspondent with the spiral eigenmode is positive; however, there are many aircraft that are spirally unstable. Table 11.7 shows that the amplitude halving time of the spiral is negative, it thus is the time to double the amplitude. This doubling time is small, so an iteration is recommended. The spiral stability can be improved by lowering the vertical tail area and thus the $C_{n\beta}$, or by changing the dihedral of the wing to increase the magnitude of the $C_{l\beta}$. From Table 11.7 it can also be seen that there is no period for both the *Roll Subsidence* and the *Spiral*. Because the eigenvalues corresponding to those eigenmodes do not have an imaginary part, therefore the period is infinite, and the magnitude of the damping ratio will be 1.

$$\begin{aligned}
 & \begin{bmatrix} C_{Y\beta} + (C_{Y\beta} - 2\mu_b)D_b & C_L & C_{Y_p} & C_{Y_r} - 4\mu_b \\ 0 & -\frac{1}{2}D_b & 1 & 0 \\ C_{l\beta} & 0 & C_{l_p} - 4\mu_b K_X^2 D_b & C_{l_r} + 4\mu_b K_{XZ} D_b \\ C_{n\beta} + C_{n\beta} D_b & 0 & C_{n_p} + 4\mu_b K_{XZ} D_b & C_{n_r} - 4\mu_b K_Z^2 D_b \end{bmatrix} \begin{bmatrix} \beta \\ \varphi \\ \frac{pb}{2V} \\ \frac{rb}{2V} \end{bmatrix} = \\
 & = \begin{bmatrix} -C_{Y\delta_a} & -C_{Y\delta_r} \\ 0 & 0 \\ -C_{l\delta_a} & -C_{l\delta_r} \\ -C_{n\delta_a} & -C_{n\delta_r} \end{bmatrix} \begin{bmatrix} \delta_a \\ \delta_r \end{bmatrix} \quad (11.47)
 \end{aligned}$$

As mentioned in Section 11.3.1 the ailerons that have been sized in Section 11.1 will most likely not be able to achieve sufficient roll performance due to the large mass moment of inertia about the x-axis. To investigate the implications of this, the lateral dynamic is used, and an aileron deflection (δ_a) of 22.5° is used. To further reduce the effect of the mass moment of inertia on the roll performance, the ailerons are now placed on the entire span of the wing to improve the roll performance. Figure 11.10a shows the results; it can be seen that in 6 seconds the *Swing* can roll 60° . The roll rate can be found in Figure 11.10b. It should be noted that this is at cruise speed and with the maximum aileron deflection, this is the best case for roll performance. Therefore, it can be concluded that the roll requirement of 60° in 3.4 seconds is not achieved. Therefore, this requirement should be critically analysed in further iterations of the design. Moreover, the roll requirement itself should be critically analysed because the roll requirement is based on small light aircraft as there is currently no roll requirement for (e)VTOLs. The current roll performance is showcased in Figure 11.11

11.9. Results and Discussion

Now that both the horizontal and the vertical stabiliser sizing methods have been described, the final tail configuration can be established. The most important tail parameters shall be described below for both the class I and the class II sizing in Table 11.8.

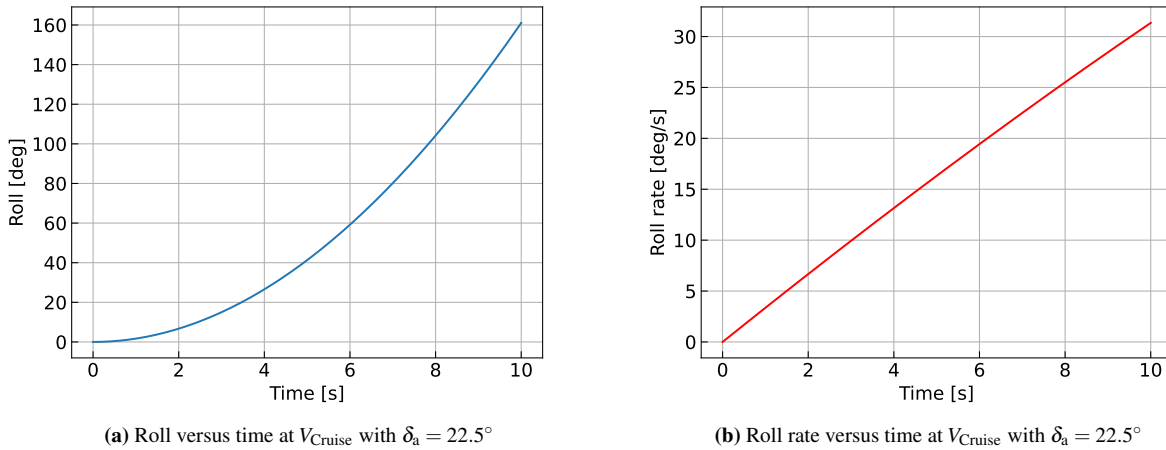


Figure 11.10: Roll performance analysis

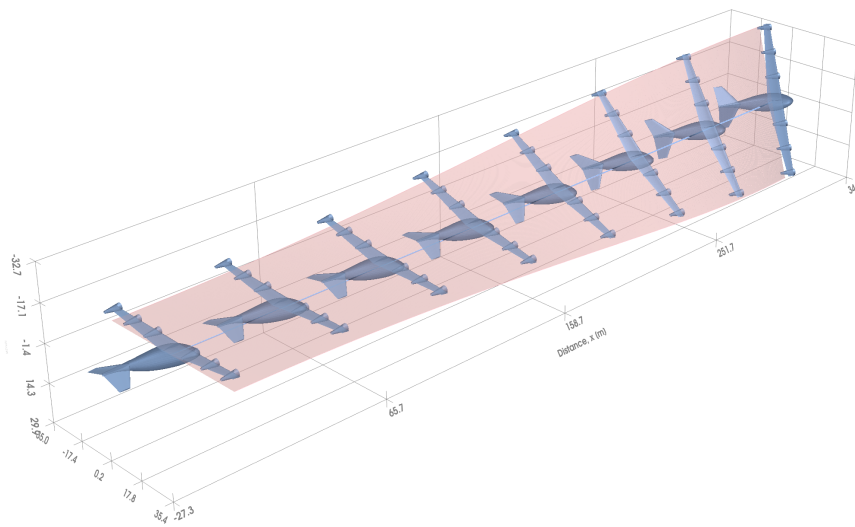


Figure 11.11: Roll performance for a duration of 6 s with $\delta_a = 22.5^\circ$ at V_{cruise} visualised in 3D space. Aircraft scale is 5-to-1 for visibility

Table 11.8: Tail Parameters

	$S_h[m^2]$	$S_v[m^2]$	$S_{tail}[m^2]$	$A_v[-]$	$A_h[-]$	$\Lambda_h[-]$	$\Lambda_v[-]$	$v[-]$	$b_{tail}[m]$	$c_r[m]$	$c_t[m]$
Preliminary	2.82	2.48	5.30	2.00	2.27	0.40	0.40	41.38	4.00	1.89	0.76
Class II	4.48	2.73	7.21	1.52	2.50	0.40	0.40	31.36	4.59	2.24	0.90

11.10. Verification & Validation

An important aspect that has to be performed to ensure the correctness of the results is the assess the quality of the code. This can be done based on verification and validation procedures.

First and foremost, several unit tests have been conceptualised in order to assess the correctness of the Python code utilised in sizing the tail. Thus, unit tests were performed on the scissor plot Python code to determine whether the outputs correspond to expected values.

Scissor Plot Unit Test

Several tests were conceptualised in order to ensure the correctness of the computed parameters. Thus, the following unit tests were performed:

Table 11.9: Scissor plot unit tests

Test ID	Technique	Description	Justification	Tolerance	Result	Confidence
SCI-1	Manual Calculation	Test correctness of parameter calculation	Easy to perform, accurate	10%	Pass	High
SCI-2	Visual inspection of plot	Test final plot correctness	Easy to perform,	N/A	Pass	High

Dynamic Model Unit Test

Another aspect that is crucial to the stability and controllability of the design is the dynamic model. Therefore, it is important to come up with unit tests for the dynamic model as well. The following unit tests were performed on the dynamic model:

Table 11.10: Dynamic model unit test

Test ID	Description	Technique	Justification	Tolerance	Result	Confidence
DYN-1	Check of Data input shape	Print shape of loaded data	Easy, Accurate	N/A	Retrieves data in correct shape	High
DYN-2	Check of Data Unit	Visual inspection of the dataset	Easy, Accurate	N/A	Units are as expected	High
DYN-3	Check output correctness	Test whether Cessna 172 aircraft is stable according to model	Verify result feasibility	N/A	Aircraft is stable	High
DYN-4	Symmetric Matrix Check	Creation of matrix	Verify that matrix is correctly constructed	N/A	Matrix matches expected outcome	High
DYN-5	Asymmetric matrix check	Creation of matrix	Verify that matrix is correctly constructed	N/A	Matrix matches expected outcome	High

Next, validation of the final design values should be performed. Since there is a lack of availability in data for eVTOL designs, validating the final tail sizes is challenging. However, to determine whether the results are feasible or not, a comparison between final design parameters and class I values can be performed. A short discussion of the discrepancies between the values is thus in order.

It can be seen that the horizontal tail is significantly larger in the class II estimation. However, the reason for this issue is that the CG is positioned very aft compared to the mean aerodynamic chord of the wing compared to a typical design. Additionally, the vertical tail size is high for the class II estimation as well since all engines are considered inoperative in the sizing of the tail.

However, a more detailed analysis of the competitor tail sizes should be performed whenever more data becomes available. It is clear from the final design values that the vertical tail is oversized, and this should be taken into account further down the road during the next design phases.

11.11. Further Iterations and Recommendation

As it can be seen, the current design of the aircraft has severe spiral instability, with a doubling time of 0.8 seconds. This is considerably below the requirement of a minimum doubling time of 5 seconds [79]. Therefore, since spiral instability is caused by the $C_{n\beta}$ coefficient, a solution to improve spiral stability is to decrease tail size.

In order to decrease tail size, it is important to note that the vertical tail sizing method has been sized for all engine inoperative scenarios. However, it is the case that the vertical tail can be sized for one critical engine inoperative scenario [80]. Based on this and using the method in Section 11.7, the following values are obtained when it comes to the new vertical tail size:

Table 11.11: Iterated values required to determine the vertical tail size for engine inoperative

N_E	N_D	ρ	V_{MC}	$C_{l,\delta_{theory}}$	$\frac{C_{l,\delta}}{C_{l,\delta_{theory}}}$	K^*	K_Λ	δ_f	l_v	S_v
74 kNm	55 kNm	1.17 kg/m ³	29.1 m/s	3.6	0.74	0.65	0.92	25°	4.74 m	1.41 m ²

These considerations lead to a halved vertical tail size, which alters the dimensions of the inverted V-tail. Based on the new parameters, the following values are obtained for the iterated tail:

Table 11.12: Iterated tail parameters

	S_h [m ²]	S_v [m ²]	S_{tail} [m ²]	A_v [-]	A_h [-]	Λ_h [-]	Λ_v [-]	v [-]	b_{tail} [m]	c_r [m]	c_t [m]
Iteration	4.48	1.41	5.89	0.79	2.50	0.40	0.40	17.52	3.93	2.14	0.86

Taking the iterated tail into account, if the spiral instability performance is analysed once again, the final doubling time value is 6.1 seconds, which is above the five-second requirement. Therefore, the vertical tail size should be reduced in further iterations. However, it is important to consider that a reduced vertical span of the tail shall influence the landing gear subsystem configuration.

Another aspect that should be taken into account is the size of the ruddervators. While a preliminary rudder sizing was performed to determine the vertical tail performance, no sizing with respect to the elevators has been considered. In order to ensure the completeness of the design, the elevator performance should be taken into account as well.

Lastly, it is clear that the roll motion performance is severely limited at the moment as mentioned in Section 11.8.2. Iterations of the location of the battery, as well as a more detailed analysis of the moment of inertia, are recommended, along with determining whether this requirement is applicable to eVTOL vehicles.

12. Autonomous System

The autonomous software design of a passenger aircraft faces many challenges, from accuracy and reliability to public acceptance. Being a new technology, the introduction of such a system shall be gradual. Firstly, a fully autonomous flight with emergency local manual control may be introduced. Then fully autonomous systems can be employed with remote safety control in case of emergency until fully autonomous flights are not completely reliable. The following chapter walks the reader through the conceptual design of the autonomous system of the *Swing* UAM. Firstly, the necessary functions of the system are investigated. Subsequently, the description of the software architecture and control modes are presented. Eventually, the critical sensors are collected to estimate the full dynamic state of the UAM.

12.1. Autonomous Software Functions

Before the conceptual design of the autonomous software, the necessary functions of such software must be summarized. Firstly, it has to find an obstacle-free path between the starting location and the destination. Meanwhile, a communication link shall be created between the vehicle and the ground control. The aircraft's steering is done with several different controllers in different flight conditions through the actuators. Finally, several diagnostic algorithms shall be implemented to ensure the safety of the passengers and the surroundings.

As mentioned before, the steering input of the UAM is calculated by different control modes. The following control modes are identified by inspecting the mission profile presented in Figure 6.1. The UAM has to perform a vertical take-off and landing in a hexacopter configuration alongside hovering. Next, the vehicle performs a forward and backward transition with complex dynamics requiring a different controller. Whilst, the fixed-wing configuration shall perform a climb, cruise and descent. The last three modes having similar dynamics are controllers with the same control mode. Lastly, a remote manual control mode is required to take safety measures. In the following section, these control modes are further elaborated, and an appropriate control architecture is selected for each.

12.2. Autonomous Software Architecture

The following section aims to present the conceptual design of the autonomous controller. To facilitate an easy understanding of the subcomponents of the design, first, the reader is provided with an overview of the structure and flow of the autonomous software. Figure 12.1 summarises the most important components and actions within the software.

The system's start-up triggers a diagnostic software ensuring the safe start of the flight and compliance with requirements Te-1-STK04-3 and Te-1-STK04-3-1. If this process runs into issues, the system blocks the possibility of flight, guaranteeing the safety of the passengers. Otherwise, the flight can commence by communicating with the air traffic database and starting the route planning block. The route planning algorithm ensures that the most efficient obstacle-free route is found whilst air traffic regulations and separation standards are met utilising the air traffic and sensor data. Here, an iterative process can be found between the air traffic centre and the local vehicle, as the aim of the algorithm is not just to find an optimal route for a single agent but for all agents. Subsequently, if the route planner executes without an error, the control mode of the aircraft is selected, then the eVTOL controller can start the operation in a closed loop. Due to the longer running time of the global route planner algorithm, the control loop is called with a higher frequency than the global route planner algorithm. If an issue is detected within the planner loop, the air traffic controller is alarmed, who will attempt to resolve the issue. In case the issue cannot be solved, the command of the aircraft is transferred to a remote manual pilot who safely navigates the UAM to the destination. In the event of flawless operation, the autonomous software ensures a smooth flight and reaches the destination in the shortest possible time.

In the following subsections, some of the software blocks are further detailed. Firstly, the conceptual design of the route planner algorithm is presented. Next, the control strategy is selected for different control modes alongside the conceptual design of the controllers. Lastly, recommendations are made for future work to complete the design and implementation of the autonomous software.

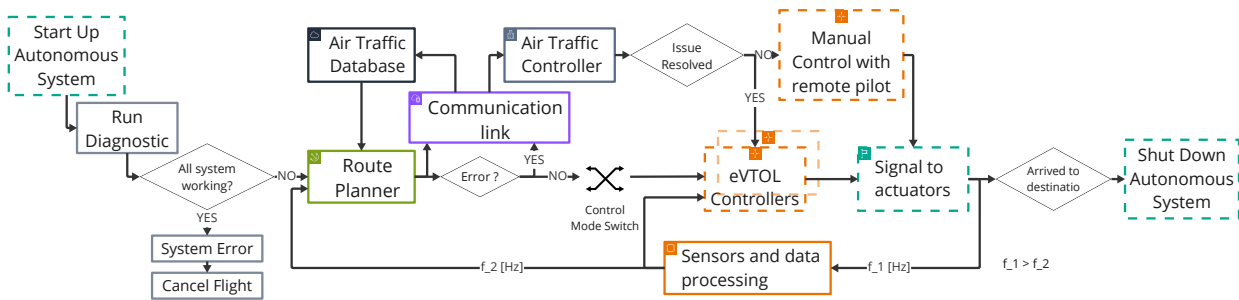


Figure 12.1: Flow diagram of the autonomous software

12.2.1. Global Route Planner

As proposed before, the global route planner holds the most importance in the autonomous software structure. This algorithm ensures that the vehicle arrives from the start location to the desired destination without any accidents. The highest level goal of this algorithm is to find a path between set waypoints (and potentially return to the starting point) without collision, minimising a pre-defined cost function. This route-finding problem is essentially a Travelling Salesman Problem (TSP), for which several approximate algorithms exist. Firstly, the existing algorithms for this problem are compared. After selecting the most suitable one, the final structure of the planner is presented.

For discrete path planning and obstacle avoidance, two widely used algorithms exist, the Probabilistic RoadMaps (PRM) and the Rapidly Exploring Random Trees (RRT) [5], [81]. Furthermore, several derivative algorithms exist and are proposed. In order to select the most suitable algorithm, a simple comparison is performed. Starting with the RRT algorithm, asymptotic stability is not ensured, meaning it does not approach the optimal route by increasing the spatial sample number. On the other hand, the simple PRM (sPRM) variant of the PRM method is proven to be asymptotically optimal. Contrary, the time complexity of the RRT ($O(n \log n)$) over-performs the one of sPRM ($O(n^2)$) [82]. Since no other major advantage difference can be detected between the two algorithms, a trade-off has to be made based on the more desired property. As the profit is indirectly influenced by the flight time, it is desirable to obtain the optimal root over the decreased computational capacity. This possibly results in an increased flight number capacity over a fixed time, implying an increased profit. Furthermore, if necessary, this process can be performed on a remote computer instead of the on-board computer allowing for faster computation. Therefore, the PRM algorithm was selected.

The PRM algorithm requires several subcomponents to operate, including point sampling, obstacle-checking and shortest-path algorithms. Roland G. et al. compare several sampling techniques for PRM planners [83]. Since no straightforward conclusion can be drawn from the study, the paper can later help to select the most appropriate technique for the case of urban air mobility. To meet requirement Co-6-STK12, the point cloud must be generated such that the air traffic regulations are met.

The next challenge of discrete path planning is the obstacle-checking algorithm. This algorithm must take into account the fixed and moving obstacles obtained from city maps and from the flight operator alongside the local obstacles detected by the radar and computer vision system. To speed up the collision checking, a safety certificate method was introduced by Joshua B. et al. can be implemented [84]. This process generates spherical safety certificates around the sample points. Consequently, the computational time required for obstacle-checking decreases exponentially with increasing certificate numbers since obstacle-checking with spheres is less computationally demanding. It is important to note that a safety margin of three meters plus the sensors' uncertainty must be considered when the radii of the safety certificates are calculated. Hence, the

violation of requirement Co-5-STK14-2-2, which requires a three-meter safety margin between any object and the vehicle, is avoided. Furthermore, to satisfy requirement Co-6-STK12, the air traffic regulations and separation standards must be met when the obstacle checking is done [85].

For path finding an A-star algorithm is proposed due to its optimality and fast computational time. However, the optimality requires an admissible heuristic, meaning that the estimated cost-to-reach must underestimate the real cost-to-reach. The proper design of the cost function and heuristic will be performed in the later stages of the design; however, it is important to note that the route has to cover the most amount of distance in the shortest time with the least amount of electricity possible. The final component of this algorithm is to fit a Dubins' tour on the achieved points, ensuring the fastest continuous path that can be fit on the discrete route [86].

The previous considerations only accounted for a single-agent system. However, it is important to emphasise that this problem contains several agents in the form of other UAMs and possibly UAVs. Therefore, to ensure global optimality and account for uncertainties, the problem must be solved as a multi-agent problem. Paul O. et al. proposed a transformation between a multi-agent TSP and an asymmetric TSP which can subsequently be solved with any routing algorithm [6].

These considerations guarantee that all the necessary components are present for a global route planner. The algorithm's essential parts and flow are shown on Figure 12.2.

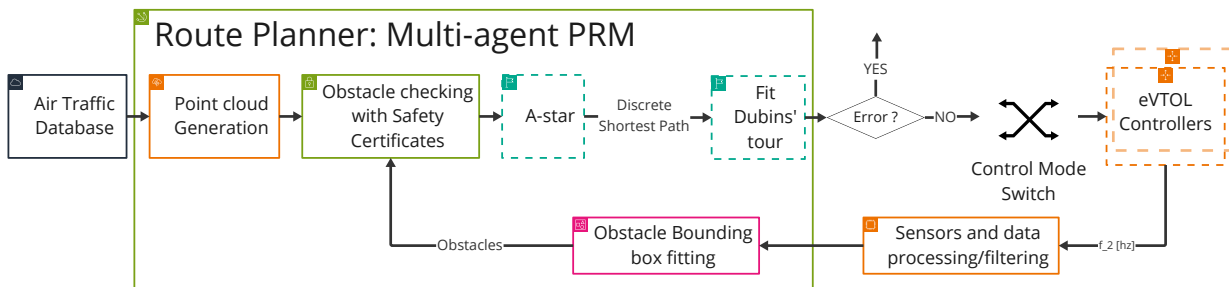


Figure 12.2: Flow diagram of route planning software

12.2.2. Hexacopter Control: Vertical Take-off, Landing and Hovering modes

The aim of the vertical take-off and landing control mode is to reach a specified altitude while maintaining the same position in the other two dimensions. Similarly, the purpose of the hovering control is to sustain a fixed position in the space. Hence, the same controller architecture was selected for both conditions. As the vehicle spends a short time in these configurations, a simple but reliable control structure is needed. Thus, the position control architecture depicted in Figure 12.3 is selected for position control.

The structure contains three separate PID controllers to successfully achieve active control over the hexacopter configuration. Firstly, three separate PD controllers estimate the necessary thrust vector compensation in the inertial frame. Subsequently, using a coordinate transformation between the inertial frame and the body frame, the desired pitch (Θ) and roll (Φ) angles are calculated and controlled to perform the attitude control of the vehicle. The PD attitude controllers calculate the virtual control inputs of thrust (U_1) and moments about the x , y and z axes (U_2, U_3, U_4), which can be transformed to the angular speeds of the motors by solving Equation (12.1). Here, b and d are the lift and drag coefficients of the rotors, x_i, y_i are the moment arms from the centre of gravity, whilst n_i takes a value of 1 if the rotor is rotating clockwise, else -1 . Since for the allocation matrix $n < m$, infinitely many solutions exist. Thus, if R is full row rank, the right pseudo inverse of R can be taken to minimise the control effort as shown in Equation (12.1) [7]. Finally, the motor

speed PID controllers sustain a stable rpm by controlling the current or potential on the actuators.

$$\underbrace{\begin{bmatrix} U_1 \\ U_2 \\ U_3 \\ U_4 \end{bmatrix}}_U = \underbrace{\begin{bmatrix} b & b & b & b & b & b \\ by_1 & by_2 & by_3 & by_4 & by_5 & by_6 \\ bx_1 & bx_2 & bx_3 & bx_4 & bx_5 & bx_6 \\ dn_1 & dn_2 & dn_3 & dn_4 & dn_5 & dn_6 \end{bmatrix}}_{R^{n \times m}} \underbrace{\begin{bmatrix} \omega_1^2 \\ \omega_2^2 \\ \omega_3^2 \\ \omega_4^2 \\ \omega_5^2 \\ \omega_6^2 \end{bmatrix}}_{\Omega} \quad \Omega = R(R^T R)^{-1} U \quad (12.1)$$

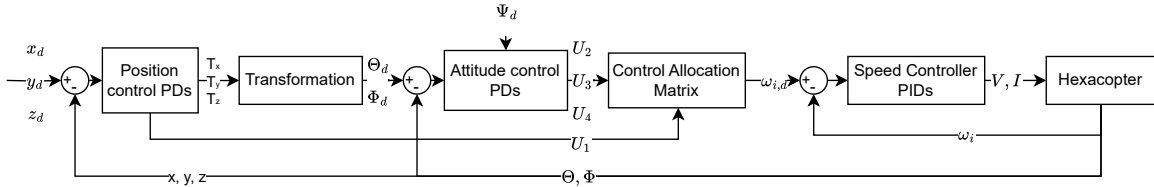


Figure 12.3: Position control loop for vertical take-off, landing and hover

In the extreme case of two frontal engine failures or the failure of more than three engines, the stabilisation and safe landing shall be ensured in hexacopter configuration. Mark W. et al. proposed a fault-tolerant multicopter controller which is capable of stabilising the vehicle in case of multiple engine failures by sacrificing the yaw control and thus passenger comfort [87]. Furthermore, if no precise state estimation is available through external sensors (GPS), the onboard computer vision can be utilised to measure the state of the vehicle [88].

12.2.3. Transition Mode

The transition control was realised utilising a combination of three controllers similarly as shown in [8]. A planar altitude controller provides stable altitude tracking, whilst an attitude controller ensures precise altitude stabilisation. Finally, a torque (τ) controller regulates the angular rate of the transition mechanism.

However, due to the highly nonlinear nature of the process, the gains of the controller cannot be optimised for all flight conditions. This issue can be resolved by employing a gain-scheduling controller. The nonlinear model can be linearised around pre-specified transition angle values (q), and the controller gains can be tuned for each working point achieving great performance [89]. The proposed controller is summarised in the block diagram of Figure 12.4. Here the actuator controller has a simple mass spring damper structure with an added estimate gravity term to eliminate the steady state error as shown in Equation (12.2). The gravity term can be calculated using the positional Jacobian between the centre of gravity and inertial frame as shown in Equation (12.2). The precise design of the terms in the attitude and altitude controllers opted to be done after the precise dynamic simulation of the transition is done.

$$\tau_d = k_p(q_d - q) + k_d(\dot{q}_d - \dot{q}) + \hat{g}(q) \quad \hat{g}(q) = \sum_{i=1}^2 -I J_{P_i} \cdot I F_{g,i} \quad (12.2)$$

12.2.4. Fixed Wing Control: Cruise, Climb and Descent Modes

The control mode possessing the most importance is the cruise controller since it is the control mode in which the aircraft spends the most amount of time. The fully autonomous passenger flight area is a developing field; therefore, no controller type has gained the trust of the engineers in this field. Thus, a simple comparison is performed on the most common controller types, LQR, PID and Model Predictive Control (MPC) to select the most suitable one.

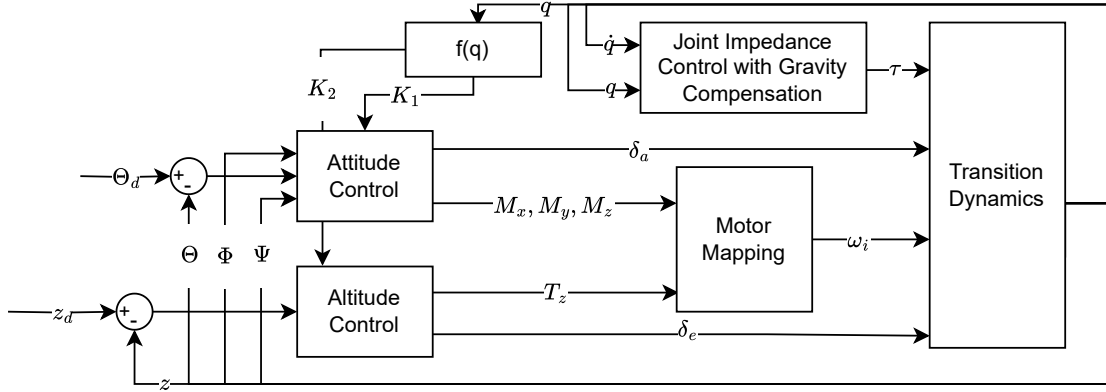


Figure 12.4: Transition control loop with attitude, altitude tracker and joint impedance controller with gravity compensation

In a disturbance-free environment, PID and LQR controllers outperform the tracking capabilities of MPC controllers. However, in cases where disturbance rejection of the controller is highly important, which is the case during cruising, MPC controllers show a better performance. In the case of the transwing eVTOL vehicle, the property of disturbance, and therefore wind, rejection is of utmost interest due to the requirement of Te-2-STK07-5-2. Furthermore, generally speaking, the control effort is much less in the case of MPC compensators compared to its opponents [9]. Additionally, the robustness of MPC controllers cannot be overlooked as it is important to achieve high accuracy in a wide range of weather and environmental conditions.

As an optimal control problem, MPC enables achieving high performance in the desired performance metrics. The availability of setting control contains can enable smooth changes between states, thus avoiding high accelerations resulting in higher passenger comfort and complying with requirements Te-2-STK07 and Te-2-STK07-1-4. Lastly, with this control scheme, it is possible to incorporate local obstacle avoidance with obstacle convexification proposed by [90]. The aforementioned list of advantages of MPC gives confidence that the best choice for cruise control is an MPC compensator.

Since the main objective of the aircraft mission is to reach the destination in the shortest time, a Model Predictive Contouring Controller (MPCC) was selected as the optimisation problem. This controller shows superior performance over conventional state trajectory tracking MPC controllers by minimizing the contouring and lag errors with respect to a pre-defined reference path described by a cubic spline [10]. The optimisation problem is formulated as shown by Equations 12.3-12.8. Here the linearised contouring error (\hat{e}^c) and the lag error (\hat{e}^l) are the transverse and lateral distances between the current position (p_k) and the estimated position on the reference path as depicted in Figure 12.5. The parameter $v_k^{\hat{\theta}}$ is the virtual tracking speed on the reference trajectory and q_c, q_l, γ are weights for the cost terms. Potentially, a cost term can be added to this optimisation statement that minimises energy consumption, whilst it shall be extended with the necessary constraints for obstacle avoidance as shown in [90].

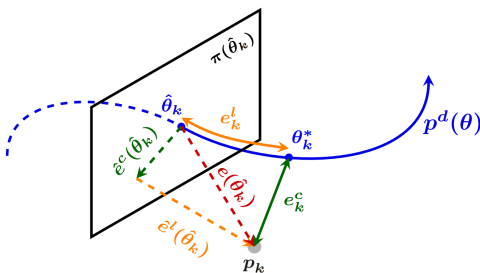


Figure 12.5: Contouring and lag error defined for the MPCC controller [10]

$$\min_{x,u,v} \sum_{k=1}^N \|\hat{e}^c(x_k, y_k, z_k, \hat{\theta}_k)\|_{q_c}^2 + \|\hat{e}^l(x_k, y_k, z_k, \hat{\theta}_k)\|_{q_l}^2 - \gamma v_k^{\hat{\theta}} \quad (12.3)$$

$$\text{subject to } \chi_0 = \chi, \quad (12.4)$$

$$\chi_{k+1} = f(\chi_k, u_k), \quad k = 1, \dots, N-1, \quad (12.5)$$

$$\chi_k \in \mathcal{X}, u_k \in \mathcal{U}, \Delta\chi_k \in \Delta\mathcal{X}, \Delta u_k \in \Delta\mathcal{U}, \quad (12.6)$$

$$\hat{\theta}_0 = \theta, \quad (12.7)$$

$$\hat{\theta}_{k+1} = \theta_k + v_k^{\hat{\theta}} \Delta t, \quad (12.8)$$

Equation (12.5) uses a nonlinear dynamic function to predict the states of the cruising UAM. Hence, optimisation can only be solved as a nonlinear program (NP). The current state-of-the-art NP solvers, such as IPOPT, implement the interior point primal-dual method. This method does not guarantee global optimality, what is more, convergence is not ensured to local minima in acceptable time [31]. Therefore, it is recommended to linearise the cruise dynamics about different working points, generating a Linear Parameter Varying (LPV) model enabling the solving of the problem with a Quadratic Program (QP). One form of such a model is shown by Equation (12.11), where A and B are the state matrices dependent on the scheduling variables of x and u . Equation (12.10) shows a flexible and easy method to perform the linearisation of the nonlinear dynamics and constructs the state matrices proposed by [91]. A necessary requirement of LPV embedding is a nonlinear state derivative at the origin, as shown in Equation (12.9).

$$\dot{x} = f(x, u) \quad f(0) = 0 \quad (12.9)$$

$$A(x, u) = \int_0^1 \frac{\partial}{\partial x} f(\lambda x, \lambda u) d\lambda \quad B(x, u) = \int_0^1 \frac{\partial}{\partial u} f(\lambda x, \lambda u) d\lambda \quad (12.10)$$

$$\dot{x} = A(x, u)x + B(x, u)u \quad (12.11)$$

After deriving the nonlinear cruise model of the vehicle, this controller can be easily implemented using a symbolic program package such as CasAdi. Furthermore, the optimisation problem, being convexified, can be solved with a QP solver. Furthermore, since a typical control update frequency of such local planners is at the magnitude of a few tens of milliseconds [10], it might be necessary to speed up the runtime of the algorithm. If further update time decrease is needed, an alternative approach to the LPV model is the application of Multiple Shooting Sequential Quadratic Programming, the nonlinear problem. This method exchanges optimality with computational time decrease with high efficiency as described in [92]. The block diagram of this controller is depicted in Figure 12.6.

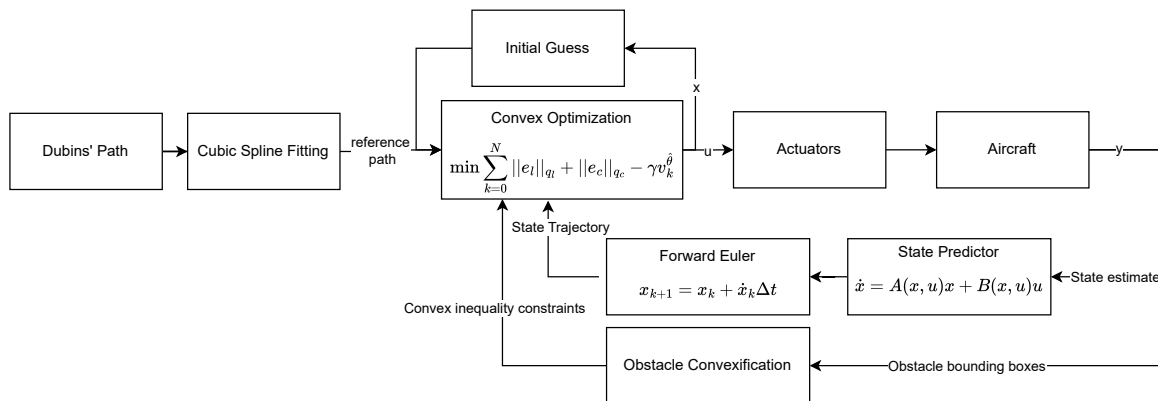


Figure 12.6: MPCC control loop for cruising

Finally, the requirement of Co-3-STK03-1 shall be considered for this control mode. It demands operation in the case of two inoperative engines. In Chapter 11, it was ensured that it is possible to control and keep the vehicle in the air in the case of two engine failures. Now the task of the autonomous software is to recognise and adapt to the changes in the system. Here, another advantage of MPC controllers appears, since after identifying the failed engines, the control system can simply add two new constraints to the optimisation problem of Equation (12.3). These new constraints ensure that the control inputs corresponding to the failed engines remain zero, allowing for accurate modelling of the system even after engine failures.

12.2.5. Future Work

In the previous sections, several different control methods were proposed. However, multiple additional steps have to be taken to produce a completely functional autonomous system. The following, section aims to provide insight into how the future development of this system will proceed.

Firstly and most importantly, the dynamic modelling of the different flight phases has to be done. In

Section 11.8, a linear model for the cruise phase was proposed. To further enhance model accuracy, a more detailed nonlinear model can be derived. Another key modelling aspect of the autonomous software design is the nonlinear modelling of the transition in both directions. This is inevitable to perform the preliminary tuning of the gain scheduling controller for transition. Finally, a simple hexacopter model can be selected to tune the PD controllers of the hexacopter position tracking controllers.

After modelling the aircraft in different flight conditions, the model identification has to start to obtain the model parameters. A fusion of simulation and experimental techniques can be used to determine the precise values of the model parameters. If all the models are sufficiently developed, the implementation and tuning of the control algorithms can be commenced. Finally, the controllers shall be tested on the real system.

12.3. Measurement System

In order to perceive the surroundings of the vehicle with sufficient accuracy in any conditions, great care must be taken to select the right types of sensors needed for the autonomous system. In the previous stages of the design, a preliminary set of sensors was selected. Now that a detailed conceptual design of the autonomous software has been done, these sensors are revised to ensure all necessary states can be measured. The following section walks through all these necessary sensors in a top-down manner, meaning first, the higher-level algorithms are considered, and finally, the lower-level controllers.

Firstly, the route planner algorithm has to be considered, which requires a full spatial location estimation with obstacle detection. As the eVTOL only operates in outdoor conditions, the GNSS and GPS sensors suffice since, in outdoor applications, it can achieve high accuracies of a few centimetres¹. Regarding obstacle detection, two approaches can be taken, passive or active depth estimation. Active computer vision utilises time-of-flight (TOF) sensors which can achieve extremely high accuracies at the expense of price and weight. Furthermore, these sensors can only measure in one direction at a time, meaning it has to scan the entire space before an image can be constructed. On the other hand, passive depth estimation uses triangulation of camera images. This strategy cannot achieve such accuracies as TOF sensors; however, they are much cheaper and more flexible as they can perceive the depth through the entire image simultaneously. Moreover, techniques, such as structured infrared light, exist to enhance the accuracy of passive methods [11].

Two more important considerations must be taken before selecting the final sensor. The requirements Te-2-STK07-5-1 and e-2-STK07-5-3 demand the ability to fly in dark and rainy conditions. TOF sensors have no problem operating in different illumination levels as they only measure the distance from the object. On the other hand, structured light cameras are equipped with infrared sensors to perceive the structured infrared light projected by the camera system. Infrared sensors are perfect for night vision. Moreover, infrared cameras can perform better than TOF sensors in poor weather conditions, such as in heavy rain [93]. Likewise, since structured light cameras can perform with 8-centimetre accuracy on 4 meters², the obstacle avoidance requirement of Co-5-STK14-2-2 can be met; thus TOF sensors are disproportionate. Additionally, passive computer vision has a limited depth estimation range; thus, the use of a radar system is justified for long-range obstacle detection.

Subsequently, the list of required sensors can be continued with the sensors needed for autonomous controllers. Since the precise model used for these controllers is not developed, the proposed sensors might change after the detailed controller development. Alongside the spatial position determination, now, the airspeed, temperature, angular rates and accelerations are required to measure the full state of the aircraft. For this purpose, as proposed beforehand, pitot tubes, inertial measurement units and thermometers can be used. Furthermore, some computer vision algorithms can aid in increasing the accuracy of the previously mentioned sensors [88]. Further, to measure and regulate the control input of the transition actuator, control surface deflection, propulsion throttle and blade pitch actuator encoders can be used. Concluding the list of sensors, if lower-level current or voltage controllers are to be used to regulate the torque of the actuators, the system has to be equipped with voltmeters or ammeters.

¹<https://www.advancednavigation.com/inertial-navigation-systems/mems-gnss-ins/certus/>

²<https://www.intelrealsense.com/stereo-depth-modules-and-processors/>

13. Electric Power System

In this chapter, the design of the electrical power system of the *Swing eVTOL* will be discussed. Firstly, the required battery mass will be calculated in Section 13.1 to obtain the required energy to complete the mission. Subsequently, a general introduction to battery design and battery cells will be given in Section 13.2, discussing the elements that influence the sizing of this subsystem. Moreover, the complete battery pack design will be presented and justified in Section 13.3, including a state of health analysis and thermal management considerations. Finally, in Section 13.4, a summary of the design will be presented as well as recommendations to consider.

13.1. Preliminary Calculation

One of the main components during the preliminary design of an electric vehicle is the battery and power system. To have an accurate estimate of the required battery size and weight, it is necessary to come up with preliminary sizing methods. Firstly, the energy required for each phase of the mission profile is computed. After which, the total energy required for the entire mission is calculated as the following summation:

$$E_{\text{tot}} = \sum_0^m E_m \quad (13.1)$$

Having defined the energy requirement, it is now possible to compute the total battery mass needed. To perform this calculation, it is necessary to define a new parameter, the energy density of the battery. This can be indicated as ρ_E [Wh/Kg] and represents how much energy a battery can store per unit of weight. The value of this parameter can be estimated to be 300 Wh/Kg for state-of-the-art batteries with current technologies [94].

Relating now the required energy and the density parameter just discussed, it is possible to retrieve the total weight of the battery:

$$w_{\text{tot}} = \rho_E \cdot E_{\text{tot}} \quad (13.2)$$

Lastly, another fundamental quantity to take into account during a battery design is the capacity C . This defines the amount of energy that can be delivered under specified conditions. For example, if $C = 100$ Ah, it means that a current of 100 A can be delivered for 1 hour. To calculate the capacity, the following equation can be used:

$$C_{\text{pack}} = \frac{w_{\text{tot}} \cdot \rho_E}{n_{\text{pack}} \cdot U_{\text{ElecSys}}} \quad (13.3)$$

Where n_{pack} is the number of battery packs, and U_{ElecSys} is the nominal voltage of the system. The calculations just shown have been performed for the initial set of requirements of 100 km of range and 200 km/h of cruise speed. The results for both mission profiles are summarised in Table 13.1.

Table 13.1: Range and battery sizing for the *Swing eVTOL*

Range [km]	E_{tot} [kWh]	m_{bat} [kg]
100	50	150

m_{bat} represents the minimum mass required to complete the mission; however, it is decided to increase the battery mass to 400 kg, extending the range and increasing the stability characteristics of the vehicle. This value has also been determined on the basis of the required CG shift during the transition that is required for stability. In Chapter 11, it has been indeed determined that a lower total battery mass would cause the aircraft to be unstable with the current design. Lastly, it is important to mention that a minor part of the energy stored in the battery will be converted to low-voltage current to power the avionics and other subsystems.

13.2. Battery Cells

As the fundamental quantities defining a battery have been discussed in the previous section, it is important to study the units that compose battery packs, the cells. Every battery is indeed composed of single cells connected in series and parallel to then form the final subsystem that delivers the required current and voltage. In order to perform further calculations, firstly, some basic parameters that belong to battery cells need to be defined:

- Discharge rate (C-Rate) represents the electrical current the battery can deliver based on its capacity.
- State of Charge (SOC) represents the energy available in the battery.
- Depth of Discharge (DOD) is the energy consumed by the battery.
- U_{nom} is the nominal voltage measured at a SOC of 50
- C_{nom} , nominal capacity measured at a SOC of 50
- $U_{\text{c-off}}$, also known as cut-off voltage, representing the lowest voltage limit after which the battery is considered empty.

These parameters can then be related to each other finding many dependencies. One of the most relevant relations is between the depth of discharge and the battery voltage. It has been proved that the cell voltages drop as the DOD increases [95]. This is a key effect to evaluate; the voltage drop leads to a drop in the maximum power that can be delivered. Thus, the battery needs to be sized to comply with the power requirements in every flight phase. The latter described effect is caused by the internal resistances of the battery due to electrochemical interactions resulting in voltage-drops, according to Ohm's law. Figure 13.1 gives a visual representation of the equivalent circuit representing this process.

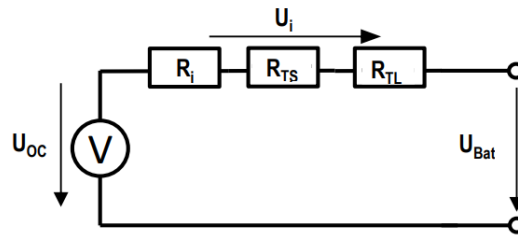


Figure 13.1: Equivalent circuit of a battery cell discharge model

In Figure 13.1, the different internal resistances are represented, but they can be simplified to one total resistance. This reduces the calculation of the total battery voltage to:

$$U_{\text{bat}} = U_{\text{oc}} - R_{e_{\text{tot}}} \cdot I \quad (13.4)$$

With $R_{e_{\text{tot}}}$ being the internal resistance. In [95], an extensive study on the battery discharge process has been conducted, and empirical relations between the internal resistances and the state of charge have been found that are listed below. Due to these equations, the voltage as a function of DOD has been obtained and plotted in Figure 13.2.

$$U_{\text{oc}} = -1.031 \cdot e^{-35 \cdot \text{SOC}} + 0.321 \cdot \text{SOC}^3 + 0.1178 \cdot \text{SOC}^2 + 0.2156 \cdot \text{SOC} + 3.685 \quad (13.5)$$

$$R_i = 0.1562 \cdot e^{-24.37 \cdot \text{SOC}} + 0.07446 \quad (13.6)$$

$$R_{TS} = 0.3208 \cdot e^{-29.14 \cdot \text{SOC}} + 0.04669 \quad (13.7)$$

$$R_{TL} = 6.6030 \cdot e^{-155.2 \cdot \text{SOC}} + 0.04984 \quad (13.8)$$

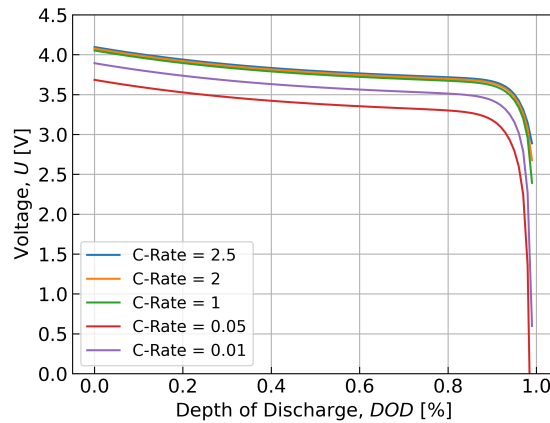


Figure 13.2: Voltage as a function of DOD per C-Rate

From Figure 13.2, it can be retrieved how, as discussed before, the voltage drops with the discharging of the battery. In particular, this effect is severe at a DOD between 80% and 100%. This drop results in a severe loss of power, thus it is advisable to not let the battery cell reach this level. Furthermore, as it will be discussed in Section 13.3.1, reaching this stage of discharge causes permanent damage, degrading the battery and shortening its life span. Lastly, in the plot, the voltages are plotted for each C-Rate, and it can be seen that for very low C-Rate values, the voltages drop as well, thus, it is necessary to also take this effect into account.

Iterative Algorithm

As it has been just described, the voltage of a battery depends on its state of charge as well. Thus, it is possible to create an iterative algorithm [96] that computes the power at each time step taking into account also the voltage changes. The current SOC and nominal capacity of the battery pack are taken as input. Subsequently, an iterative process starts to determine the actual voltage of the battery. The voltage that the battery can provide at each time instance of the mission profile has been plotted in Figure 13.3.

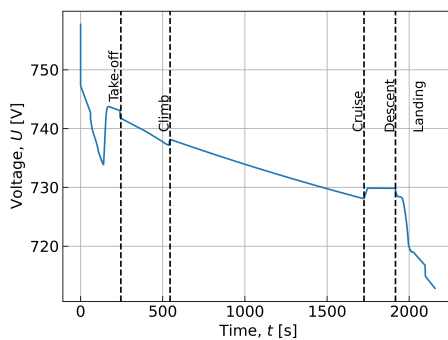


Figure 13.3: Battery pack voltage as a function of time

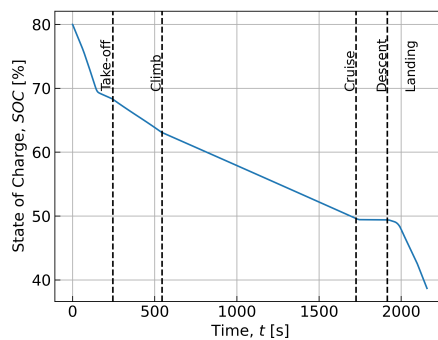


Figure 13.4: Battery SOC as a function of time

It is visible how the voltage decreases with time, following the previously discussed relation with SOC; however, it is important to notice that for the current battery configuration, the voltage is always above the required one from the engines of 710 V, thus this requirement has been satisfied.

Following the algorithm successively, it is possible to calculate the SOC as a function of time as well. To do so, it is necessary to calculate the actual capacity of the battery C_{act} . As well as the capacity of the battery, which is a function of the voltage, also drops with time. Hence, the new one can be estimated with the following equations.

$$C_{act} = r_c \cdot C_{nom} \quad (13.9)$$

Where r_c represents the relative capacity and can be obtained as a function of time from [96]. After retrieving this parameter, the last step of the iteration can be performed, and the battery charge as a function of time can be calculated. This is done through the following integration:

$$\text{SOC}(t) = \text{SOC}_{\text{start}} - \int_0^t \frac{I}{C_{\text{act}}}, dt \quad (13.10)$$

To complete this calculation, an initial condition for the SOC needs to be set. As seen before, and as it will be discussed in Section 13.3.1, the best operating range for a battery is between SOC of 20% and 80%, thus S_{start} has been set to 80%. Integrating the whole mission profile leads then to the generation of Figure 13.4.

From the plot, the battery discharge pattern can be seen over the whole mission profile. It is immediately noticeable that the most energy-consuming phase is the vertical take-off, since the battery percentage drops by 14% in roughly 4 minutes. This is sensible; as in the take-off, all the lift is generated by the propellers, thus the highest power is required, leading to this peak in consumption. It can then be seen how the climb and especially the cruise are very efficient phases. This is because the motors have to spin at a lower rate as the wings generate the majority of the required lift. It is noticeable, particularly, how only 14% of the battery energy is used during a cruise phase lasting 20 minutes. After this, a plateau can be seen; as during the descent, the engines are set to a very low power setting since a loss in height is required. Lastly, another peak in energy consumption can be noticed during landing; similar to the take-off, the motors will have to spin at very high rotational speeds to have a controlled descent. Furthermore, one thing that can be immediately seen from Figure 13.4 is how only 40% of the total battery capacity is used, this means that the range could be increased further. In particular, keeping the battery SOC between 20% and 80%, the SOC for the new mission profile can be plotted:

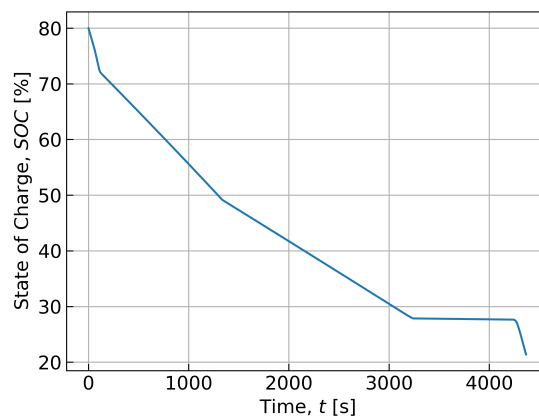


Figure 13.5: SOC over time for the new mission profile

Since the cruise speed does not vary and the cruise time is known, the new range is calculated to be 220 km. This means that as discussed in Section 2.2 the eVTOL would be able to reach more destinations in the contest of inter-urban mobility. Lastly, the C-rate and the current as a function of time can be plotted as well. For verification of the model purposes, the two curves should have the same shape since they are linearly proportional. Furthermore, the C-Rate plot it is crucial to control the degradation of the battery, as really high C-Rates lead to heat generation. The two plots can be seen in the Figures 13.6 and 13.7. As previously mentioned, the two plots have the same shape as respected. Furthermore, the C-Rate shows peaks at the take-off due to the high power consumption, however, it never peaks too much, limiting degradation.

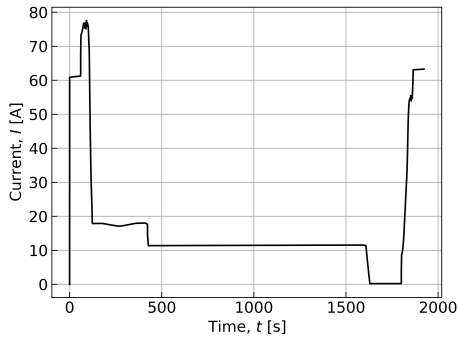


Figure 13.6: Current as a function of time

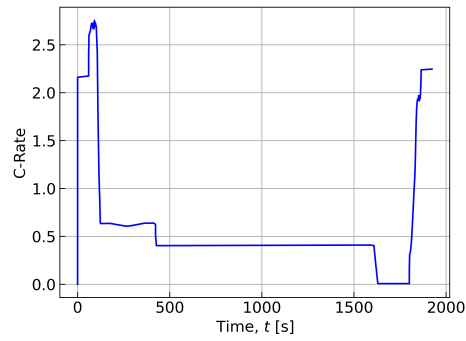


Figure 13.7: C-Rate as a function of time

13.3. Battery Design

In the previous sections, all the battery cell parameters and how they vary with time, thus with SOC, have been defined and discussed. Building upon that, it is now possible to analyze the final battery pack configuration. Firstly, the type of cells composing the pack needs to be chosen. Currently, the three most deployed cell types for electric vehicles are pouch, cylindrical and prismatic. The different configurations can be seen in Figure 13.8.



Figure 13.8: Equivalent circuit of a battery cell discharge model

Starting from cylindrical cells, they are the most used cell type in the automotive industry. This is because they are characterised by high energy densities while being structurally strong and easy to cool due to their low dimensions. On the other side, pouch cells are mechanically sensitive, since they do not have a rigid structure covering them; thus the probability of accidental damages increases, which leads to weight savings. Additionally, thermal management is more complicated due to the swelling of the cells during usage. Lastly, the prismatic cells, have great mechanical properties and energy densities. However, their dimension is larger than the other two options, which limits the applicability of this project as the space in the nacelle is very limited. After a careful evaluation, the cylindrical cells have been chosen. Mainly for their dimensions, ease of thermal management, and the mechanical properties that give this technology an edge over pouch cells in the design of the *Swing*.

Once the cell type has been chosen, the cell layout is needed. It has been decided to use six different battery packs, each of which powers one engine. The voltage U_{sys} is 710 V, while the required capacity has been determined to be 28 Ah, using Equation (13.3). In order to obtain these results, cylindrical cells with the following properties have been considered:

- $U_{\text{nom}} = 3.7 \text{ V}$
- $C_{\text{nom}} = 7000 \text{ mAh}$

To increase the voltage, cells need to be connected in series, meaning that the anode of one cell connects to the cathode of another. When connecting cells in this way, the total voltage can be calculated as:

$$U_{\text{tot}} = N_{\text{series}} \cdot U_{\text{cell}} \quad (13.11)$$

Being U the voltage and N_{series} the number of cells in series. Inverting this formula, it can be found that in order to reach a $U_{tot} = 710V$, 192 cells connected in series are thus needed. Once the voltage requirements are met, the capacity requirement needs to be analysed as well. In order to increase capacity, cells need to be connected in parallel. Similarly to the voltage, the total capacity can be computed as:

$$C_{tot} = M_{parallel} \cdot C_{cell} \tag{13.12}$$

Having each cell a capacity of 7 Ah, it can be found that four cells connected in parallel are needed to reach the capacity of 28 Ah. The pack could now be designed in one single module with the following configuration 192S x 4P. However, a single-module design has several disadvantages. Mainly, in case of minor defects, can lead to changing the whole battery in addition to the fact that the battery becomes less accessible. Opting for a multiple-module configuration, helps with the modularity of the design, leading to only certain parts of the battery being replaced if needed. Each module has been designed to have twelve cells in series and 4 in parallel, 12S x 4P configuration. Then sixteen modules are connected in series to reach the voltage requirement. A visualisation of each module has been produced in Figure 13.9.

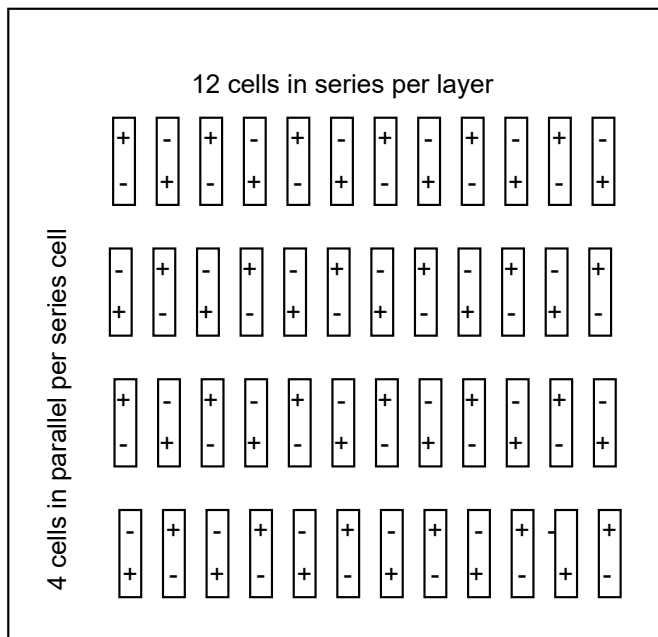


Figure 13.9: Configuration of each battery module

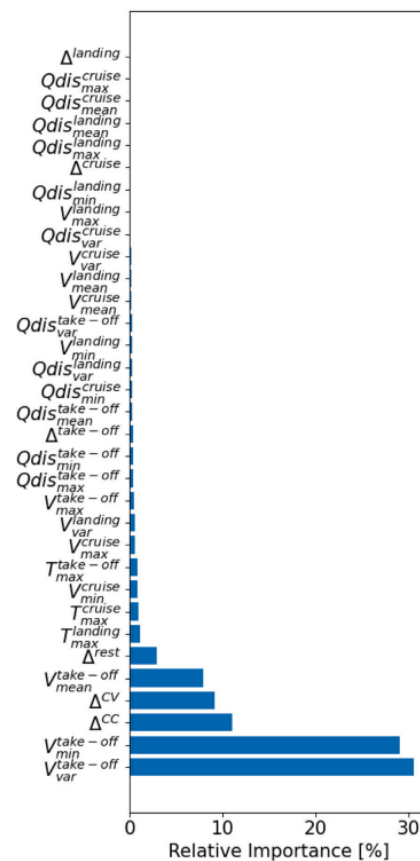


Figure 13.10: Relative importance of battery parameters on degradation [97]

13.3.1. Battery Degradation and Health Estimations

One of the main areas of concern when developing an electric power vehicle is battery health management. This is even more relevant in the case of eVTOLs, where the discharge rates are very high during the take-off and landing phases, impacting the overall lifespan of a pack [97].

The process that decreases the capacity of a lithium-ion battery is also called Solid Electrolyte Interphase (SEI) degradation. SEI is a thin layer of organic material that forms on the anode of the battery. Its main characteristics are facilitating the passage of ions, as well as protecting the anode from any decomposition. This thin layer, however, damages with time, resulting in decreased battery capacity, and an increase in

internal resistance[98]. Knowing the degradation process, it is now useful to understand which parameters influence it, thus estimating how to limit it to increase the lifespan of the battery pack. These parameters have been studied in [97]. Here a machine learning predictive model has been developed, thus the State of Health (SOH) of batteries has been estimated, indicating the effect of each flight phase on the degradation of the capacity. The algorithm used in [97] has been trained on public data for different mission profiles for the Airbus Havana eVTOL. From the results presented by the paper, visible in Figure 13.10 [97], it has been found that the voltage variance during take-off ($\Delta U_{\text{take-off}}$) has the highest impact, followed by the minimum voltage during take-off and charging phase duration.

These results can be explained by the fact that during the take-off, the battery has to provide very high power coupled with high C-Rates, as can be seen in Figure 13.7. The charging time instead is a function of the voltage and current. The faster the charging, the higher the power rating, which leads to batteries heating up, causing permanent damage to the SEI layer, and decreasing capacity drastically. Lastly, as mentioned before, the SOC is another parameter that must be taken into account when dealing with SOH management. It has been found by [99], Li-Ion batteries are particularly sensitive when operating and charging close to the cut-off voltage. This happens when going above a SOC of 80% or below 20%. For example, for a specific battery, it has been found that charging fully and going then to SOC of 0% in each cycle would lead to only 1000 cycles of life span. On the other side, charging between SOC of 40% and 70% leads to a life span of 2000 cycles [99]. For this reason, it has been decided to size the battery such that can meet the range requirement, operating only between the optimal SOC of 20% to 80%.

Once these have been defined, the total battery life span for the eVTOL design can be estimated. In order to do so, the power per cell during take-off has been calculated:

$$P_{\text{cell}} = I_{\text{cell}} \cdot V_{\text{cell}} \quad (13.13)$$

$$I_{\text{cell}} = \frac{I_{\text{pack}}}{m_{\text{parallel}}} \quad (13.14)$$

$$P_{\text{cell}} = 51 \text{ W} \quad (13.15)$$

This calculation results in a power per cell of 51 W, which is very similar to the one of the Havana of 54 W [99]. Furthermore, the nominal voltage for the cells is identical at 3.7 V, making a comparison a reasonable method to estimate the life-cycle. From the database, it can thus be found that the battery life span for this kind of battery averages around 800 cycles. It is, however, important to note that the end of life is defined at the point the pack reaches the 85% of its nominal capacity. This is a high limit, but necessary for safety reasons, especially during the take-off phase, the battery needs to be able to provide enough voltage without drops.

Lastly, the charging power rating for the battery has to be determined. In particular, it has been decided to use a power rating of 250 kW, in this way the 120 kWh battery could be completely charged in less than 30 minutes. This power rating has been decided upon research on ground electric vehicles. As an example, Tesla superchargers use the same rating [100] and their batteries are designed to last at least 1500 charging cycles. This indicates that this is a feasible rating that puts a compromise between low charging time and battery capacity conservation.

13.3.2. Battery Cooling

From Section 13.3.1 it is clear that keeping the battery at an optimal temperature is fundamental during operations. If the temperature increases too much, the battery will not deliver the expected power and will be permanently damaged, leading to a decrease in the lifespan. From the mission profile analysis, it is clear that the battery will deliver the highest power during vertical off and descent, thus in these phases, there will be the highest heat generation, leading to a severe increase in temperature. To avoid this, air-cooling could be adopted. However, during the vertical ascent, the airspeed is very low. Even the stream of the propeller would not be optimal to keep the batteries at a controlled temperature. Furthermore, having additional openings in the aircraft will create additional drag during the cruise, reducing aerodynamic performances.

For this reason, it has been decided to opt for a liquid-cooling thermal management system, similar to Joby aviation [101]. The cooling system will be composed of a pump and several tubes containing coolant that will tangentially touch each cylindrical cell, extracting the heat from the cell. An exemplification of this can be seen in Figure 13.11 [102], while a diagram of the heat extracting system has been produced in Figure 13.12.

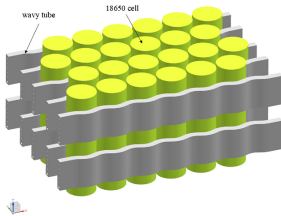


Figure 13.11: Cylindrical cells liquid cooling [102]

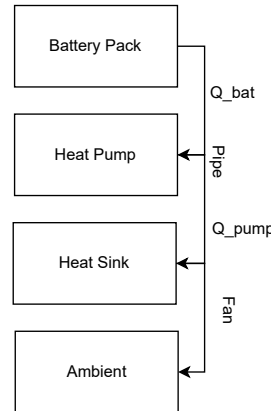


Figure 13.12: Heat pump scheme

Lastly, it is important to note that the battery capacity is enough to account for the consumption of the cooling system without drastically compromising the range.

13.4. Design Summary and Recommendations

The design of the battery has been divided into many steps with several layers that might be hard to understand at first sight, thus this section aims to give a clear overview of the final results. Figure 13.13 illustrates the complete battery design from a top-level perspective showcasing how each pack is made and all its layers. In addition to this, Table 13.2 presents the final values for many parameters of the aircraft batteries.

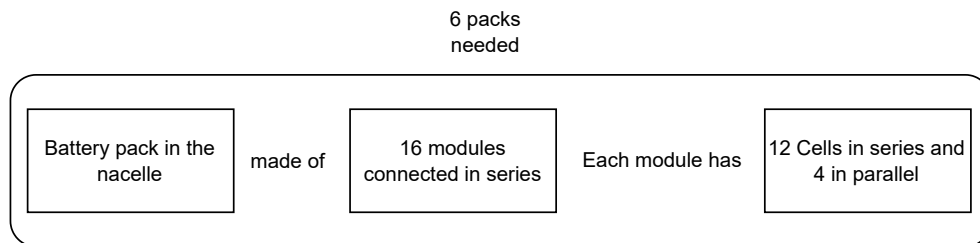


Figure 13.13: Complete battery system overview

Table 13.2: Battery parameters summary

N_{cells} [-]	N_{tot} [-]	w_{cell} [-]	w_{tot} [kg]	E_{pack} [kWh]	E_{tot} [kWh]
768	4608	0.09	400	20000	120

Lastly, as the field of battery development is currently a thoroughly studied field, some recommendations for further development are necessary. In this paper, standard Li-Ion cells have been considered, however, new developments of new types of cells are being developed. For instance, particular attention shall be paid to the developments of lithium-sulfur [103] and solid-state batteries[104], which can offer overall better performances, increasing capacity and thus reducing weight. In addition to this, companies like Tesla should be paid, as they are developing new highly efficient cylindrical cells (Tesla 4680) [105] that are very close to the state-of-the-art energy density of the current technologies.

14. Structures and Materials

In this chapter, the material selection for the most crucial aircraft components will be performed. Additionally, the wing structure shall be designed taking the limit load factors into account. Lastly, based on the wing design, the load applied on the hing, as well as the folding mechanism, shall be sized. Finally, the landing gear configuration shall be discussed.

14.1. Materials selection

Materials are an essential part of aircraft structural design. It is the different material properties that allow for the sizing of structural components. Different materials are suitable for different parts based on their properties and loads to be carried. Table 14.1 introduces the characteristics of the materials considered in the design of the eVTOL. Density (ρ), Young's Modulus (E), ultimate tensile ($\sigma_{t,ult}$), compressive ($\sigma_{c,ult}$), and shear (τ_{ult}) stresses, as well as the poisson ratio (ν) are indicated.

Table 14.1: Structural materials mechanical properties

	ρ [g/cm ³]	E [GPa]	G [GPa]	$\sigma_{t,ult}$ [MPa]	$\sigma_{c,ult}$ [MPa]	τ_{ult} [MPa]	ν [-]
Al 7040-T7451 [106]	2.82	66	24.5	438	351	303	0.33
CF Fabric [107]	1.60	70	5.0	600	570	90	0.10

Before a structural analysis is performed, materials can already be selected based on the functions to be fulfilled by the different parts, the types of loads expected, and the literature. General structural design criteria useful for material selection - like the one shown by P. Jerome [108] - have thus been revised for the *Swing* and are shown in Figure 14.1.

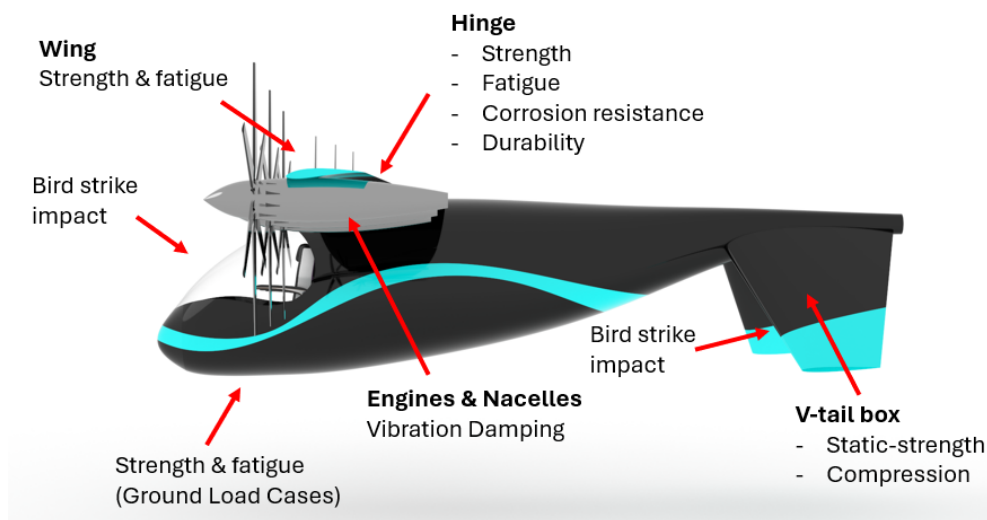


Figure 14.1: Structural design criteria

The use of composites in aircraft has increased drastically in the past decades. Take, for example, the Airbus A380: a lot of new Carbon-Fibre Reinforced Polymer (CFRP) parts have been added and tested, including the main and tail wing box [108]. This demonstrates the ability of these components to withstand more important loads. The use of CFRP comes with incredible weight advantages, leading to 20% to 50% savings [109]. In addition, the availability of bigger autoclaves compared to the past allows for the manufacturing of bigger composite parts, facilitating the assembly process. These types of composites,

however, do come with disadvantages like higher costs and non-visible material damage. Figure 14.2 [108] showcases how manufacturing and material costs of composites compare to metals, with a comprehensive cost of composite parts around 40% higher than that of metals [110]. The higher costs of metal in terms of aircraft manufacturing shown in the figure is due to the higher number of components that need to be assembled due to the limited size of metal parts. More extensive considerations on the cost are made in the cost analysis in Chapter 19. It can be said, however, that the increase in cost remains within the production cost constraints initially established. Last but not least, the sustainability of these materials will be evaluated in Chapter 18.

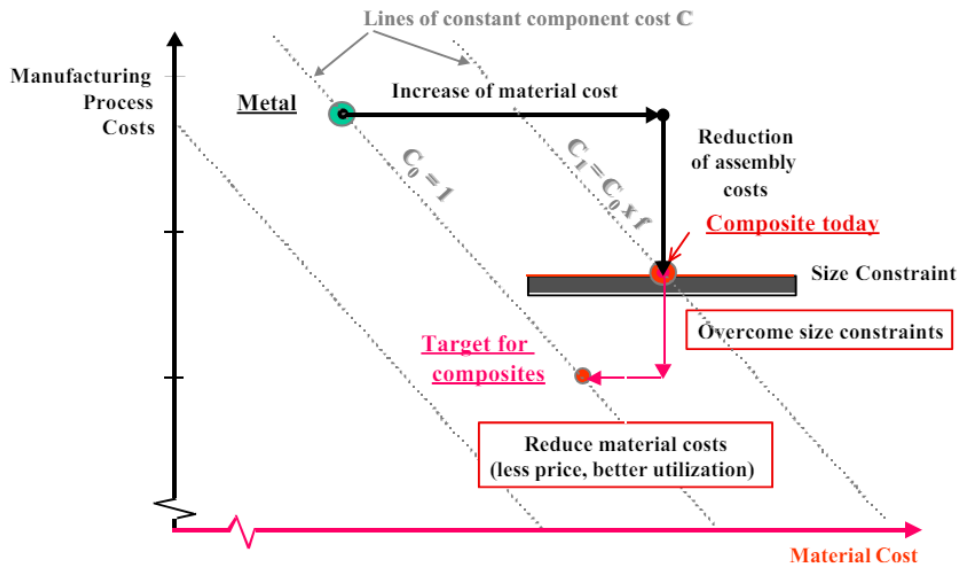


Figure 14.2: Status and targets for cost of composite structures [108].

A preliminary material selection is carried out. This might be revised in later stages in case the structural analysis uncovers deficiencies in the design. CFRP is expected to be used on most of the aircraft structure given its weight advantages. Compared to general aviation aircraft, fatigue loads acting on the fuselage are not considered critical given the absence of fuselage pressurisation. This allows the use of materials like CFRP, for which crack growth is of bigger concern compared to, for instance, aluminium alloys. Taking inspiration from aircraft like the A380, the wing box, as well as the ribs, are constructed with CFRP, with the rest of the internal structure in aluminium. The entirety of the tail, instead, is expected to be manufactured with CFRP.

Fiber Metal Laminates (FMLs) are also considered. In particular, Glass Reinforced laminate (Glare) is preferred over CARALL (carbon-reinforced aluminium laminate) and ARALL (aramid-reinforced aluminium laminate) due to its more widespread use in the aerospace industry as well as its low weight. It is its lightweight properties that make it not suitable for structural elements. It will instead be used for leading edges and the parts of the fuselage most exposed to impact. This is thanks to the excellent tolerance to impact and damage of this composite, as found by Annamalai et al. [111].

Fuselage Soundproofing

In order to meet the 60dBA of requirement CO-3-STK07-2, the fuselage needs to be soundproof enough to be able to cut the near-field noise of 80dBA (at a 7ft distance, Figure 10.4) down to 60dBA (decrease of 20dBA). State-of-the-art soundproofing materials and techniques can ensure reductions in noise levels of up to 55dBA, putting the *Swing* in an ideal spot with respect to a low cabin noise. For instance, covering the inside of the fuselage in a single layer of 1/8 inch Mass-Loaded Vinyl (MLV) already provides a reduction of about 26 dBA. This improvement could, however, be hindered by the presence of a large frontal window, which is likely to be a weak point in soundproofing. Double-glazing windows, consisting of two layers of glass with an air gap in between, would be needed to ensure the 26dBA reduction is kept inside the cabin at

all times. While MLV is a very affordable, easily available OTS material, double glazing windows might turn out to be costly (even in the order of \$10,000 for custom, irregularly-shaped windows); this has to be accounted for in Section 19.1.

14.2. *V-n* Diagram

Using a load diagram, the maximum load factor can be determined. The *V-n* diagram is created based on the method described by Roskam [69]. The load diagram can be found in Figure 14.3; from the load diagram, it can be seen that the manoeuvre speed is higher than the cruise speed. This is because the manoeuvre speed is calculated based on empirical formulas in contrast, the cruise speed is defined based on requirement **Te-2-STK07-3-2**. Additionally, it can be seen that the maximum load factor is caused by the manoeuvre loading.

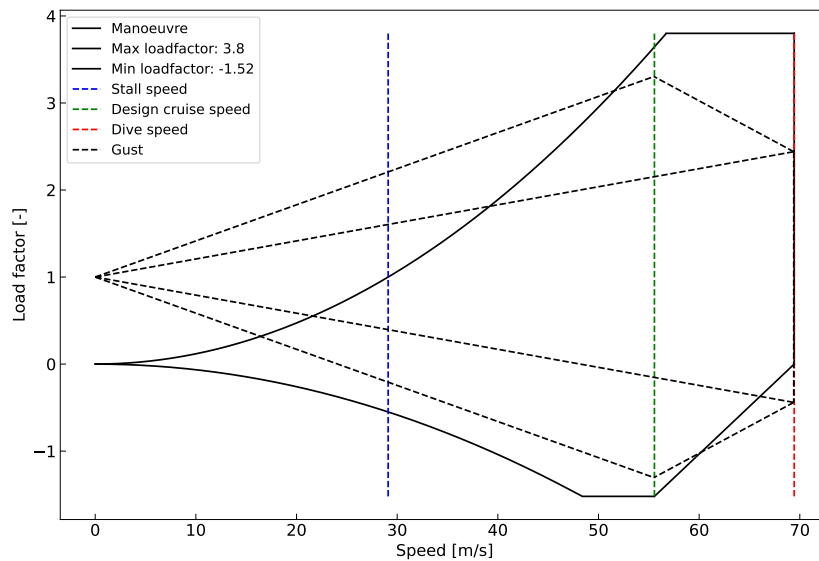


Figure 14.3: Final load diagram

14.3. Wing Structural Design

In order to design the structure of the wing, it is essential to first identify what the critical load cases are. For this scope, both configurations, cruise and take-off, are analysed. Spars, ribs, and skin are then sized accordingly. A separate discussion is then carried out with regard to the hinge design and mechanism.

14.3.1. Load Cases

In order to calculate what each section of the structure needs to be able to withstand, all loads acting on the wing need to be accounted for. These are shown in Figure 14.4 for cruise and take-off configurations. The distributed loads of lift (L) and wing weight (W_{wing}) are assumed to be elliptical and trapezoidal respectively. Point forces are then introduced by the engine weight (W_{eng}) and thrust (T_{eng}). Several considerations need to be made to construct the shear force, bending moment, and torque diagrams. Firstly, the aerodynamic centre and the CG at each section of the wing are assumed to be at 0.25 and 0.4 of the chord length. Secondly, the engine's longitudinal CG is also considered at 25% of the chord. This can be easily reached by slight adjustments in position, nacelles, and component distribution. These displacements of aerodynamic forces and engine weight compared to the CG of the section are the main contributors to the twist of the wing. Thirdly, the battery weights (W_{bat}) are assumed to be equally distributed in the two outer nacelles. The resulting diagrams are shown in Figures 14.5 and 14.6.

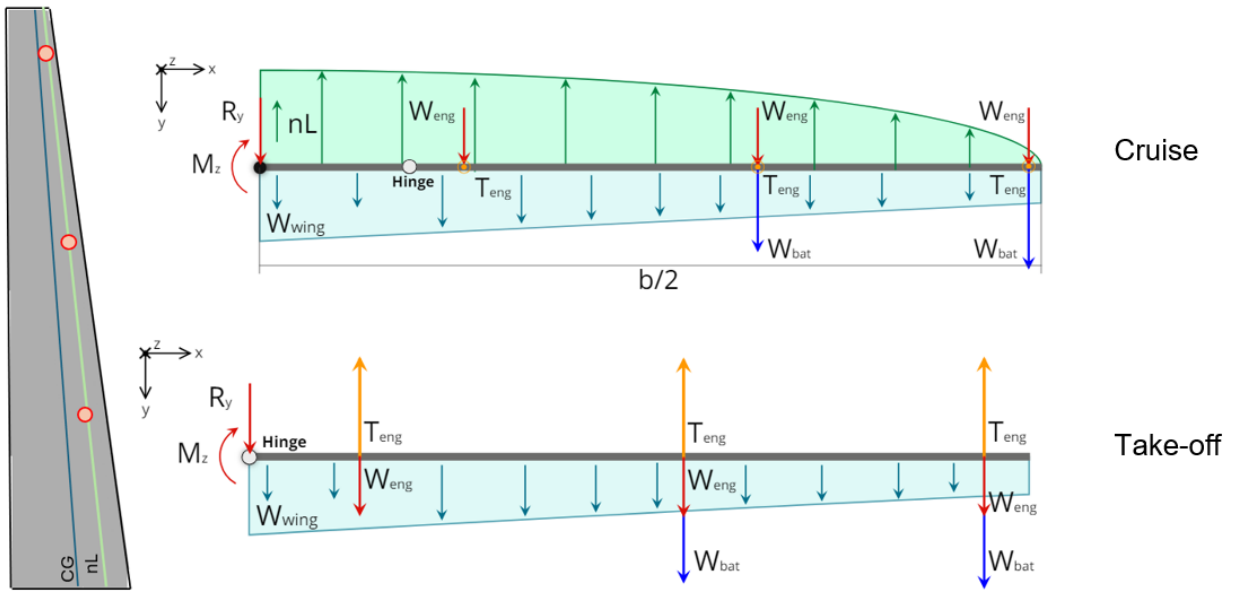


Figure 14.4: All forces and moments acting on the wing in cruise and take-off configurations. The top view (left) shows the location of the resultant aerodynamic forces and the cg of the engines (red dots) with respect to the chord.

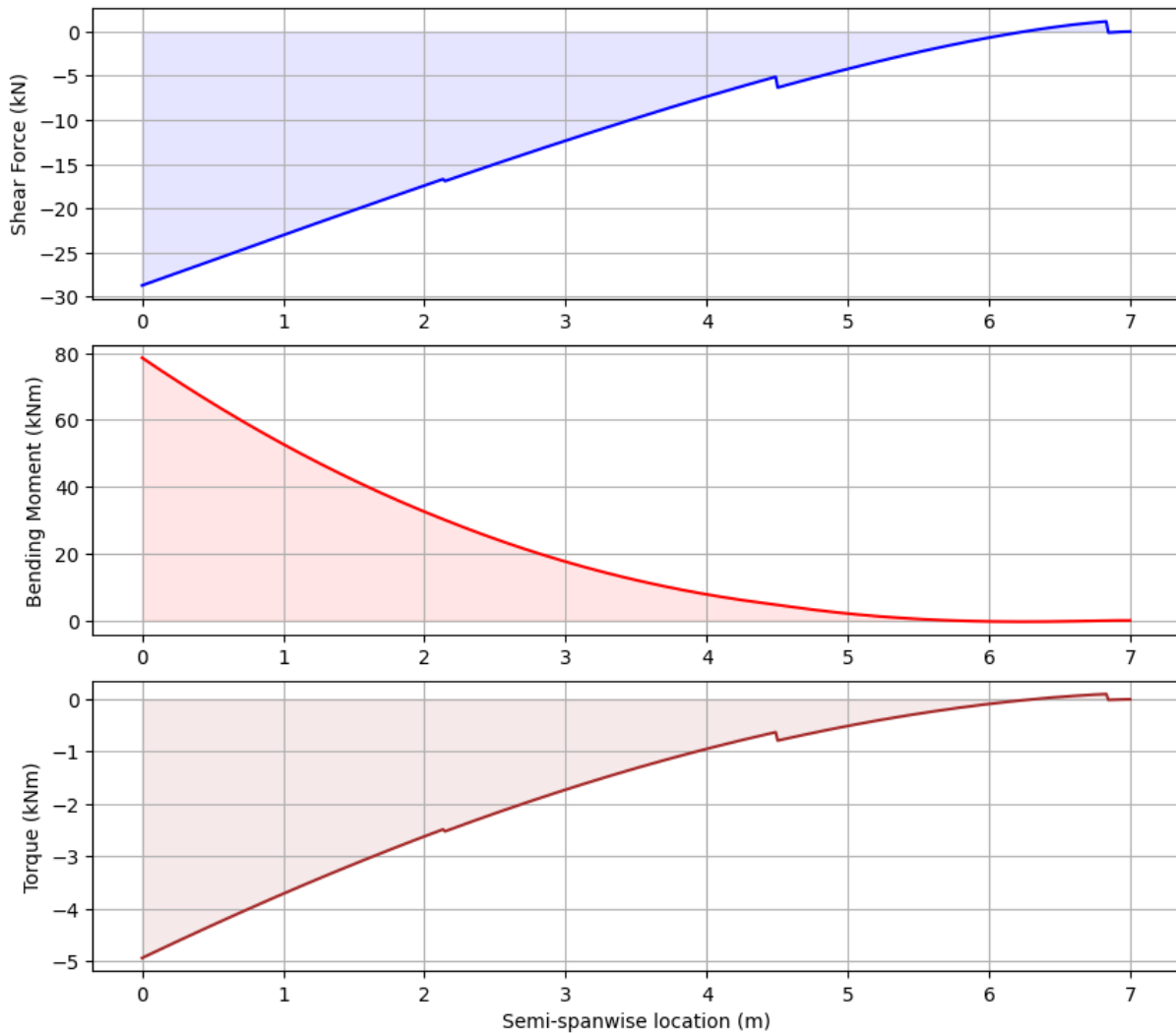


Figure 14.5: Shear force, bending moment, and torque diagrams in cruise, $n = 4.1$

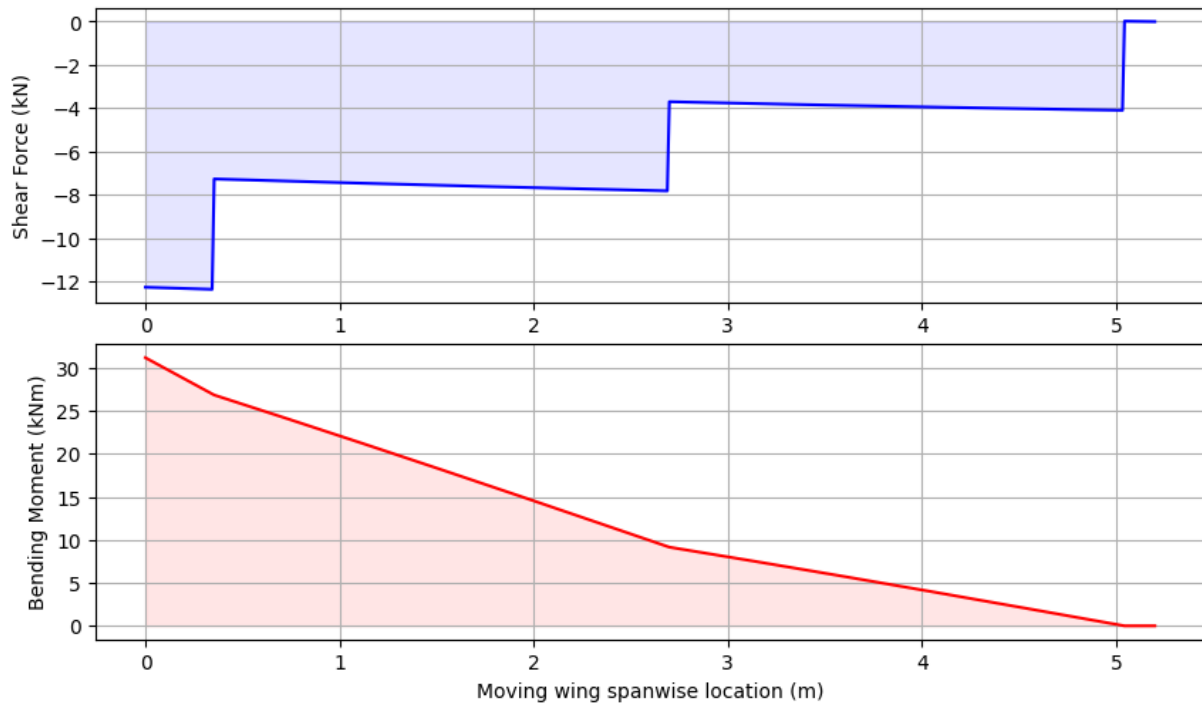


Figure 14.6: Shear force and bending moment diagrams in take-off, $T/W = 2$

It can be noticed how the wing span considered in the two scenarios is different. This is because in Figure 14.6 only the diagram concerning the moving part of the wing is shown. The most critical loads are identified to be as follows:

- 29 kN shear force at the root of the wing during cruise;
- 80 kNm of bending at the root of the wing during cruise;
- 32 kNm of torque on the fixed part of the wing during take-off.

These loads will prevail in the sizing of the central wing box, while a different discussion is carried out with regard to the hinge in Section 14.5. In order to simplify the analysis and sizing of the wing structure, conservative assumptions are made on the carrying capabilities of each component. The bending moments are assumed to be taken by the spars and the stringers. Ribs, instead, introduce local loads into the structure, transfer aerodynamic loads from the skin to the structure, and prevent buckling. A rectangular torsion box is finally analysed to ensure the spars, together with the stiffened skin panels, can withstand the induced torques. It is important to note that the integration of all of these components together is not an easy exercise, and the ribs-stiffeners interactions need particular attention to ensure the load paths are not disturbed. Finally, a safety factor of 1.5 is used for all dimensions to overcome uncertainties in the calculations as well as guarantee safety during most unexpected scenarios.

14.3.2. Wing Spars

Two spars are placed in the wing, each one at the edges of the wingbox and located at 25% and 75% of the chord, respectively. For sizing, however, most bending moments are assumed to be taken by the front spar and the stiffeners. This assumption is conservative and adds to the safety factor already considered. A variable thickness with a linear distribution is considered throughout the span to ensure minimum weight while still allowing for changing loads. A fixed thickness, however, is used in the fixed part of the wing, where the main torsion box is placed. This is done to ensure the robustness of the structure. The spars are made of aluminium 7040-T7451 as selected in Section 14.1, and its mechanical properties, assuming linearly elastic behaviours, apply to the calculations. Furthermore, the interruption of the spars due to the cut in the folding wing is neglected in the analysis. This is because the hinge design and its locking mechanisms are considered able to create load paths that well reproduce those of a standard wing. Last but not least, a

symmetric wingbox is assumed ($I_{xy} = 0$) such that the stresses caused by the bending moments are calculated as follows:

$$\sigma_z = \frac{M_x I_{yy} y + M_y I_{xx} x}{I_{xx} I_{yy}} \quad (14.1)$$

Here, the M 's refer to the bending moments in different directions, the I 's refer to the area moments of inertia, and x and y correspond to the respective coordinates within the cross-section. As the area moments of inertia are greatly dependent on the shape of the cross-section, a standard I-beam spar design is chosen. By taking into consideration both cruise and take-off conditions, the optimal spar design for minimal weight is found.

The spars, however, constitute the side walls of the wingbox, which also take care of counteracting the torque. The shear flow caused by the shear forces (Equation (14.2)) as well as the torques (Equation (14.3)) acting on the wing is thus considered, and their effect is summed up.

$$q_2 - q_1 = -\frac{V_y}{I_{xx}} \int_{s_1}^{s_2} t y \, ds - \frac{V_x}{I_{yy}} \int_{s_1}^{s_2} t x \, ds \quad (14.2)$$

$$t_{\min} = \frac{1}{\tau_{\text{shear,max}}} \frac{T}{2 \cdot A_{\text{enclosed}}} \quad (14.3)$$

In these equations, q indicates shear flow, V refers to the shear forces as calculated previously, and A_{enclosed} is the area enclosed by the cross-section of the wing box. The integrals are computed across the entire perimeter. The spar thickness is thus calculated again and compared to the one needed to withstand the bending moments. The maximum value is chosen and used in the wing. Some reference values are shown in Table 14.2.

14.3.3. Wing Ribs

As explained by Sedaghati et al. [112], the ribs are responsible for three kinds of loads: aerodynamic loads introduced from the skin-stiffeners panel, point loads on the wing, and body forces, like the weight of the wing. Furthermore, while running from the leading to the trailing edge of the wing, the ribs are divided into three sections, in between which spars are accommodated.

For the positioning of the ribs, it is thus chosen to place them where the engines are placed, at the edges of the ailerons, and close to the hinge. Furthermore, as the distance between the ribs may influence the buckling performance of the skin, this is later checked to be sufficient. Following this reasoning, the ribs have been placed at the x locations indicated in Table 14.2, starting from the root. As far as their dimensions are concerned, similar dimensions to the spars placed at different locations are used.

14.3.4. Stiffeners-Reinforced Skin Panel

As the biggest wing deflections are expected in the upward direction during cruise flight, buckling of the upper skin panel is considered critical. The critical stress for buckling of a panel can be calculated using Equation (14.4).

$$\sigma_{cr} = C \frac{\pi^2 E}{12(1 - \nu^2)} \left(\frac{t}{b}\right)^2 \quad (14.4)$$

Where E is the Young's modulus, ν is the Poisson ratio, t the thickness of the plate, and b is the panel span in the load's direction. Finally, C is a function of the aspect ratio and boundary conditions of the plate. Here, a C of 4.0 with the conservative assumption of the skin panel being simply supported on all sides is considered. Taking into account that the skin is supported by stiffeners, their crippling stress needs to be calculated. This is done by slightly modifying Equation (14.4):

$$\frac{\sigma_{cc}}{\sigma_y} = \alpha \left[\frac{C}{\sigma_y} \frac{\pi^2 E}{12(1-\nu^2)} \left(\frac{t}{b}\right)^2 \right]^{1-n} \quad (14.5)$$

where σ_{cc} and σ_y are the crippling and yield stress of the material, $\alpha = 0.8$, and $n = 0.6$. This calculation is applied to each panel forming the stiffener and using appropriate boundary conditions. A weighted average with the areas is then performed to find the crippling stress of the entire stiffening element. By use of Equation (14.6), the influence of the stringer on the panel is calculated, and the buckling stress of the stiffened panel is finally obtained.

$$w_e = \frac{t}{2} \sqrt{\frac{C\pi^2}{12(1-\nu^2)} \frac{E}{(\sigma_{cc})_{\text{stiffener}}}} \quad (14.6)$$

In the case of a reinforced skin panel, the cross-section of the stiffening elements influences the assumptions on the panel boundary conditions, as this can greatly influence the torsional stiffness. For this reason, Hat types are considered for stringers, resulting in a $C = 6.98$ [113]. The value of C , in reality, is also based on the spanwise length of the panel, thus revealing the dependence of the buckling capabilities of the skin on the ribs positioning. The rib spacing is used here, as found in Section 14.3.3 An iterative process to minimise the mass has been adopted.

As it was done for the spars, the skin is subjected to the shear flow due to torque and shear. The same procedure as in Section 14.3.2 is adopted, and the highest value for the skin thickness is chosen. The results obtained are shown in Table 14.2.

14.3.5. Final Wing Structure Parameters

Figure 14.7 shows one section of the wing and the internal wing box structure. The parameters considered for the design are indicated here. Their final values for each of the wing sections are in Table 14.2.

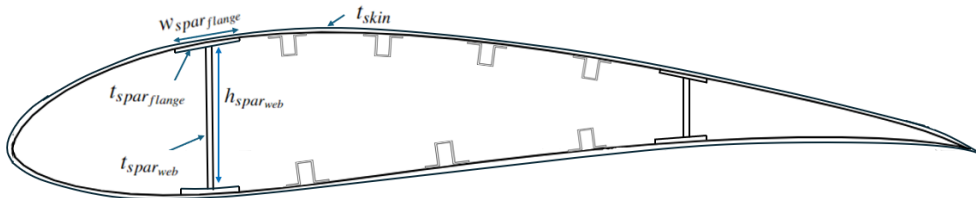


Figure 14.7: Wing section showing the internal wing box structure

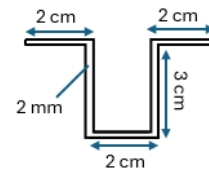


Figure 14.8: Hat stiffeners dimensions

Table 14.2: Transposed wing structure parameters, with x [m] as the distance from the root

x [m]	$h_{\text{spar}_{\text{web}}}$ [mm]	$t_{\text{spar}_{\text{web}}}$ [mm]	$w_{\text{spar}_{\text{flange}}}$ [mm]	$t_{\text{spar}_{\text{flange}}}$ [mm]	t_{skin} [mm]	$N_{\text{stringers}_{\text{top}}}$ [-]	$N_{\text{stringers}_{\text{bottom}}}$ [-]
0.00	227	1.50	50	2.8	1.5	4	3
0.85	211	1.50	50	2.8	1.5	4	3
1.80	192	1.34	50	2.5	1.0	4	3
2.15	185	1.31	50	2.5	1.0	4	2
4.50	140	1.11	50	2.5	1.0	3	2
6.84	94	0.91	50	2.5	1.0	2	1

Inspection of Table 14.2 can help get a better overview of what the final wing structure design looks like. It is important to highlight how the number of stringers for each wing section was chosen based on meeting buckling and bending moment requirements. Buckling was, in fact, found to be critical in the fixed part of the wing, while bending required a higher number of stiffeners in the outer part. Furthermore, the different numbers of stringers on the top and bottom skin are due to the lower absolute value in the minimum load factor.

14.4. Aeroelastic Analysis

To achieve aeroelastic certification in accordance with CS23 requirements, the aircraft must exhibit no signs of aeroelastic effects across airspeeds ranging from 0 to $1.15V_D$ at all operational altitudes [114]. Several aeroelastic effects need to be evaluated, including wing divergence, control reversal, and flutter. While a comprehensive aeroelastic analysis is recommended for the future, the current focus is solely on wing divergence.

Wing divergence is a critical aeroelastic phenomenon where the aerodynamic forces acting on a wing structure become sufficiently strong to cause static instability. This leads to a dramatic and often catastrophic deformation of the wing. Understanding and predicting the divergence speed at which this instability occurs is essential for the safe design of aircraft wings. The divergence boundary represents the critical dynamic pressure threshold that distinguishes between conditions where an aircraft experiences divergence and where it does not. This boundary is called such because the airspeed corresponding to this dynamic pressure changes with altitude. As a result, when the divergence speed is plotted against altitude, a boundary curve is formed. Beyond this speed, the twist angle of the wing increases without bound in response to a perturbation. Equation (14.7) is used to calculate the divergence dynamic pressure. A detailed derivation can be found in the “AE4ASM506 Fundamentals of Aeroelasticity” lecture notes.

$$q_{\text{div}} = \frac{K_{\theta}}{C_{L_{\alpha}} e S} \quad (14.7)$$

In Equation (14.7) q_{div} represents the divergence boundary in $[\text{N/m}^2]$, K_{θ} the torsional stiffness of the section in $[\text{Nm/rad}]$, $C_{L_{\alpha}}$ the lift curve slope of the airfoil in $[1/\text{rad}]$, S the wing surface area per unit span of the total aircraft in $[\text{m}^2]$, and e the distance between the aerodynamic centre and the elasticity axis $[\text{m}]$. The latter is considered to be at the centre of the wingbox as a consequence of its previously assumed symmetry. The section at the MAC is taken into consideration for the analysis. It is thus assumed that this section of the aircraft wing exhibits a similar aeroelastic response to that of the full 3D wing. When this section is aeroelastically stable, the full 3D wing will be also stable. Assuming that the elasticity axis is located at the centre of the wingbox, and with a calculated K_{θ} of 144.9 kNm/rad , Equation (14.7) yields a $q_{\text{div}} = 91.6 \text{ kN/m}^2$, corresponding to a sea level speed of 1392.5 km/h . A wing divergence speed of 1400 km/h is quite high and would typically be associated with high-performance aircraft, such as military jets or high-speed experimental aircraft. This high divergence speed indicates a very stiff and strong wing structure, capable of withstanding significant aerodynamic forces without experiencing divergence.

14.5. Hinge & Folding Mechanism Design

The finished detailed wing structure design allows the sizing of the hinge and folding mechanism enabling the ground footprint of the UAM. In the following section, the steps taken to realise the design of this subsystem are presented. Firstly, the design of the degrees of freedom is performed by building a kinematic simulation. Subsequently, the hinge is sized for the identified maximum load case. Ultimately, the actuation system is selected which can counteract the torques during the transition.

14.5.1. Hinge Axis of Rotation

The design of the hinge, facilitating the transition of the vehicle, starts with the appropriate selection of the degrees of freedom and rotational axes. From previous aircraft designs, it was found that such wing transformations can be done about only one rotational axis [115]. Thus, it is opted to select a joint design with only one rotational degree of freedom, since this decision decreases the complexity of the design and consequently increases the safety of the vehicle operations.

To aid the selection of the rotational axis, it was parameterised with the angles α and β as depicted on Figure 14.9. Furthermore, the unit vector \mathbf{n} parallel to this axis is given by Equation (14.8). Finally, the rotation matrix about a unit vector n by a rotation angle q is given by Equation (14.8), where the skew-symmetric matrix, n_{\times} , is constructed from the vector n . Utilizing this equation, the full range of rotational motion can be simulated for a given rotational axis. To facilitate a better understanding of this one degree

of freedom motion, a visual kinematic simulation of the motion was developed in Python. Two frames of this simulation can be seen in Figures 14.9 and 14.10. This tool could then be used to select the optimal values of the parameters. It is desired that the wing is horizontal and almost vertical, with a slight tilt towards the outside, in the body frame at the start and the end of the transition respectively. Thus, after running the simulations for different parameters, it was found that an α -value of 45° , a β -value of 40° and a rotation angle range of $q \in [0^\circ; 110^\circ]$ results in a satisfactory range of motion.

$$\mathbf{C}_n(q) = \cos(q)\mathbf{I}_{3 \times 3} + \sin(q)\mathbf{n}_\times + (1 - \cos(q))\mathbf{nn}^T \quad \mathbf{n} = \frac{[\cos(\alpha) \quad \sin(\alpha) \quad \sin(\beta)]^T}{\sqrt{\cos(\alpha)^2 + \sin(\alpha)^2 + \sin(\beta)^2}} \quad (14.8)$$

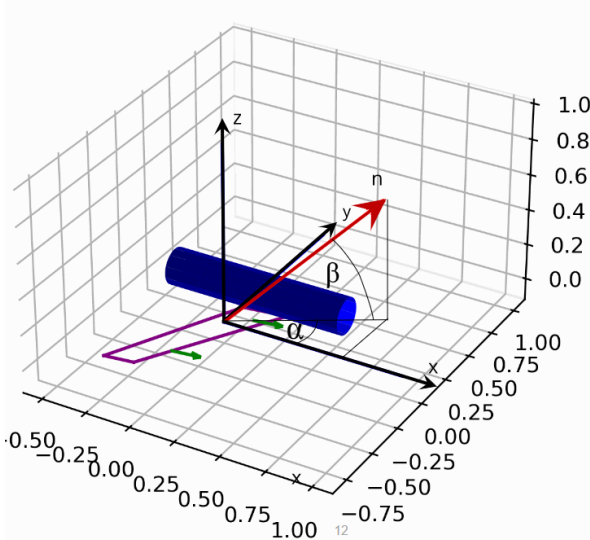


Figure 14.9: Snapshot of the kinematic wing rotation simulation, midway through transition

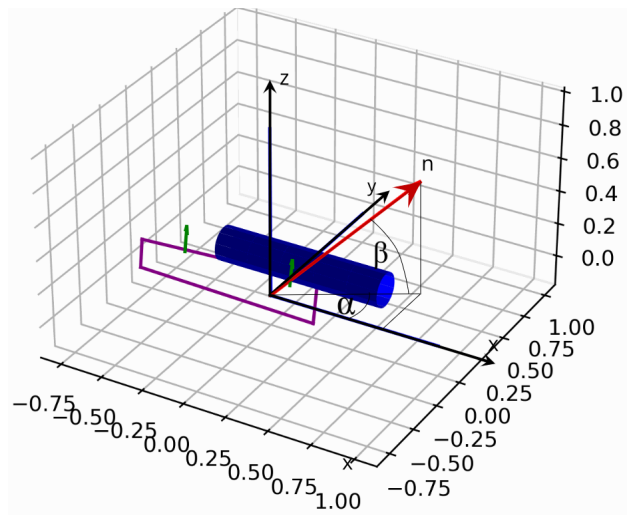


Figure 14.10: Snapshot of the kinematic wing rotation simulation, hexacopter configuration

14.5.2. Hinge Sizing

As the hinge allowing the transition between take-off and cruise configuration is considered critical for the design, a thorough analysis of the loads that this needs to withstand is performed and the hinge is sized accordingly. The axis of rotation identified in Section 14.5.1 is used to choose the type of hinge. For ease of certification, as well as a reduction in design and production costs, it is opted for the adaptation of a pre-existing hinge mechanism. In particular, the STO Wing folding mechanism used by the Grumman F4F-4 Wildcat was found to be of particular interest (Figure 14.11).



Figure 14.11: Grumman F4F-4 Wildcat STO wing folding mechanism

For the structural analysis, the hinge is modelled as a rod-lug mechanism with the rod in the direction of the axis of rotation. Loads at the hinge location are taken from Section 14.3.1 and a coordinate system

transformation is performed as shown in Figure 14.12 in order to decompose the forces and moments in the rod-lug directions. The stresses are then considered. Stainless steel, Al 7075-T6 and titanium were used for the analysis. Taking into account cost factors and weight, titanium was chosen as the hinge material with a density of 4500 kg/m^3 and a tensile ultimate strength of 220 MPa.

Table 14.3 shows the results obtained in terms of forces and moments. Although the moments in the z - and y -directions are perpendicular, meaning the maximum normal stresses they cause in the rod do not sum up, they are here superimposed and used in Equation (14.1). This is a rather conservative assumption and counts as a safety factor. Normal stresses caused by normal forces are also accounted for ($\sigma = N/A$). Performing these calculations for the rod yields a minimum radius of 7.8 cm. This, together with a length of 25 cm based on the height of the wing and inclination of the hinge, yields an estimated mass of the hinge of 21.5 kg.

As Kothia et al. [116] have performed an adaptation of the same joint to a Boeing 787 with a comprehensive study of sizing via Finite Element Method (FEM) analysis and their results are used for validation. A linear scaling of the weight of the aircraft leads to a hinge weight of $\approx 18 \text{ kg}$ each. This is not too far off the 21.5kg calculated, which did indeed take several conservative assumptions into account.

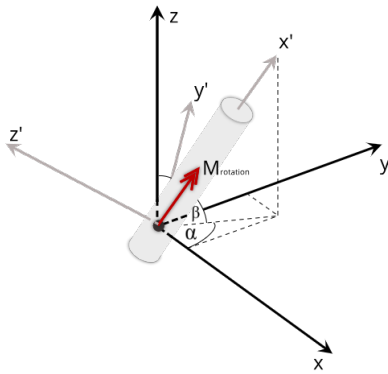


Table 14.3: Maximum loads experienced by the hinge. Note that all occur during cruise with $n = 4.1$

Load Type	Magnitude
Normal force (x)	18.4 kN
Moment in y	43.4 kNm
Moment in z	-36.5 kNm

Figure 14.12: Coordinate transformation to decompose forces in the direction of the hinge.

In the previous calculations, the entirety of the loads were assumed to act on the hinge itself. However, locking mechanisms and load-carrying structures are to be placed at the cut of the wing. Specifically, locking arms are expected to extend out from the moving wing to its fixed part, connecting the two and also preventing discontinuities in the wing twist caused by aerodynamic forces. These ensure a more homogeneous transfer of the loads between the two parts of the wing, as well as help relieve the loads on the hinge.

14.5.3. Actuator Choice & Power

Once the hinge has been designed, its actuator system needs to be implemented. The power used for the folding and unfolding of the wing is first estimated by looking at the moments acting in the direction of the axis of rotation, as decomposed in Figure 14.12. Assuming transition can be initiated during cruise conditions (with $n = 1$) or during take-off, the latter was found to be constrained in terms of power required, with a moment of $\approx 15 \text{ kNm}$ to be provided to the hinge. The power is then estimated assuming a constant angular velocity around the axis during transition. With a rotation of 110° needed and 63 seconds used to transition (see Section 6.2.3), this comes down to an angular speed of $\omega = 0.0305 \text{ rad/s}$. The power required is finally estimated with $P_r = \omega \cdot M_{\text{rotation}} = 458 \text{ W}$. This value is added to the power budget computed in Chapter 15. Note, however, that especially during the unfolding of the wing, the thrust of the engines is expected to reduce the power needed from the actuator.

Linear actuators which would pull and push the trailing edge of the wing were considered. However, it is ultimately opted for actuators located within the wing structure. Having the booms of the actuator running between the wing and fuselage on the outside of the aircraft was, in fact, found not to be ideal in terms of aerodynamics and reliability. Two main types are thus considered:

- **Rotary gears** (Figure 14.13): a motor can be disposed within the rotating wing portion to rotate a drive gear that can be meshed with a stationary gear rack placed on the fixed wing portion. This would result in the drive gear travelling around the circumference of the other rack.
- **Opposed linear actuators** (Figure 14.14): these can be hydraulic, electric, or pneumatic linear actuators and would allow the rotation of the joint by extension of the arms.

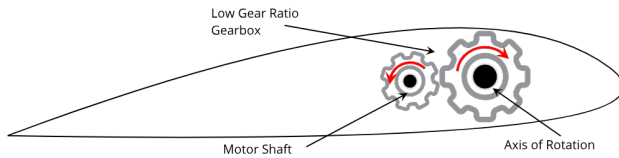


Figure 14.13: Rotary gears schematics.

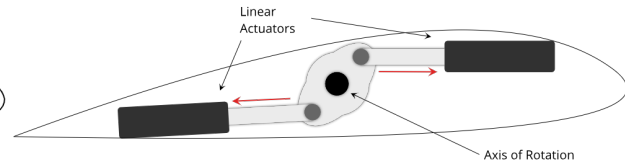


Figure 14.14: Linear actuators schematics.

For rotary gear actuators, a low-ratio gearbox with a high-torque motor would be needed to counteract the moments experienced by the wing during transition. Such actuators are relatively large, thus, the integration of it into a slender wing would be challenging. Furthermore, high power is required to operate the high-torque motor. Hence, the application of such an actuator is not favourable.

Ultimately, it was thus chosen to use the linear actuators shown in Figure 14.14. The little arm between the actuators and the axis of rotation would allow for smaller forces to be applied. Furthermore, failure of one of the actuators would not hinder the folding capabilities of the wing, with each of the actuators designed to provide enough torque alone, despite resulting in a smaller angular velocity. Figure 14.15 shows the positioning of the actuators in the wing as presented by Pterodynamics [117]. The entire wing structure is modified around the cut to accommodate the presence of the actuator and to allow proper redistribution of forces and moments.

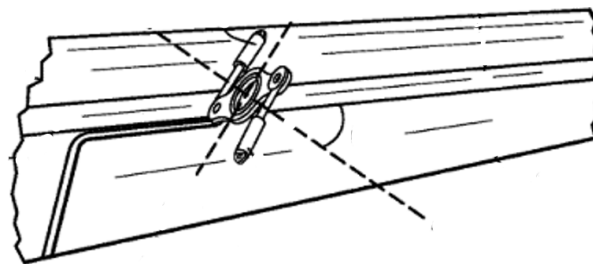


Figure 14.15: Integration of the linear actuator in the wing structure. The dashed line indicates the top view projection of the axis of rotation and its perpendicular [117]

Amongst the different kinds of linear actuators, a choice has to be made. Electric actuators are chosen based on their excellent precision and control, with the ability to achieve precise positioning. Furthermore, they can easily be integrated with the computer control systems and automation setups. High efficiency with minimal energy losses is also guaranteed. Hydraulic actuators are excluded due to their higher weight (water is present), their complexity, and the need for regular maintenance. Pneumatic actuators, instead, can lead to less precise control and positioning due to air compressibility.

14.6. Undercarriage Design

There are different configurations for the design of the landing gear for an eVTOL. There are two main options. The first option is to use a non-retractable landing gear, skid or wheels, however, this will induce a lot of drag during flight and increase the c_{d0} which is unwanted. The other option is to use retractable landing gear, which will come at the cost of extra power and space needed in the fuselage. An efficient solution for this is to use a small nosewheel, similar to Lilium Jet (7-seater) [118] and have the other main landing gears inside the downward V-tail. The nosewheel is covered by a cover to minimise the drag induced. This is similar to a tricycle landing gear with the difference that the distance between the main landing gear

and CG will be relatively high.

The tricycle landing gear has a single nosewheel and two main landing wheels. However, stability has to be accounted for in the configuration since the aircraft can tip over. The longitudinal location of the CG is set at 3.68 m. The nosewheel must be located in front of this, and the main landing wheels must be located behind, which will be the case since they are in the tail. Moreover, it is not allowed to place rigid structural components underneath the passengers due to safety reasons. Therefore, the location of the nosewheel should be in front of the front seat [45] at a location of 1.5 m from the nose. The main landing gears will be located in the empennage and the distance l_m will be 3.5 m.

The y -location of the main landing gear is dependent on the tip-over angle, ψ , the distance between the nose and the main landing gear and the longitudinal centre-of-gravity, l_n and l_m , and the vertical centre-of-gravity location, z which is 1.15 m from the ground, as seen in Chapter 11. The final equation can be seen in Equation (14.9).

$$Y_{MLG} > \frac{l_n + l_m}{\sqrt{\frac{l_n^2 \tan^2 \psi}{z^2} - 1}} \quad (14.9)$$

Equation (14.9) states that the y -location should be greater than 2.419. This is to ensure that the vehicle does not tip over with the assumption that the tip-over angle should be lower than 55° [32]. The horizontal span of the V-tail is 3.9 m, so in the case of $Y_{MLG} = 3.9$ the vehicle is stable.

The height of the landing gear has to be minimised to adhere to the vertical height requirement of two meters. The landing gear consists of an absorber or damper which absorbs most of the energy during a hard landing. The absorber stroke length, s , is set to 0.2 m [32]. The final values are put in Table 14.4.

Table 14.4: Undercarriage sizing

ψ	55	degrees
l_n	2.0	m
l_m	3.5	m
Y_{MLG}	2.42	m
z	1.15	m
s	0.2	m

14.7. Verification & Validation

Verification and validation procedures are essential to ensure the accuracy of structural calculations in the code. To achieve this, the following steps are taken:

- Repeated testing with known results: the code has undergone extensive testing by performing smaller exercises with known outcomes across different functions.
- Optimization procedure verification: the optimisation process was rigorously checked by adjusting and varying each optimisation parameter individually. This controlled variation ensured that the optimisation parameters function correctly and sensibly within the intended range.
- Assumption verification: the equations used in the calculations often rely on certain underlying assumptions. Each of these assumptions is thoroughly checked to confirm their validity in the given context, ensuring that the equations are applicable and accurate for the specific scenario.
- Critical evaluation of results: the results were critically examined to ensure they are realistic and consistent with expected physical behaviour. This step helped identify any discrepancies or anomalies that could indicate errors in the calculations or underlying assumptions.

By implementing these steps, the code's robustness and the reliability of the structural calculations it performs is ensured.

15. Resource Allocation and Budget Breakdown

Due to the novelty of the UAM eVTOL market, it sustains a highly competitive nature, where companies share little to no data on their vehicles. Therefore, it is hard to predict and analyse a breakdown of the conceptual design stage’s mass, cost and power. Moreover, there were no requirements on the power and mass budget, only on costs, which created some freedom in the mass and power budget to create the optimum design. Although the cost budget was set at 2000 k€.

Mass Budget

The preliminary mass of the vehicle is 1643 kg, subdivided into the subsystem masses, which can be seen in Table 15.1. This mass is based on a class II tool used to calculate and iterate the mass, which, in the end, always converges to a certain value. Therefore, the mass of the propellers or the fuselage were computed based on literature, using sizing methods such as Roskam[69].

Additionally, some values, like the payload and motor masses, are fixed based on requirements or the final chosen design configuration. For example, the mass of one Emrax 228 motor is known to be 13.5 kilograms as shown in Table 10.3. Therefore, the total motor mass is 81 kg since there are six motors. The class II tool resulted in the following accurate budget after the detailed design phase. However, no margins are applied, and some values still need to be adjusted. For instance, the hinge mass needs to be updated since the initial mass of 20 kg is an estimate. No constraint was set on the MTOW, hence contingency was not considered.

Table 15.1: Mass budget of the *Swing eVTOL*

Subsystem	Mass [kg]	[%]	Subsystem	Mass [kg]	[%]
Payload	400	24	Furnishings	50.3	3
Battery	400	24	Tail	26.5	2
Wing	329	21	Hinge	20	1
Fuselage	213	13	Landing gear	11.3	1
Motors	81	5	Oxygen system	8.4	1
Propellers	84	5			
Total	1624				

Power Budget

The power budget of the vehicle is important for battery sizing, as it gives an overview of the required power for the different subsystem elements that use power. The vehicle has electric propulsion, so the power budget is mainly influenced by this subsystem since the required power is significantly higher than any other subsystem. Therefore, this is omitted from the final table. The total maximum power for the vertical take-off is 340 kW; during cruise, the average power level will be 50 kW, as explained in Section 6.2. The power usages for other subsystems are based on Pranoto, Wirawan and Purnamasari [119], which estimates the power values for UAV with a MTOW smaller than 2700 kg. The estimation for total power needed for air conditioning inside the vehicle is estimated to be less than 3 kW, as analysed by Farrington and Rugh [120]. The final power budget can be seen in Table 15.2.

Cost Budget

A production cost analysis is performed in Chapter 19, in which the DAPCA-IV method is used to estimate the fixed and variable costs for aircraft production. These production costs are estimated for a production rate of 200 aircraft per five years. The requirement CO-1-STK05-1 stated that the total production cost must

Table 15.2: Power budget of the *Swing eVTOL*

Element	Required Power [W]	[%]
Avionics	252	6
Lighting	117	3
Air-conditioning	3000	75
Autopilot	151	4
Hinge	458	12
Total	3978	

be less than 2000 k€, which means that there is a surplus of almost 600 k€. This is only 30% of the budget, which can be seen in Table 15.3. It is important to note that there might still be extra costs due to inflation or underestimation of the costs, due to the novelty of the design. Contingency must be added; however, due to the surplus of 30%, this will not induce problems.

Table 15.3: Cost budget for N = 200 aircraft

Variable Costs [k\$/Unit]			Variable Costs [k\$/Unit]		
Manufacturing	\$568.6	37%	Power Plant	\$ 27.9	2%
Quality Control	\$103.5	7%	Propeller blades	\$157.4	10%
Raw Materials	\$ 44.7	3%	Battery	\$ 13.2	1%
Avionics	\$159.9	10%	Hinge	\$100.0	7%
Product Liability	\$254.6	17%	Power Management System	\$ 97.9	6%
Production Costs			Production Costs		
1.53 million \$			1.42 million €		

16. Interfaces

The interfaces act as the main vessel for keeping track of all connections throughout the *Swing*; hence, they should be correctly followed. Section 16.1 further elaborates upon the interfaces of all the (sub)systems of the eVTOL, which helps the understanding of all parameter correlations. Subsequently, the hardware diagram in Section 16.2 provides the extensive interface picture from within the vehicle, broadening the scope further than only the autonomous system. This will be further strengthened by the Data Handling Diagram in Section 16.3, completing the interface perspective.

16.1. N2 Chart

The N2 chart can be seen as the main tool for understanding the relations between interfaces of all relevant (sub)systems. The green boxes in Section 16.1 represent the main subsystems of the *Swing eVTOL*. Each is connected to its distinctive in- and outputs, following a clockwise motion. For instance, when looking at Aerodynamics and Flight Performance, the inputs for Flight Performance are aerodynamic coefficients and wing planform. It will then output the cruise and stall speed, climb rate, climb angle, and flight envelope. In return, these will act as inputs for the Aerodynamics system, which will then deliver new values for the aerodynamic coefficients and wing planform. Therefore, the N2 Chart showcased in Section 16.1 provides a clear overview of all in- and outputs between (sub)systems.

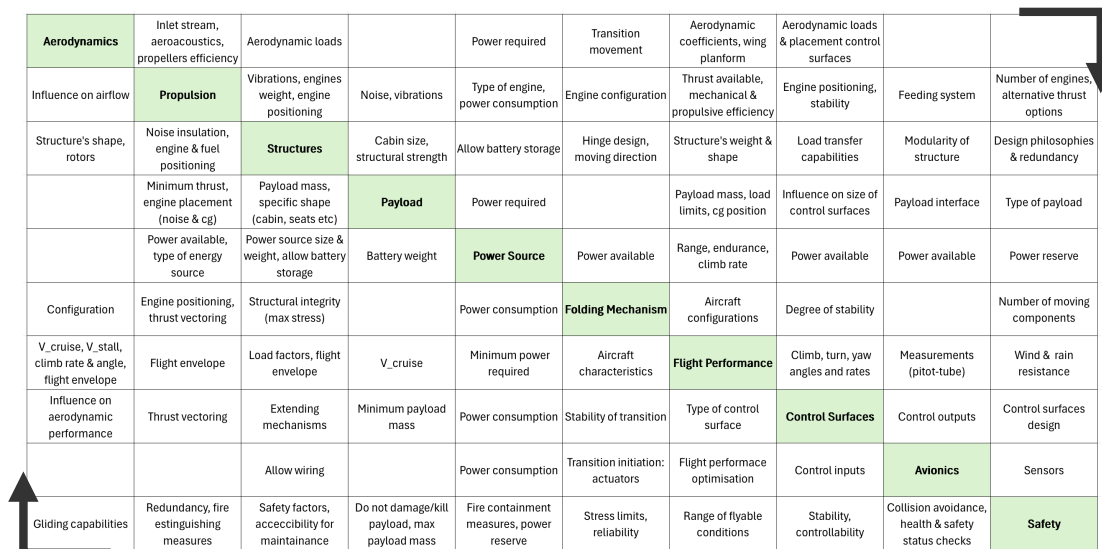


Figure 16.1: N2 chart of (sub)systems

16.2. Hardware Diagram

To clearly visualise the hardware components of the *Swing eVTOL*, Figure 16.2 accompanied by an acronym list in Table 16.1 fully show it. The main hardware components or groups are distinguished by white boxes, the actuation and sensoring groups, given their diversity in composing parts, are instead grouped into the red and yellow frames respectively. The sections of the diagram relative to the ground segment can be deduced by their parallelogram shapes.

Table 16.1: List of acronyms with reference to Figure 16.2

FCC	Flight Control Computer	GNSS	Global Navigation Satellite System
VMS	Vehicle Monitoring Sensors	IMU	Inertial Measurement Unit
BMS	Battery Management System	PDU	Power Distribution Unit

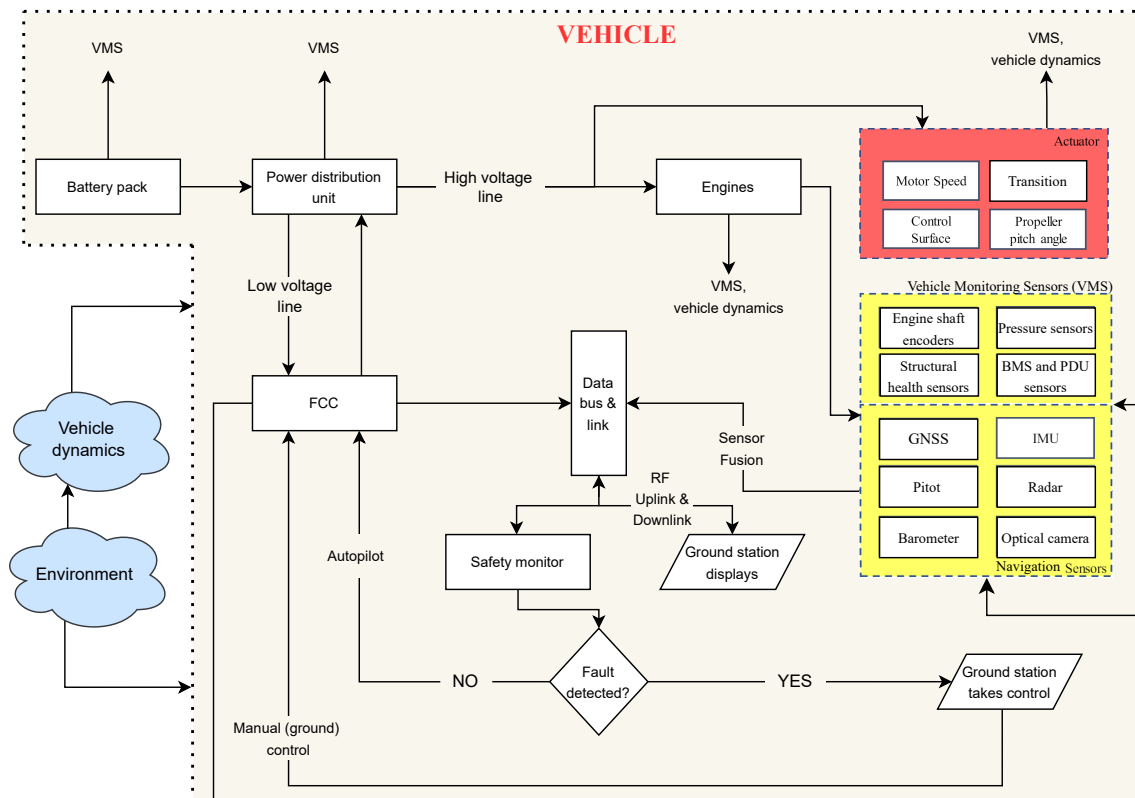


Figure 16.2: H/W diagram

16.2.1. Diagram Flow Discussion

The PDU manages the battery energy, which appropriately distributes it to the components of interest. It follows orders from the FCC, which is the “brain” of the vehicle, where the main navigation, control and vehicle-handling software is located and executed. The orders outputted are based on the current power requirements and vehicle state. Two power lines can be distinguished coming from the PDU due to the substantially different power (power = voltage × current) requirements: high- and low-voltage lines. The high-voltage line powers the actuators and engines according to the thrust and attitude settings dictated by the FCC. Whereas the low-voltage line is connected directly to the FCC, which distributes the energy to all the low-power components in the vehicle, such as sensors.

The state of the aircraft is constantly monitored by a set of sensors measuring the state of the vehicle, speed, and attitude. The actuators change the aircraft’s state and configuration in hover or cruise. Sensor data is processed via sensor fusion algorithms before being fed to the FCC for analysis. A safety monitoring board is connected to the data bus, and if a critical functional flaw is detected, action is taken. It is finally important to underline the iterative nature of this diagram: in every cycle the vehicle responds to the environment and its dynamics via the actuators, which in turn leads to a change in vehicle dynamics, thus yielding a new set of commands. This is represented by those arrows ending on and coming from the dotted line, figuratively representing the vehicle update cycle iteration.

16.2.2. Sensors

A list of the sensors used is provided below, along with a rationale for each component (the unit numbers will be established in later design phases):

- **Engine shaft encoders:** allowing for real-time determination of the RPMs per engine and accurate thrust adjustments.
- **Pressure sensors:** allowing to measure and monitor, for instance, hydraulic pressures, pressure

differential across the cabin, etc.

- **Structural health sensors:** group of sensors delegated to perform damage detection, event and monitoring (i.e. Mechanical Impact Diagnosis using passive piezoelectric sensors, impact damage diagnosis) [121].
- **BMS and PDU sensors:** allowing for constant monitoring of battery and power lines health.
- **GNSS:** “providing positioning, navigation, and timing using navigational satellites from other networks beyond the GPS system” [122]
- **IMU:** determines the specific angular rate, body orientation and force acting on it, using a combination of accelerometers, gyroscopes and magnetometers.
- **Pitot tube:** enables computation of the vehicle’s speed.
- **Radar:** allows for automated collision avoidance procedures.
- **Barometer:** allows for the vehicle’s altitude computation.
- **Optical camera:** can transmit real-time footage back to the ground and allow for the implementation of computer vision algorithms.

16.2.3. Actuators

A list of the main actuators used is provided below, along with a rationale for each component (the unit numbers will be established in later design phases):

- Control of **motor speed** and **control surfaces deflection angles** directly influences the vehicle’s state, adapting it to its current settings.
- Actuation of **transition** mechanisms regulates the configuration change.
- Adjusting the **RPM** of the propellers mainly allows one to optimise the aircraft settings based on its current configuration.

16.3. Data Handling Diagram

Finally, the data handling flow diagram shows the communication and data management within the UAM’s hardware. Three external data sources are present in the process. Data is collected through telecommunication from ground control and other vehicles, as well as measurements of the digital and analogue sensors. After analogue filtering and converting, the necessary signals are converted to digital signals, and two possibilities arise. The data can either flow directly to the Central Processing Unit (CPU), through the serial bus or be fed to a microcontroller. If the second option is used, one directional communication can be achieved, and the CPU can also send data to the sensor, adding the possibility of measurement range and offset adjustments. The bus further ensures the communication link with the actuator controllers. Finally, the transmitter antenna closes the communication loop with the ground control. The described data handling diagram is shown in Figure 16.3

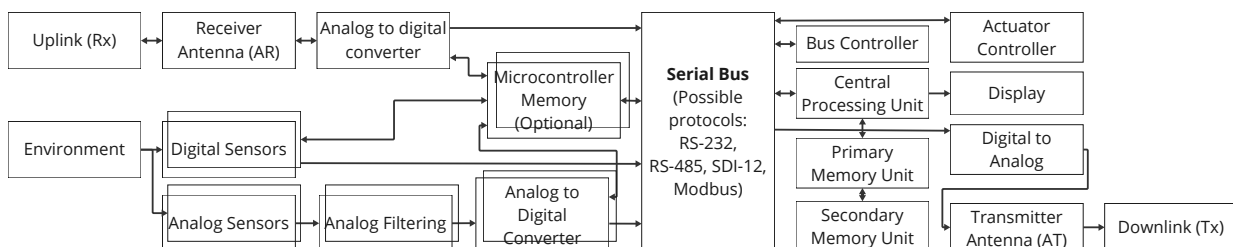


Figure 16.3: Data handling flow diagram

17. Operations and Logistics

The logistics and operations involved in designing and managing an autonomous eVTOL fleet are extensive. Monitoring the vehicles, their environments, such as Air Traffic Control (ATC) and vertiports operations, requires Remote Operations Centres (ROCs). These ROCs will stay crucial to monitor fleet operations, address emergencies, and, most importantly, ensure safety. This chapter analyses the vertiports operations and logistics in Section 17.1, and conducts a Reliability, Availability, Maintainability and Safety (RAMS) analysis in Section 17.2.

17.1. Vertiports

Due to the versatility of the *Swing* design, many different vertiport configurations are possible. As earlier stated in the Market Analysis (Chapter 2), there are three main vertiport configurations: vertistops, vertihubs, and vertibases. All three are different in size, services, and placement; however, there are even more possible configurations, as can be seen from Figures 17.1 and 17.2. These differences account for specific operations and logistics, which would be too extensive for the scope of this report; hence, the following paragraph will discuss the three typical configurations split up into flight scheduling, pre-flight, take-off, in-flight, approach and landing, and post-flight [123].

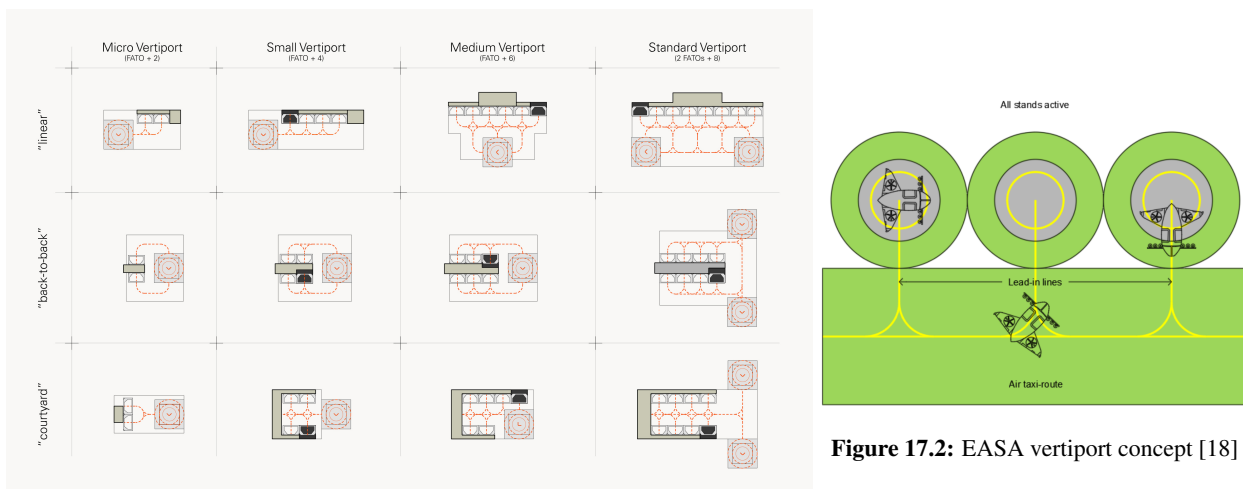


Figure 17.1: Lilium vertiport sizing [23]

Flight Scheduling

The flight scheduling starts when the ROC receives demand forecasts for flights between vertiports. The operator sets the mission up and checks with ATC and the vertiport for a time slot and gate occupancy. The operator submits the mission intent to the vertiport and initially reserves FATO and gate access. Moreover, it will send the ATC the flight plan for verification and ask the Third-party Service Provider (TSP) to reserve a necessary spectrum for the data links.

Pre-Flight

Before the vehicle can take off, several operations have to be performed. The ROC will update the mission with the latest weather forecast to create a high-fidelity mission intent and send it to the ATC. When the ATC has confirmed and officially approved the flight plan, the vertiport will confirm FATO and gates, and the TSP will confirm the spectrum reservation. Afterwards, the preflight checks and the turnaround operations can start.

The turnaround operations consist of loading and unloading of the payload, and charging of the batteries. First, the batteries must be charged, which will only be done at the vertihubs and vertibases. Vertistops ought

to be seen as the quickest stop that is only there to accommodate the last-mile transport, which is highly suitable for the *Swing* with its low ground footprint. The charger station uses a charging power of 240 kW, thus the total charging time is 25 minutes (Chapter 13). During the charging, the passengers can board the eVTOL from the side. Passengers can enter via the door placed in front of the wing. Due to the high wing configuration and the transformative wing, there is enough space for the passengers to enter. A sliding seat provides access to the rear seats, as explained in Section 7.4.

After boarding and charging and vehicle system checks are complete, ground personnel can give clearance to start the towing to the take-off area.

Take-Off

The vertiport manager will provide authorisation for the towing to the FATO. If the vehicle is located at a vertistop, moving it will not be necessary. After the vehicle is located at the FATO and ready for take-off, a final request for departure, including the flight plan, is requested to the ATC. If the final approval of the ATC is received and the vertiport manager confirms a safe FATO, the vehicle will take off.

In-Flight

The ROC will supervise the airspace, flight path, and aircraft health during the flight using the vehicle's current data. Next to the ROC, the ATC will also monitor the flight path and can instruct the ROC to alter the flight path. However, this will not happen often since the vehicles will fly on a predefined UAM route network.

If a hazard occurs and the autonomous system fails, or if the vehicle is deemed unsafe and the automatic emergency landing system does not respond, a remote override must be performed from the ground station. For example, if an external critical sensor fails to identify the landing site and clearance, the ROC operator has to coordinate that a standby pilot on the ground is the PIC and safely land the vehicle.

Landing

Before landing, the ROC will verify with the vertiport manager of the designated vertiport and ATC that the landing intent is still valid, that the landing spot is available and that there will be no traffic during the approach. After this is confirmed, the vehicle will land, after which the engines will be automatically turned off and towed to the apron by ground personnel.

Post-Flight

After the vehicle has arrived at the apron, which is situated near the terminal gate, the passenger unloading can start. After that, the aircraft will undergo a quick visual and general system inspection to check for wear or tear on critical components. The flight data will be reported, and post-flight logging will be reported or printed. Moreover, after the passengers are unloaded, a quick cleaning of the vehicle's interior will be done to ensure hygienic comfort for the passengers. A total turnaround for the vehicle, including the red expected critical path, is shown in Figure 17.3, which starts when the vehicle is in-block.

Maintenance

Besides the regular quick inspections during post-flight operations, a more extensive inspection has to be performed on the *Swing*.

All subsystems are visually, mechanically, and electrically inspected during this inspection. The hinge, especially, should have regular inspection and maintenance since it must withstand high loads and is a critical subsystem. The subsystems bought from other companies, such as the electric motors, will be inspected by the designated company.

The vehicle must adhere to the regulations set by EASA, because EASA provides the Airworthiness Readiness Certificate (ARC) for aviation in Europe. The eVTOL needs to comply with EASA's continuing airworthiness requirements, which include regular maintenance, inspection and updates to the aircraft. An approved Part M Continuing Airworthiness Management Organisation (CAMO) issues these ARC's, which are often valid for one year. Therefore, constant and extensive maintenance should be conducted and the Aircraft Maintenance Program (AMP) should be updated [124].

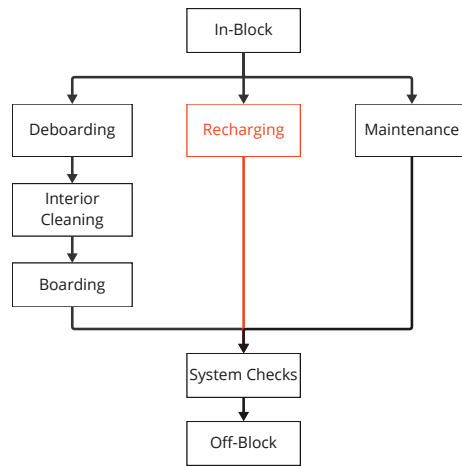


Figure 17.3: Turnaround diagram *Swing* including the expected critical path

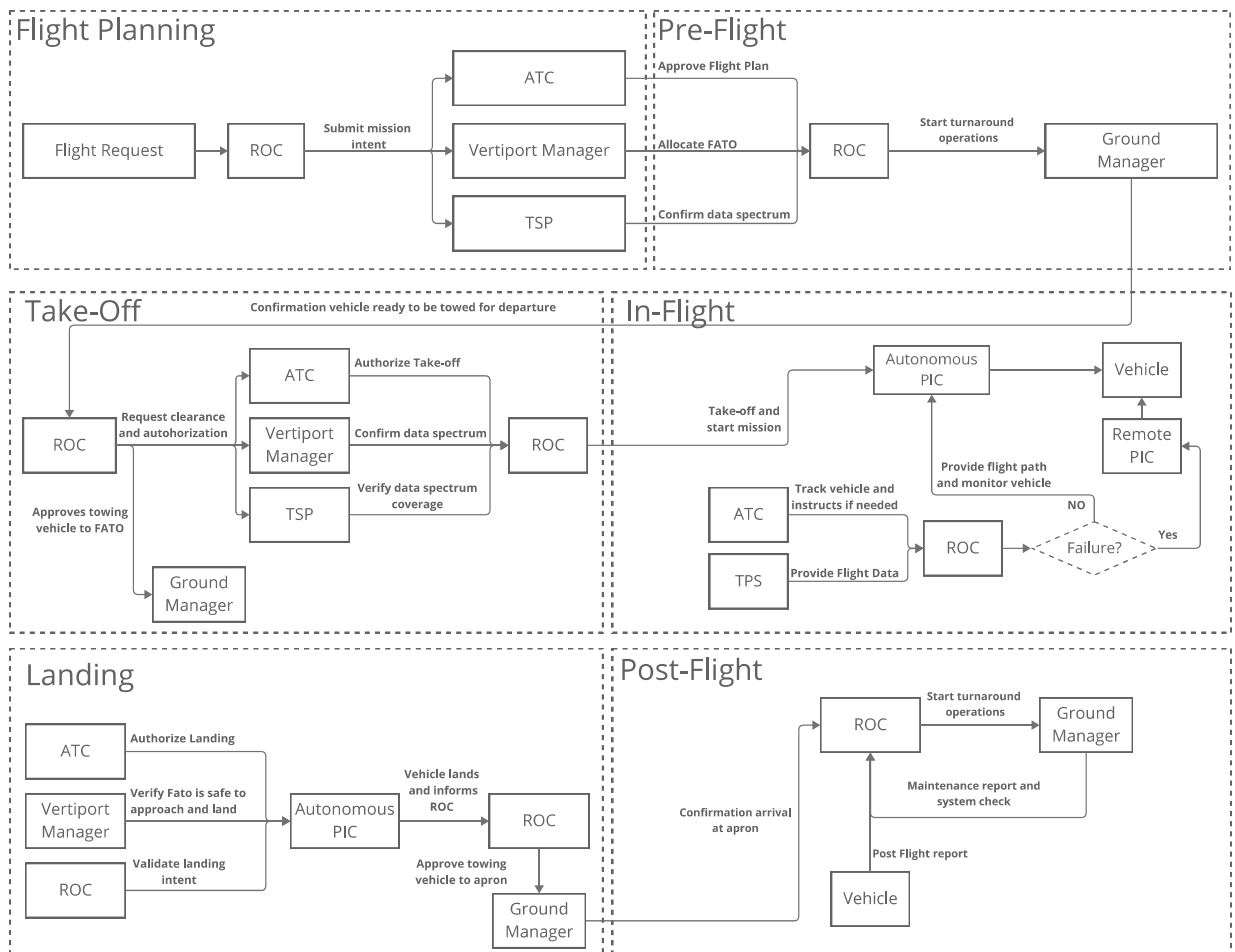


Figure 17.4: Operation diagram *Swing*

Storage

The vehicles are stored or placed on standby in the vertihubs and vertibases. The benefit of the *Swing*, with its reduced ground footprint of four parking spaces due to the rotating wings, is that it can be stored easily. The vehicles will be charged during storage, so the vehicle battery is charged when deployed. To release the constant bending moment on the hinge the wings will be supported by a wing support strut during storage. This decreases the fatigue on the hinge and increases the reliability and safety of the vehicle.

17.1.1. Downwash Protection Area

One of the main operational concerns of vertiports are the huge downwash speeds created by eVTOLs, which need to be carefully managed. Figure 17.5 shows the maximum downwash speeds per area that EASA established [18], based on the CASA regulations, which differ quite a bit per type of area. Hence, the vertiport must account for a so-called downwash protection area, in order to realise safe operations and logistics. This protection area is meant to prevent injury to passengers, personnel, and affected public, but also damage to vertiports, buildings, vehicles, and utilities.

17.1.2. Autonomous Flight

Due to the autonomous system onboard of the *Swing eVTOL*, the vertiport configuration can vastly differ from the classical heliport style. In particular, the current lighting guidance is mostly based on pilot guidance, historical measures, and overseas regulations, which would not be needed for autonomous eVTOLs. Think of the possibilities of integrated LEDs that can change the size and shapes of markings, or even QR codes that help the eVTOL approach or send important information about landing conditions [125]. This is further illustrated by Figure 17.6, showing only some of the wide array of possibilities.

Maximum downwash velocity	Type of area
60 km/h	for areas of a vertiport traversed by flight crew, or passengers, boarding or leaving an aircraft
60 km/h	for public areas, within or outside the vertiport boundary, where passengers or members of the public are likely to walk or congregate
80 km/h	for public areas where passengers or others are not likely to congregate
50 km/h	for public roads where the vehicle speed is likely to be 80 km/h or more
60 km/h	for public roads where the vehicle speed is likely to be less than 80 km/h
80 km/h	for any personnel working near an aircraft
80 km/h	for equipment on an apron
100 km/h	for buildings and other structures

Adapted from the Australian Government Civil Aviation Safety Authority Part 139 (Aerodromes) Manual of Standards 2019¹

Figure 17.5: Maximum downwash speeds [18]

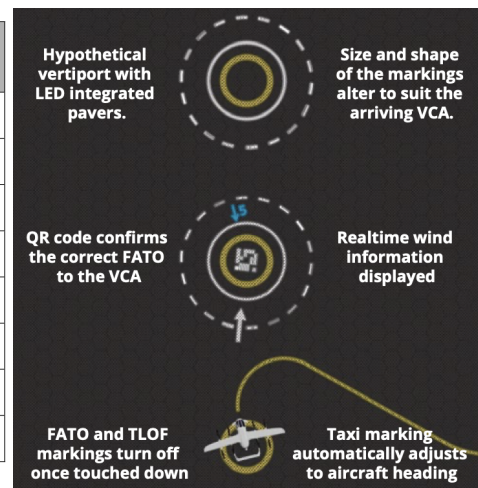


Figure 17.6: Vertiport possibilities [125]

17.2. RAMS Analysis

The design’s reliability, availability, maintainability and safety (RAMS) must be analysed to reduce the impact and occurrence of any failures during operation. The market position of the vehicle will increase if the vehicle adheres to these constraints.

Reliability

The reliability quantifies how failure-free a system is during a predefined operational time. It is crucial to express this numerically since it is important to the stakeholders’ needs and has to adhere to general testing guidelines. The Failure Rate (FR) is a unit that represents this discipline. Often the Mean Time Between Failure (MTBF), is used to express the reliability, however, the failure rate is more useful as this frequently appears in engineering and statistical calculations [126].

The reliability can be estimated for the system and the subsystems based on parameters like the MTOW or

partial weight of the subsystems, aircraft design role, sophistication level, complexity level, technological aircraft age and aircraft maintenance.

The estimation of the total failure rate of the system can be approached by the bottom-up or top-down method. In the bottom-up method, the total failure rate of the system is the summation of each subsystem, as seen in Equation (17.1), where λ_{E_i} is the failure rate of the subsystem.

$$\lambda = \sum_i \lambda_{E_i} \quad (17.1)$$

The other approach is the top-down method, where the failure rate of the subsystem is obtained through the allocation of the system failure rate, which is defined on historical data.

- **Technological Age Index (IA)**, is an index for the technology level used during the design process.
- **Complexity Index (IC)** indicates the aircraft's complexity.
- **Role Index (IR)** states the importance of the role of the aircraft.

Using these definitions, the failure rate of the aircraft can be determined, seen in Equation (17.2). Where $\left(\frac{\lambda}{\text{MEW}}\right)_{\text{MCA}}$ is the failure rate divided by the Maximum Empty Weight (MEW) for Medium Civil Aircraft (MCA), and is assumed to be equal to $1.8 \frac{\text{failures}}{1000\text{FH}\cdot\text{t}}$ [126]. Here, FH represents flight hours and t is time.

$$\lambda = \left(\frac{\lambda}{\text{MEW}}\right)_{\text{MCA}} \cdot \text{IR} \cdot \text{IC} \cdot \text{IA} \cdot \text{MEW} \quad (17.2)$$

IA	IC	IR	MEW [kg]
0.6	1.4	1.0	1300
Total Failure Rate			2.0

Table 17.1: Failure rate λ of the vehicle

The estimated failure rate for the system can be seen in Table 17.1. The subsystem weights were used as input together with historical data to estimate the failure rate, using Equation (17.3). Where λ is the system failure rate, K_i a normalised failure rate coefficient differing per subsystem that is obtained from historical data, $W_i\%$ the subsystem percentage weight and $\lambda_{i_{nm}}$ the non-normalised subsystem failure rate. From historical data, the K_i value is obtained [126] and the final result can be seen in Table 17.2.

$$\lambda_i = \lambda \frac{K_i W_i \%}{\sum_i \lambda_{i_{nm}}} \quad (17.3)$$

Table 17.2: Failure rate per subsystem top-down method

Subsystem	Mass [kg]	W [%]	K_i	$\lambda_{i_{nm}}$	λ_i
Structures	580	47	0.07	3	0.04
Propulsion	184	15	1.59	24	0.30
Battery	400	32	3.04	98	1.24
Other	78.7	6	5.32	34	0.43

Since the top-down method is used, the failure rate per subsystem sums to 2.0. A more extensive method

should be used for further reliability analysis, where more subsystems and more accurate failure rates are included.

Safety

The safety concerns to the state where the risk level of the design is acceptable and not exceeded. It is related to the reliability of the design with a focus on catastrophic failures. The Safety Failure Rate is the performance figure to assess safety. Moreover, safety factors are included during the design process to omit the probability of catastrophic system failures. The total system failure is estimated by Equation (17.4)

$$\lambda_S = \frac{\lambda}{RL} < \lambda_{S_{\max}} \quad (17.4)$$

Where λ is equal to the failure rate and RL is the Role Index equal to 10^6 for civil aircraft [126]. The non-standardised safety failure rate $\lambda_{S_{inn}}$ of the i_{th} subsystem is obtained using the following expression.

$$\lambda_{S_{inn}} = \frac{\lambda_i}{RL \cdot (RD)^2} \cdot DC \cdot CR \cdot CP \cdot \sqrt{TC} \quad (17.5)$$

Where:

- **Subsystem redundancy coefficient (RD)** takes the value of 1.7 in case of redundancy.
- **Subsystem duty cycle coefficient (DC)** expresses the ratio between the operation time of the subsystem and the aircraft life cycle, in terms of flight hours. It has a value between 0.1 and 1.
- **Subsystem criticality coefficient (CR)** takes a value smaller than one if the subsystem strongly influences aircraft safety and greater than one if the subsystem is not critical for aircraft safety.
- **Subsystem complexity coefficient (CP)** expresses the complexity of the subsystem. If the subsystem is complex, the value is greater than one; otherwise, it is equal to one.
- **Subsystem technological sophistication coefficient (TC)** expresses the technological level and novelty of each subsystem and uses the same scale as IC.

The summation of all the safety failure rates of the aircraft subsystems has to be equal to the total safety failure rate, therefore, it has to be normalised as seen in Equation (17.6)

$$\lambda_{S_i} = \lambda_{S_{inn}} \frac{\lambda_S}{\sum_i \lambda_{S_{inn}}} \quad (17.6)$$

The final values are put in Table 17.3, where the coefficients are preliminary and estimated.

Table 17.3: Safety failure rate

Subsystem	RD	DC	CR	CP	TC	$\lambda_{S_{inn}}$ [10^{-7}]	λ_{S_i} [10^{-7}]
Structures	1.7	1	0.8	1.2	1.3	1.6	6.8
Propulsion	1.7	1	0.5	1.3	1.5	8.2	3.6
Battery	1.7	1	0.6	1.1	1.1	3.0	1.3
Other	1.7	0.5	0.9	1	1	6.6	2.9

The safety failure rates must be validated to see if the order of magnitude is valid. A paper by Bendarkar, Sarojini, Harrison et al. [127] estimates the order of magnitude of failure rates for eVTOL and small general electric aircraft. For different assessment levels, the failure rate had a similar order of magnitude in the range of 10^{-6} to 10^{-9} . There also has to be accounted for ground regulation safety. During take-off and landing, there should be enough ground clearance and strict guidelines to mitigate the risk of accidents occurring,

and therefore increase safety. This is described in Section 17.1, where the ground operation logistics are analysed.

Maintainability

Maintainability in aircraft design refers to the likelihood that an item will be kept in, or restored, to a specified condition within a given time frame, when appropriate and predefined procedures and resources are used [128]. The Maintenance Man Hours per Flight (MMH/FH) is a commonly used maintainability performance figure, which divides the labour hours spent on maintenance by the flight hours during that period and is estimated, on system level, using the following relation in Equation (17.7).

$$\frac{\text{MMH}}{\text{FH}} = \frac{1}{6} \text{IRM} \cdot \text{CDTM} \cdot \text{IC} \cdot \text{IA} \cdot \text{MEW}^{0.25} \quad (17.7)$$

Where IRM is the Maintenance Role Index, which is equal to 1.5 for civil aircraft and CDTM the Design to Maintain Coefficient that is dependent on the total attention paid to the maintenance, during the design process. CDTM can be estimated by historical data, following from Giovingo [126], which estimates the coefficient value based on the level of maintenance performed. From this paper, the third level (RAMS discipline considered in design requirements) was chosen, which had a value of 1.2. The paper estimates the fraction 1/6 to account for the better technology that is available and the fact that the way of performing maintenance has changed.

The system value for the $\frac{\text{MMH}}{\text{FH}} = 0.3$, which is a preliminary value and has to be verified and validated. An analysis conducted by Sieb, Michelmann, Flöter et al. [129], provided values ranging from 0.38 to 0.44 MMH/FH, which is in the same range. However, the complex transwing mechanism is novel and, therefore, requires extensive maintenance. This also accounts for the electric propulsion and V-tail configuration. Therefore, a more intensive subsystem analysis has to be conducted to estimate a better MMH/FH.

Availability

Availability translates the maintainability and system reliability characteristics into an index of effectiveness. If both the characteristics have a high value, then the availability will be high consequently. The vehicle ought to have high availability because it has to adhere to requirement Te-2-STK07-5, stating that the vehicle has to be operational for 345 days per year. This includes weather conditions, according to requirement Te-2-STK07-5-2, stating the vehicle shall be able to withstand winds of up to 7 Beaufort. Moreover, since the goal is to maximise the number of trips, the turnover time is kept as low as possible.

18. Sustainability Approach

The *Swing* aims to revolutionise the transportation industry by providing a sustainable alternative to traditional ground transportation. In the face of the urgent challenges posed by climate change, with approximately 24% of global carbon emissions attributed to the transportation sector [130], it is crucial to assess the environmental impact of this innovative vehicle. Evaluating the *Swing*'s sustainability is essential to ensure it contributes positively to reducing the carbon footprint and promoting a greener future for urban mobility. In this chapter, the energy consumption of the *Swing* will be compared to that of competitors (Section 18.1); the impact of the vehicle on urban environments is then considered in Section 18.2; Section 18.3 covers a qualitative evaluation of the emissions; finally, the reusability requirements are addressed in Section 18.4.

18.1. Energy Consumption

Firstly, it is important to acknowledge that the *Swing* is a fully electric vehicle that utilises renewable energy sources, such as solar and wind, for most of its power. This commitment to renewable energy places the *Swing* ahead of the vast majority of current ground and air transport options. According to the International Energy Agency (IEA), as of 2023, approximately 95% of the world's transportation sector continues to rely on fossil fuels.

Secondly, it is important to compare the energy consumption of the *Swing* as found in Chapter 13 with that of an electric vehicle (EV) like the BMW i3 60 Ah REx. The data in Table 18.1 shows that the eVTOL consumes approximately 2.5 to 3.25 times more energy than the BMW i3, depending on the driving cycle used for comparison. This difference in energy consumption is less significant when considering that the BMW i3 is an exceptionally efficient EV, with an average energy consumption of 0.135 kWh/km to 0.179 kWh/km [131], while the typical EV averages around 0.188 kWh/km. Note, however, that these differences become less pronounced over longer distances. During cruise, in fact, the average energy consumption of the *Swing* is approximately 0.162 kWh/km, which is comparable to that of electric cars. The energy required for vertical ascent thus becomes relatively less significant as the travel distance increases, highlighting the efficiency gains of the eVTOL over longer journeys.

Table 18.1: Energy consumption of electric vehicles during different phases

	Cruise [kWh/km]	Vertical Flight [kWh]	Climb [kWh]
BMW	0.157	-	-
Avg EV	0.188	-	-
Joby s4	0.304	30	50
<i>Swing</i>	0.162	20.7	6.7

Despite its higher overall energy consumption, *Swing* offers significant advantages in terms of travel time. The eVTOL can cover 100 km in approximately 30 minutes with a 200 km/h cruise speed. In comparison, the BMW i3, assuming an average highway speed of 130 km/h, takes about 46 minutes to travel the same distance. Additionally, roads often do not connect places in a straight line, resulting in longer travel distances by car compared to the more direct routes possible in the air. This reduction in travel time highlights the eVTOL's potential for faster commutes, particularly in urban settings where road congestion is a major issue.

A study performed by N.André and M.Hajek [132] on the emissions of eVTOLs concludes that only very lightweight vehicles for Urban Air Mobility can be more sustainable than traditional EVs. They further conclude that, with a combination of the most optimistic assumptions, Urban Air Mobility concepts may environmentally compete with battery-powered cars. However, it is our belief that the *Swing* has great potential in achieving highly sustainable UAM. For this reason, Section 18.3 focuses on qualitatively evaluating the emission performance of the vehicle as well as End-of-Life (EoL) reusability concepts.

A comparison regarding energy consumption must also be made with one of the main competitors: Joby. Table 18.1 already introduced values concerning this vehicle as used in [133]. A clear distinction can be seen in the climb and cruise phases. This can be easily attributed to the higher wing surface area of the *Swing* as well as its high lift capabilities. Instead, the difference in energy needed for vertical take-off and landing is most likely given by the difference in mass.

Two examples are used and shown in Table 18.2 to give a better overview. Here, a short and a long-range mission are taken into account. As a short-range mission, one which crosses an urban environment is chosen: London City Airport (LCY) to London Heathrow Airport (LHR). Amsterdam Schiphol Airport to Brussels Airport (BRU) is chosen for the long-range one. From the energies calculated in Table 18.2, it is clear how the *Swing* outperforms its competitors in this matter. Additionally, the “last-mile” problem is a significant consideration. The *Swing* is designed to penetrate urban environments, allowing it to start and/or end missions at locations other than traditional airports. This capability addresses the challenges of the last leg of the journey, enhancing accessibility and convenience for users.

Table 18.2: Sample missions energy consumption [kWh]. Vertical flights includes take-off and landing hovering phases

	D_{ground} [km]	D_{air} [km]	Avg EV [kWh]	Joby s4 [kWh]	Swing [kWh]
LCY-LHR	62	35	12	90	33
AMS-BRU	203	158	38	128	53

18.2. Impact of the *Swing* on Urban Environments

One significant advantage of air taxis is their potential to reduce the number of vehicles on the road, thereby alleviating traffic congestion and shifting some of it to the skies. This could decrease noise and carbon emissions from ground vehicles, promoting cleaner urban environments. As highlighted by Arbin Instruments [134], the extensive infrastructure required for the adoption of electric public transport is a major undertaking for larger cities. In contrast, eVTOLs require only transportation hubs, eliminating the need for additional roads or tracks.

Compared to its competitors, one of the main advantages of the *Swing* is its low ground footprint, occupying only the equivalent of four car parking spaces. This compact footprint is significantly smaller than that of other air transport vehicles, making it highly adaptable to urban environments. The reduced ground space requirement allows for more efficient use of available land, enabling the installation of eVTOL landing and take-off pads in densely populated areas where space is at a premium. This can facilitate closer proximity to passenger destinations, reducing the need for extensive ground travel and enhancing urban commutes' efficiency. Additionally, the smaller footprint minimises the environmental impact on urban landscapes, preserving green spaces and reducing the need for large-scale infrastructure projects. This adaptability and efficiency make the *Swing* a versatile and sustainable solution for future urban transportation needs.

18.3. Emission Performance Evaluation

End-of-Life Considerations

In evaluating the emission performance of the *Swing*, the end-of-life (EoL) possible impacts such as recycling, incineration, or landfill disposal [135] are not included in the primary analysis. This decision is based on several factors. Firstly, as detailed in the section Section 18.4, a comprehensive reusability strategy is adopted for the *Swing*, including modular design and standardisation, which further mitigate EoL impacts and reduce incineration and landfill disposal to the bare minimum. Secondly, according to Ashby's emission indices [135], the carbon emissions from the incineration of materials are an order of magnitude smaller than that of production. Given that the impact of production itself is much smaller than the operational emissions over the vehicle's lifecycle [132], the role of incineration in the overall carbon footprint is negligible. Lastly, previous studies on battery lifecycle assessment often exclude EoL impacts. Zackrisson et al.[136], for instance, focus instead on the transport of used batteries to recycling facilities. They highlight that environmental benefits from recycling should be attributed to the next product lifecycle. Similarly, Majeau-Bettez et al.

[137] suggest that excluding recycling impacts presents a worst-case scenario, as it does not account for the potential benefits of secondary material use.

Emissions During Production

During the production phase, the *Swing* faces challenges in emission performance due to the use of CFRP. CFRP production is energy-intensive and associated with higher carbon emissions compared to other materials, with a Global Warming Potential (GWP) of 28.5–35.2 [138]. This is opposed to aluminium, with a GWP of 8.3–27.7 [139]. However, the operational efficiency and reduced emissions during the use phase offset the initial production impact. The study performed by N.André and M.Hajek [132] on three types of eVTOLs suggested by [140], is insightful in understanding the relative contribution of the production of different subsystems to the CO₂ emissions. This is illustrated in the left of Figure 18.1 [132], where Green House Gasses (GHG) emissions are shown.

Emissions in the Operational Phase

As found by N.André and M.Hajek [132], the operational phase is the most significant in terms of emissions when it comes to eVTOLs. As illustrated in the right plot of Figure 18.1 [132], the carbon footprint varies widely based on the electric grid’s composition. Canada has a high share of its energy produced via hydropower. Regions with a higher proportion of renewable energy sources will thus see significantly lower operational emissions compared to those reliant on fossil fuels. The *Swing*’s environmental impact during operation is highly dependent on the source of electricity used for charging.

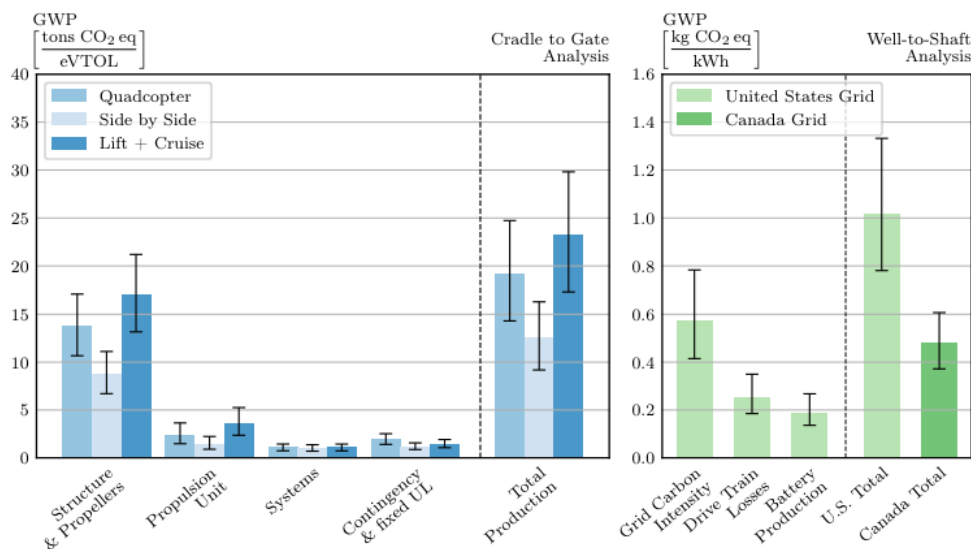


Figure 18.1: GHG Emissions due to the production of materials (left) and due to the consumption of electric energy during operation (right). Quadcopter, side by side, and lift + cruise refer to different eVTOLs concepts. [132]

Additionally, looking at the analysis performed on different eVTOLs (Figure 18.2 [132]), a very clear dependency of the emissions on the velocity can be seen. For all concepts, the minimum emissions speed is recorded between 150 km/h and 200 km/h. The *Swing*’s cruise speed of 200 km/h is thus very close to the optimal speed for minimising (GWP). This efficiency in operation further reduces the overall environmental impact during the vehicle’s lifecycle.

18.4. Reusability of Vehicle Parts: the “Cradle to Cradle” Approach

Committing to sustainability, the *Swing* not only aims to revolutionise urban transportation but also to set new standards for the reusability of its components. Embracing the “cradle to cradle” approach, as opposed to the traditional “cradle to grave” concept, we are dedicated to ensuring that every part of the vehicle can be repurposed or recycled, minimising waste and environmental impact.

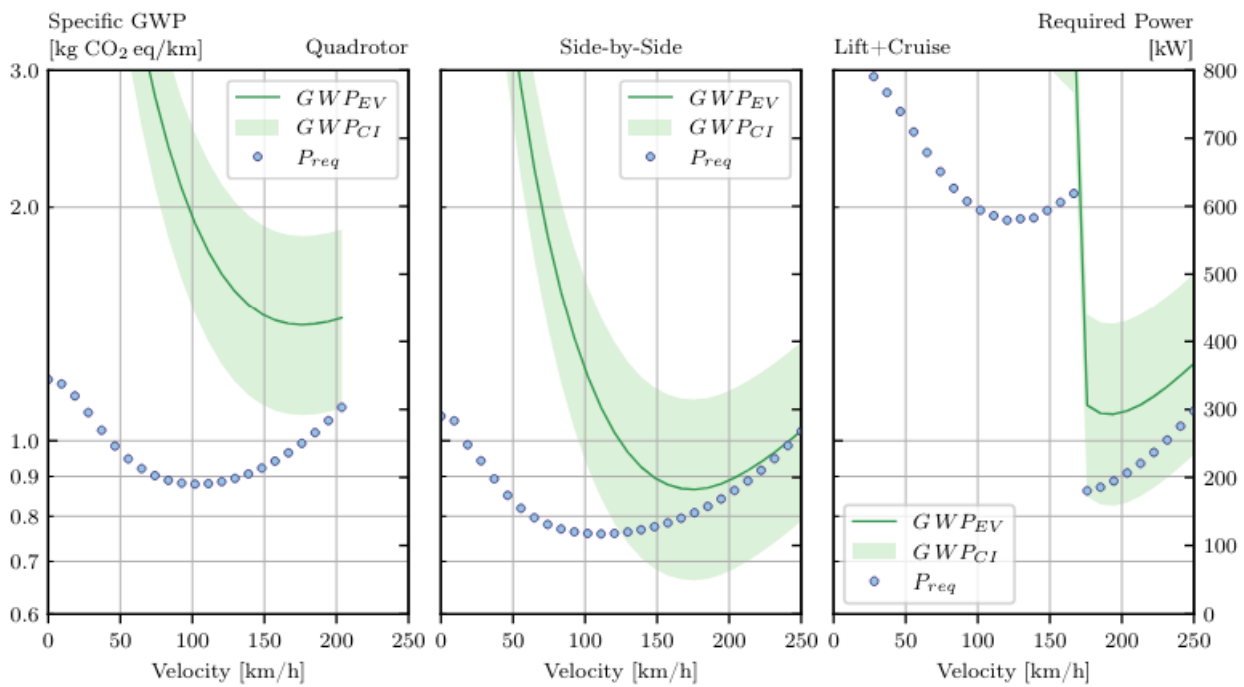


Figure 18.2: Powers (blue dots) and distance-specific emissions (green lines) over forward flight speed for the three eVTOL concepts. A 95% confidence interval (CI) is indicated together with the mean (EV) [132].

Partnerships for Component Repurposing

Partnerships are planned with industry leaders such as Tarmac Aerosave and Satir, known for their expertise in aircraft component recycling and repurposing. These collaborations will enable the effective management of the end-of-life cycle of the *Swing*, ensuring that its parts are given a second life. By working with these companies, components can be disassembled, repurposed, and recycled; thereby significantly reducing the environmental footprint of the vehicles.

Additionally, inspired by initiatives like the Lufthansa Upcycling Collection and Airbus’ A Piece of Sky, we are launching our homeware collection, “*Swing Reimagined*”. This collection will feature unique items made from repurposed parts of the *Swing*, offering our customers a chance to own a piece of aviation history while promoting sustainability. Figures 18.3a and 18.3b show some example pieces part of the *Swing Reimagined* Collection.

Tactics to Facilitate the Repurposing Process

To maximize the reusability and recyclability of our vehicle components, several key strategies are adopted:

- **Modularity:** by designing the *Swing* with a modular structure, we ensure that its components can be easily disassembled and reassembled. This facilitates the repurposing process and allows for straightforward upgrades and maintenance.

For instance, the batteries are modular, allowing for the replacement of individual modules rather than the entire battery system in the event of a failure. Moreover, the batteries are strategically placed in the nacelles rather than the wings, simplifying maintenance and replacement procedures.

- **Standardisation:** implementing standardised components and interfaces ensures compatibility with future technologies and systems. This not only simplifies repairs and replacements but also enhances the longevity and adaptability of the vehicle.

Recycling Goals and Industry Standards

According to the Aircraft Fleet Recycling Association (AFRA), it is estimated that around 80% to 85% of aircraft parts are recycled when an aircraft reaches retirement. Our goal is to exceed this standard by aiming to recycle close to 95% of the *Swing*’s components. By striving for this ambitious target, we demonstrate our



(a) CFRP wing skin structure repurposed as a bookshelf. [OpenAI generated image]

(b) Front fuselage structure and seats repurposed as a comfortable Swing [OpenAI generated image]

Figure 18.3: Swing reimaged collection

commitment to leading the industry in sustainable practices and setting a benchmark for future developments in urban air mobility.

Long-Term Reusability Requirements

We have set stringent requirements for the reusability of our vehicle to ensure long-term sustainability. Specifically, requirements Co-4-STK13-1-5 and Co-4-STK13-1-6 guide our design and production processes. Requirement Co-4-STK13-1-6 states: “The vehicle structure shall be reusable for at least 10 years after its life.” This ensures that the core components of the *Swing* are built to last, further enhancing the vehicle’s sustainability credentials.

18.5. Economic Sustainability of the *Swing* Project

Beyond its technological and operational benefits, the *Swing* project promises substantial economic sustainability by positively impacting the local economy in several key ways.

Firstly, the *Swing* project will create numerous job opportunities in both the manufacturing and operational sectors. Establishing production facilities for the *Swing* will boost local employment rates by generating manufacturing, assembly, and quality control jobs. Additionally, the ongoing need for regular maintenance and operational support will create further employment in technical services, ground operations, and customer support.

Secondly, the *Swing* will enhance mobility and connectivity, significantly benefiting the local economy. By providing efficient and rapid transportation, the *Swing* improves access between urban and rural areas, facilitating easier access to jobs, education, healthcare, and other essential services. This enhanced connectivity allows for greater economic integration, enabling businesses to expand their markets and workforce and stimulating economic activity and growth.

Finally, the *Swing* can potentially boost tourism and commerce within the region. Its capability to offer quick and convenient transportation can attract more tourists, making travel between attractions and cities more accessible. For business professionals, the *Swing* provides a fast and efficient mode of travel, promoting increased business interactions and commerce, further stimulating the local economy.

19. Financial Analysis

This chapter discusses the financial analysis of the *Swing eVTOL*. In Section 19.1, a cost breakdown of the eVTOL is performed, and in Section 19.2, the direct operational costs of the *Swing* are estimated. Finally, Section 19.3 estimates the return on investment of the *Swing*.

19.1. Cost Breakdown Structure

The cost breakdown aims to analyse the production costs of the eVTOL, requirement **Co-1-STK05-1** states that: “The vehicle cost of production per unit shall be less than 2000k€”. The method used to perform the cost breakdown is the method from Gudmundsson[39](2012). The method is generated to estimate the cost of a small general aviation aircraft therefore, the assumption is that the size and characteristics of an VTOL is similar to a small GA aircraft. To incorporate the electric propulsion of the eVTOL in the cost analysis, the analysis from Finger et al.[141] is used. The analysis from Finger et al. is a modified version of the analysis of Gudmundsson to analyse the cost of a hybrid electric aircraft GA aircraft.

Gudmundsson starts by calculating the man-hours needed for the project. The engineering, tooling and manufacturing man-hours can be calculated.

$$H_{\text{ENG}} = 0.0396 \cdot W_{\text{airframe}}^{0.791} \cdot V_H^{1.526} \cdot N^{0.183} \cdot F_{\text{CERT}} \cdot F_{\text{CF}} \cdot F_{\text{COMP}} \cdot F_{\text{PRESS}} \quad (19.1)$$

Where w_{airframe} is the weight of the bare structural skeleton in lbs, this weight does not include the engines and controls. V_H is the maximum airspeed in KTAS, N is the number of planned eVTOLs to be produced over a five-year period, N is assumed to be 200. Finally, F_{CERT} , F_{CF} , F_{COMP} and F_{PRESS} are judgement factors based on the certification, the flap system, the composites in the aircraft and the pressurisation. For these estimates, it is assumed that the carbon fibre material fraction of the *Swing* is 0.8.

$$H_{\text{TOOL}} = 1.0032 \cdot W_{\text{airframe}}^{0.764} \cdot V_H^{0.899} \cdot N^{0.178} \cdot Q_m^{0.066} \cdot F_{\text{TAPER}} \cdot F_{\text{CF}} \cdot F_{\text{COMP}} \cdot F_{\text{PRESS}} \quad (19.2)$$

Where Q_m is the estimated production rate in the number of aircraft per month, F_{TAPER} is a judgement factor based on the wing's taper.

$$H_{\text{MFG}} = 9.6613 \cdot W_{\text{airframe}}^{0.74} \cdot V_H^{0.543} \cdot N^{0.524} \cdot F_{\text{CERT}} \cdot F_{\text{CF}} \cdot F_{\text{COMP}} \quad (19.3)$$

Once the number of hours has been determined, the costs can be calculated by multiplying these with the hourly rates.

$$C_i = 2.0969 \cdot CPI_{2012} \cdot H_i \cdot R_i \quad (19.4)$$

Where CPI_{2012} is the consumer price index relative to the year 2012, which, according to the U.S. Bureau of Labor Statistics, is 1.39¹. H_i is the number of man-hours of i , R_i is the hourly labour rate of i . The summation is multiplied by a factor of 2.0969, this factor is the CPI from 1986 to 2012. As suggested by Gudmundsson, the hourly rates are taken as \$92, \$61 and \$53 for engineering, tooling and manufacturing. The development costs can be calculated with Equation (19.5), and the cost of the flight tests can be calculated with Equation (19.6). Together with the engineering and tooling costs, the costs to certify can be calculated. Where N_p is the number of prototypes built to perform flight testing, this has been assumed to be eight prototypes. Furthermore, for simplicity, it is assumed that the prototypes will not be sold.

¹https://www.bls.gov/data/inflation_calculator.htm [Accessed on 17/06/24]

$$C_{DEV} = 0.06458 \cdot W_{airframe}^{0.873} \cdot V_H^{1.89} \cdot N_P^{0.346} \cdot CPI_{2012} \cdot F_{CERT} \cdot F_{CF} \cdot F_{COMP} \cdot F_{PRESS} \quad (19.5)$$

$$C_{FT} = 0.009646 \cdot W_{airframe}^{1.16} \cdot V_H^{1.3718} \cdot N_P^{1.281} \cdot CPI_{2012} \cdot F_{CERT} \quad (19.6)$$

The costs that are associated with the quality control are calculated with Equation (19.7) where, C_{MFG} is the cost of the manufacturing. The costs of the raw materials that are used to manufacture the eVTOL are calculated with Equation (19.8).

$$C_{QC} = 0.13 \cdot C_{MFG} \cdot F_{CERT} \cdot F_{COMP} \quad (19.7)$$

$$C_{MAT} = 24.896 \cdot W_{airframe}^{0.689} \cdot V_H^{0.624} \cdot N^{0.792} \cdot CPI_{2012} \cdot F_{CERT} \cdot F_{CF} \cdot F_{PRESS} \quad (19.8)$$

All costs that are calculated up till now depend on the number of planned eVTOLs to be produced over a five-year period (N). However, there are also costs which are not dependent on the planned amount. The costs of the Avionics and the propellers are based on the method of Gudmundsson; these can be found in Equations (19.9) and (19.10).

$$C_{AV} = 15000 \cdot CPI_{2012} + 100000 \quad (19.9) \quad C_{FIXPROP} = 3145 \cdot N_{PP} \cdot N_{motor} \cdot CPI_{2012} \quad (19.10)$$

Where \$15000 is the typical cost for the avionics of a general aircraft certified to FAR 23 regulations. However, since the *Swing eVTOL* is autonomous \$15000 for the avionics will not be sufficient to incorporate the costs of the autonomous autopilot system \$100000 is added to the avionics costs. N_{PP} is the number of propeller blades per motor and N_{motor} is the number of motors. The \$3145 is the typical cost for a fixed pitch propeller blade in 2012. In contrast, the costs of the power management system and the battery are based on Finger et al., these can be found in Equations (19.11) and (19.12). The cost of the electric motors is the actual price of the selected motor. \$4650 is the costs of one electric engine².

$$C_{PMS} = 150 \cdot P_{EM,total} \cdot CPI_{2012} \quad (19.11) \quad C_{BAT} = 110 \cdot E_{BAT} \cdot CPI_{2012} \quad (19.12)$$

Where $P_{EM,total}$ is the total power of the engines in hp, and \$150 is the costs per hp in 2012. The additional costs of cables and further miscellaneous electronic devices are neglected[142].

Where E_{BAT} is the energy of the battery and \$110 is the cost per kWh [143]. The costs of the hinges used in the *Swing eVTOL* are assumed to be \$50000 per hinge. Finally, costs associated with the product liability are accounted for by Finger et al. suggest to add 20% of the production costs. Now the production costs can be calculated with Equation (19.13).

$$C_{PROD} = \left(\frac{C_{MAN} + C_{QC} + C_{MAT}}{N} + C_{AV} + C_{FIXPROP} + C_{EM} + C_{PMS} + C_{BAT} \right) \cdot 1.2 \quad (19.13)$$

$$N_{Break-even} = \frac{C_{CERT}}{\text{Unit sell price} - C_{PROD}} \quad (19.14)$$

Finally, in Table 19.1 the cost breakdown of the *Swing eVTOL* can be found, and it can be seen that the production costs are €1,42 million. This means that the requirement for the production costs of *Swing* has been met. Using Equation (19.14) the break-even number eVTOLs can be calculated, using a unit price of €2.2 million the break-even number eVTOLs is 66. This cost analysis is largely based on statistical relations and empirical formulas; therefore, the cost analysis should be reiterated in a later stage of the design

²<https://emrax.com/get-a-quote> [Accessed on 17/06/24]

process. For instance, Section 14.1 mentions that double glass will be used to lower the noise levels inside the fuselage, these double glass windows will increase the production costs of the *Swing eVTOL*.

Table 19.1: Cost breakdown for $N = 200$ eVTOL's

Cost to certify (Fixed Costs)[\$]			
Engineering	\$ 29,516,934.74	Development	\$ 1,569,374.63
Tooling	\$ 22,513,628.27	Flight Test Operations	\$ 958,110.62
Total:	\$ 54,558,048.26	Total:	€ 50,738,984.89
Production Costs (Variable Costs) [\$ /Unit]			
Manufacturing	\$ 568,646.41	Power Plant	\$ 27,900.00
Quality Control	\$ 103,493.65	Propeller blades	\$ 157,375.80
Raw Materials	\$ 44,716.46	Battery	\$ 13,200.00
Avionics	\$ 159,850.00	Hinge	\$ 100,000.00
Product Liability	\$ 254,608.68	Power Management System	\$ 97,861.09
Total:	\$ 1,527,652.09	Total:	€ 1,420,716.44

19.2. Operational Costs

To calculate the operational costs, Gudmundsson [39] and Kreimeier [144] are used. Only the direct operational costs are analysed because different air taxi operators might have different options for funding the eVTOL. The Maintenance, storage, inspection, insurance and engine overhaul costs are estimated with Gudmundsson (Equations (19.15) to (19.17)). The storage costs are estimated to be \$3000 per year, while the inspection costs are \$500 per year. F_{MF} is the ratio of flight hours to maintenance hours, 0.38 is used. R_{AP} is the hourly wage of a certified mechanic, \$60 per hour is used [39]. Q_{FLGT} is the number of flight hours per year; for this, it is assumed that the *Swing*, on average, can fly 12 flights of 40 minutes per day. Finally, C_{AC} is the insured value, this is taken as the unit sell price of €2.2 million.

$$C_{AP} = F_{MF} \cdot R_{AP} \cdot Q_{FLGT} \quad (19.15) \quad C_{INS} = 500 + 0.015 \cdot C_{AC} \quad (19.16)$$

$$C_{COVER} = 5 \cdot N_{PP} \cdot Q_{FLGT} \quad (19.17) \quad C_C = R_{Pilot} \cdot \frac{t_{block}}{f_{gp-acft}} \quad (19.18)$$

Even though the *Swing* is autonomous, there are crew costs. According to Kreimeier “If the aircraft itself can fly without a pilot, a ground pilot is required for safety reasons” [144]. Equation (19.18) is used to calculate these costs, t_{block} is the block time of the flight, this is found as 40 minutes from the mission profile. $f_{gp-acft}$ is the number of aircraft a ground pilot can manage simultaneously, Kreimeier proposes this to be 5. R_{Pilot} is the hourly wage of the ground pilot, Finger et al. proposes this to be \$60 per hour [141].

$$C_{VERTIPORT} = 0.01 \cdot (m_{MTOW} - 1100) \cdot F_{Noise} \cdot N_{Landing} \quad (19.19)$$

To estimate the cost of the vertiports, apart from the energy costs, Equation (19.19) is used [144]. The equation is used to estimate the costs at regional airports, and it is assumed that these costs are comparable to those at vertiports.

$$C_{BATD} = C_{BAT} \cdot E_{BAT} \cdot \frac{N_{flight} \cdot C}{N_{cycle}} \quad (19.20) \quad C_E = \frac{\tau_E \cdot E_{flight}}{\eta_{charge}} \quad (19.21)$$

Where N_{cycle} is the number of cycles per flight, this has been assumed to be 0.667 (1.5 flights per cycle). N_{cycle} is the number of cycles of the battery. The energy costs used during the flight are estimated with Equation (19.21). τ_E is the price per kWh of energy and η_{charge} is the charging efficiency, this is taken as 0.85 [144]. Kreimeier also proposes ground handling fees of €7 per passenger per flight.

Table 19.2: Operational costs of the *Swing*

Operational Costs [\$/year]			
Maintenance	\$ 92,540.64	Vertiport	\$ 50,085.30
Storage	\$ 3,000.00	Crew	\$ 29,200.00
Insurance	\$ 33,500.00	Battery Depreciation	\$ 48,180.00
Energy	\$ 103,058.82	Engine Overhaul	\$ 87,600.00
Inspection	\$ 500.00	Ground handling	\$ 122,640.00
Total costs per year	\$ 570,304.76	Total costs per year	€ 530,383.43
Costs per flight			
Costs per flight hour	\$ 195.31	Costs per flight hour	€ 181.64
Costs per flight	\$ 130.21	Costs per flight	€ 121.09

The operational costs of the *Swing* can be found in Table 19.2. It should be noted again that these are only the direct costs. Air-taxi operators will have to charge a higher price per flight due to other costs related to eVTOL operations. Those costs include but are not limited to depreciation costs, cost of financing, taxes, marketing costs, and costs related to office facilities.

19.3. Return on Investment

Based on the Gantt chart from Section 21.2 a timeline has been created. This timeline can be found in Table 19.3. It can be seen that the first delivery of the *Swing* is expected in 2033. Using a discount rate of 5%, the timeline, the net present value, the internal rate of return and return on investment can be calculated. The net present value (NPV) is 47.8 million \$, the internal rate of return is 15%, and the return on investment is 10%.

Table 19.3: Cash flow timeline

Timeline [M\$]								
Year	2024	2025	2026	2027	2028	2029	2030	2031
Units Sold								
Unit sale price								
Revenue								
Engineering Costs	-4.03	-8.05	-8.05	-8.05	-1.34			
Tooling Costs					-4.09	-4.09	-4.09	-4.09
Development Costs	-0.09	-0.17	-0.17	-0.17	-0.17	-0.17	-0.17	-0.17
Flight Test Operation Costs								
Production Cost								
Cash flow	-4.11	-8.22	-8.22	-8.22	-5.61	-4.27	-4.27	-4.27
Year	2032	2033	2034	2035	2036	2037	2038	-
Units Sold		20	40	40	40	40	20	
Unit sale price		2.37	2.37	2.37	2.37	2.37	2.37	
Revenue		47.31	94.62	94.62	94.62	94.62	47.31	
Engineering Costs								
Tooling Costs	-4.09	-2.05						
Development Costs	-0.17	-0.09						
Flight Test Operation Costs								
Production Cost		-30.55	-61.11	-61.11	-61.11	-61.11	-30.55	
Cash flow	-4.27	14.62	33.52	33.52	33.52	33.52	16.76	-

20. Production Plan

This chapter outlines the proposed production strategy for the *Swing eVTOL*. Specifically, in Section 20.1, it compares in-house production with outsourcing for each subsystem, highlighting the chosen production method in Section 20.2. The production line and timeline are also detailed in Section 20.3.

20.1. Vertical or Horizontal Integration

There is a clear need for customised and high-quality parts in the manufacturing process of complex systems such as eVTOLs. These parts can either be produced in-house, through vertical integration, or produced by specialised contractors through horizontal integration. In the Competition Analysis (Section 2.5), the main competitors were established in the Joby S4 and Archer Midnight; hence, those are interesting to compare with. Most notably, Joby follows a vertical integration model, arguing that it leads to a more optimised product designed specifically for its application. While Archer chose the more classical way of production in a horizontal integration model, outsourcing over 80% of its components [145]. According to Archer, this approach results in lower initial investments and a smoother market entry, as many subsystems from suppliers are already fully certified.

In-house production offers several advantages, and more so in serial production contexts. Intellectual property and innovation are critical in the aerospace industry, making it safer to shield competitors from accessing technical details and innovations. For instance, the novel hinge mechanism used in the *Swing*, to realise the transformative wing concept, benefits from in-house production by reducing the risk of leaks. Quality control is another significant reason for choosing self-production; it is easier to perform it in-house than outsourced, which adds another layer of quality control to the production process. An incident in January 2024 involving a Boeing 737-MAX, where a door blew out mid-flight, highlighted quality issues with a subcontractor-produced door handle. Although subcontracted components can undergo quality assurance, in-house production provides greater control over product quality. This may be less relevant in the initial production stages due to the small team size, but it becomes crucial as production scales up. Moreover, supply-chain risks are also to be considered, as outsourcing can introduce delays if any contractor fails to deliver on time, potentially disrupting the entire production line and causing significant economic losses. However, the Technical Risk Analysis (Chapter 4) accounts for these risks posed with horizontal integration; thus the team is readily prepared for such situations.

Despite the earlier stated disadvantages, outsourcing also has its benefits. For components requiring highly specialised machinery, starting new in-house production lines can severely increase the production costs, thus higher startup cost, which will increase the price of the *Swing*. Subcontractors often specialise in specific technological areas, providing high-quality products that meet the requirements while already having the highly needed equipment available. For instance, the outsourcing of electric motors, as described in Section 10.3, is more cost-effective and time-efficient than investing heavily in R&D and production facilities. Outsourcing can also account for the scalability of this project, allowing specialised companies to produce larger batches of components or reduce production during slowdowns without the need to shut down factories.

20.2. Production Method by Subsystem

Understanding the main criteria for choosing between in-house production and outsourcing, allows drawing some conclusions for each subsystem, as well as the fact that more subsystems have already been defined in their respective chapters. The criteria considered are outlined in Table 20.1. In each chapter, the subsystem was evaluated against these criteria to determine the most advantageous production method, as well as concluding if in-house production is even possible. For the sake of clarity, the results are summarised in Table 20.2.

Table 20.1: Evaluation criteria production method

ID	Criterion	Description
PR-01	Costs	Costs related to the production
PR-02	Expertise required	Specific knowledge and expertise needed
PR-03	Quality control	Expected production quality of the product
PR-04	Confidential technology	Need to protect novel technology from competitors
PR-05	Supply chain	Dependency and availability of the supply chain
PR-06	Scalability	Flexibility of scaling production up or down

Table 20.2: Subsystem production methods

Subsystem	Method	Reasoning	Supplier
Electric motor	Outsource	High development costs and specialised knowledge needed	Emrax
Landing Gear	Outsource	Common component produced by multiple companies	Liebherr
Fuselage	Outsource	High-quality control and supply chain stability	N/A
Hinge Mechanism	In-house	Protect intellectual property of novel technology	N/A
Battery cells	Outsource	High-performance product produced by few companies	Melasta
Electronics and Wiring	Outsource	Numerous suppliers offer off-the-shelf products	Collins Aerospace
Autonomous System	Outsource	Market has several specialised companies	Collins Aerospace
Wings and Control Surfaces	In-house	High-quality control and supply chain stability	N/A
Bolts, Fasteners	Outsource	Numerous suppliers offer off-the-shelf products	TriMas Aerospace
Glass windows	Outsource	Common component produced by multiple companies	Swift Glass
Sensors	Outsource	Market has several specialised companies	Honeywell
Structural elements	Outsource	Common components produced by several companies	Magellan Aerospace

20.3. Assembly Line

Once the necessary in-house and outsourced components are produced and delivered respectively, the *Swing eVTOL* can be assembled. Most notably, the production philosophy is based on outsourcing as much as possible, which is favourable for this project. Although, the main assembly will be performed in-house, to account for specific design customisation. Each subsystem is first assembled in its own subassembly line, which then progresses through the production line until the final assembly station. For example, the wing comprises several subassemblies that are individually assembled before being combined in the final wing assembly line.

The final aircraft assembly begins after the fuselage parts are joined. Subsequently, all subsystems are mounted onto the vehicle, making up for the completed product. The optimisation and coordination between different departments are important to ensure a time- and cost-effective production. Furthermore, quality control is crucial throughout the manufacturing and assembly process. Guaranteeing quality at each station, and thus subassembly, helps identify and correct flaws early in production. It shows the chronological order of the total process, however, specific time spans per phase have not yet been established.

21. Future Development Of Project

Now that the *Swing* design has been detailed and expanded, there are only several steps required to make this design a reality. In this chapter, the future of the *Swing* project is expanded upon. First and foremost, a development logic diagram shall be created. Based on this diagram, a detailed Gantt Chart is constructed.

21.1. Design and Development Logic

This section presents the design and development logic for the future. Based on the flow diagram showcased in Figure 21.1, it can be seen that there are nine more steps that have to be finalised before the design reaches maturity. The first step that has to be performed is the finalisation of the detailed aircraft design. This has to be done taking into account the requirements that have not yet been complied with, as described in Chapter 22. Thus, the wind gust performance, especially during the hover phase, should be analysed, as well as the roll performance and the hinge design.

After the conceptual design is completed, it is crucial that the team ensures that there is sufficient financial backing in order to achieve success. This can be achieved through the promotion of the design to different operators, as well as negotiations with different potential investors.

An example of a desired investor for the *Swing eVTOL* project would be an airline company such as KLM. A crucial marketing aspect of the *Swing eVTOL* design is the fact that the design is a great solution for the “last-mile problem”. Therefore, the design can be marketed as a feeder system for the airlines to take VIP passengers and bring them to the aircraft in a quicker and more efficient way. This would enable picking passengers up from the city centre of Amsterdam and bringing them to the airport within half an hour, avoiding traffic and the hustle of public transport. Another positive aspect of the design is that it would enable KLM to compete with companies such as NS on the short-haul segment of business passengers. Therefore, there are plenty of reasons why an airline such as KLM would be persuaded to ensure financial backing for the *Swing* project.

With the financial backing ensured, the prototype of the design should be produced and then tested, in order to reach certified status. Once certification of the design is ensured, the design should be marketed to different operators. This would enable the start of mass production, which would lead to commercial operation commencement. Lastly, customer support should be provided by the manufacturer to the customers to achieve a successful end product.

Based on the aforementioned considerations, the project development logic diagram was constructed and is showcased in more detail in Figure 21.1. It is important to note that the diagram has three layers of detail. More detail is presented in the first layers due to closer proximity to the current state of the project and thus a more clear overview of the required steps left to be taken, especially when considering finalising the design.

21.2. Gantt Chart

After the future steps that have to be taken for the project have been expanded upon, a more detailed Gantt Chart can be provided. This shall contain all the relevant tasks that are yet to be performed, along with the responsible person and the expected number of hours. The Gantt Chart is showcased in the Appendix.

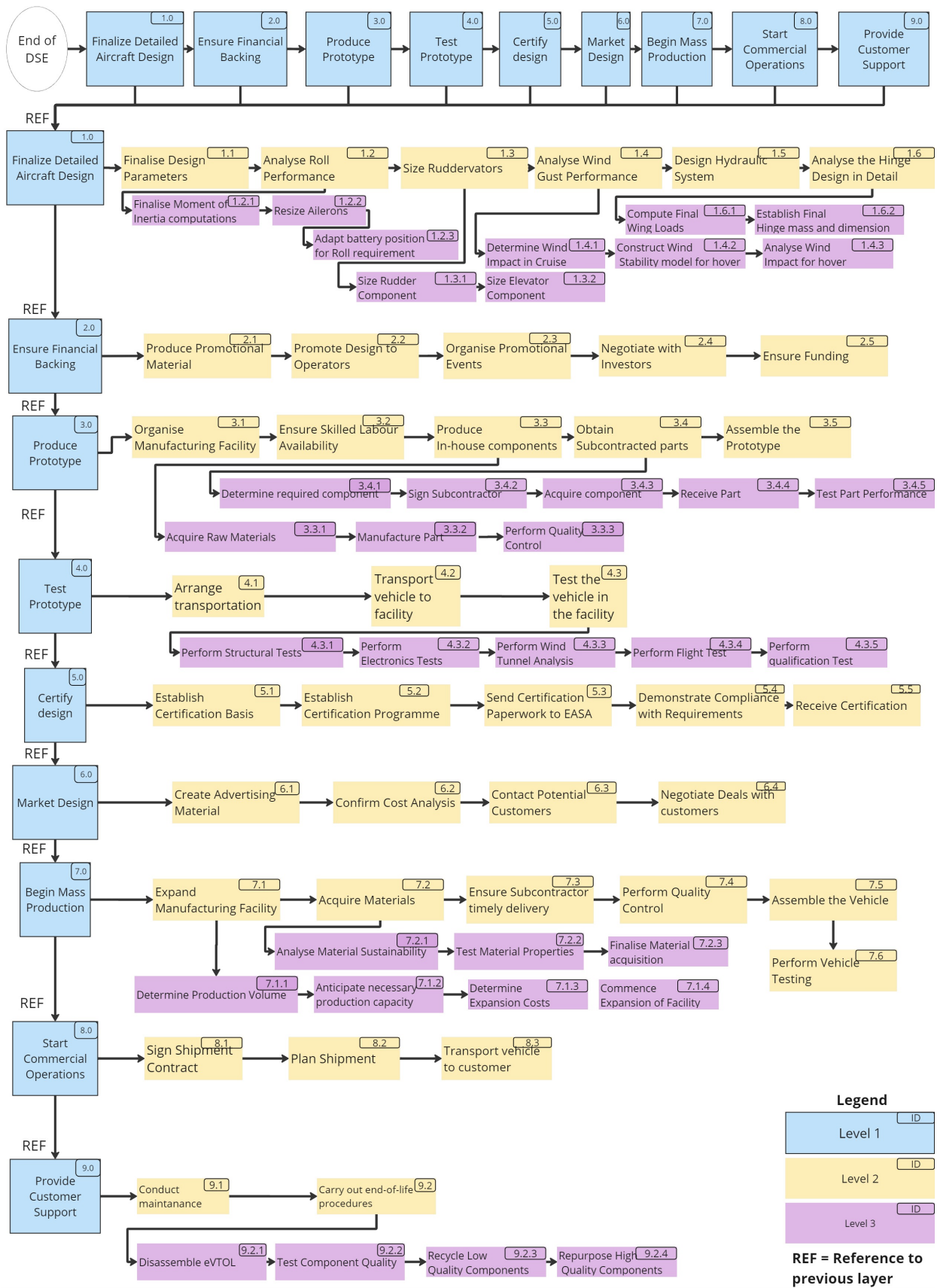


Figure 21.1: Project logic diagram

22. Requirements Compliance

An important step to be considered, when analysing the progress of the *Swing* design, is determining the requirement compliance. This can be done based on the requirements compliance matrix, which contains information with regard to the completion of a given criteria, justification for the status of the requirement, as well as steps necessary to be taken to ensure compliance in the future. First and foremost, a list of all the key requirements and constraints is provided in this section. Afterwards, based on the key requirements, the compliance matrix shall be detailed. Hence, the first thing that shall be presented in this section is a list of all the key requirements and constraints, as defined in the Baseline Report [146]. The key requirements for the design are to be found Table 22.2.

Table 22.1: Key requirements

Air Taxi Operators (STK 03)	
TE-1-STK03-1-1	The vehicle shall be able to charge at a minimum power of 250[KW]
TE-1-STK03-3	The vehicle shall be able to carry at least 400 [kg] of payload
TE-1-STK03-4-1	The vehicle shall be able to fly autonomously.
Maintenance Contractors (STK 06)	
TE-1-STK06-3-1	The vehicle components requiring regular maintenance shall be easily accessible.
Passengers (STK 07)	
TE-2-STK07-3-2	The vehicle shall have a cruise speed of 200 [km/h]
TE-2-STK07-5-2	The vehicle shall be able to withstand winds of up to 7 Beaufort.

Another important aspect to consider in the compliance matrix is the constraints that have been imposed on the design phase, in order to reach a successful design as well as satisfy the different stakeholders. The constraints on the design are given in Table 22.2 and have been determined based on the Baseline report [146].

Table 22.2: Key constraints

Private Customers (STK 05)	
CO-1-STK05-1	The vehicle cost of production per unit shall be less than 2000k[€].
Passengers (STK 07)	
CO-3-STK07-1	The vehicle predicted reliability shall be of maximum one failure per million flight hours (10^{-6} reliability) [50].
CO-3-STK07-2	Cabin noise shall never exceed 60dBA
Air Taxi Operators (STK 03)	
CO-3-STK03-1	The vehicle shall be able to fly with only 75% of the propulsion system working.
CO-3-STK03-2	The disk loading shall be kept below 400 kg/m ² at all times, during nominal flight.
CO-3-STK03-3	The vehicle shall have a design thrust to weight ratio of 2.
Environmental Organisations (STK 13)	
CO-4-STK13-1-1	The vehicle shall be fully electric
CO-4-STK13-1-4	The vehicle shall have maximum dimensions of 8x4x2 m ³ on the ground.
CO-4-STK13-1-5	The vehicle shall have a lifetime greater than 10 years
CO-4-STK13-1-6	The vehicle structure shall be reusable for at least 10 years after its life.
Affected Public (STK 14)	
CO-5-STK14-1-1	The noise level at 500[m] from the vehicle shall not exceed 45.2[dB].
National Government (STK 16)	
CO-5-STK16-1-1	The vehicle shall have an electric power autonomy of 100 km plus reserve.
Aircraft Regulators (STK 21)	
CO-5-STK21-1-1	The vehicle shall comply with CS23 Roll Requirements
CO-5-STK21-1-2	The vehicle shall comply with CS23 lateral control engine inoperative requirement

Now that the key requirements and constraints have been listed, the compliance matrix can be realised. Thus, it will be assessed whether each requirement has been complied with, and a justification for the conclusion is provided. Additionally, further steps will be mentioned wherever necessary. As it shall be, most of the main requirements are complied with. The only aspects that are not compliant are the roll requirement and the wind gust requirement. The compliance matrix is provided in Table 22.3

After all the requirements have been verified, it is important to understand the impact that each of the non-compliant requirements may have on the design of the *Swing*. A small explanation of the impact caused by the lack of compliance shall be given in Table 22.4.

Table 22.3: Compliance matrix

Requirement Code	Status	Justification	Further Steps
TE-1-STK03-1-1	Complaint	The value was discussed in Chapter 13	
TE-1-STK03-3	Compliant	Sizing was performed with payload weight in mind. Value was assumed in CG computations in Section 11.3.1	-
TE-1-STK-04-1	Compliant	Autonomous Control designed in Chapter 12	Tune PID controller algorithm
TE-1-STK-06-3-1	To be complied	No analysis of accessibility of components has been considered yet	Perform maintenance accessibility analysis
TE-2-STK07-3-2	Compliant	Mission Profile Sized taking requirement into account	-
TE-2-STK07-5-2	To be Complied	No Wind Gust sizing performed as of this moment	Perform hover dynamic analysis and check wind gust requirement
Co-1-STK05-1	Compliant	Explained in Cost analysis in Chapter 19	-
Co-3-STK07-1	To be Complied	No analysis was performed on reliability yet	Determine components reliability and whether the requirement is respected
Co-3-STK03-1	Compliant	Vertical Tail sizing takes into account 3 engine failure, hover controllability accounts for two engine failure. Power is also sized to ensure enough thrust in 75% power scenario	-
Co-3-STK03-2	Compliant	Engine selection allows to keep the disk loading below 400 kg/m ²	-
Co-3-STK03-3	Compliant	Propulsion sized for a T/W of 2	-
Co-3-STK07-2	Compliant	Appropriate fuselage soundproofing was designed, following from near-field noise estimations	-
Co-4-STK13-1-1	Compliant	Showcased in Chapter 13	-
Co-4-STK13-1-4	Compliant	Showcased in Fuselage Design, empennage sized for requirement	-
Co-4-STK13-1-5	Compliant	The batteries in the nacelles are easily replaced without the disassembling of the rest of the aircraft and the rest of the structure is predicted to last longer than 10 years.	-
Co-4-STK13-1-6	Compliant	The “Cradle-to-Cradle” concept allows a long-term reusability of the aircraft components	-
Co-5-STK14-1-1	Compliant	Justified in Section 10.2.1	-
Co-5-STK16-1-1	Compliant	Justified in Section 6.3.2	-
CO-5-STK21-1-1	Discarded	Roll requirement is not achieved due to Battery placement as shown in Section 11.8	Adapt Battery placement and iterate
CO-5-STK21-1-2	Compliant	Taken into account in the sizing of the vertical tail	-

Table 22.4: Impact of non-compliant requirements on design

Requirement Code	Impact on Design
TE-1-STK06-3-1	Reduced accessibility of the design can lead to a negative public perception of the design as well as reduced passenger numbers.
TE-2-STK07-5-2	Reduced wing gust resistance may lead to the impossibility of operating the design for long periods of time. A reduced dependability on the design leading to the reduced number of vehicles sold will be the impact on the design.
CO-3-STK07-1	Poor reliability can lead to long periods of time where the vehicle is unusable, leading to losses for the operator and therefore reducing the number of sold vehicles.
CO-5-STK21-1-1	Roll requirement not reached can lead to difficulty in certifying the design, as well as difficulty in controllability of the aircraft and obstacle avoidance.

23. Conclusion and Recommendations

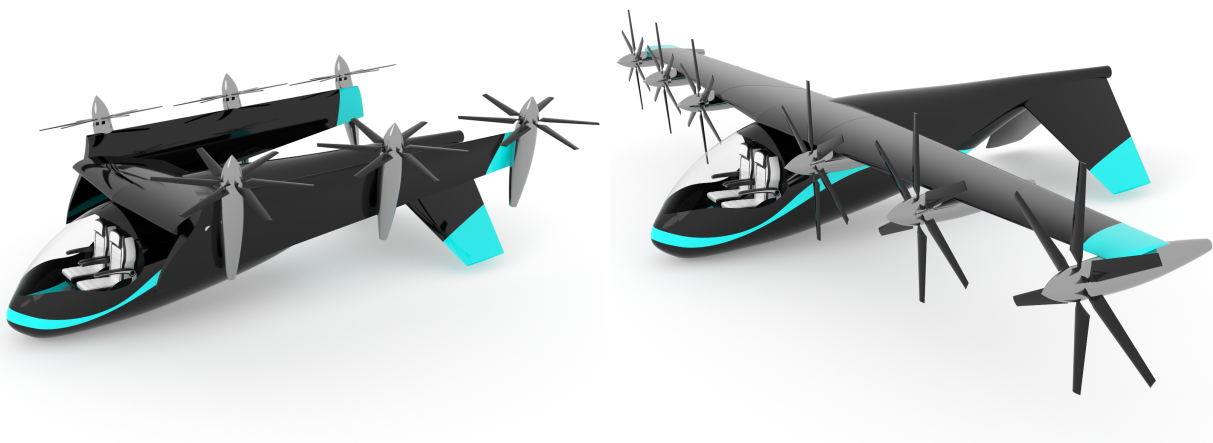
The increasing population density in metropolitan areas, coupled with the faster pace of everyday life, calls for the development of Inter-Urban Air Mobility (UAM) solutions. Currently, there is a gap in the market since there is no competitor that can facilitate all market segments and also provide “last-mile transport” by air. This is where the mission of this project comes into play, with the following objective:

“Design a low ground footprint, sustainable, urban transwing electric Vertical Take-Off and Landing vehicle within production costs of 2 M€, by ten students in ten weeks time.”

The final design achieved this objective, and its performance makes it a very competitive eVTOL. The final design can be found in Figure 23.1a and Figure 23.1, and its parameters can be found in Table 23.1. The biggest advantage of the *Swing eVTOL* is its ground footprint of 32 m², which is more than half the main competitors. Furthermore, its range is 1.4 times longer than the *Joby S4* and more than three times as much as the *Archer Midnight*. Finally, it is also 10% more energy efficient than *Joby S4*, currently the most efficient eVTOL. And all of these advantages come at a very competitive price, making the *Swing eVTOL* a very attractive aircraft for aircraft operators.

Table 23.1: Final design parameters of the *Swing eVTOL*.

MTOW	1643	kg	Wing span	14.0	m
OEM	1243	kg	Wing area	14.0	m ²
Range	250	km	MAC	1.06	m
Payload	400	kg	Fuselage length	8.0	m
Battery mass	400	kg	No. Engines	6	–
Cruise speed	200	km/h	Battery energy	120	kWh
Stall speed	105	km/h	No. Passengers	4	–
Total Power	344	kW	Production Cost	1.42	M€
Consumed Power in Cruise	0.162	kWh/km	Ground Footprint	32	m ²



(a) Final design of *Swing eVTOL* in hover configuration

(b) Final design of *Swing eVTOL* in cruise configuration

Figure 23.1: Final design of *Swing eVTOL*

Given the limited time available to produce this report, for each subsystem, there are some recommendations to further develop the design of the *Swing eVTOL*. Firstly, for control and stability, it is recommended that another design iteration be done on the empennage and aircraft to improve the roll rate performance of

the aircraft as well as improving the spiral performance, which is currently too unstable to be considered controllable. Then, for the structure subsystem, it is recommended that the hinge is comprehensively sized also for dynamic loading, since the report now only considers static loading. For the electrical system, the next step is to look at the heat generated by the batteries and to design a cooling system to deal with this heat properly. The autonomous control can be improved by dynamic modelling for the different flight phases and tuning of the controllers. Finally, it is recommended that for propulsion, a Blade Element Momentum model is implemented since the current propeller sizing is based on empirical methods.

These recommendations aim to refine and optimise the already strong design, ensuring that the *Swing eVTOL* remains at the forefront of the emerging UAM market.

References

- [1] Daniel P. Raymer. *Aircraft Design: A Conceptual Approach*. Second Edition. AIAA Education Series. Washington, DC: American Institute of Aeronautics and Astronautics, Inc., 1992. ISBN: 0-930403-51-7.
- [2] Peter D. Sharpe. ‘AeroSandbox: A Differentiable Framework for Aircraft Design Optimization’. MA thesis. Massachusetts Institute of Technology, 2021.
- [3] Guang-Xun Du, Quan Quan, Binxian Yang et al. ‘Controllability analysis for multirotor helicopter rotor degradation and failure’. In: *Journal of Guidance, Control, and Dynamics* 38.5 (2015), pp. 978–985. DOI: <https://doi.org/10.2514/1.G000731>.
- [4] Brian Roth. *Control Power Design Requirements for Aircraft Flying Qualities*. 2009.
- [5] L.E. Kavvaki, P. Svestka, J.-C. Latombe et al. ‘Probabilistic roadmaps for path planning in high-dimensional configuration spaces’. In: *IEEE Transactions on Robotics and Automation* 12.4 (1996), pp. 566–580. DOI: 10.1109/70.508439.
- [6] Paul Oberlin, Sivakumar Rathinam and Swaroop Darbha. ‘Today’s Traveling Salesman Problem’. In: *IEEE Robotics & Automation Magazine* 17.4 (2010), pp. 70–77. DOI: 10.1109/MRA.2010.938844.
- [7] R. (Rens) Werink. *On the Control Allocation of Fully-Actuated and Over-Actuated Multirotor UAVs*. MSc Report 001RAM2019. Enschede, The Netherlands: University of Twente, Jan. 2019.
- [8] Yih Tang Yeo and Hugh H. Liu. ‘Transition Control of a Tilt-Rotor VTOL UAV’. In: *2018 AIAA Guidance, Navigation, and Control Conference*. DOI: <https://doi.org/10.2514/6.2018-1848>.
- [9] Maidul Islam and Mohamed Okasha. ‘A Comparative Study of PD, LQR and MPC on Quadrotor Using Quaternion Approach’. In: *2019 7th International Conference on Mechatronics Engineering (ICOM)*. 2019, pp. 1–6. DOI: 10.1109/ICOM47790.2019.8952046.
- [10] Angel Romero, Sihao Sun, Philipp Foehn et al. ‘Model Predictive Contouring Control for Time-Optimal Quadrotor Flight’. In: *IEEE Transactions on Robotics* PP (Dec. 2022), pp. 1–17. DOI: 10.1109/TR0.2022.3173711.
- [11] Rusinkiewicz Szymon, Weyrich Tim, Matusik Wojciech et al. ‘3 - ACQUISITION’. In: *Point-Based Graphics*. Ed. by MARKUS GROSS and HANSPETER PFISTER. The Morgan Kaufmann Series in Computer Graphics. Burlington: Morgan Kaufmann, 2007, pp. 18–93. ISBN: 978-0-12-370604-1. DOI: <https://doi.org/10.1016/B978-012370604-1/50004-3>.
- [12] Manfred Hader, Stephan Baur, Sven Kopera et al. ‘Urban air mobility, USD 90 billion of potential: how to capture a share of the passenger drone market’. In: *Roland Berger* (2020).
- [13] Technavio. *Urban Air Mobility (UAM) Market Analysis North America, Europe, APAC, Middle East and Africa, South America - US, China, Germany, UK, France - Size and Forecast 2023-2027*. Accessed: 10-6-2024. Feb. 2023. URL: <https://www.technavio.com/report/urban-air-mobility-market-analysis>.
- [14] Rohit Goyal, Colleen Reiche, Chris Fernando et al. ‘Advanced air mobility: Demand analysis and market potential of the airport shuttle and air taxi markets’. In: *Sustainability* 13.13 (2021), p. 7421. DOI: <https://doi.org/10.3390/su13137421>.
- [15] Qi Long, Jun Ma, Feifeng Jiang et al. ‘Demand analysis in urban air mobility: A literature review’. In: *Journal of Air Transport Management* 112 (2023), p. 102436. DOI: <https://doi.org/10.1016/j.jairtraman.2023.102436>.
- [16] Stephan Baur, Stephan Schickram, Andre Homulenko et al. ‘Urban air mobility - The rise of a new mode of transportation’. In: *Roland Berger* (2018).
- [17] UK Air Mobility Consortium. *The launch of electric urban aviation*. 2022.
- [18] European Union Aviation Safety Agency (EASA). *Vertiports Prototype Technical Specifications for the Design of VFR Vertiports for Operation with Manned VTOL-Capable Aircraft Certified in the Enhanced Category (PTS-VPT-DSN)*. 2022.
- [19] Berna Gungen, Catarina Araújo, Hylke Broekema et al. *Verkennde Studie Vertiports Eindrapport*. Eindrapport/versie 02. Nov. 2023.

- [20] McKinsey Company. ‘Study on the societal acceptance of Urban Air Mobility in Europe’. In: (2021).
- [21] Paul S Moller. *Review of Selected Advanced Air Mobility Aircraft*. 2022.
- [22] Kyle A Pascioni, Michael E Watts, Mary Houston et al. ‘Acoustic flight test of the joby aviation advanced air mobility prototype vehicle’. In: *28th AIAA/CEAS Aeroacoustics 2022 Conference*. 2022, p. 3036. DOI: <https://doi.org/10.2514/6.2022-3036>.
- [23] Lilium. ‘Designing a scalable vertiport’. In: *Lilium Newsroom* (July 2020). URL: <https://lilium.com/newsroom-detail/designing-a-scalable-vertiport>.
- [24] UK Air Mobility Consortium. *Urban Air Mobility Concept of Operations for the London Environment*. 2022.
- [25] The Vertical Flight Society. *eVTOL Aircraft Directory*. Accessed: 2024-06-10. 2024. URL: <https://evtol.news/aircraft>.
- [26] Joby Aviation. *Joby Confirms Revolutionary Low Noise Footprint Following NASA Testing*. Accessed: 2024-06-14. 2022. URL: <https://www.jobyaviation.com/news/joby-revolutionary-low-noise-footprint-nasa-testing/>.
- [27] Osita Ugwueze, Thomas Statheros, Nadjim Horri et al. ‘An Efficient and Robust Sizing Method for eVTOL Aircraft Configurations in Conceptual Design’. In: *Aerospace* 10 (Mar. 2023), p. 311. DOI: <https://doi.org/10.3390/aerospace10030311>.
- [28] J. Roskam. *Airplane Design*. Airplane Design dl. 5. DARcorporation, 1985. ISBN: 9781884885501. URL: <https://books.google.nl/books?id=mMU47Ld7yQkC>.
- [29] Matthew Kelly. ‘An Introduction to Trajectory Optimization: How to Do Your Own Direct Collocation’. In: *SIAM Review* 59.4 (2017), pp. 849–904. DOI: <https://doi.org/10.1137/16M1062569>.
- [30] Joel A E Andersson, Joris Gillis, Greg Horn et al. ‘CasADi – A software framework for nonlinear optimization and optimal control’. In: *Mathematical Programming Computation* 11.1 (2019), pp. 1–36. DOI: <https://doi.org/10.1007/s12532-018-0139-4>.
- [31] Andreas Wächter and Lorenz T. Biegler. ‘On the implementation of an interior-point filter line-search algorithm for large-scale nonlinear programming’. In: *Mathematical Programming* 106.1 (2006), pp. 25–57. ISSN: 0025-5610. DOI: <https://doi.org/10.1007/s10107-004-0559-y>.
- [32] Roelof Vos, Maurice F.M. Hoogreef and Barry T.C. Zandbergen. *Aerospace Design and Systems Engineering Elements I – AE1222-II*. Presentation slides. TU Delft. 2024.
- [33] Noah López, Alejandro Santamaría and Saullo Castro. ‘Preliminary aerodynamic design and load calculation of a long-range eVTOL aircraft’. In: Jan. 2022. DOI: 10.2514/6.2022-1331.
- [34] Luca Piancastelli, Merve Sali and Christian Leon-Cardenas. ‘Basic considerations and conceptual design of a VSTOL vehicle for urban transportation’. In: *Drones* 6.5 (2022), p. 102. DOI: <https://doi.org/10.3390/drones6050102>.
- [35] Richard Eppler. *Airfoil design and data*. Berlin, Heidelberg: Springer-Verlag Berlin Heidelberg, 1990. ISBN: 978-3-662-02648-9. DOI: 10.1007/978-3-662-02646-5.
- [36] *afCDB: Airfoil Database*. <https://aerodynamics.lr.tudelft.nl/cgi-bin/afCDB>. Accessed: 2024-06-05. 2024.
- [37] RHM Goossens, CJ Snijders and T Fransen. ‘Biomechanical analysis of the dimensions of pilot seats in civil aircraft’. In: *Applied ergonomics* 31.1 (2000), pp. 9–14. DOI: [https://doi.org/10.1016/S0003-6870\(99\)00028-9](https://doi.org/10.1016/S0003-6870(99)00028-9).
- [38] Xinhe Yao, Yayu Ping, Yu Wolf Song et al. ‘Sitting comfort in an aircraft seat with different seat inclination angles’. In: *International Journal of Industrial Ergonomics* 96 (2023), p. 103470. DOI: <https://doi.org/10.1016/j.ergon.2023.103470>.
- [39] Snorri Gudmundsson, ed. *General Aviation Aircraft Design: Applied Methods and Procedures*. Butterworth-Heinemann, 2013. ISBN: 978-0-12-397308-5.
- [40] RD Finck, DE Ellison and LVPI Malthan. ‘USAF (United States Air Force) Stability and Control DATCOM (Data Compendium)’. In: *Defense Technical Information Center* (1978).
- [41] M. Pavel. *Helicopter Performance Reader*. Course material. Course conducted at TU Delft. TU Delft, 2023.

- [42] Federal Aviation Administration. *Helicopter Flying Handbook*. Vol. Chapter 2. Federal Aviation Administration, 2019. URL: https://www.faa.gov/sites/faa.gov/files/regulations_policies/handbooks_manuals/aviation/helicopter_flying_handbook/hfh_ch02.pdf.
- [43] Akshay R Kadhiresan and Michael J Duffy. ‘Conceptual design and mission analysis for eVTOL urban air mobility flight vehicle configurations’. In: *AIAA aviation 2019 forum*. 2019, p. 2873. DOI: <https://doi.org/10.2514/6.2019-2873>.
- [44] Srikanth Goli, Dilek Funda Kurtuluş, Luai M Alhems et al. ‘Experimental study on efficient propulsion system for multicopter UAV design applications’. In: *Results in Engineering* 20 (2023), p. 101555. DOI: <https://doi.org/10.1016/j.rineng.2023.101555>.
- [45] Javier Alba-Maestre, Egon Beyne, Michael Buszek et al. *Final Report - Multi-Disciplinary Design and Optimisation of a Long-Range eVTOL Aircraft*. Nov. 2021. DOI: 10.5281/zenodo.5576103.
- [46] D Felix Finger, Carsten Braun and Cees Bil. ‘A review of configuration design for distributed propulsion transitioning VTOL aircraft’. In: *Asia-Pacific International Symposium on Aerospace Technology-APISAT*. Korean Soc. for Aeronautical and Space Sciences Seoul, Korea. 2017, pp. 3–5.
- [47] M Judd and SJ Newman. ‘An analysis of helicopter rotor response due to gusts and turbulence’. In: (1975).
- [48] Akshay R Kadhiresan and Michael J Duffy. ‘Conceptual design and mission analysis for eVTOL urban air mobility flight vehicle configurations’. In: *AIAA aviation 2019 forum*. 2019, p. 2873. DOI: <https://doi.org/10.2514/6.2019-2873>.
- [49] Youngshin Kang, Am Cho, Seongwook Choi et al. ‘Evaluating one engine inoperative conditions in subscale electric vertical take-off and landing aircraft: An in-depth tethered hover test analysis’. In: *Proceedings of the Institution of Mechanical Engineers, Part G: Journal of Aerospace Engineering* 238.3 (2024), pp. 303–317. DOI: <https://doi.org/10.1177/09544100231220471>.
- [50] NASA. ‘Aircraft Working Group: Expected Safety Level for AAM’. In: *NASA Advanced Air Mobility (AAM)*. 2022.
- [51] J.A. Melkert Th. van Holten. *Helicopter Performance, Stability and Control*. Translation and revision of the original Dutch version by Ben Marrant and Marilena Pavel. 2002.
- [52] Marilena D Pavel. ‘Understanding the control characteristics of electric vertical take-off and landing (eVTOL) aircraft for urban air mobility’. In: *Aerospace Science and Technology* 125 (2022), p. 107143. DOI: <https://doi.org/10.1016/j.ast.2021.107143>.
- [53] Furkat Yunus, Damiano Casalino, Francesco Avallone et al. ‘Efficient prediction of urban air mobility noise in a vertiport environment’. In: *Aerospace Science and Technology* 139 (2023), p. 108410. DOI: <https://doi.org/10.1016/j.ast.2023.108410>.
- [54] D. W. Kurtz J. E. Marte. ‘A Review of Aerodynamic Noise From Propellers, Rotors, and Lift Fans’. In: *Technical Report 32-7462* (Jan. 1970).
- [55] William J Fredericks, Mark D Moore and Ronald C Busan. ‘Benefits of hybrid-electric propulsion to achieve 4x cruise efficiency for a VTOL UAV’. In: *2013 International Powered Lift Conference*. 2013, p. 4324. DOI: <https://doi.org/10.2514/6.2013-4324>.
- [56] Panagiotis Alexandros Koutsoukos. ‘Aerodynamic and Aeroacoustic Interaction Effects of a Distributed-Propeller Configuration in Forward Flight’. MA thesis. Delft University of Technology, 2022.
- [57] AcousticalEngineer.com. *A-Weighting table*. URL: <https://acousticalengineer.com/a-weighting-table/>.
- [58] E. Hartman D. Biermann. *Wind-tunnel tests of four- and six-blade single- and dual-rotating tractor propellers*. NASA Technical Report. 1993.
- [59] Andrew Wood. *Aircraft Engine and Propeller Sizing*. URL: <https://aerotoobox.com/thrust-cruise-speed/#propeller-pitch>.
- [60] Tom CA Stokkermans, Daniele Usai, Tomas Sinnige et al. ‘Aerodynamic interaction effects between propellers in typical eVTOL vehicle configurations’. In: *Journal of Aircraft* 58.4 (2021), pp. 815–833. DOI: <https://doi.org/10.2514/1.C035814>.
- [61] Tao Zhang, GN Barakos et al. ‘On the aerodynamic performance of redundant propellers for multi-rotor eVTOL in cruise’. In: *Aerospace Science and Technology* 145 (2024), p. 108846. DOI: <https://doi.org/10.1016/j.ast.2023.108846>.

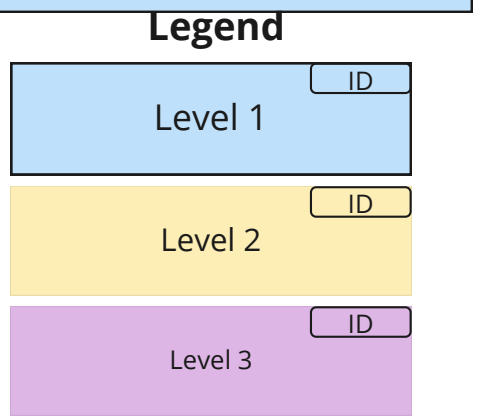
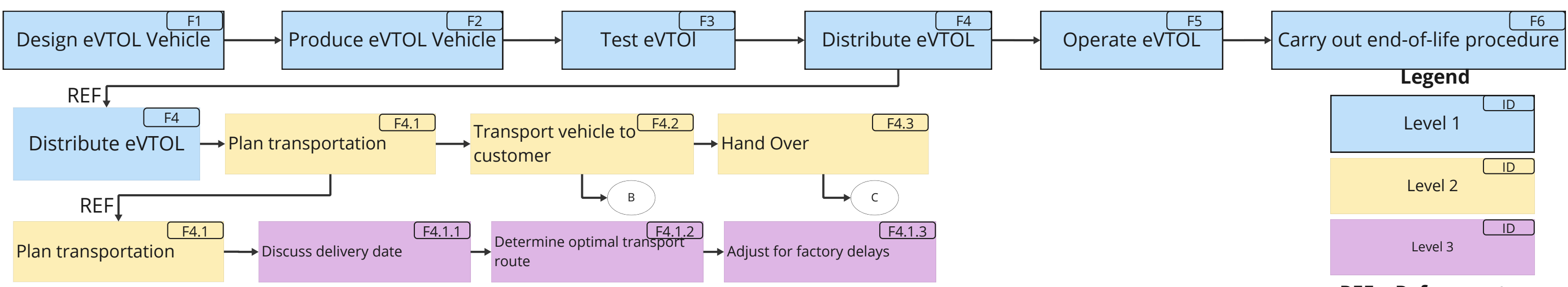
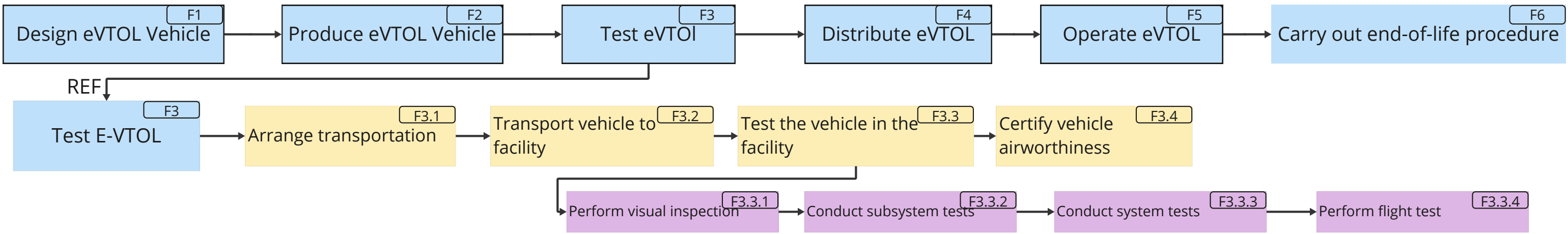
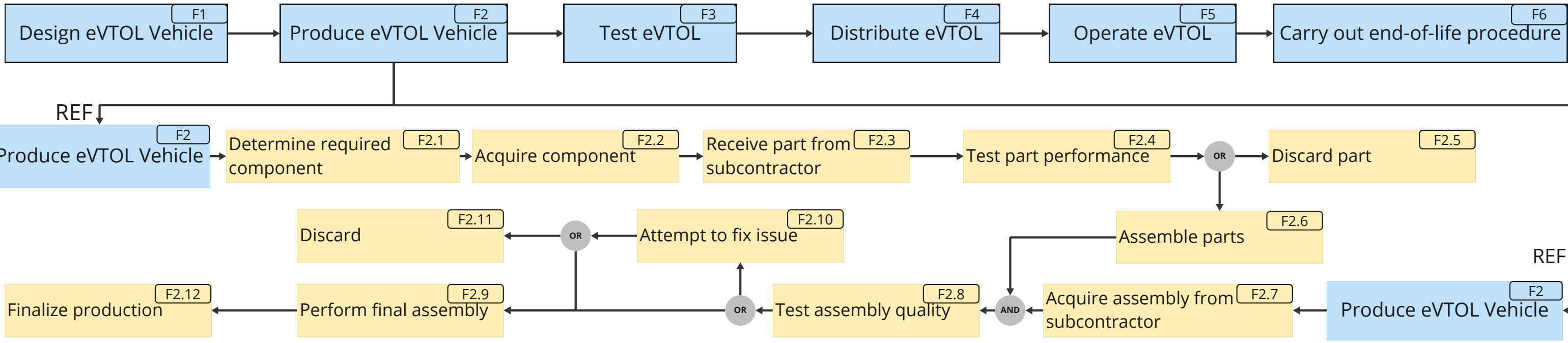
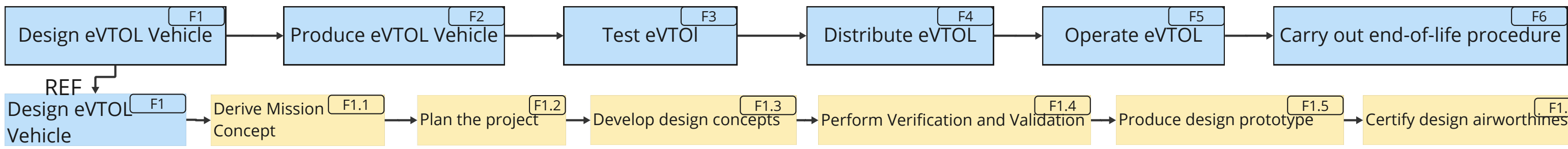
- [62] Emanuel A Marcus, Reynard de Vries, Akshay Raju Kulkarni et al. 'Aerodynamic investigation of an over-the-wing propeller for distributed propulsion'. In: *2018 AIAA Aerospace Sciences Meeting*. 2018, p. 2053. DOI: <http://dx.doi.org/10.2514/6.2018-2053>.
- [63] Donald R Boldman, C Iek, DP Hwang et al. 'Effect of a rotating propeller on the separation angle of attack and distortion in ducted propeller inlets'. In: *Aerospace Sciences Meeting and Exhibit*. NASA-TM-105935. 1993. DOI: <https://doi.org/10.2514/6.1993-17>.
- [64] Jian Guo. 'Project Management and Systems Engineering in the DSE'. In: *AE3200* (2024).
- [65] European Union Aviation Safety Agency. *Certification Specifications for Normal-Category Aeroplanes (CS-23)*. Accessed: 25-05-2024. EASA. Cologne, Germany, 2020. URL: <https://www.easa.europa.eu/document-library/certification-specifications/cs-23-amendment-5>.
- [66] Eric M Hadder and Timothy T Takahashi. 'Minimum Control Speed Estimation for Conceptual Design'. In: *17th AIAA Aviation Technology, Integration, and Operations Conference*. 2017, p. 3764. DOI: <https://doi.org/10.2514/6.2017-3764>.
- [67] 'Design of Control Surfaces'. In: *Aircraft Design*. John Wiley & Sons, Ltd, 2012. Chap. 12, pp. 631–753. ISBN: 9781118352700. DOI: <https://doi.org/10.1002/9781118352700.ch12>.
- [68] Paul Pounds, Robert Mahony, Peter Hynes et al. 'Design of a four-rotor aerial robot'. In: *The Australian Conference on Robotics and Automation (ACRA 2002)*. 2002, pp. 145–150.
- [69] J. Roskam and University of Kansas. *Airplane Design: Part 2 - preliminary configuration design and integration of the propulsion system*. DARcorporation, 1985. URL: <https://books.google.nl/books?id=1Ia-tAEACAAJ>.
- [70] Dieter Scholz. 'Empennage sizing with the tail volume complemented with a method for dorsal fin layout'. In: *INCAS bulletin* 13.3 (2021), pp. 149–164. DOI: <https://doi.org/10.13111/2066-8201.2021.13.3.13>.
- [71] HAW University Hamburg. *9-Empennage General Design*. URL: https://www.fzt.haw-hamburg.de/pers/Scholz/H00U/AircraftDesign_9_EmpennageGeneralDesign.pdf.
- [72] Universidad de Sevilla. *Chapter 6 Tail Design*. URL: http://aero.us.es/adesign/Slides/Extra/Stability/Design_Tail/Chapter%206.%20Tail%20Design.pdf.
- [73] Egbert Torenbeek. 'Synthesis of Subsonic Airplane Design'. In: (1982). DOI: <https://doi.org/10.1007/978-94-017-3202-4>.
- [74] Bernard Etkin and Lloyd Duff Reid. *Dynamics of Flight: Stability and Control*. 3rd. ISBN: 978-0-471-03418-6. New York: John Wiley & Sons, 1996. DOI: 10. xxxx/xxxxx.
- [75] J.A. Mulder, W.H.J.J. van Staveren, J.C. van der Vaart et al. *Flight Dynamics Lecture Notes*. Delft University of Technology, 2013.
- [76] David A. Caughey. *Introduction to Aircraft Stability and Control Course Notes for M&AE 5070*. Sibley School of Mechanical & Aerospace Engineering Cornell University - Ithaca, New York, 2011.
- [77] HAW University Hamburg. *11 Empennage Sizing*. URL: https://www.fzt.haw-hamburg.de/pers/Scholz/H00U/AircraftDesign_11_EmpennageSizing.pdf.
- [78] HAW University Hamburg. *8 High Lift Systems and Maximum Lift Coefficients*. URL: https://www.fzt.haw-hamburg.de/pers/Scholz/H00U/AircraftDesign_8_HighLift.pdf.
- [79] Michael V Cook. *Flight dynamics principles: a linear systems approach to aircraft stability and control*. Butterworth-Heinemann, 2012.
- [80] Fabrizio Nicolosi, Danilo Ciliberti, Pierluigi Della Vecchia et al. 'A comprehensive review of vertical tail design'. In: *Aircraft Engineering and Aerospace Technology* 89.4 (2017), pp. 547–557.
- [81] Steven M. LaValle. 'Rapidly-exploring random trees : a new tool for path planning'. In: *The annual research report* (1998). URL: <https://api.semanticscholar.org/CorpusID:14744621>.
- [82] Sertac Karaman and Emilio Frazzoli. 'Sampling-based algorithms for optimal motion planning'. In: *The International Journal of Robotics Research* 30.7 (2011), pp. 846–894. DOI: 10.1177/0278364911406761.
- [83] RJ Geraerts, Mark H Overmars et al. 'Sampling techniques for probabilistic roadmap planners'. In: (2003).

- [84] Sertac Karaman Joshua Bialkowski Michael Otte and Emilio Frazzoli. 'Efficient collision checking in sampling-based motion planning via safety certificates'. In: *The International Journal of Robotics Research* 35.(7) (2021), pp. 767–796. DOI: 10.1177/0278364915625345.
- [85] Vladimir Gorodetsky, Oleg Karsaev, Vladimir Samoylov et al. 'Multi-Agent Technology for Air Traffic Control and Incident Management in Airport Airspace'. In: (Jan. 2008).
- [86] Israel Lugo-Cárdenas, Gerardo Flores, Sergio Salazar et al. 'Dubins path generation for a fixed wing UAV'. In: May 2014, pp. 339–346. ISBN: 978-1-4799-2376-2. DOI: 10.1109/ICUAS.2014.6842272.
- [87] Mark W. Mueller and Raffaello D'Andrea. 'Relaxed hover solutions for multicopters: Application to algorithmic redundancy and novel vehicles'. In: *The International Journal of Robotics Research* 35.8 (2016), pp. 873–889. DOI: <https://doi.org/10.1177/0278364915596233>.
- [88] Sihao Sun, Giovanni Cioffi, Coen de Visser et al. 'Autonomous Quadrotor Flight Despite Rotor Failure With Onboard Vision Sensors: Frames vs. Events'. In: *IEEE Robotics and Automation Letters* 6.2 (2021), pp. 580–587. DOI: <https://doi.org/10.1109/LRA.2020.3048875>.
- [89] Wilson J. Rugh and Jeff S. Shamma. 'Research on gain scheduling'. In: *Automatica* 36.10 (2000), pp. 1401–1425. ISSN: 0005-1098. DOI: [https://doi.org/10.1016/S0005-1098\(00\)00058-3](https://doi.org/10.1016/S0005-1098(00)00058-3).
- [90] Daniel Dueri, Yuanqi Mao, Zohaib Mian et al. 'Trajectory optimization with inter-sample obstacle avoidance via successive convexification'. In: *2017 IEEE 56th Annual Conference on Decision and Control (CDC)* (2017), pp. 1150–1156. DOI: 10.1109/CDC.2017.8263811.
- [91] P. J. W. Koelewijn and R. Tóth. *Automatic Grid-based LPV Embedding of Nonlinear Systems*. Technical Report TUE CS. Eindhoven University of Technology, 2021.
- [92] Xin-She Yang. 'Chapter 23 - Optimization'. In: *Engineering Mathematics with Examples and Applications*. Academic Press, 2017, pp. 267–283. DOI: <https://doi.org/10.1016/B978-0-12-809730-4.00031-8>.
- [93] Erwan Bernard, Nicolas Rivière, Mathieu Renaudat et al. 'Active and thermal imaging performance under bad weather conditions'. In: *6th International Symposium on Optronics in Defence and Security (OPTRO 2014)*. Paris, FR, 2014. URL: <https://oatao.univ-toulouse.fr/11729/>.
- [94] Michel Armand & Peter Axmann. 'Lithium-ion batteries – Current state of the art and anticipated developments'. In: *Journal of Power Sources* 479 (2020), p. 228708. DOI: <https://doi.org/10.1016/j.jpowsour.2020.228708>.
- [95] M. Chen and G. A. Rincon-Mora. 'Accurate Electrical Battery Model Capable of Predicting Runtime and I–V Performance'. In: *IEEE Transactions on Energy Conversion* 21.2 (2006), pp. 504–511. DOI: 10.1109/TEC.2006.874229.
- [96] Patrick Vratny, Corin Gologan, Clément Pernet et al. 'Battery Pack Modeling Methods for Universally-Electric Aircraft'. In: Sept. 2013.
- [97] Mihaela Mitici, Birgitte Hennink, Marilena Pavel et al. 'Prognostics for Lithium-ion batteries for electric Vertical Take-off and Landing aircraft using data-driven machine learning'. In: *Energy and AI* 12 (2023), p. 100233. DOI: <https://doi.org/10.1016/j.egyai.2023.100233>.
- [98] Toshihiro Yoshida, Michio Takahashi, Satoshi Morikawa et al. 'Degradation Mechanism and Life Prediction of Lithium-Ion Batteries'. In: *Journal of The Electrochemical Society* 153 (Mar. 2006), A576–A582. DOI: <https://doi.org/10.1149/1.2162467>.
- [99] D Li, M Zhimao, C Mingsheng et al. 'Influence factors and identification of state-of-health for traction battery'. In: *IOP Conference Series: Materials Science and Engineering* 1043.5 (Jan. 2021), p. 052037. DOI: 10.1088/1757-899X/1043/5/052037. URL: <https://dx.doi.org/10.1088/1757-899X/1043/5/052037>.
- [100] Tesla. *Introducing V3 supercharging*. URL: <https://www.tesla.com/blog/introducing-v3-supercharging>.
- [101] Joby. *Battery thermal management system and method*. URL: <https://patents.google.com/patent/US10960785B2/en>.
- [102] Jiale Guo, Fei Liu, Yalong Xu et al. 'Optimization Design and Numerical Study of Liquid-Cooling Structure for Cylindrical Lithium-Ion Battery Pack'. In: *Journal of Energy Engineering* 147.4 (2021), p. 04021017. DOI: [https://doi.org/10.1061/\(ASCE\)EY.1943-7897.0000768](https://doi.org/10.1061/(ASCE)EY.1943-7897.0000768).

- [103] Caiwei Wang, Liyun Cao, Jianfeng Huang et al. 'Divergent thinking and its application in biomass carbon electrode preparation'. In: *Renewable and Sustainable Energy Reviews* 138 (2021), p. 110564. ISSN: 1364-0321. DOI: <https://doi.org/10.1016/j.rser.2020.110564>.
- [104] Abniel Machín, Carmen Morant and Francisco Márquez. 'Advancements and Challenges in Solid-State Battery Technology: An In-Depth Review of Solid Electrolytes and Anode Innovations'. In: *Batteries* 10.1 (2024). ISSN: 2313-0105. DOI: <https://doi.org/10.3390/batteries10010029>.
- [105] Manuel Ank, Alessandro Sommer, Kareem Abo Gamra et al. 'Lithium-Ion Cells in Automotive Applications: Tesla 4680 Cylindrical Cell Teardown and Characterization'. In: *Journal of The Electrochemical Society* 170 (Dec. 2023). DOI: <https://doi.org/10.1149/1945-7111/ad14d0>.
- [106] Ansys GRANTA EduPack software. ANSYS, Inc., Cambridge, UK. URL: www.ansys.com/materials.
- [107] Performance Composites. *Mechanical properties of carbon fibre composite materials, fibre / epoxy resin (120°C cure)*. URL: https://www.performance-composites.com/carbonfibre/mechanicalproperties_2.asp.
- [108] PORA Jerome. 'Composite materials in the airbus A380-from history to future'. In: *Beijing: Proceedings 13th International Conference on Composite Materials (ICCM-13)*. 2001.
- [109] Mária Mrázová. 'Advanced composite materials of the future in aerospace industry'. In: *INCAS BULLETIN* 5 (Sept. 2013), pp. 139–150. DOI: 10.13111/2066-8201.2013.5.3.14.
- [110] JPC Pinto. 'Economic comparison between materials in the aerospace industry'. In: *no. June* (2017).
- [111] I. Annamalai, K. Karthik, Nitheesh Kumar et al. 'Experimental investigation of mechanical properties of GLARE composite with different layup sequences'. In: *Materials Today: Proceedings* 46 (2021). 28th International Conference on Processing and Fabrication of Advanced Materials (PFAM28), pp. 1371–1375. ISSN: 2214-7853. DOI: <https://doi.org/10.1016/j.matpr.2021.02.487>.
- [112] Ramin Sedaghati, P Eng and Mostafa SA Elsayed. 'Wing-Box Structural Design Optimization'. In: *Department of Mechanical and Industrial Engineering Conchordia University. Ref. No: CRIAQ* (2006).
- [113] Howard D Curtis. 'Fundamentals of aircraft structural analysis'. In: *(No Title)* (1997).
- [114] CS23 EASA. *Easy Access Rules for Normal-Category Aeroplanes (CS-23)(CS Amendment 5, AMC/GM Issue 2)*. 2018.
- [115] PteroDynamics Inc. *PteroDynamics: Autonomous VTOL Aircrafts*. Accessed: 17-05-2024. 2024. URL: <https://pterodynamics.com>.
- [116] Dishant Kothia, Japneet Singh and Akanksha Dadhich. 'Design, Analysis and Optimization of folding wing mechanism for effective utilization of air side area'. In: *Int. J. Aerosp. Mech. Eng.* 3 (2016), pp. 22–28.
- [117] Pterov. *Vertical Takeoff and landing airframe*. US 10 , 252 , 798 B2. Sept. 2019. URL: <https://patents.google.com/patent/US10252798B2>.
- [118] eVTOL News. *Lilium Jet (7-Seater)*. 2024. URL: <https://evtol.news/lilium-gmbh-lilium-jet-7-seater>.
- [119] FS Pranoto, A Wirawan and DA Purnamasari. 'Electrical power budgeting analysis for LSA-02 UAV technology demonstrator'. In: *IOP Conference Series: Materials Science and Engineering*. Vol. 160. 1. IOP Publishing. 2016, p. 012088. DOI: <https://doi.org/10.1088/1757-899X/160/1/012088>.
- [120] Rob Farrington and John Rugh. *Impact of vehicle air-conditioning on fuel economy, tailpipe emissions, and electric vehicle range*. Tech. rep. National Renewable Energy Lab.(NREL), Golden, CO (United States), 2000.
- [121] Clean Aviation. *SMARTWISE shrinks aircraft health tech*. Accessed: 08-05-2024. URL: <https://www.clean-aviation.eu/media/news/smartwise-shrinks-aircraft-health-tech>.
- [122] GPS.gov. *Other Global Navigation Satellite Systems (GNSS)*. Accessed: 08-05-2024. URL: [https://www.gps.gov/systems/gnss/#:~:text=Global%20navigation%20satellite%20system%20\(GNSS,a%20global%20or%20regional%20basis..](https://www.gps.gov/systems/gnss/#:~:text=Global%20navigation%20satellite%20system%20(GNSS,a%20global%20or%20regional%20basis..)

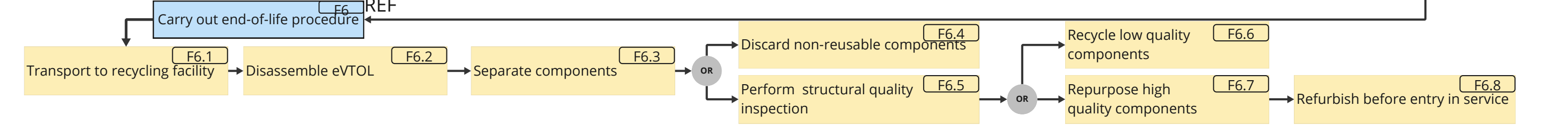
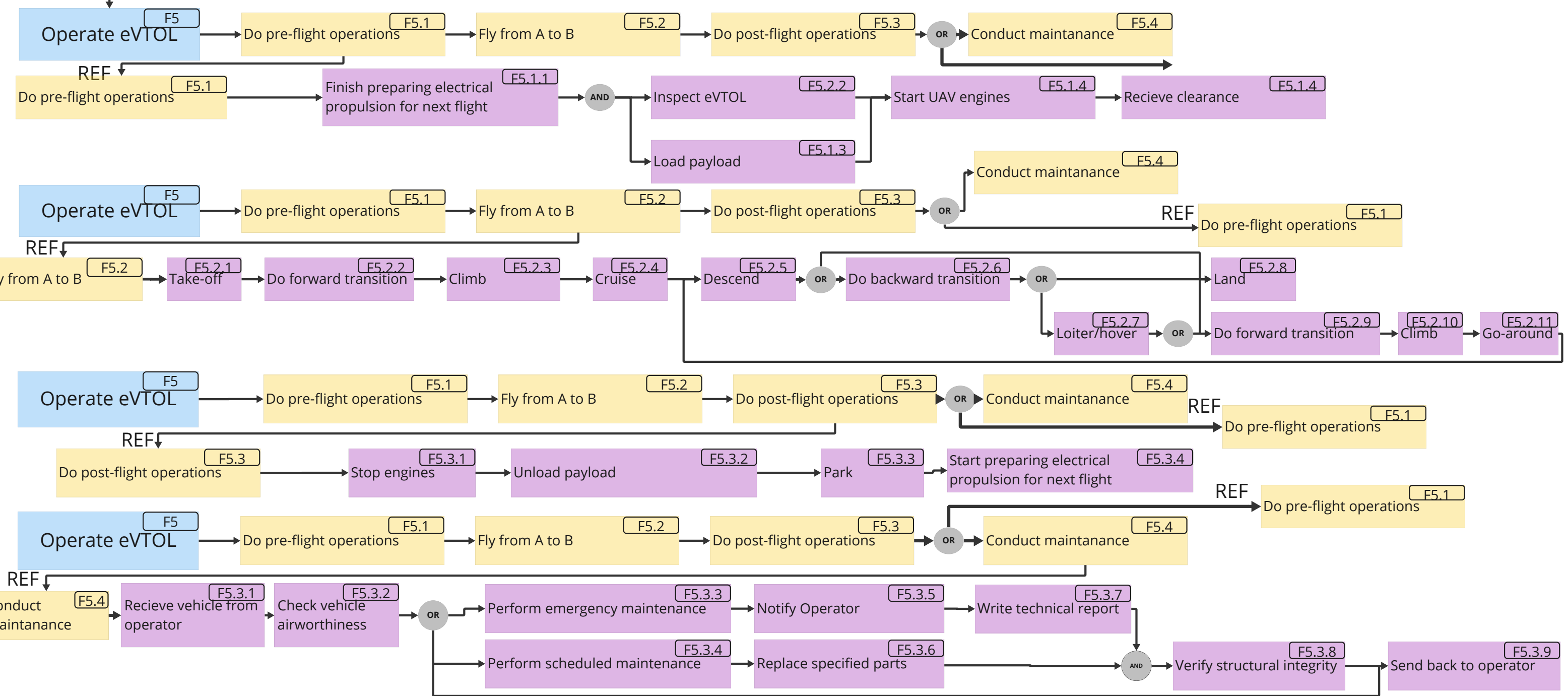
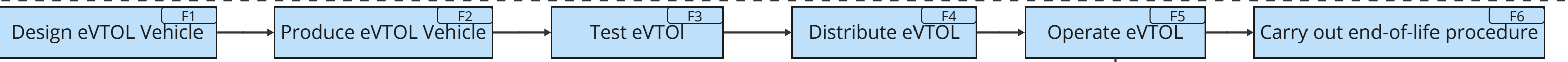
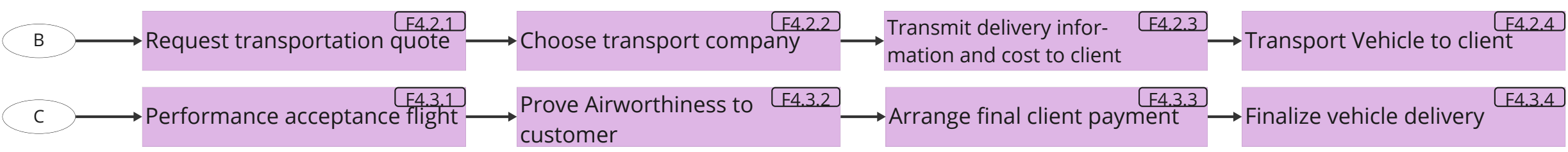
- [123] Boeing. *Concept of Operations for Uncrewed Urban Air Mobility*. Accessed: 2024-06-19. 2021. URL: <https://www.boeing.com/content/dam/boeing/boeingdotcom/innovation/con-ops/docs/Concept-of-Operations-for-Uncrewed-Urban-Air-Mobility.pdf>.
- [124] *Syllabus for Part-M Maintenance Training*. European Union Aviation Safety Agency (EASA). 2009. URL: https://www.easa.europa.eu/sites/default/files/dfu/approvals-and-standardisation-docs-syllabi-Syllabus_Part_M_Maintenance_05022009.pdf.
- [125] Australian Government - Civil Aviation Safety Authority. *Guide to vertiport design*. 2024.
- [126] Daniela Angelica Giovingo. 'RAMS and Maintenance cost assessment in a Multidisciplinary Design Optimization environment'. PhD thesis. Politecnico di Torino, 2019.
- [127] Mayank V Bendarkar, Darshan Sarojini, Evan Harrison et al. 'Evaluation of off-nominal performance and reliability of a distributed electric propulsion aircraft during early design'. In: *AIAA Scitech 2021 Forum*. 2021, p. 1723. DOI: <https://doi.org/10.2514/6.2021-1723>.
- [128] John C Conlon. *Test and evaluation of system reliability, availability, maintainability: a primer*. Office of the Director, Defense Test and Evaluation, Under Secretary of ..., 1982.
- [129] P. Sieb, J. Michelmann, F. Flöter et al. 'Identifying challenges in maintenance planning for on-demand UAM fleets using agent-based simulations'. In: *CEAS Aeronaut J* 14 (2023), pp. 637–660. DOI: 10.1007/s13272-023-00665-y.
- [130] H. Ritchie and M. Roser. *Cars, planes, trains: Where do CO2 emissions from transport come from?* 2024. URL: <https://ourworldindata.org/co2-emissions-from-transport>.
- [131] Ilyès Miri, Abbas Fotouhi and Nathan Ewin. 'Electric vehicle energy consumption modelling and estimation—A case study'. In: *International Journal of Energy Research* 45.1 (2021), pp. 501–520.
- [132] N.André and M.Hajek. 'Robust environmental life cycle assessment of electric VTOL concepts for urban air mobility'. In: *AIAA aviation 2019 forum*. 2019, p. 3473.
- [133] Ayush Jha, Nirmal Prabhakar, Dominik Karbowski et al. 'Urban Air Mobility: A preliminary case study for Chicago and Atlanta'. In: *2022 IEEE Transportation Electrification Conference & Expo (ITEC)*. IEEE. 2022, pp. 300–306.
- [134] Arbin Instruments. *The Advantages and Challenges of Urban Air Mobility*. Accessed: 21-05-2024. Jan. 2021. URL: <https://arbin.com/the-advantages-and-challenges-of-urban-air-mobility/>.
- [135] Michael F Ashby. *Materials and the environment: eco-informed material choice*. 2nd Edition. Elsevier, 2012. ISBN: ISBN: 9780123859716.
- [136] Mats Zackrisson, Lars Avellán and Jessica Orlenius. 'Life cycle assessment of lithium-ion batteries for plug-in hybrid electric vehicles—Critical issues'. In: *Journal of cleaner production* 18.15 (2010), pp. 1519–1529.
- [137] Guillaume Majeau-Bettez, Troy R Hawkins and Anders Hammer Strømman. 'Life cycle environmental assessment of lithium-ion and nickel metal hydride batteries for plug-in hybrid and battery electric vehicles'. In: *Environmental science & technology* 45.10 (2011), pp. 4548–4554.
- [138] Göran Finnveden, Michael Z Hauschild, Tomas Ekvall et al. 'Recent developments in life cycle assessment'. In: *Journal of environmental management* 91.1 (2009), pp. 1–21.
- [139] Gregor Wernet, Christian Bauer, Bernhard Steubing et al. 'The ecoinvent database version 3 (part I): overview and methodology'. In: *The International Journal of Life Cycle Assessment* 21 (2016), pp. 1218–1230.
- [140] Christopher Silva, Wayne R Johnson, Eduardo Solis et al. 'VTOL urban air mobility concept vehicles for technology development'. In: *2018 Aviation Technology, Integration, and Operations Conference*. 2018, p. 3847.
- [141] D Felix Finger, Falk Goetten, Carsten Braun et al. 'Cost estimation methods for hybrid-electric general aviation aircraft'. In: *Proceedings of 11th Asia-Pacific International Symposium on Aerospace Technology (APISAT 2019), Gold Coast, Australia*. 2019, pp. 4–6.
- [142] Julian Hoelzen, Yaolong Liu, Boris Bensmann et al. 'Conceptual Design of Operation Strategies for Hybrid Electric Aircraft'. In: *Energies* 11.1 (2018). ISSN: 1996-1073. DOI: <https://doi.org/10.3390/en11010217>.

- [143] et al. Michel Armand. 'Lithium-ion batteries – Current state of the art and anticipated developments'. In: *Journal of Power Sources* 479 (2020), p. 228708. ISSN: 0378-7753. DOI: <https://doi.org/10.1016/j.jpowsour.2020.228708>. URL: <https://www.sciencedirect.com/science/article/pii/S0378775320310120>.
- [144] Michael Kreimeier. 'Evaluation of on-demand air mobility concepts with utilization of electric powered small aircraft'. Dissertation. Aachen: RWTH Aachen University, 2018, 1 Online-Ressource (XIX, 165 Seiten) : Illustrationen, Diagramme, Karten. DOI: <https://doi.org/10.18154/RWTH-2018-223676>.
- [145] Ben Goldstein. *Joby Versus Archer: Vertical Integration Strategy Is A Key Split*. Accessed: 19-06-2024. May 2024. URL: <https://aviationweek.com/business-aviation/aircraft-propulsion/joby-versus-archer-vertical-integration-strategy-key-split>.
- [146] Project Group 01. *Transwing eVTOL Baseline Report*. Delft, the Netherlands: Delft University of Technology, 2024.

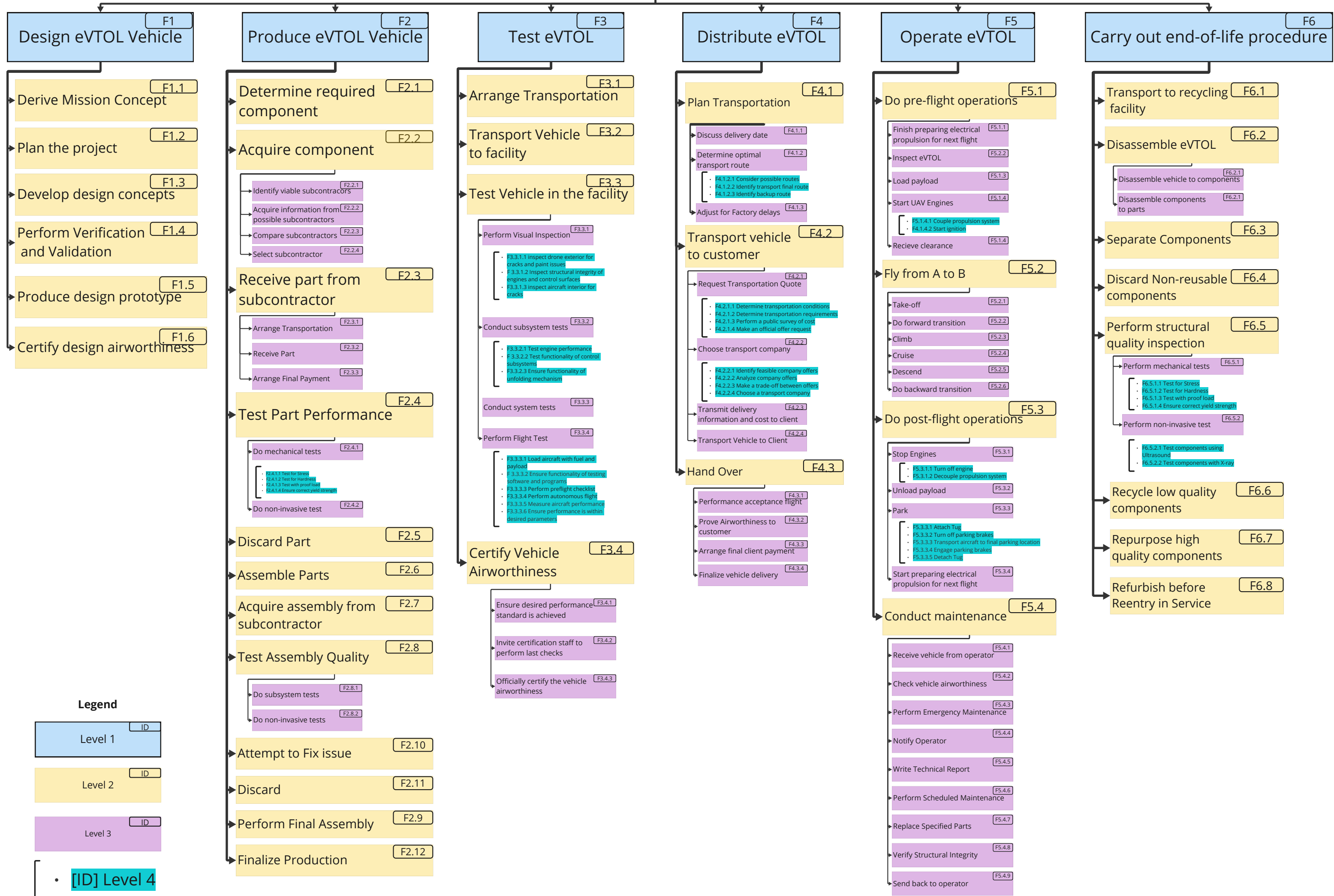


REF = Reference to previous layer

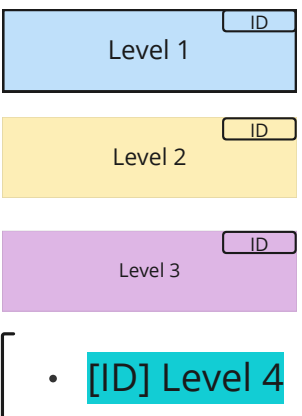
Level 1	ID
Level 2	ID
Level 3	ID

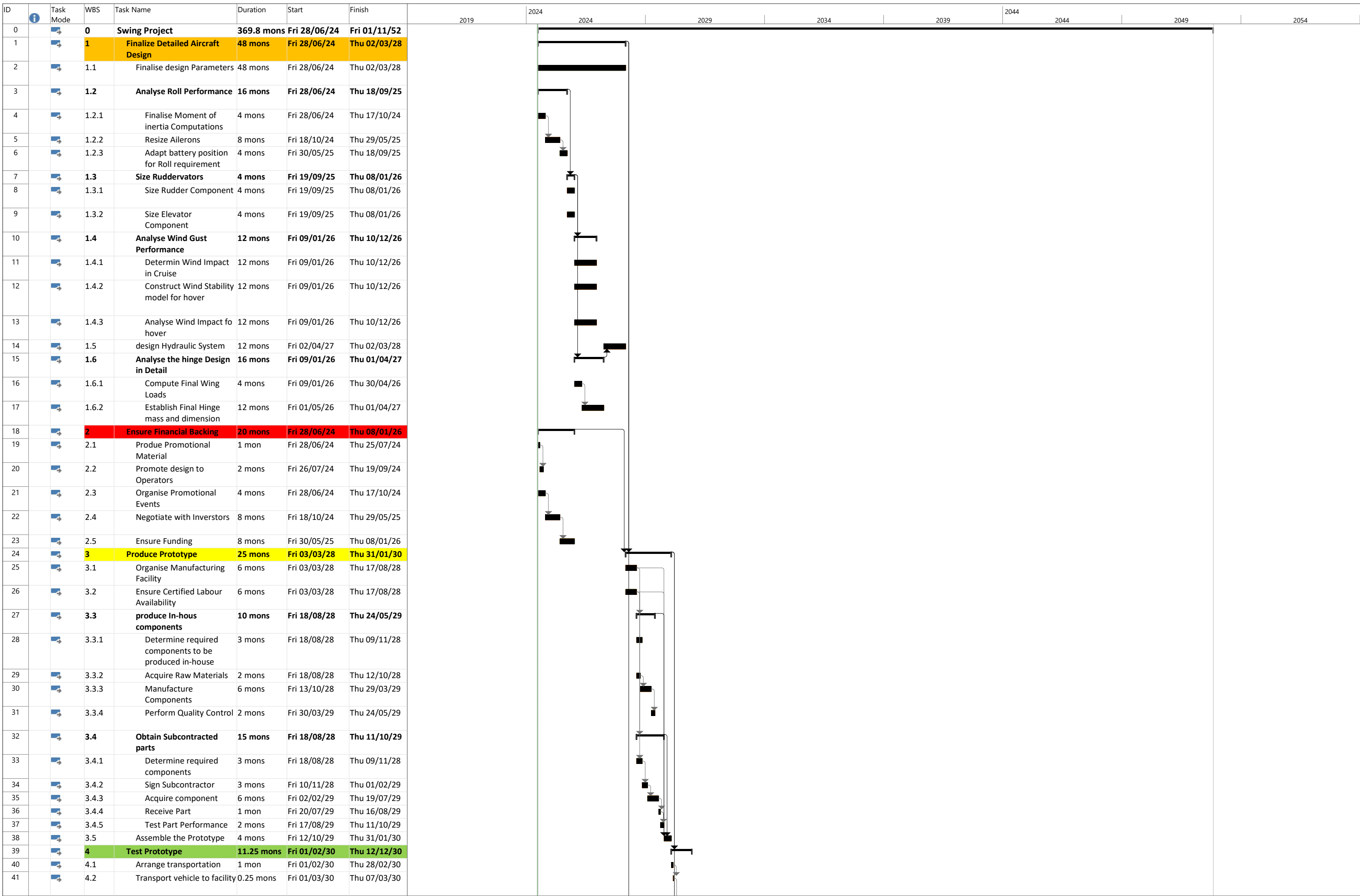


eVTOL mission



Legend

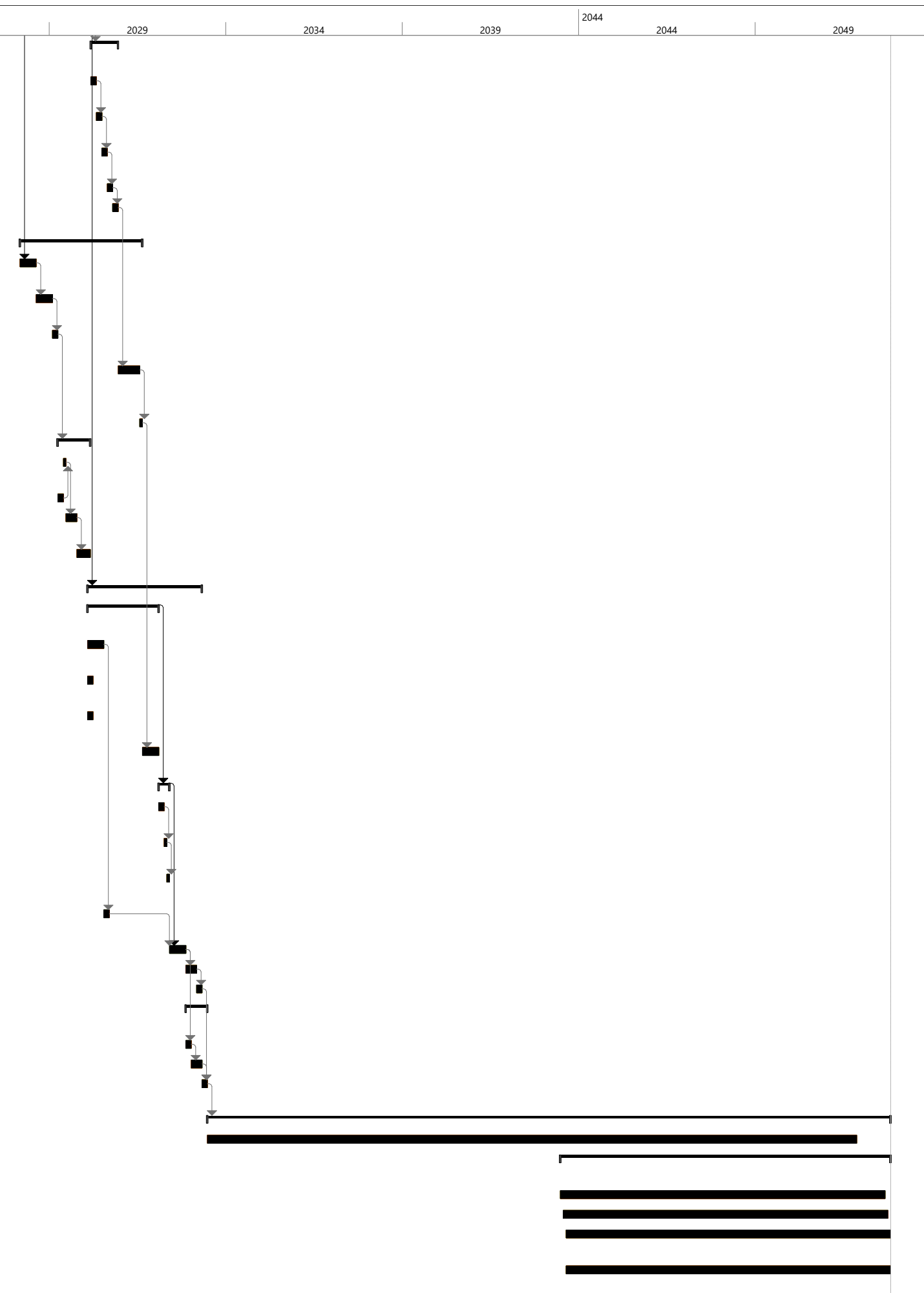




Project: Swing Project
Date: Wed 19/06/24

Tasks	Start Commercial operations	Market Design	Test Prototype	Ensure Financial backing	Summary
Provide Customer Support	Begin Mass Production	Certify Design	Produce Prototype	Finalize Detailed Aircraft Design	Swing Project

ID	Task Mode	WBS	Task Name	Duration	Start	Finish	2019	2024	2029	2034	2039	2044	2049	2054
42		4.3	Test the vehicle in the facility	10 mons	Fri 08/03/30	Thu 12/12/30								
43		4.3.1	Perform Structural Tests	2 mons	Fri 08/03/30	Thu 02/05/30								
44		4.3.2	Perform Electronics Tests	2 mons	Fri 03/05/30	Thu 27/06/30								
45		4.3.3	Perform Wind Tunnel Analysis	2 mons	Fri 28/06/30	Thu 22/08/30								
46		4.3.4	Perform Flight Test	2 mons	Fri 23/08/30	Thu 17/10/30								
47		4.3.5	Perfrom qualification Test	2 mons	Fri 18/10/30	Thu 12/12/30								
48		5	Certify Design	45.25 mons	Fri 03/03/28	Thu 21/08/31								
49		5.1	Establish Certification Basis	6 mons	Fri 03/03/28	Thu 17/08/28								
50		5.2	Establish Certification programme	6 mons	Fri 18/08/28	Thu 01/02/29								
51		5.3	Send Certification paperwork to EASA	2 mons	Fri 02/02/29	Thu 29/03/29								
52		5.4	Demonstrate Compliance with Requirements	8 mons	Fri 13/12/30	Thu 24/07/31								
53		5.5	Receive Cetrification	1 mon	Fri 25/07/31	Thu 21/08/31								
54		6	Market Design	12 mons	Fri 30/03/29	Thu 28/02/30								
55		6.1	Create Advertising Material	1 mon	Fri 25/05/29	Thu 21/06/29								
56		6.2	Confirm Cost Analysis	2 mons	Fri 30/03/29	Thu 24/05/29								
57		6.3	Contract Potential Customers	4 mons	Fri 22/06/29	Thu 11/10/29								
58		6.4	Negotiate deals with customers	5 mons	Fri 12/10/29	Thu 28/02/30								
59		7	Begin Mass Production	42.25 mons	Fri 01/02/30	Thu 28/04/33								
60		7.1	Expand Manufacturing Facility	26.25 mons	Fri 01/02/30	Thu 05/02/32								
61		7.1.1	Determine Production Volume	6 mons	Fri 01/02/30	Thu 18/07/30								
62		7.1.2	Anticipate necessary production capacity	2 mons	Fri 01/02/30	Thu 28/03/30								
63		7.1.3	Determine Expansion Costs	2 mons	Fri 01/02/30	Thu 28/03/30								
64		7.1.4	Commence Expansion of Facility	6 mons	Fri 22/08/31	Thu 05/02/32								
65		7.2	Acquire Materials	4 mons	Fri 06/02/32	Thu 27/05/32								
66		7.2.1	Analyse Material Sustainability	2 mons	Fri 06/02/32	Thu 01/04/32								
67		7.2.2	Test Material Properties	1 mon	Fri 02/04/32	Thu 29/04/32								
68		7.2.3	Finalise Material acquisition	1 mon	Fri 30/04/32	Thu 27/05/32								
69		7.3	Ensure Subcontractor timely delivery	2 mons	Fri 19/07/30	Thu 12/09/30								
70		7.4	Perform Quality Control	6 mons	Fri 28/05/32	Thu 11/11/32								
71		7.5	Assemble the Vehicle	4 mons	Fri 12/11/32	Thu 03/03/33								
72		7.6	Perfrom Vehicle Testing	2 mons	Fri 04/03/33	Thu 28/04/33								
73		8	Start Commercial operations	8 mons	Fri 12/11/32	Thu 23/06/33								
74		8.1	Sign Shipment contract	2 mons	Fri 12/11/32	Thu 06/01/33								
75		8.2	Plan Shipment	4 mons	Fri 07/01/33	Thu 28/04/33								
76		8.3	Transport vehicle to customer	2 mons	Fri 29/04/33	Thu 23/06/33								
77		9	Provide Customer Support	252.55 mons	Fri 24/06/33	Fri 01/11/52								
78		9.1	Conduct maintanance	240 mons	Fri 24/06/33	Thu 16/11/51								
79		9.2	Carry out end-of-life procedures	122.15 mons	Wed 24/06/43	Fri 01/11/52								
80		9.2.1	Disassemble eVTOL	120 mons	Wed 24/06/43	Tue 03/09/52								
81		9.2.2	test Component Quality	120 mons	Fri 24/07/43	Thu 03/10/52								
82		9.2.3	Recycle Low Quality Components	120 mons	Mon 24/08/43	Fri 01/11/52								
83		9.2.4	Repurpose High Quality Components	120 mons	Mon 24/08/43	Fri 01/11/52								



Project: Swing Project
Date: Wed 19/06/24

Tasks	Start Commercial operations	Market Design	Test Prototype	Ensure Financial backing	Summary
Provide Customer Support	Begin Mass Production	Certify Design	Produce Prototype	Finalize Detailed Aircraft Design	Swing Project